CONTENTS

Kacper Fiedurek, Paweł Szroeder, Marek Macko, Aneta Raszkowska-Kaczor, Marcin Borowicz, Natalia Puszczykowska
Introduction to Modelling the Correlation Between Grain Sizes of Feed Material and the Structure and Efficiency of the Process of Co-Rotating Twin-Screw Extrusion of Non-Flammable Composites with a PLA Matrix 301

Silvia Maláková, Samuel Sivák
GPS Application in the Design of Gearboxes 309

Daniel Kaczor, Krzysztof Bajer, Grzegorz Domek, Piotr Madajski, Aneta Raszkowska-Kaczor, Paweł Szroeder
Influence of Extruder Plasticizing Systems on the Selected Properties of PLA/Graphite Composite 316

Elżbieta Gawrońska, Robert Dyja, Maria Zych, Grzegorz Domek
Selection of the Heat Transfer Coefficient using Swarming Algorithms 325

Michał Bembenek, Andrzej Uhryński
The Use of Thermography to Determine the Compaction of a Saddle-Shaped Briquette Produced in an Innovative Roller Press Compaction Unit 340

Artem Artyukhov, Jan Krmela, Vladimira Krmelova, Dastan Ospanov
Vortex-Type Granulation Machines: Technological Basis Of Calculation And Implementation Roadmap 347

Paweł Sułkowicz, Robert Babiarz, Jan Burek, Jarosław Buk, Kamil Gancarczyk
A Method of Increasing the Accuracy of Low-Stiffness Shafts: Single-Pass Traverse Grinding without Steady Rests 357

Kamil Krasuski, Janusz Ćwiklak, Mieczysław Bakuła, Magda Mrozik
Analysis of the Determination of the Accuracy Parameter for Dual Receivers Based on Egnos Solution in Aerial Navigation 365

Noureddine Aimeur, Noureddine Menasri
Computational Investigation of vibration Characteristics Analysis for Industrial Rotor 373

Roman Mediukh, Vira Mediukh, Vasyl Labunets, Pavlo Nosko, Oleksandr Bashta, Irina Kondratenko
Investigation of Structure Formation and Tribotechnical Properties of Steel Plasma Coatings after Chemical-Heat Treatment and Liquid-Phase Impregnation 382

Ryszard Szczebiot, Roman Kaczyński, Leszek Gołdyn
Numerical Criterion for the Duration of Non-Chaotic Transients in ODEs 388

Andrzej Kazberuk
Application of the Deformation Fracture Criterion to Cracking of Disc Specimens with a Central Narrow Slot 393

Adam Adamowicz
Determination of Thermal Diffusivity Values Based on The Inverse Problem of Heat Conduction – Numerical Analysis 399

Wojciech Horak, Barbara Stępień, Bogdan Sapiński
Experiment and Analysis of the Limit Stresses of Magnetorheological Fluid 408

Rached Miri, Mohamed A. Abbassi, Mokhtar Ferhi, Ridha Djebali
Second Law Analysis of MHD Forced Convective Nanoliquid Flow Through a Two-Dimensional Channel 417

Abstracts XXIX

acta mechanica et automatica, vol.16 no.4 (2022)

ABSTRACTS

Kacper Fiedurek, Paweł Szroeder, Marek Macko, Aneta Raszkowska-Kaczor, Marcin Borowicz, Natalia Puszczykowska
Introduction to Modelling the Correlation Between Grain Sizes of Feed Material and the Structure and Efficiency of the Process of Co-Rotating Twin-Screw Extrusion of Non-Flammable Composites with a PLA Matrix

Co-rotating twin-screw extrusion is an energy consuming process that is generally not fully optimised to a specific polymer. From the point of view of the efficiency of the extrusion process, the starting material should be characterised by small grain sizes in comparison to the screw channel area, small surface area to volume ratio and small internal friction between the pellets. To develop a model describing the effect of polylactide (PLA) grain size on the extrusion efficiency, a series of experiments with a twin-screw extruder were carried out during which the energy consumption; torque on shafts and temperature of the melt on the extruder die were monitored. As feed material, both the neat PLA with different grain sizes and the PLA with expandable graphite fillers and phosphorous-based flame retardants were used. Morphology and dispersion quality of the composites were examined using scanning electron microscopy (SEM); flammability, smoke production, mass loss and heat release rates were tested using cone calorimetry; and melt flow rate was determine using a plastometer. Moreover, the thermal properties of the obtained composites were determined using differential scanning calorimetry (DSC). The results show that the choice of the starting material affects both the efficiency of the extrusion process and the flame retardancy properties of the composite materials.

Silvia Maláková, Samuel Sivák
GPS Application in the Design of Gearboxes

The integrated geometrical product specification (GPS) system for workpiece geometry specification and verification is an improved engineering tool for product development and production. The goal of the GPS system is to provide tools for cost-effective management of variability in products and processes. This can be achieved by using a more precise way of expressing the functional requirements of the workpiece, complete and well-defined specifications and integrated verification approaches. The intended function of the product is ensured by controlling the geometry and material properties of the workpiece parts, which make up the product. GPS is a language just for checking geometry, and further development is based on computational mathematics and correct, consistent logic using general sets of rules that can be applied to all types of specifications. This article deals with the application of GPS rules in the design of gearboxes.

Daniel Kaczor, Krzysztof Bajer, Grzegorz Domek, Piotr Madajski, Aneta Raszkowska-Kaczor, Paweł Szroeder
Influence of Extruder Plasticizing Systems on the Selected Properties of PLA/Graphite Composite

Twin-screw extrusion is a crucial method for the direct inserting of carbon micro- and nanomaterials into a polymer matrix using a dry procedure. The study aimed to determine the influence of the parameters of the twin-screw extruder plasticizing system on the dispersion homogeneity and distribution of graphite filler in the polylactide polymer matrix and overall quality of the composite. As a filler, a graphite micropowder with a 5 μm lateral size of platelets was used at concentration of 1 wt.%. Three configurations of screws with different mixing intensity and various types segments were considered in the extrusion experiments. Morphology and chemical structure of the obtained composites were examined using scanning electron microscopy (SEM), Fourier transform infrared spectroscopy – attenuated total reflectance (FTIR-ATR) and Raman spectroscopy. Differential scanning calorimetry (DSC) and melting flow rate measurements (MFR) were used to asses thermal and rheological properties of the composites. Samples of the polylactide/graphite composites were also subjected to mechanical tests. The results show that the selection of the mechanical parameters of twin-screw extruder plasticizing system plays a key role in the preparation of the homogeneous PLA/graphite composites. Incorrect selection of the screw geometry results in poor mixing quality and a significant deterioration of the mechanical and thermal properties of the composites. Optimised mixing and extrusion parameters can be the starting point for the design of efficient twin-screw extruder plasticizing system for fabrication of PLA composites with carbon nanotube and graphene fillers.

Elżbieta Gawrońska, Robert Dyja, Maria Zych, Grzegorz Domek
Selection of the Heat Transfer Coefficient using Swarming Algorithms

The article presents the use of swarming algorithms in selecting the heat transfer coefficient, taking into account the boundary condition of the IV types. Numerical calculations were made using the proprietary TalyFEM program and classic form of swarming algorithms. A function was also used for the calculations, which, during the calculation, determined the error of the approximate solution and was minimalised using a pair of individually employed algorithms, namely artificial bee colony (ABC) and ant colony optimisation (ACO). The tests were carried out to select the heat transfer coefficient from one range. Describing the geometry for a mesh of 408 fine elements with 214 nodes, the research carried out presents two squares (one on top of the other) separated by a heat transfer layer with a κ coefficient. A type III boundary condition was established on the right and left of both edges. The upper and lower edges were isolated, and a type IV boundary condition with imperfect contact was established between

the squares. Calculations were made for ABC and ACO, respectively, for populations equal to 20, 40 and 60 individuals and 2, 6 and 12 iterations. In addition, in each case, 0%, 1%, 2% and 5% noise of the reference values were also considered. The obtained results are satisfactory and very close to the reference values of the κ parameter. The obtained results demonstrate the possibility of using artificial intelligence (AI) algorithms to reconstruct the IV type boundary condition value during heat conduction modelling.

Michał Bembenek, Andrzej Uhryński
The Use of Thermography to Determine the Compaction of a Saddle-Shaped Briquette Produced in an Innovative Roller Press Compaction Unit

The unit compacting pressure in the fine-grained material consolidation process in the roller press can reach >100 MPa and is a parameter that results, among other things, from the properties of the consolidated material and the compaction unit geometry. Achieving the right pressure during briquetting is one of the factors that guarantee the proper consolidation and quality of briquettes. The distribution of the temperature on the surface of the briquettes correlates with locally exerted pressure. The present work aimed to analyse the briquetting process of four fine-grained materials in a roller press equipped with saddle-shaped briquette-forming rollers based on images obtained from the thermography conducted immediately after their consolidation. The tests were carried out in a roller press that was equipped with forming rollers of 450-mm diameter and having a cavity with a volume of 4 cm^3, as described by patent PL 222229 B1. Two mixtures of hydrated lime with 9.1 wt% and 13.0 wt% water, a mixture of scale and a mixture of electric arc furnace (EAF) dust were used for the tests. In most mixtures, the highest temperatures were achieved in the middle-upper part of the briquettes. The briquettes from the EAF dust mixture heated locally the most on the surface up to 37.7 °C. The difference between the maximum briquette temperature and the ambient temperature was 20.2 °C.

Artem Artyukhov, Jan Krmela, Vladimira Krmelova, Dastan Ospanov
Vortex-Type Granulation Machines: Technological Basis Of Calculation And Implementation Roadmap

This work is devoted to describing the technological foundations and the main stages of calculating granulation machines with active hydrodynamic modes. The optimisation criterion is substantiated when choosing the design of the granulation machine. The work uses methods of analysis and synthesis, search for cause-and-effect relationships, theoretical and computer modelling, and experimental studies. The nodes of the vortex granulator directly influence the formation of a vortex fluidised bed, and the directional movement of granules of various sizes are determined. A technique for carrying out a computer simulation of the hydrodynamic operating conditions of a granulation machine in various operating modes with an assessment of the quality of granulated products (e.g., the production of porous ammonium nitrate) is proposed. The results of a computer simulation of the process of formation of a vortex fluidised bed are presented. A variant of the solution for developing an automation scheme for a vortex-type granulation machine is shown. A roadmap for introducing granulation technology in vortex-type granulation machines is described with details of the main stages. The prospects for improving the design of a vortex-type granulation machine and optimising the operation of a granulation plant to produce porous ammonium nitrate are outlined.

Paweł Sułkowicz, Robert Babiarz, Jan Burek, Jarosław Buk, Kamil Gancarczyk
A Method of Increasing the Accuracy of Low-Stiffness Shafts: Single-Pass Traverse Grinding without Steady Rests

The article presents a method of increasing the shape and dimensional accuracy of low-stiffness shafts manufactured in a single pass of a grinding wheel in traverse grinding. One-pass manufacturing is one of the ways for reducing machining time and increasing efficiency, thus lowering production costs. However, maintaining the necessary accuracy proves to be a challenge because the whole machining allowance has to be removed at once, leaving no room for errors that could be fixed in additional passes of the tool. It is especially true in finishing operations, such as traverse grinding. In addition, grinding the workpiece in a single pass of a grinding wheel leads to high forces, which cause elastic deformation of the part. The lower the stiffness of the part, the more difficult it is to achieve the required accuracy. As a result, there are many methods of improving the accuracy of grinding such parts, but they tend to be either expensive or reduce the machining efficiency. Thus, it is important to seek new methods that would allow improving the accuracy of the machining without reducing its efficiency. The proposed method does not require using steady rests and is based on the measurement of the normal grinding force component. Knowing the value of the grinding force when grinding with a set grinding depth, the elastic deformation of the machine tool–tool–workpiece system is calculated in each position of the grinding wheel. Based on the calculated deformation, the additional infeed of the grinding wheel is implemented in order to stabilise real grinding depth and to increase the accuracy of the produced part. The experimental tests were conducted to prove the effectiveness of the proposed method.

Kamil Krasuski, Janusz Ćwiklak, Mieczysław Bakuła, Magda Mrozik
Analysis of the Determination of the Accuracy Parameter for Dual Receivers Based on Egnos Solution in Aerial Navigation

The paper presents the results of research on the determination of the accuracy parameter for European Geostationary Navigation Overlay System (EGNOS) positioning for a dual set of on-board global navigation satellite system (GNSS) receivers. The study focusses in particular on presenting a modified algorithm to determine the accuracy of EGNOS positioning for a mixed model with measurement weights. The mathematical algorithm considers the measurement weights as a function of the squared inverse and the inverse of the position dilution of precision (PDOP) geometrical coefficient. The research uses actual EGNOS measurement data recorded by two on-board GNSS receivers installed in a Diamond DA 20-C airplane. The calculations determined the accuracy of EGNOS positioning separately for each receiver and the resultant value for the set of two GNSS receivers. Based on the conducted tests, it was determined that the mixed model with measurement weights in the form of a function of the inverse square of the PDOP geometrical coefficient was the most efficient and that it improved the accuracy of EGNOS positioning by 37%–63% compared to the results of position errors calculated separately for each GNSS receiver.

Noureddine Aimeur, Noureddine Menasri
Computational Investigation of vibration Characteristics Analysis for Industrial Rotor

During the operation of a rotor, various types of vibrations appear in this mechanical system and often limit the performance and endanger the safety of the operation. Therefore, dynamic analysis is essential because precise knowledge of the vibration behaviour is essential to ensure proper operation. This article presents a set of scientific techniques for the modelling and simulation of rotor vibrations. To work out the equations of the vibratory movement of the rotor, we used the energy approach of Lagrange. To achieve this, a model with one blading wheel carried by a shaft supported by two hydrodynamic bearings is chosen basedon the characteristics of the rotor studied (Fan 280 cement draft fan). It is an arduous task to manually ascertain the analytical resolution of the differential equations that characterise the vibratory behaviour of the rotor. The numerical approach employing the finite element method, programmed on the ANSYS software, made it possible to perform the vibration analysis of the rotor. First, the FAN 280 cement draft fan rotor is modelled using SolidWorks 3D software and reverse design using the coordinate measuring machine (CMM) for the design of the fins. Then, the modal characteristics of the fan rotor model were analysed using the finite element analysis (FEA) software ANSYS Workbench. Also, to study the effect of blade wear on critical speeds, the Campbell diagram was obtained. Finally, harmonic analysis was performed to determine the amplitude of the rotor vortex at critical speeds obtained with and without blade wear.

Roman Mediukh, Vira Mediukh, Vasyl Labunets, Pavlo Nosko, Oleksandr Bashta, Irina Kondratenko
Investigation of Structure Formation and Tribotechnical Properties of Steel Plasma Coatings after Chemical-Heat Treatment and Liquid-Phase Impregnation

The paper is focused on the studies of the microstructure development and physical and mechanical properties of metal-matrix composite coatings based on steel 11Cr18MoWCu deposited using plasma and galvanoplasma methods. The expediency of combining gas-thermal spraying processes of plasma coatings with open porosity up to 16%–18%, with their subsequent thermodiffusion saturation (chromium plating) or liquid-phase impregnation with eutectic alloys of previously applied Ni–B galvanic layer, is shown. The study of the tribotechnical properties of the proposed coatings showed a significant improvement in their performance under conditions of various types of intensive wear, as well as in corrosive environments.

Ryszard Szczebiot, Roman Kaczyński, Leszek Gołdyn
Numerical Criterion for the Duration of Non-Chaotic Transients in ODEs

The paper proposes an original numerical criterion for the duration analysis of non-chaotic transients based on the Euclidean norm of a properly defined vector. For this purpose, transient trajectories, prior to their entering a small neighbourhood of the limit cycle, are used. The vector has been defined with its components constituting the lengths of the sections, which connect the origin of the coordinate system with appropriately determined transient trajectory points. The norm of the vector for the analysis of non-chaotic transients has also been applied. As an assessment criterion of transients, the convergence of the norm to small neighbourhood of the limit cycle with the assumed accuracy is used. The paper also provides examples of the application of this criterion to the Van der Pol oscillators in the case of periodic oscillations.

Andrzej Kazberuk
Application of the Deformation Fracture Criterion to Cracking of Disc Specimens with a Central Narrow Slot

Using the method of singular integral equations, the elastic-plastic problem for cracked Brazilian disk was solved. Based on the Dugdale model and deformation fracture criterion, the relationships between critical load, notch tip opening displacement and length of the plastic strips were established. Also, the comparison between the present solution for the finite domain and the known solution obtained for the semi-infinite notch in the elastic plane was performed.

Adam Adamowicz
Determination of Thermal Diffusivity Values Based on The Inverse Problem of Heat Conduction – Numerical Analysis

This paper presents a discussion on the accuracy of the method of determining the thermal diffusivity of solids using the solution of the inverse heat conduction equation. A new measurement data processing procedure was proposed to improve the effectiveness of the method. Using the numerical model, an analysis of the sensitivity of the method of thermal diffusivity determination to changes in operational and environmental parameters of the test was carried out. The obtained results showed that the method was insensitive to the parameters of the thermal excitation impulse, the thickness of the tested sample, and the significant influence of convection cooling on its accuracy. The work was completed with the formulation of general conclusions concerning the conditions for determining the thermal diffusivity of materials with the use of the described method.

Wojciech Horak, Barbara Stępień, Bogdan Sapiński
Experiment and Analysis of the Limit Stresses of Magnetorheological Fluid

This paper presents the results of a rheological test of a commercial magnetorheological (MR) fluid (MRF-132DG). The research includes the problem of measuring and interpreting limit stresses under conditions close to the magnetic saturation of the fluid. Four different limit stresses were determined, two related to the yield point and two related to the flow point. Methods for determining limit stresses, especially due to excitation conditions, were also analysed. The aim of this study is to determine the effect of selected parameters on the values of limit stresses of the selected MR fluid. An additional objective is to highlight the problems of defining and interpreting individual limit stresses in MR fluids, particularly in the context of selecting the values of these stresses for the purpose of modeling systems with MR fluids.

Rached Miri, Mohamed A. Abbassi, Mokhtar Ferhi, Ridha Djebali
Second Law Analysis of MHD Forced Convective Nanoliquid Flow Through a Two-Dimensional Channel

The present study deals with fluid flow, heat transfer and entropy generation in a two-dimensional channel filled with Cu–water nanoliquid and containing a hot block. The nanoliquid flow is driven along the channel by a constant velocity and a cold temperature at the inlet, and the partially heated horizontal walls. The aim of this work is to study the influence of the most important parameters such as nanoparticle volume fraction ($0\%\leq\phi\leq4\%$), nanoparticle diameter ($5\text{ nm}\leq dp\leq55\text{ nm}$), Reynolds number ($50\leq Re\leq200$), Hartmann number ($0\leq Ha\leq90$), magnetic field inclination angle ($0\leq\gamma\leq\pi$) and Brownian motion on the hydrodynamic and thermal characteristics and entropy generation. We used the lattice Boltzmann method (LBM: SRT-BGK model) to solve the continuity, momentum and energy equations. The obtained results show that the maximum value of the average Nusselt number is found for case (3) when the hot block is placed between the two hot walls. The minimum value is calculated for case (2) when the hot block is placed between the two insulated walls. The increase in Reynolds and Hartmann numbers enhances the heat transfer and the total entropy generation. In addition, the nanoparticle diameter increase reduces the heat transfer and the irreversibility, the impact of the magnetic field inclination angle on the heat transfer and the total entropy generation is investigated, and the Brownian motion enhances the heat transfer and the total entropy generation.

DOI 10.2478/ama-2022-0036

acta mechanica et automatica, vol.16 no.4 (2022)
Special Issue "Machine Modeling and Simulations 2022"

INTRODUCTION TO MODELLING THE CORRELATION BETWEEN GRAIN SIZES OF FEED MATERIAL AND THE STRUCTURE AND EFFICIENCY OF THE PROCESS OF CO-ROTATING TWIN-SCREW EXTRUSION OF NON-FLAMMABLE COMPOSITES WITH A PLA MATRIX

Kacper FIEDUREK[*,**], **Paweł SZROEDER**[***], **Marek MACKO**[**]
Aneta RASZKOWSKA-KACZOR[*], **Marcin BOROWICZ**[****], **Natalia PUSZCZYKOWSKA**[*,**]

[*]Łukasiewicz Research Network, Institute for Engineering Polymer Materials and Dyes, Skłodowskiej-Curie 55, 87-100 Toruń, Poland
[**]Faculty of Mechatronics, Kazimierz Wielki University, Mikołaja Kopernika 1, 85-074 Bydgoszcz, Poland
[***]Institute of Physics, Kazimierz Wielki University, Powstańców Wielkopolskich 2, 85-090 Bydgoszcz, Poland
[****]Institute of Materials Engineering, Kazimierz Wielki University, J. K. Chodkiewicza 30, 85-064 Bydgoszcz, Poland

kacper.fiedurek@impib.lukasiewicz.gov.pl, pawelsz@ukw.edu.pl, mackomar@ukw.edu.pl,
aneta.raszkowska-kaczor@impib.lukasiewicz.gov.pl, m.borowicz@ukw.edu.pl, natalia.puszczykowska@impib.lukasiewicz.gov.pl

received 28 June 2022, revised 29 July 2022, accepted 31 July 2022

Abstract: Co-rotating twin-screw extrusion is an energy consuming process that is generally not fully optimised to a specific polymer. From the point of view of the efficiency of the extrusion process, the starting material should be characterised by small grain sizes in comparison to the screw channel area, small surface area to volume ratio and small internal friction between the pellets. To develop a model describing the effect of polylactide (PLA) grain size on the extrusion efficiency, a series of experiments with a twin-screw extruder were carried out during which the energy consumption; torque on shafts and temperature of the melt on the extruder die were monitored. As feed material, both the neat PLA with different grain sizes and the PLA with expandable graphite fillers and phosphorous-based flame retardants were used. Morphology and dispersion quality of the composites were examined using scanning electron microscopy (SEM); flammability, smoke production, mass loss and heat release rates were tested using cone calorimetry; and melt flow rate was determine using a plastometer. Moreover, the thermal properties of the obtained composites were determined using differential scanning calorimetry (DSC). The results show that the choice of the starting material affects both the efficiency of the extrusion process and the flame retardancy properties of the composite materials.

Key words: introduction to modelling; extrusion; parameters of the process; biodegradable polymers; polymers; flame retardancy

1. INTRODUCTION

The extrusion is the most common and the most widely used method in the production of thermoplastic composites and obtaining polymer mixtures with fillers, functional additives and modifiers [1,2]. The compounding process, as well as extrusion in general, can be described as 'constant dosing, transporting, plasticising, mixing and forming a polymer/composite stream' [1]. The greatest advantages of this process include the relatively low cost of energy inputs per kilogram of product, relative simplicity of processing equipment, possible scalability of the process and versatility of solutions. One extruder can be easily adapted to produce composites from different components. This is often done without interfering with mechanical parameters such as the geometry of the plasticising system and the shape of the head. Only the temperature settings, rotational speed of the screw and dosing amount are adjusted [3]. Several types of extruders are known, but for the purpose of producing composites, co-rotating twin-screw extruders are used, which provide a larger available surface of the extruder barrel, which already results in improved mixing properties of the components. The greatest advantage of the twin-screw extruders over the single-screw extruders is the possibility of using interlocking kneading segments, as well as mixing screws, thanks to which the mixing takes place both on the edge (screw-barrel) and on the above-mentioned elements inducing the shear forces [3,4]. The combination of these two features allows for better dispersion of the filler in the polymer matrix, but a limitation of the process is the fact that the shear forces cause an increase in temperature due to friction [5,6]. It is difficult to describe this process mathematically because there are many variables here that are specific both for the polymers themselves and even for polymer-filler systems [7–10]. Often, as modelling is conducted, a single section or even a single-screw element of an extruder is referred. Excessively high temperatures and friction alone can lead to the degradation of the polymer material, where the obtained product may lose its properties, which in turn may translate into problems in the processes of further forming the finished polymer composite.

The selection of the appropriate configuration of the plasticising system can therefore be presented as a search for a compromise between the best mixing of components and the lowest possible degradation of components, especially polymers [11,12]. One way to avoid the impact is to crush commercially available granules of polymers to reach smaller grain sizes [1,13]. The polymers are usually supplied in the form of pellets which are easy to dose in single-screw extruders and injection moulding machines. The ratio of the bulk density to the actual density is also the parameter that affects the possibility of obtaining the right, high pressure during product formation. In the case of the production of composites, however, the aim is to obtain the best possible distribution of the filler in the polymer matrix, the lowest possible polymer degradation with simultaneous energy savings and the lowest possible wear of mechanical elements of the plasticising system: no high pressure is required, and it is even undesirable; what is more is that some of additives are fragile to temperature, shear forces and residue time in extruder [14–16].

All parameters of the co-rotating twin-screw extrusion process are selected each time because they depend not only on the polymer but also on the fillers and even their amount; so, it is practically impossible to create one, especially theoretical mathematical model, describing this process in its entirety and in every possible way. Combinations of materials, therefore, for the purpose of 'personalised' practical models are made, adequate for a given case, and its properties are also limited [17]. Modelling of this type consists of four parts: the selection of initial parameters and obtaining the assumed properties, components and their form based on the experiment, the next determination of the process input parameters [constants and variables] and the assumed output parameters, the boundaries of which will be used for the model according to the selected model, for example, the Hartley Plan or any other field of experimental research. Then, model calculations are performed, and finally, the model is validated [18–20].

Polylactide [PLA] was chosen as the polymer matrix because it is a biodegradable thermoplastic polymer and is the most produced among biodegradable solutions. It is also a material that, in order to be used in many products, requires modification of properties and additives, which makes it justified to conduct research on eco-friendly composites with the use of this material [21–23].

Carbon fillers are widely used in the processing of polymeric materials. The multitude of carbon structures allows to obtain many modification effects: from more complicated mechanical, cross-linking, thermal, electrical to basic ones, such as colorant and processing additives. Among graphitic fillers, the expandable graphite attracts attention due to its flame retardant properties. If it is heated, the flakes will expand and cut off the access of oxygen, which is called as 'intumescent effect' [1,24–27].

For flame retardant agents used in polymers, three main groups can be highlighted: mineral, chlorinated/brominated and phosphorus-based substances [28]. Mineral substances, such as aluminium and magnesium hydroxides, are less expensive but also provide poor flame-retarding effect, requiring higher concentrations, which, in turn, affect processing behaviour and physical and mechanical properties of final product negatively [29]. Chlorinated/brominated substances are proved to be very harmful for mankind and nature; so, usage of these substances in polymers, especially in biodegradable compositions, does not make sense [30,31]. Phosphorus-based formulations are a most promising choice due to their low toxicity and high efficiency [32,33]. Among them, ammonium phosphate [AP] is often used in research works by scientists for flame retarding of biodegradable polymers; so, it is a good choice for flame-retarding systems to decrease flammability of PLA [34,35].

This paper aims to indicate and develop initial constant parameters of extrusion (temperature, screw speed, throughput) for future modelling purposes and confirms their correctness, practical pre-proof for proposed composite and form of materials, as well influence of additives on base material. For temperature and shear forces, e.g., expandable graphite (fragile additive), it is crucial to provide sufficient mixing and filler particle distribution, combined with fast throughput and low shearing during process. As powdered polymers are sometimes used in the industry for polyolefins, especially masterbatches, there is no article, patent or industrial practice to use small-grain biodegradable polymers in processing, and for any polymer, influence and benefits of this solution is not widely described in scientific sources, such as articles, projects etc., especially lack numerical and mechanical descriptions and comparisons. This research will provide data that were never published before and that could be helpful to develop new class of composites with better properties, alongside with reduced wear of machines and significant energy savings during process, as well as decreasing usage of harmful and volatile stabilizers and lubrication agents in polymer processing.

2. MATERIALS, RESEARCH EQUIPMENT, SAMPLE PREPARATION AND METHODOLOGY

2.1. Materials

PLA LX175 in form of 3-mm-diameter pellets with melt flow ratio (MFR) 4–5 g/10 min (190°C, 2.16 kg) and density of 1.25 g/cm^3 was supplied from Total-Energies-Corbion bv, The Netherlands. Pellets were also pulverised to obtain powder with 200 µm medium and 300 µm maximum sized grains. Pre-expanded flake graphite (GR) GrafGuard® 250–50N with an average particle size of 350 µm and activation temperature of 250°C was delivered by Keyser & MacKay from NeoGraf Solutions, LLC, OH, USA. Ammonium polyphosphate Exolit AP 428 (AP) with mass percentage content of phosphorous 31–32 and nitrogen 14–15, average particle size 20 µm was brought by Clariant International Ltd, Switzerland.

2.2. Research equipment

A laboratory co-rotating twin-screw extruder (Buhler AG, Switzerland) with 20-mm diameter screws, 40 L/D (length-to-diameter ratio), 36 Nm max. torque on shafts, one free flow degassing unit, 3-hole forming head and interchangeable screw configuration was used. The temperatures of zones and screws speed were set even for every composition. Initial parameters are listed in Tab. 1, and configuration of screws is shown in Fig. 1.

Tab. 1. Initial parameters of extruder

Parameter	Designation	Value
Screw speed	RPM (revolutions per minute)	200
Temperature – I zone	°C	155
Temperature – II zone	°C	165
Temperature – III zone	°C	175
Temperature – IV zone	°C	180
Temperature – extruder head	°C	185

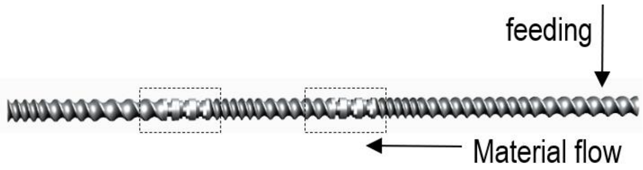

Fig. 1. Screw configuration

Screws are composed of 30 segments each, where, despite normal transporting/compression elements, two sections of kneading elements with significant shear forces can be highlighted – where first section is responsible for intensive melting/plasticising effect (16.25–19 L/D), while the second one brings mixing performance (27–29.75 L/D). After every kneading section, free-flow degassing units are implemented to avoid gas or moisture residues in the final composite.

Both kneading sections are arranged from three right kneading elements each, where two have five discs with 45° offset of adjacent discs, and one has three discs with 90° offset of discs. After kneading sections, long two-flight (2D length) transportation segments are used to reduce the flow pressure on the free degassing unit. Kneading section is shown in Fig. 2.

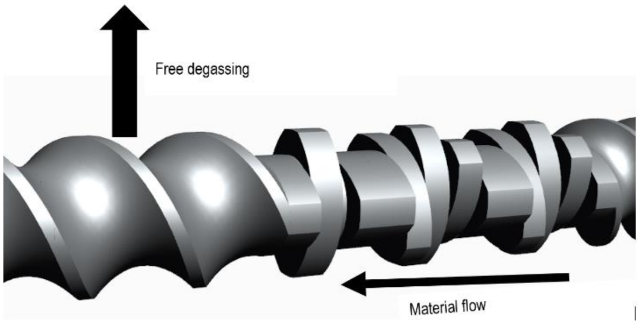

Fig. 2. Screw kneading section

PLA powder was obtained on modified disc-mill pulveriser, with self-designed milling discs with air-flow supply of material and compressed air cooling (20°C) of discs, with ≈300 kg/h efficiency of process.

For pre-drying of composite components, components were dried in drying ovens with forced air convection: SLW-53 and SLW-180 (Pol-Eko, Poland). Temperatures and time of drying were set at 65°C/7 h and 110°C/4 h for PLA and graphite filler, respectively. AP was not dried – it was added directly from sealed containers, delivered by the manufacturer of additives.

Components were fed by a volumetric dosing unit (Brabender Technologie GmbH, Germany), equipped with a coil screw and 3-finger agitator. The device was calibrated for every sample by three runs each, where the amount of inserts in the dose reservoir was strictly kept on same level, and after designating proper screw speed, four measurements of 5 min each were proceeded to ensure that material is fed with planned efficiency.

2.3. Sample preparation

Polylactide/Graphite/ammonium phosphate (PLA/GR/AP) composites were made on co-rotating twin-screw extruders mentioned in Section 2.2. Components were dried, weighted and premixed in a mixer to achieve a homogenous mixture. After mixing, materials were fed by a calibrated volumetric dosing unit to extruder the hopper. Composite left device in the form of straws, transported on belt conveyor with air cooling (fans), stainless steel dry gutter to stand-alone pelletizer. Obtained pellets were then dried and ready for examinations. Symbols and contents of composites are listed in Tab. 2.

Tab. 2. Labelling of neat PLA and PLA/GR/AP composites

Symbol	PLA (%wt)	Graphite (%wt)	AP (%wt)	Approx. throughput (kg/h)
S1	100	0	0	5
S2	100	0	0	2
S3	80	10	10	5
S4	80	10	10	2
G1	100	0	0	5
G2	100	0	0	2
G3	80	10	10	5
G4	80	10	10	2

AP, ammonium phosphate; PLA, polylactide

2.4. Research methodology

2.4.1. Extrusion process evaluation

During the process of preparing composites, described in Section 2.3, data were obtained for comparison and empirical proof of the effectiveness of the composite production process depending on the degree of fragmentation of the polymer matrix. Moreover, the prepared composites were subjected to the tests described below.

Parameters, which were measured by built-in extruder sensors, are the mean of three reads taken every 5 min after 10-min stabilisation of one extrusion run for every sample.
The parameters recorded during extrusion are listed in Tab. 3.

Tab. 3. Measured parameters of extrusion

Parameter	Designation
Torque on screws	Nm
Energy consumption (main drive power)	kW
Throughput	kg/h
Real temperatures of zones	°C
Temperature of melt on extruder head	°C

The experimental extrusions were carried out to maintain equal screw speed and temperature sets for every run, with two throughputs for every sample.

2.4.2. Phase morphology analysis

Scanning electron microscopy (SEM, SU8010, Hitachi, Japan) was used for examination of the morphology of both the pure PLA resin and PLA/GR/AP composites. For SEM imaging, composite straws were cracked, and breakthrough surface was then sputtered with gold.

2.4.3. MFR measurement

For research purposes, MFR measurements were conducted using LMI 4003 Plastometer (DYNISCO, USA), partially according to PN-EN ISO 1133:2011 standard. The measurements were carried out under the piston load of 2.16 kg at 190°C for each sample.

2.4.4. Thermal properties measurement

Differential scanning calorimetry (DSC) was performed with a METTLER TOLEDO DSC1 calibrated with pure indium and zinc standards, under nitrogen atmosphere, at a gas flow rate of 50 cm^3/min. Samples of about 5–7 mg, sealed in aluminium crucible, were used. The samples were heated at a constant rate of 10°C/min from 0°C to 300°C.

The experiment was performed in accordance with the ISO 11357-1:2016 and ISO 11357-6:2018 standards.

The room temperature crystallinity, X_c, of PLA composites was evaluated using the following expression:

$$X_c = (\Delta H_m - \Delta H_{cc} w \Delta H^0_m) \times 100\%$$

where ΔH_m is the enthalpy of melting (J/g), ΔH_{cc} is the cold crystallization enthalpy (J/g), ΔH^0m is the melting enthalpy of 100% crystalline PLA (93 J/g) and *w* is the fraction of the polymer in the composite materials (13).

2.4.5. Cone calorimeter flammability testing

The cone calorimeter testing was conducted using FIRE TESTING TECHNOLOGY iCONE CLASSIC where specimens with dimensions of 100 mm x 100 mm x 6 mm were placed on a testing plate layered with aluminium foils and placed under the burner device. Heat flux was set at 50 kW/m^2. The final result is the mean of burning of two specimens made from the same composite.

The experiment was performed according to the ISO 5660:2015 standard.

3. RESULTS AND DISCUSSION

3.1. Extrusion process evaluation

As mentioned in Section 2.4.1, parameters of extrusion of an extruder are obtained and listed in Tab. 4.

Tab. 4. Parameters from extrusion process

Sample	S1	S2	S3	S4	G1	G2	G3	G4
Throughput (kg/h)	5	2	5	2	5	2	5	2
Real throughput (g/h)	5017.06	2004.11	5026.23	1998.84	4931.5	1998.26	4712.24	2014.22
Torque on shafts (Nm)	20.16	15.12	18.36	11.16	27.36	19.44	27	20.88
Energy consumption (kW)	0.73	0.54	0.57	0.4	0.97	0.69	1.02	0.75
Energy consumption per kg (kW/kg)	0.146	0.269	0.113	0.200	0.197	0.345	0.216	0.372
Temperature of melt (°C)	197	198	198	199	199	200	201	201
Real temperature on heating sections (°C)								
I	156	156	156	155	156	157	155	155
II	168	167	166	167	166	166	162	162
III	178	176	174	177	177	178	177	179
IV	181	180	180	181	180	181	181	183
Extruder head	183	185	185	186	185	185	186	187
Losses on degassing unit					*		*	

Parameters of the extrusion process reveal that changing of polymer particle size significantly decreases torque on shafts and energy consumption: pure PLA brings 26% and 22% decrease on energy per kilogram for 5 kg/h and 2 kg/h, respectively. For samples with pulverised PLA, graphite lube effect is observed. What is more, for G series samples, energy is consumed mostly for shear melting of granules on first shear section, eliminating positive lube effect of graphite fillers. This phenomenon is also proved by energy consumption per kilogram of composite – for PLA/GR/AP composites, using smaller granules brings lowering of 48% for 5 kg/h throughput and 46% for 2 kg/h. What is more, while using smaller PLA particles, no sign of polymer was found on degassing units. For both 5 kg/h throughputs in G series, escaping of material through degassing channel is observed, especially in G3 sample case.

During extrusion of G3 and G4 specimens, the mixture of ingredients tends to separate in volumetric dose reservoirs: powders of graphite and ammonium phosphate flame retardant concentrated at the bottom of reservoir, while PLA pellets went up. The effect was partially neutralised by constant mixing using a 3-finger agitator in a volumetric dose reservoir, but separation was still visible.

3.2. Phase morphology analysis

Fig. 3 shows SEM images of neat PLA (samples G1 and G2) and PLA/GR/AP composites (G3 and S3). Differences in morphology between neat polymer and composite are apparent. Neat polymer after processing is homogeneous, whereas composite materials have porous structure. The pore distribution is homogeneous; the individual pores have a regular cylindrical shape. The cylinder diameters are ≈50 µm. The presence of pores is probably related to the expansion of the graphite flakes during the extrusion process.

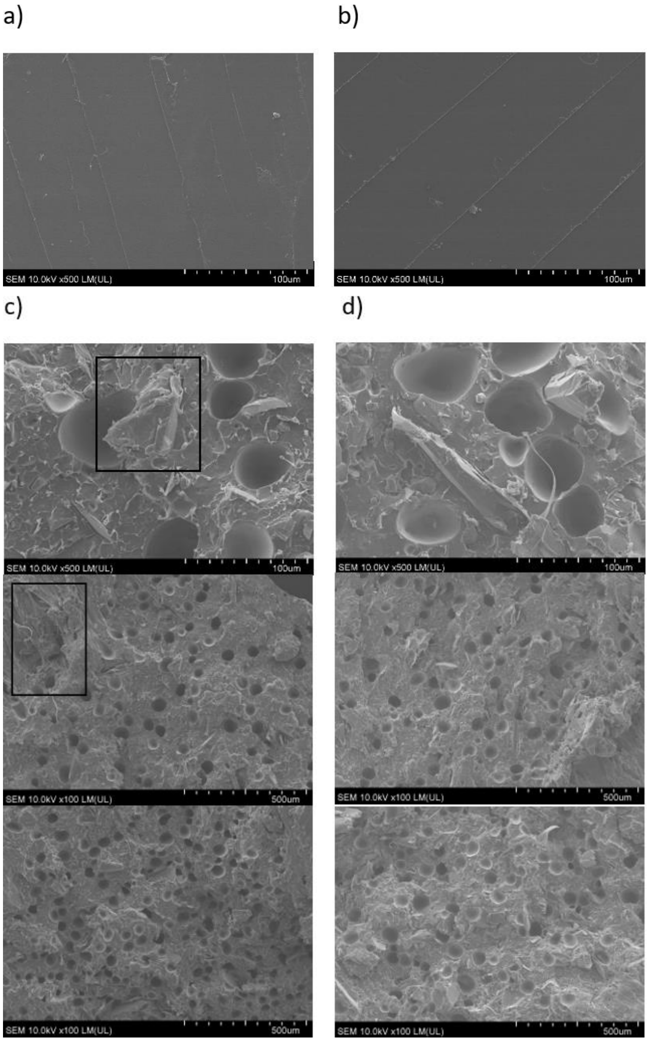

Fig. 3. SEM images of samples – (a) G1, (b) G2, (c) G3, (d) S3. Agglomeration in sample G3 is highlighted in black frame
SEM, scanning electron microscopy

The distribution of the filler in the PLA matrix in the spaces between the pores is homogeneous. However, comparing samples G3 and S3 leads to the conclusion that the filler dispersion in S3 is slightly better than that in G3. In sample G3, single agglomerates of graphite are visible

3.3. MFR measurement

MFR results for individual samples are listed in Tab. 5.

MFR is often a used method for examination of polymeric materials and composites and, among others, in comparable trials can reveal degradation processes. Results of measurement indicates that configuration of a screw used in co-rotational twin-screw extrusion process does not affect degradation of polymers through the process. For sample S1, MFR measurement proved that additional pulverisation of PLA did not result in extended degradation in comparison to sample G1. Lower values of MFR parameter of samples S3 and G3 against non-graphite samples may be due to an increase in flow resistance associated with the use of solid filler point to conclusion, that additives did not affect in degradation of composite, in fact, lowering of MFR is right phenomenon for providing standard, inert fillers, as [36,37].

Tab. 5. MFR values

Sample	MFR (g/10 min)
Pure PLA (pellets)	5.51
S1	5.48
S3	4.41
G1	5.44
G3	4.00

MFR, melt flow ratio; PLA, polylactide.

3.4. Thermal property measurement

Thermal data, such as the glass transition temperature (T_g), crystallization temperature (T_c), cold crystallization temperature (T_{cc}), melting temperature (T_m), crystallization enthalpy (ΔH_c), cold crystallization enthalpy (ΔH_{cc}) and melting enthalpy (ΔH_m), are summarised in Tab. 6 and Fig. 5P.

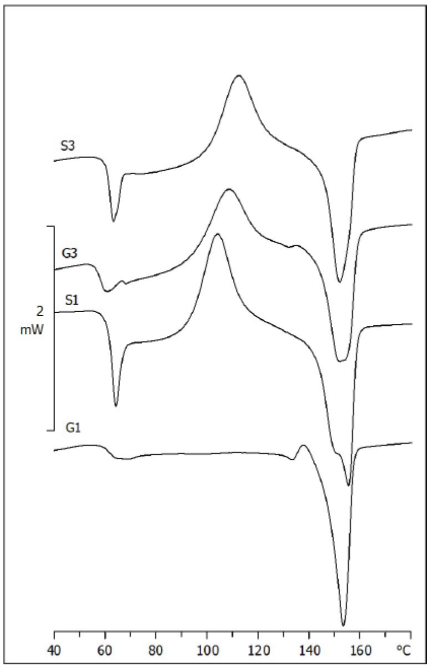

Fig. 4. First heating DSC thermograms of samples
DSC, differential scanning calorimetry

There were no changes in the thermograms during cooling stages. Glass transition temperatures in the second heating are similar and amount to about 60°C for all tested samples. A similar situation occurs in the case of melting temperatures, where the differences between the melting points of individual samples are also small. The conducted research shows that the addition of pre-expanded graphite reduces the melting enthalpy and the cold crystallization enthalpy in the second heating and increases the cold crystallization temperature. This effect may be due to the large size of graphite flakes (~400 µm), which makes it difficult to obtain sufficient dispersion of graphite in the polymer matrix [24]. For sample S1 during the first heating, the presence of two melting peaks was observed. The two melting peaks are related to the presence of two types of crystallites of different sizes and disorder [38]. The melting peak at lower temperature is attributed to the melting and recrystallization of the primary crystals into a more stable form. The second peak appearing at a higher temperature corresponds to the melting of the newly formed crystals [39]. All samples, except S1, showed an amorphic characteristic.

Tab. 6. DSC – Heating 1

Sample	Heating1					
	T_m (°C)	ΔH_m (J/g)	T_g (°C)	T_{cc} (°C)	ΔH_{cc} (J/g)	X_c (%)
G1	153.01	–25.99	61.18	-	-	-
S1	150.80/ 155.24	–27.37	62.47	103.85	23.23	4.5
G3	151.96	–22.99	58.07	108.36	21.68	0
S3	151.79	22.31	61.75	112.20	21.49	0

DSC, differential scanning calorimetry

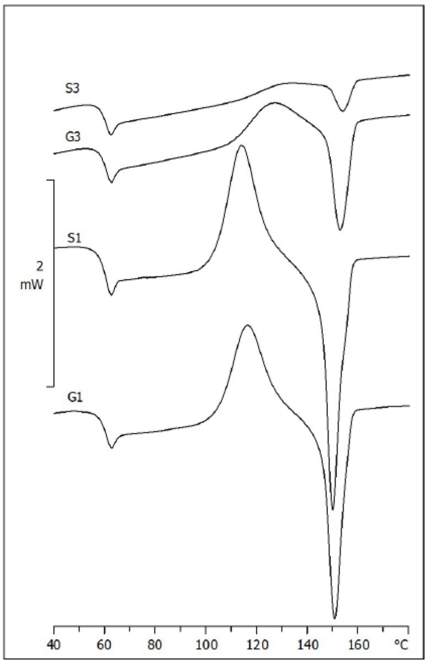

Fig. 5. Second heating DSC thermograms of samples
DSC, differential scanning calorimetry

Tab. 7. DSC – Heating 2

Sample	Heating 2					
	T_m (°C)	ΔH_m (J/g)	T_g (°C)	T_{cc} (°C)	ΔH_{cc} (J/g)	X_c (%)
G1	150.58	–26.23	60.43	116.53	27.81	0
S1	149.71	–27.62	60.04	114.02	27.90	0
G3	152.80	–11.74	60.08	125.86	11.72	0
S3	154.00	–2.77	60.70	133.51	3.17	0

DSC, differential scanning calorimetry

3.5. Cone calorimeter flammability testing

Flammability tests carried out using a cone calorimeter show that additives do not stop the combustion process completely. Nevertheless, additives lead to changes in the flammability parameters, which are compared in Tab. 8. Namely, the ignition time has been reduced significantly by 10–13 s in PLA/GR/AP composites in comparison to neat PLA. Flame retardancy effect is apparent as well. Despite the reduced time to ignition (TTI), peak heat release ratio (pHRR) in PLA/GR/AP is decreased by 30%–40%.

Tab. 8. Cone calorimeter data

Sample	TTI (s)	THR (MJ/m²)	pHRR (kW/m²)	MLR (g/[s·m²])	TTF (s)	TSP (m³)
G1	35	124.1	597.59	19.81	354	0.1
S1	34	110.6	576.86	18.13	331	0.1
G3	24	89.5	375.19	4.08	1442	3.23
S3	22	112.5	395.39	8.75	725	4.6

TTI, time to ignition, THR, total heat release, pHRR, peak heat release ratio, MLR, mass loss ratio, TTF, time to flameout, TSP, total smoke production

The improvement in flame retardant properties is also reflected in the two and a half times increased time needed to burn the whole specimen. It has also been observed that the presence of expandable graphite prevents the polymer from dripping during combustion. Mass loss ratio (MLR) decreased significantly, what is connected to time to flameout (TTF), because in all cases specimens were burnt fully without sudden stop of burning process. Additives affect smoke production: neat PLA was fully burned into CO2, while combustion of the PLA composites results in releasing more volatile gases. This is a consequence of the fact that the oxygen supply is cut off by the expanded graphite, which prevents complete combustion.

4. CONCLUSIONS

Results confirmed that, as expected, grain size of polymer matrix changed processing properties of composites significantly, as well as material properties, uniformity and behaviour. Research brings sufficient proofs of advantages of using powdered PLA to conduct wider and detailed research trials to obtain data with variable initial parameters (screw speed, different temperatures, filler content, throughputs) for mathematical modelling of process in next stage of research.

Decreases in energy consumption and torque, as well as lesser temperature rise in extruder is undisputable and can affect in more energy efficient processing, as well as slower wear of mechanical elements of extruder machine, as well as proper work of degassing units and improved throughput.

SEM analysis proved that premixing along with a decreased particle size of a polymer leads to better particle distribution of powdered fillers. What is more, using of pellets cause agglomeration, which was not found in S series samples.

MFR measurements revealed that for both polymer grain sizes, flow rate values are similar. This fact is important because grinding of polymer can lead to degradation of material, which did not occur in this case or as processing degraded pellets to a greater extent; after processing both composites, flow remains congenial.

The addition of solid fillers did not contribute to changes in the glass transition temperature and melting temperature. The effect of graphite addition on the enthalpy of melting, cold crystallization and the temperature of cold crystallization was noticed, which may result from not sufficient dispersion of graphite in the polymer matrix related to the large size of the flakes of the graphite used.

A cone calorimeter shows that modification with pre-expandable graphite and AP tend to flame retardancy of PLA by lowering MLR, pHRR and TTF. Samples made from granules were found out to be more flame resistant, which was is caused by agglomerates, which gathered near the surface, slowing combustion on first stages of burning. Despite promising results, more testing on additives is needed.

REFERENCES

1. Fiedurek K, Szroeder P, Macko M, Raszkowska-Kaczor A, Puszczykowska N. Influence of the parameters of the extrusion process on the properties of PLA composites with the addition of graphite. IOP Conf Ser: Mater Sci Eng. 2021;1199(1):012057.
2. Stasiek J, Bajer K, Stasiek A, Bogucki M. Co-rotation twin-screw extruders for polymer materials. A method for experimental studying the extrusion process. Przemysl Chemiczny. 2012;91:224–30.
3. Martin C. Twin Screw Extruders as Continuous Mixers for Thermal Processing: a Technical and Historical Perspective. AAPS PharmSci Tech. 2016;17(1):3–19.
4. Lewandowski A, Wilczyński K. Modeling of Twin Screw Extrusion of Polymeric Materials. Polymers. 2022;14(2):274.
5. Flitta I, Sheppard T. Effect of pressure and temperature variations on FEM prediction of deformation during extrusion. Materials Science and Technology. 2005;21(3):339–46.
6. Mechanisms of mixing in single and co-rotating twin screw extruders - Lawal - 1995 - Polymer Engineering & Science - Wiley Online Library [Internet]. [cited 2022 Jun 12]. Available from: https://onlinelibrary.wiley.com/doi/10.1002/pen.760351702
7. Carneiro O, Covas J, Vergnes B. Experimental and Theoretical Study of Twin-Screw Extrusion of Polypropylene. Journal of Applied Polymer Science. 2000;4:78.
8. Dittrich C, Pecenka R, Løes AK, Cáceres R, Conroy J, Rayns F, et al. Extrusion of Different Plants into Fibre for Peat Replacement in Growing Media: Adjustment of Parameters to Achieve Satisfactory Physical Fibre-Properties. Agronomy. 2021;11.
9. Eitzlmayr A, Khinast J, Hörl G, Koscher G, Reynolds G, Huang Z, et al. Experimental characterization and modeling of twin-screw extruder elements for pharmaceutical hot melt extrusion. AIChE Journal. 2013;59(11):4440–50.
10. Kuo CFJ, Huang CC, Lin YJ, Dong MY. A study of optimum processing parameters and abnormal parameter identification of the twin-screw co-rotating extruder mixing process based on the distribution and dispersion properties for SiO2/low-density polyethylene nano-composites. Textile Research Journal. 2020;90(9–10): 1102–17.
11. Kalyon DM, Malik M. An Integrated Approach for Numerical Analysis of Coupled Flow and Heat Transfer in Co-rotating Twin Screw Extruders. International Polymer Processing. 2007 Jul 1;22(3):293–302.
12. Andersen P. Fundamentals of twin-screw extrusion polymer melting: Common pitfalls and how to avoid them. In Cleveland, Ohio, USA; 2015 [cited 2022 Jun 12]. 020007.
13. Li M. Effects of API particle size on the dissolution rate in molten polymer excipient matrices during hot melt extrusion, conducted in a co-rotating twin-screw extruder. Theses [Internet]. 2013; Available from: https://digitalcommons.njit.edu/theses/172
14. Stasiek A, Raszkowska-Kaczor A, Formela K. Badania wpływu nieorganicznych napełniaczy proszkowych na właściwości polipropylenu. Przemysł Chemiczny. 2014;888–92.
15. Zhang B, Zhang Y, Dreisoerner J, Wei Y. The effects of screw configuration on the screw fill degree and special mechanical energy in twin-screw extruder for high-moisture texturised defatted soybean meal. Journal of Food Engineering. 2015;157:77–83.
16. Akdogan H. Pressure, torque, and energy responses of a twin screw extruder at high moisture contents. Food Research International. 1996;29(5):423–9.
17. Andrzej Stasiek. Badania procesu współbieżnego dwuślimakowego wytłaczania modyfikowanego polipropylenu przy zmiennej geometrii ślimaków [PhD Thesis]. [Bydgoszcz]: Uniwersytet Technologiczno-Przyrodniczy; 2015.
18. Zbigniew Polański. Współczesne metody badań doświadczalnych, Warszawa: Wiedza Powszechna; 1978:215
19. Kazimierz Mańczak. Technika planowania eksperymentu Warszawa: WNT; 1976:277
20. Mieczysław Korzyński. Metodyka eksperymentu.Planowanie, realizacja i statystyczne opracowanie wyników eksperymentów technologicznych [Internet]. 2006th ed. Warszawa: WNT; 2006;278
21. Murariu M, Dubois P. PLA composites: From production to properties. Advanced Drug Delivery Reviews. 2016;107:17–46.
22. Puszczykowska N, Rytlewski P, Macko M, Fiedurek K, Janczak K. Riboflavin as a Biodegradable Functional Additive for Thermoplastic Polymers. Environments. 2022;9(5):56.
23. Kosmalska D, Janczak K, Raszkowska-Kaczor A, Stasiek A, Ligor T. Polylactide as a Substitute for Conventional Polymers—Biopolymer Processing under Varying Extrusion Conditions. Environments. 2022;9(5):57.
24. Kaczor D, Fiedurek K, Bajer K, Raszkowska-Kaczor A, Domek G, Macko M, et al. Impact of the Graphite Fillers on the Thermal Processing of Graphite/Poly(lactic acid) Composites. Materials. 2021;14(18):5346.
25. Pang Q, Kang F, Deng J, Lei L, Lu J, Shao S. Flame retardancy effects between expandable graphite and halloysite nanotubes in silicone rubber foam. RSC Adv. 2021;11(23):13821–31.
26. Modesti M, Lorenzetti A, Simioni F, Camino G. Expandable graphite as an intumescent flame retardant in polyisocyanurate–polyurethane foams. Polymer Degradation and Stability. 2002;77(2):195–202.
27. Tomiak F, Rathberger K, Schöffel A, Drummer D. Expandable Graphite for Flame Retardant PA6 Applications. Polymers. 2021;13(16):2733.
28. Grover T, Khandual A, Chatterjee kalesh nath, Jamdagni R. Flame retardants: An overview. 2014;61:29–36.
29. Yan L, Xu Z, Wang X, Deng N, Chu Z. Synergistic effects of aluminum hydroxide on improving the flame retardancy and smoke suppression properties of transparent intumescent fire-retardant coatings. J Coat Technol Res. 2018;15(6):1357–69.
30. Wikoff DS, Birnbaum L. Human Health Effects of Brominated Flame Retardants. In: Eljarrat E, Barceló D, editors. Brominated Flame Retardants [Internet]. Berlin, Heidelberg: Springer; 2011;19–53. (The Handbook of Environmental Chemistry).
31. Morel C, Schroeder H, Emond C, Turner JD, Lichtfouse E, Grova N. Brominated flame retardants, a cornelian dilemma. Environ Chem Lett [Internet]. 2022 Jan 23 [cited 2022 Jul 29]; Available from: https://doi.org/10.1007/s10311-022-01392-2
32. Ding D, Liu Y, Lu Y, Chen Y, Liao Y, Zhang G, et al. A Formaldehyde-free P-N Synergistic Flame Retardant Containing Phosphonate and Ammonium Phosphate for Cotton Fabrics. Journal of Natural Fibers. 2022;0(0):1–11.
33. Li S, Zhong L, Huang S, Wang D, Zhang F, Zhang G. A novel flame retardant with reactive ammonium phosphate groups and polymerizing ability for preparing durable flame retardant and stiff cotton fabric. Polymer Degradation and Stability. 2019;164:145–56.

34. Shukor F, Hassan A, Islam MS, Mokhtar M, Hasan M. Effect of ammonium polyphosphate on flame retardancy, thermal stability and mechanical properties of alkali treated kenaf fiber filled PLA biocomposites. 2014;
35. Chow W, Teoh E, Karger-Kocsis J. Flame retarded poly(lactic acid): A review. Express Polymer Letters. 2018;12:396–417.
36. Noor Zuhaira AA, Rahmah M. Effects of Calcium Carbonate on Melt Flow and Mechanical Properties of Rice Husk/HDPE and Kenaf/HDPE Hybrid Composites. Advanced Materials Research. 2013; 795:286–9.
37. Gallagher LW, McDonald AG. The effect of micron sized wood fibers in wood plastic composites. Maderas Ciencia y tecnología. 2013; 15(3):357–74.
38. Ahmed J, Mulla MZ, Vahora A, Bher A, Auras R. Polylactide/graphene nanoplatelets composite films: Impact of high-pressure on topography, barrier, thermal, and mechanical properties. Polymer Composites. 2021;42(6):2898–909.
39. Bartczak Z, Galeski A, Kowalczuk M, Sobota M, Malinowski R. Tough blends of poly(lactide) and amorphous poly([R,S]-3-hydroxy butyrate) – morphology and properties. European Polymer Journal. 2013;49(11):3630–41.

Acknowledgments: the work has been accomplished as partial result of Poland Ministry of Education and Science’ “doktoraty wdrożeniowe” program. Research was conducted with Kazimierz Wielki University and Łukasiewicz Research Network - Institute for Engineering Polymer Materials and Dyes internal founding.

Kacper Fiedurek: https://orcid.org/0000-0003-4859-5755

Paweł Szroeder: https://orcid.org/0000-0002-4266-4206

Marek Macko: https://orcid.org/0000-0002-8743-6602

Aneta Raszkowska-Kaczor: https://orcid.org/0000-0002-6868-6833

Marcin Borowicz: https://orcid.org/0000-0001-8099-5244

Natalia Puszczykowska: https://orcid.org/0000-0002-5184-6052

DOI 10.2478/ama-2022-0037

acta mechanica et automatica, vol.16 no.4 (2022)
Special Issue "Machine Modeling and Simulations 2022"

GPS APPLICATION IN THE DESIGN OF GEARBOXES

Silvia MALÁKOVÁ[*], **Samuel SIVÁK**[*]

[*]Faculty of Mechanical Engineering, Department of Structural and Transportation Engineering,
Technical University of Košice, Letná 1/9, 042 00 Košice, Slovak Republic

silvia.malakova@tuke.sk, samuel.sivak@tuke.sk

received 27 June 2022, revised 26 July 2022, accepted 26 July 2022

Abstract: The integrated geometrical product specification (GPS) system for workpiece geometry specification and verification is an improved engineering tool for product development and production. The goal of the GPS system is to provide tools for cost-effective management of variability in products and processes. This can be achieved by using a more precise way of expressing the functional requirements of the workpiece, complete and well-defined specifications and integrated verification approaches. The intended function of the product is ensured by controlling the geometry and material properties of the workpiece parts, which make up the product. GPS is a language just for checking geometry, and further development is based on computational mathematics and correct, consistent logic using general sets of rules that can be applied to all types of specifications. This article deals with the application of GPS rules in the design of gearboxes.

Key words: gearbox, geometrical product specifications, tolerancing, drawing

1. INTRODUCTION

Gear mechanisms allow the transmission of torque from the drive shaft to the driven shaft. They are mainly used for gears with a constant gear ratio and a small shaft axial distance. Spur gears are among the most widely used gearing mechanisms in a wide range of mechanical engineering practice. They are the basic elements by which the transmission and transformation of mechanical energy and motion are carried out in machines. The basic part of the gear is the gear train, which consists of a pair of gears – driving and driven – that mesh together. We can say that gears have become a symbol of engineering [1]. At the same time, gears are also one of the most commonly used types of automotive gears.

The quality of gears is mostly determined by their geometric design. If the geometric design is faulty, even the use of the highest quality materials will not ensure the reliability of the gearing. Conversely, sometimes, an excellent geometric design of the gearing can save the cost of expensive materials. Adequate attention must be paid to the design of gears. In the geometric design of gearing, it is necessary to choose basic geometric parameters. The basic parameters of the spur gear include the number of teeth, the size of the module, the pressure angle and the helical angle. But the choice of corrections and modifications of gearing also come into play here. Next, it is necessary to choose clearances in the gearing. Geometric tolerances of form, orientation and position play their role here.

The design process starts with a list of functional requirements and continues with technical specifications. At this stage, the designer begins to create solutions to the problem and can view the product – the pre-driving mechanism the designer wants to produce [2, 3]. The design can be realised by using conventional methods like engineering drawings or computer-aided design (CAD). CAD is a software tool that provides the computer-aided designer with the ability to produce fast and accurate drawings. The CAD system allows the designer to create a three-dimensional representation of a part or product and displays views from different angles to check for functionality and appearance (Fig. 1).

To meet the design requirements and specifications of the product, the designer nowadays uses the CAD system, finite element analysis (FEA) and mathematical modelling [4]. In order to resolve all possible aspects to the benefit of all involved in the process, it is necessary to seek an answer to the question of whether it is possible to design a part in such way to make its manufacture easier. An integral part of this is the creation of drawing documentation [5].

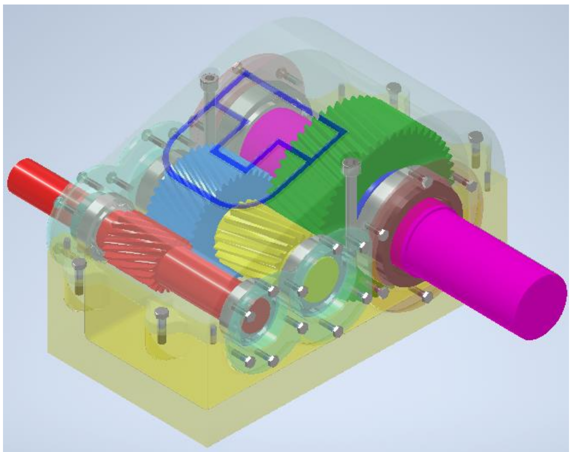

Fig. 1. Example of a gearbox CAD model. CAD, computer-aided design

DOI 10.2478/ama-2022-0037

Insufficient drawing documentation leads to production delays and rework of assembly procedures on the production floor. Regarding the conventions and symbols used in production documentation, international and national standards are used, and there is no reason to duplicate this proven methodology, rather an overview is offered of what is important in communicating how to translate knowledge into purposeful action at the level of the production drawing board. The goal of technical drawing is to depict the requirements for a functional design with clear and relevant information so that the product is manufactured, and these requirements are verified [6–8]. The methods used in the design process should be clear and concise so as not to cause confusion in the interpretation of the design and, consequently, should enable the interpretation of the design requirements by all those involved in the process. The geometric specifications of the gears also play an important role in the optimisation of gear transmissions [9].

Production produces parts that are not entirely accurate and that show deviations from nominal values and from each other. The parts are measured to compare them with the specification [10–12]. The geometrical product specification (GPS) defines, on an engineering drawing, the shape (geometry), dimensions and surface characteristics that provide the optimum function of the part, along with the variance around the optimum that will still provide satisfactory function.

2. GEOMETRICAL PRODUCT SPECIFICATION

The GPS describes the conditions that the component or part of the component must meet. These conditions are expressed from the geometric characteristics between or on the geometric elements. The geometric elements as a whole are considered for non-ideal surfaces of the component as a whole (skin model). The non-ideal surface of the component is modelled by the closed surface of the material–surrounding interface of the component. The interface is defined by a data set of all points belonging to the interface.

The integrated GPS system for specification and verification of workpiece geometry is an enhanced engineering tool for product development and production. The system is essential because companies in an international environment are rapidly adopting advanced technologies, new manufacturing processes, new materials and new products by outsourcing certain activities. The goal of an improved GPS system is to provide tools for cost-effective management, but not variability, in products and processes [13]. This can be achieved by using a more precise way of expressing the functional requirements of the workpiece, complete and well-defined specifications, and integrated verification approaches. This improved GPS has clarified current practice and harmonised the work of other relevant International Standards Organisation (ISO) and Technical Commissions (TCs). This harmonisation, for example, allows better integration with 3D CAD/CAM/CAQ systems.

The intended function of the product is provided by controlling the geometry and material properties of the workpiece component(s), which make up the product. GPS is a geometry-only control language, and further development is based on computational mathematics and correct, consistent logic using general rule sets that can be applied to all types of specifications [14]. The challenge for the future is to enrich the GPS language to allow the expression of requirements that cover a wide range of workpiece functions. The introduction of an improved GPS system is a prerequisite for continuous improvement of product quality and reduction of time to market.

A default global specification is available for each type of GPS, based on simplicity and overall cost reduction. Additionally, there are many simplified designations to cover commonly occurring workpiece functions, for example, notation to accommodate kinematic pairs.

2.1. Geometric dimensioning

Geometric dimensioning and tolerancing (GD&T) is a system for defining and communicating engineering tolerances. It is a set of instructions designed specifically for quoting and designing so that the part is correctly interpreted and allows the designer's intent to be translated into all stages of the product cycle. It provides instructions for drawing and dimensional inspection.

GD&T uses markers and computer-aided three-dimensional solid models in the drawing documentation that explicitly describe the nominal geometry and its allowable deviations. GD&T finds its widest application in mass production, where interchangeability of manufactured parts without counterparts is necessary.

The basic idea of GD&T is to determine the base of a component element or assembly group. This, of course, refers to the actual position and functional connections. The bases are selected as starting points for the dimensioning and the use of tolerances or tolerance zones. Functional bases must be selected and they are simply one of the elements of the component that determine the actual position of the component in the manufactured assembly (product). The use of any other base system, that is, axes – changes the overall tolerance.

2.2. Geometric tolerancing

Geometric tolerances are determined by the functional requirements of the product and the functional surfaces of the product; can be influenced by the manufacture and inspection of finished products; and are used in addition to dimensional tolerances and used to control more precise profiles and shapes of products. They are used only when the profile or shape has a specific function and errors could impair its performance.

Standard ISO 1101 contains basic information and specifies requirements for geometric tolerancing of products. Geometric tolerances are divided into the following categories:

- form tolerance (does not require a reference – base);
- orientation tolerance (requires a reference – base);
- position tolerance (requires a reference – base);
- runout tolerance (requires a reference – base).

Standard ISO 22432:2011 gives more detailed taxonomy of features and links and the concept of the surface model between nominal features, specification features and verification features. More elements such as geometric specifications, characteristics and conditions can be found in standard ISO 25378:2011. Requirement of geometric characteristics and condition is defined by each and every GPS (Fig. 2).

Differences from the nominal shape are called deviations. Geometric tolerances determine the deviation of a workpiece element from its shape, orientation or position and from the theoretically accurate (ideal) shape, orientation or position without reference to the dimensions of the elements.

However, the surface of the parts is also a separate element, for example, a cylinder or two parallel planes. Geometric tolerances are applied independently of the actual local dimensions of the individual elements, and they should only be prescribed if justified, for example, from a functional point of view.

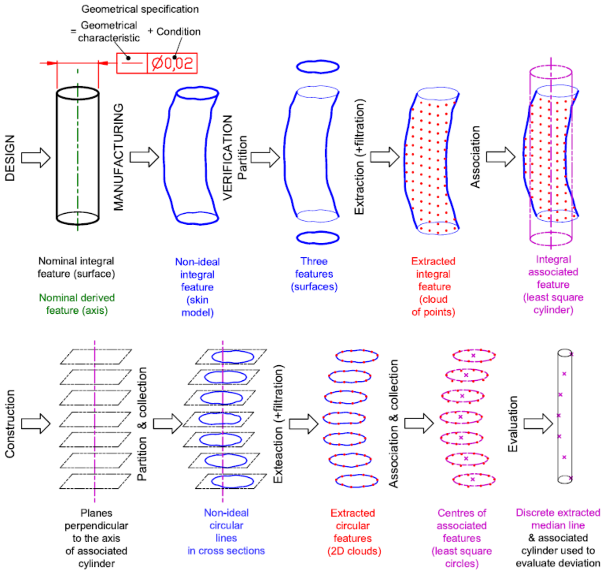
Geometrical specification
= Geometrical characteristic
+ Condition
Ø0,02
DESIGN
MANUFACTURING
VERIFICATION
Partition
Extraction (+filtration)
Association
Nominal integral feature (surface)
Nominal derived feature (axis)
Non-ideal integral feature (skin model)
Three features (surfaces)
Extracted integral feature (cloud of points)
Integral associated feature (least square cylinder)
Construction
Partition & collection
Exteaction (+filtration)
Association & collection
Evaluation
Planes perpendicular to the axis of associated cylinder
Non-ideal circular lines in cross sections
Extracted circular features (2D clouds)
Centres of associated features (least square circles)
Discrete extracted median line & associated cylinder used to evaluate deviation

Fig. 2. Definition of the basic idea of GPS
GPS, geometrical product specification

3. APPLICATION OF GEOMETRIC SPECIFICATION OF PRODUCTS IN THE DESIGN OF GEAR COMPONENTS

Gears are most often composed of non-standardised and standardised components. Non-standardised components include shafts, gears, bottom and top of the gear case, lids, spacers and separator rings. Standardised components include in particular fasteners, seals, wedges and screws and also bearings and seals. For all non-standardised gearbox components, it is necessary to create drawing documentation, which is used for the actual production of the component and for its inspection. In addition to the shape and dimensions, the drawings must contain other data, including the definition of tolerances, which play an important role in the assemblability of the final product. These geometric specifications when creating drawing documentation using CAD applications can be defined in the library of the relevant program or defined manually. In this case, they were manually defined according to the standards.

3.1. Condition of assemblability of components

The installation or assembly of the manufactured machine components depends on a combination of two interrelated effects, namely, dimension and tolerance. Dimensions are obtained by measuring a finite number of points of element feature of size – the quantity of accuracy, geometric deviations of extracted features and their derived geometric features; for example, a set of holes (in a pair of plates) and the rivets that connect them – quantity of accuracy.

The smallest clearance occurs when each of the dimensional elements to be joined has the dimension of the maximum of the material and when the geometric deviations of the dimensional elements (e.g., deviation of shape, orientation and position) and their derived geometric elements (centre line or median plane) are also larger.

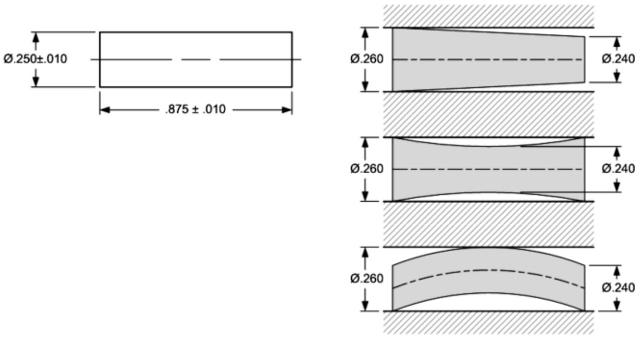
Ø.250±.010
.875 ± .010
Ø.260
Ø.240
Ø.260
Ø.240
Ø.260
Ø.240

Fig. 3. Typical setting situations

The largest clearance occurs when the dimensions of the kinematically associated dimensional elements have the largest deviation from the dimension of the material maximum (e.g., the shaft with the smallest diameter and the hole with the largest diameter) and when the geometric deviations of the dimensional elements (e.g., deviations in shape, orientation and position) and their derived elements are zero.

It follows that when the actual dimensions of the parts to be joined do not reach the maximum dimension of the material, the geometric tolerance of the dimensional elements and their derived elements can be increased without compromising the assemblability of the parts. Typical situations that may arise when a pin is seated in a gear case bore, as shown in Fig. 3.

The position tolerances (position, concentricity, symmetry) for some functional cases are not sufficient to ensure their function. The projected tolerance zone indicates these functional requirements more clearly on the drawing. This notation means that the prescribed tolerance zone for the toleranced element is projected into the direction of the facing (associated) counterpart. The length of the projected tolerance zone and its position with respect to the workpiece are pre-written with a marking.

For practical reasons, the exact theoretical value of the projected length is chosen to be equivalent to the functional length of the counterpart.

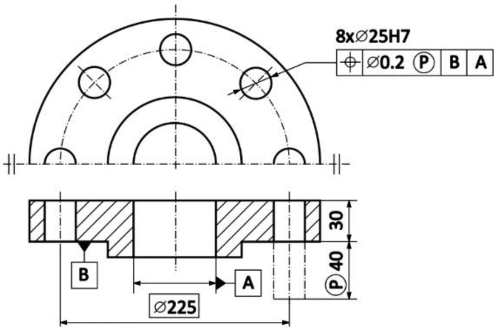
8xØ25H7
⌖ Ø0.2 Ⓟ B A
B
A
Ø225
30
Ⓟ 40

Fig. 4. Example of dimensioning a hole on the gearbox cover

The standard is applied in those specific cases where geometric tolerance is required in the space outside the component itself, most often in a second component that forms a fit with the component to be toleranced. The tolerance zone is moved from the part to a specific position, the length of which must be dimensioned.

The requirement for an offset tolerance zone is expressed by writing the letter P in a circle after the numerical tolerance value in the tolerance box. The outline of the displaced toleranced element (pin, bolt, pin, etc.) should be marked with a thin dotted line with two dots, the position of the element should be coded, and the P in the circle should be entered before the numerical value of the dimension. A typical example is the dimensioning of a hole on the gear case lid (Fig. 4). The prescription will ensure, for example, the correct position of the pins that are pressed into the holes 25H7.

In Fig. 5, an example of the application of the offset tolerance zone prescription in conjunction with geometric location tolerance is selected. The screw (position number 3 in Fig. 5) is loosely seated in the upper part of the gear case body (position number 2 in Fig. 5) and is screwed into the lower part of the gear case body (position number 1 in Fig. 5). When assembled, clearance in the holes of component 2 must be guaranteed. In the case of a geometric location tolerance prescription without an offset tolerance zone prescription, the screwed-in bolt may take a position that will not allow the components to be assembled. The prescription of a displaced tolerance zone means that the prescribed cylindrical positioning tolerance of the T = 0.2 mm axis with a length of 27 mm is displaced to component 2. This ensures that parts 2 and 3 can be assembled with the same value of geometric location tolerance (T = 0.2 mm).

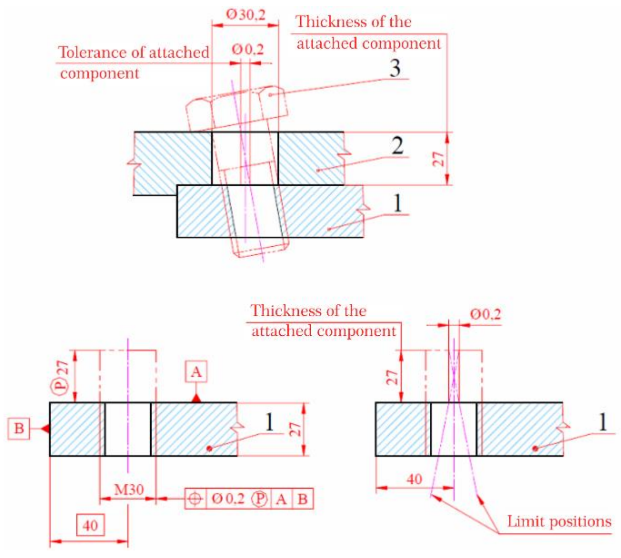
Ø30.2
Thickness of the attached component
Tolerance of attached component
Ø0.2
3
2
27
1
Ⓟ27
A
B
1
27
M30
Ø0.2 Ⓟ A B
40
Thickness of the attached component
Ø0.2
27
1
40
Limit positions

Fig. 5. Example of application of the offset tolerance zone prescription for gearbox assembly

The envelope inspection condition may be applied to a single element (e.g., the surface of a cylinder) or to a surface formed by two parallel planes (e.g., a groove).

The envelope condition is prescribed on the drawing by a mark E in a circle placed after the tolerance of the corresponding length dimension (Fig. 6a).

The condition is advantageous for the elements that will together form the fit. The prescription of the enveloping area condition (by the entry of the E mark in the ring and the entry TOLERATION ISO 8015) ensures that despite the validity of the independence of dimensions and geometry, no part of a cylindrical element or of an element formed by two parallel planes can exceed the enveloping area of the correct geometric shape with a dimension at the maximum limit of the material (e.g., due to geometric variations of shape and orientation). This means that the geometrically correct shape of the element must be respected for the dimensions of the element at the maximum limit of the material.

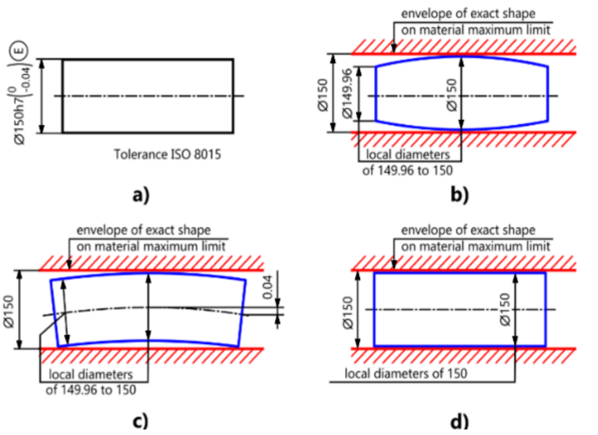
Ø150h7 0/-0.04 Ⓔ
Tolerance ISO 8015
a)
envelope of exact shape on material maximum limit
Ø150
Ø149.96
Ø150
local diameters of 149.96 to 150
b)
envelope of exact shape on material maximum limit
Ø150
0.04
local diameters of 149.96 to 150
c)
envelope of exact shape on material maximum limit
Ø150
Ø150
local diameters of 150
d)

Fig. 6. Prescription of the envelope condition for the shaft: (a) marking on the drawing, (b) deviation of geometric shape, (c) deviation of geometric shape and (d) shaft with diameters at the maximum limit of the material

For elements of the character of the shaft (Fig. 6), which is one of the main elements of the gearbox, for example, the condition of the enveloping area of the cylindrical shaft prescribed in the drawing of the element according to Fig. 6a), is thereby determined:

- that the entire toleranced element (e.g., cylindrical shaft) must lie inside the envelope of the correct geometric shape with a dimension equal to the upper limit dimension of the toleranced element (material maximum), that is, 150 mm;
- that each actual local shaft dimension must be within the tolerance zone IT7 = 0.04 mm and can vary from 149.96 mm to 150 mm (Figs. 6b, c). The lower limit shaft dimensions (149.96–150 mm) can only be checked by two-point measurement.
- this means that if the shaft has actual local diameters at the maximum of the shaft material, that is, with an upper limit dimension of 150 mm, the shaft must be exactly cylindrical (Figs. 6d).

3.2. Position tolerances

Position tolerances include position, concentricity and symmetry. Position tolerances have their application on production drawings of the lids (Fig. 4), as well as on drawings of the top and bottom parts of the gear case.

The position tolerances, which are determined by the geometric elements related to the base, do not define the shape tolerances of the geometric elements of the base itself. It should be noted that the position tolerances include shape tolerances and orientation tolerances of the toleranced feature.

Fig. 7 is an example of the tolerance of the position of the centre of a sphere related to a basic system formed by three planes.

The tolerance zone is defined by the limits of a sphere with diameter t = 0.3 mm, with the tolerance value prefixed by the mark Ø. The centre of the spherical tolerance zone is given by the arrangement of the theoretically accurate dimensions relative to the bases A, B and C. The selected centre of the sphere is to be located within a spherical centre zone of diameter 0.3 mm, which is identical to the theoretically accurate location of the sphere with respect to the base formed by the planes A, B and C.

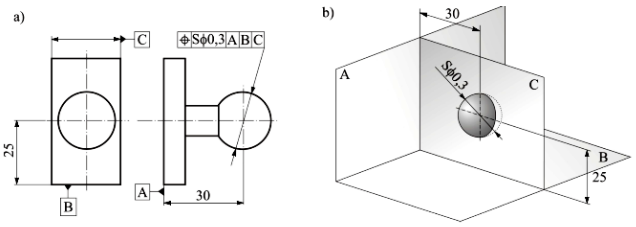

Fig. 7. Location of the centre of the sphere related to the base system formed by the three planes: (a) prescription on the drawing and (b) tolerance zone

Fig. 8 shows an example of the tolerance of the axis location related to the system formed by the three planes. It is an example of tolerancing the position of the hole on the gearbox mounting flange, which is used to attach the gearbox to the base – the frame. The tolerance zone is defined by the cylinder or diameter t, with the tolerance value prefixed by the mark Ø. The axis is given by the theoretically exact dimensions with respect to the bases C, A and B. In the example, the extracted (derived) axes should be in a cylindrical zone with an axis diameter of 0.08 mm, which coincides with the theoretically exact location of the hole, relative to the base formed by planes C, A and B.

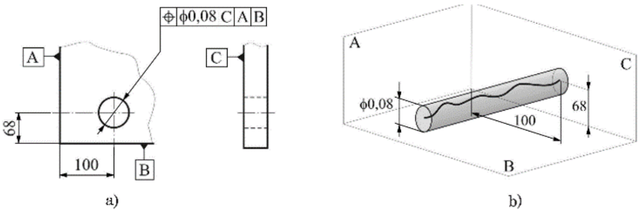

Fig. 8. Location of the axes related to the system formed by the three planes: (a) prescription on the drawing and (b) tolerance zone

Another element used in shaft tolerancing is the tolerance of concentricity. In Fig. 9, the extracted (true) centreline of the toleranced cylinder must be inside a cylindrical zone 0.08 mm in diameter whose axis is identical to the common A-B base line.

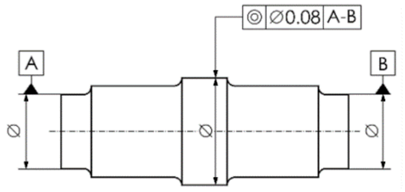

Fig. 9. Example of concentricity tolerance

Another tolerance used on gear shaft drawings is the tolerance for the symmetry of the midplane.

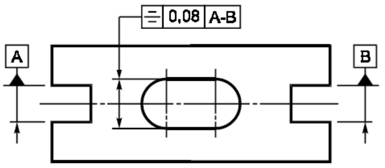

Fig. 10. Example of symmetry tolerance

In Fig. 10, the extracted (true) midplane must be located between two parallel planes spaced apart by a tolerance value of 0.08 mm, which are symmetrically arranged to the common A-B base plane.

3.3. Form tolerance

The irregularity of surfaces or profiles can be divided into shape, waviness and roughness according to the ratio of the distance between the irregularities (deviations, waves, cracks, etc.) and their depth. Form deviation is the value of the deviation of the actual shape of the workpiece from its nominal designed shape as indicated on the drawing, or defined in the standard as the maximum permissible distance of points of the actual surface from the envelope surface.

The cylindricity tolerance defines the limits of the straightness deviation, the deviation of the cylinder forming lines (axes), the roundness deviation of the cylinder cross-sections and the deviation of the parallelism of the opposite forming lines of the elements. The tolerance zone is defined by two concentric cylinders. When checking the deviation of the form, the complete surface of the real cylinder should not exceed the pitch of the two concentric cylinders, which are spaced apart by a minimum distance, without considering the size of the cylinder (Fig. 11).

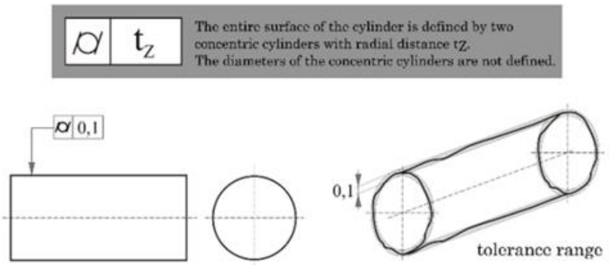

The entire surface of the cylinder is defined by two concentric cylinders with radial distance tZ.
The diameters of the concentric cylinders are not defined.

Fig. 11. Definition and explanation of cylindricity deviation

The cylindricity tolerance is used on production drawings of shafts and drawings of gear case bodies, to tolerate the cylindricity of holes.

3.4. Runout tolerance

In general, runout refers to the description of workpiece surfaces that have a rotationally symmetrical shape and their deviations from a theoretically accurate circular shape. On production drawings of gear shafts, the tolerance of the total circular runout finds its application. Tolerance of total runout is characterised by the fact that the locations of the zones for the different cuts are strictly related – they all have the same initial zero point.

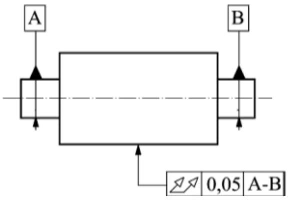

Fig. 12. Total runout tolerance

The total runout is indicated by a mark with two arrows in the tolerance box (Fig. 12). The zone is the volume defined by two concentric cylinders whose axes are coincident with the dotted axis defined by the basic system and whose radii differ by a prescribed tolerance value. For the workpiece, the actual area must be within the volume between two concentric cylinders whose radii differ by 0.05 mm and whose axes are coincident with the general datum formed by the straight line A-B.

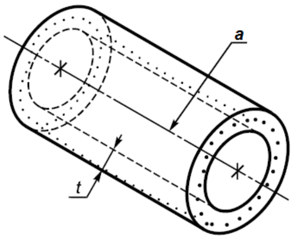

Fig. 13. Definition of tolerance zone: a – base A-B

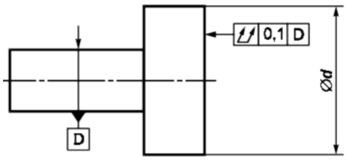

Fig. 14 Designation and explanation of axial total runout

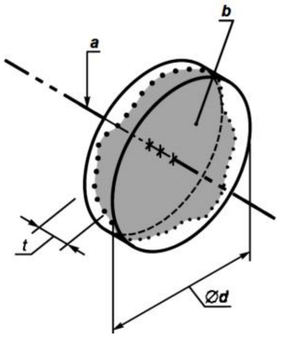

Fig. 15. Definition of tolerance zone: a – base D, b – extracted surface

The tolerance zone is bounded in Fig. 13 by two concentric cylinders whose radial distance is equal to the value of t and whose axes are identical to the baseline.

In addition to radial runout, axial runout is also used, an example of which is shown in Fig. 14.

In Fig. 14, the extracted (true) surface must be located between two parallel planes whose radial distance is equal to a tolerance value of 0.1 mm and which are perpendicular to the axis of the base D.

The tolerance zone is bounded in Fig. 15 by two parallel planes spaced apart by t, which are perpendicular to the base.

3.5. Example of gearbox shaft tolerance

Fig. 16 shows part of the gearbox input shaft fit. The example of shaft dimensioning will illustrate the dimensioning rule for individual tolerances on the manufacturing drawing of the shaft.

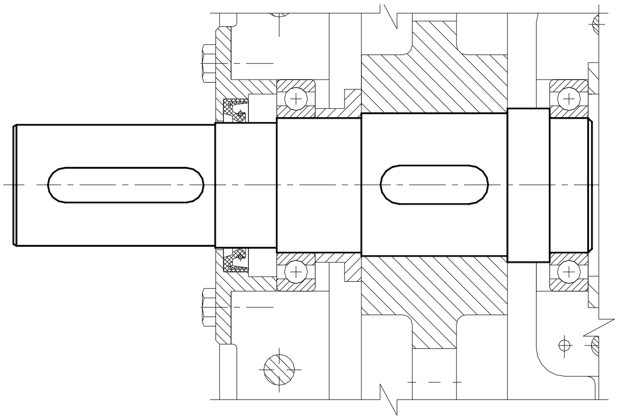

Fig. 16. Gearbox input shaft arrangement

Fig. 17 illustrates the prescribed tolerances for the individual functional dimensions, which are selected as follows. Under position number 1, this is the prescription for the cylindricity tolerance: its value is ‘10 μm = 0.01 mm’ and is determined from the standard for the nominal dimension Ø63m6 (nominal dimension range from 50 mm to 120 mm) and precision grade 6.

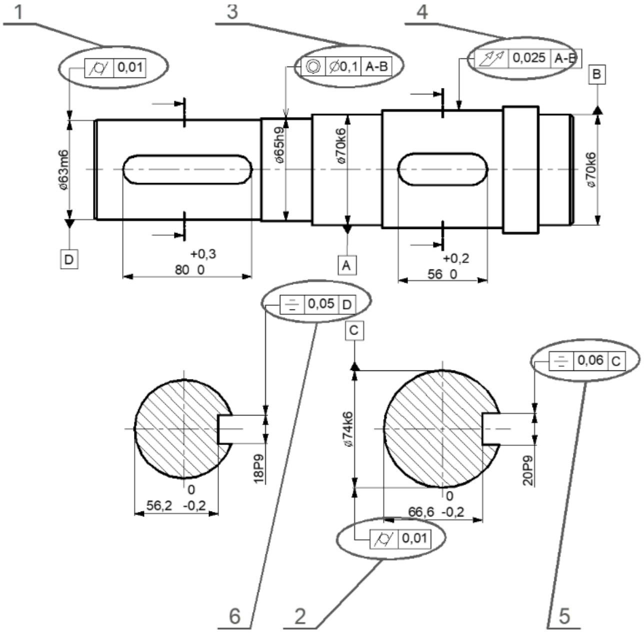

Fig. 17. Prescription of geometric tolerances on the shaft – example

Under position number 2 is the cylindricity tolerance. The value of the cylindricity tolerance “10 μm = 0.01 mm’ is determined according to the standard for the nominal dimension Ø74k6 (nominal dimension range from 50 mm to 120 mm) and accuracy grade 6.

Under position number 3 is the tolerance of concentricity. The value of the concentricity tolerance is ‘100 μm = 0.1 mm’ for the nominal dimension, that is, for the diameter of the considered rotating surface Ø65h9 and accuracy grade 9.

An example of a total circumferential runout tolerance prescription is given under position number 4. The tolerance value of the total circumferential runout is ‘25 µm = 0.025 mm’ for the nominal dimension, that is, for the diameter of the rotating surface under consideration Ø74k6 and accuracy grade 6.

An example of a symmetry tolerance prescription is indicated by position numbers 5 and 6. In the first case, the value of the symmetry tolerance is ‘60 µm = 0.06 mm’ and is determined for the nominal dimension of the groove width for the tight pen 20P9. In the second case, the value of the symmetry tolerance is ‘50 µm = 0.05 mm’ and is determined by standard for the nominal dimension, that is, for the dimension between the faces forming the element 18P9.

4. CONCLUSIONS

Based on the analysis of the application of the basic principles of GPS, the drawing documentation of each non-normalised gearbox element must satisfy the following rules:

- All dimensions must have a tolerance. Every element on a manufactured component is subject to variation, and therefore, tolerances must be prescribed. Upper and lower tolerance limits are prescribed directly for the dimension, or a block of basic parallel dimensions is used. For basic dimensions, geometric tolerances are indirectly prescribed by means of a tolerance box. The only exceptions are minimum and maximum dimensions, semi-finished products or starting points.
- Dimensioning and tolerancing must fully define the nominal geometry and tolerance.
- Technical drawings define the requirements for finished (complete) components. It is required that every dimension and tolerance that define the finished part are indicated on the drawing. If additional dimensions are required but not necessary, they may be marked as reference ones.
- Dimensions should be applied to elements and arranged in such a way as to represent the function of the element.
- Descriptions of manufacturing processes should be avoided. The geometry should be described without explicitly defining the method of manufacture.
- If a dimension is needed in the manufacturing process but is not required in the final geometry (due to dilation or other reasons), then it should be marked as informative.
- For maximum clarity, all dimensions and tolerances should be placed so that they are at the dimension and extension lines and at the correct elements.
- If it common practice to check geometry by limit gauges or by a marked code (e.g., a blank material code), then such dimensions should have the limit gauge or code indicated in brackets or below the dimension.
- Unless otherwise indicated on the drawing, all prescribed dimensions and tolerances apply at 20°C.
- Unless otherwise expressly stated, all dimensions and tolerances apply to the un-preloaded condition.
- Dimensions and tolerances refer to the overall length, width and depth of the element.

REFERENCES

1. Lin W, Chen N. Research on New Geometrical Product Specifications (GPS)-Geometrical Tolerancing. 5th International Conference on Mechanical, Control and Computer Engineering (ICMCCE). 2020: 2106-2109. https://doi.org/10.1109/ICMCCE51767.2020.00458
2. Cai N, Answer N, Scott P. J, Qiao L, Jiang X. A new partitioning process for geometrical product specifications and verification. Precision Engineering. 2020;62:282-295. https://doi.org/10.1016/j.precisioneng.2019.12.009
3. Moravec J. Extrusion in Hydroenvironment in laboratory Conditions, XXI. AEaNMiFMaE-2018,MATEC Web of Conference 168, 07003, 2018. https://doi.org/10.1051/mateccof/201816807003.
4. Humienny Z. State of art in standardization in the geometrical product specification area a decade later. CIRP Journal of Manufacturing Science and Technology. 2021;33:42–51. https://doi.org/10.1016/j.cirpj.2021.02.009
5. Figlus T, Koziol M, Kuczynski L. The Effect of Selected Operational Factors on the Vibroactivity of Upper Gearbox Housings Made of Composite Materials. Sensors. 2019; 19(19), 4240:1-17. https://doi.org/10.3390/s19194240
6. Sinčák PJ, Virgala I, Kelemen M, Prada E, Bobovský Z, Kot T. Chimney Sweeping Robot Based on a Pneumatic Actuator. *Applied Sciences*. 2021; 11(11):4872. https://doi.org/10.3390/app11114872
7. Qi Q, Pagani L, Jiang X, Scott P. J. Enabling metrology-oriented specification of geometrical variability – A categorical approach. Advanced Engineering Informatics. 2019;39:347–358. https://doi.org/10.1016/j.aei.2018.11.001
8. Cheng Y, Wang Z, Chen X, Li Y, Li H, Wang H. Evaluation and Optimization of Task-oriented Measurement Uncertainty for Coordinate Measuring Machines Based on Geometrical Product Specifications. Applied Sciences. 2019;9(1):1-6. https://doi.org/10.3390/app9010006.
9. Can E, Bozca M. Optimisation of gear geometrical parameters using KISSsoft. Machines, Technologies, Materials. 2019;13(1),7-10.
10. Sapietková A. Simplified computation methodology for contact forces on tapered rolling bearing with flexible parts. Scientific Journal of Silesian University of Technology. Series Transport. 2018;99:177–182. https://doi.org/10.20858/sjsutst.2018.99.16
11. Moravec J, Bury P, Černobila F. Investigation of Forging Metal Specimens of Different Relative Reductions Using Ultrasonic Waves. Materials. 2021;14(9), 2406. https://doi.org/10.3390/ma14092406
12. Humienny Z. Can ISO GPS and ASME Tolerancing Systems Define the Same Functional Requirements? Applied Sciences. 2021;11, 8269. https://doi.org/10.3390/app11178269
13. Wejrzanowski T, Ibrahim SH, Skibinski J, Cwieka K, Kurzydlowski KJ.: Appropriate models for simulating open porous materials. Image Analysis & Stereology. 2017;36:105-110. https://doi.org/10.556/ias.1649
14. Yu Y, Wang Q, Ni J, Xu D, Li J. A GPS-based force rendering model for virtual assembly of mechanical parts. The International Journal of Advanced Manufacturing Technology. 2022;118,465–477. https://doi.org/10.1007/s00170-021-07939-x

Acknowledgments: This paper was developed within the project implementation KEGA 029TUKE-4/2021 “Implementation of modern educational approaches in the design of transmission mechanisms.”

Silvia Maláková: https://orcid.org/0000-0003-1660-6333

Samuel Sivák: https://orcid.org/0000-0002-9820-4874

DOI 10.2478/ama-2022-0038

INFLUENCE OF EXTRUDER PLASTICIZING SYSTEMS ON THE SELECTED PROPERTIES OF PLA/GRAPHITE COMPOSITE

Daniel KACZOR[*,**], **Krzysztof BAJER**[*], **Grzegorz DOMEK**[**]
Piotr MADAJSKI[***], **Aneta RASZKOWSKA-KACZOR**[*], **Paweł SZROEDER**[****]

[*]Łukasiewicz Research Network Institute for Engineering of Polymer Materials and Dyes,
Marii Skłodowskiej-Curie 55, 87-100 Toruń, Poland
[**]Faculty of Mechatronics, Kazimierz Wielki University, Kopernika 1, 85-074 Bydgoszcz, Poland
[***]Faculty of Chemistry, Nicolaus Copernicus University, Gagarina 7, 87-100 Toruń, Poland
[****]Institute of Physics, Kazimierz Wielki University, Powstańców Wielkopolskich 2, 85-090 Bydgoszcz, Poland

daniel.kaczor@impib.lukasiewicz.gov.pl, krzysztof.bajer@impib.lukasiewicz.gov.pl, gdomek@ukw.edu.pl
piotr.madajski@doktorant.umk.pl, aneta.kaczor@impib.lukasiewicz.gov.pl, psz@ukw.edu.pl

received 28 June 2022, revised 23 July 2022, accepted 24 July 2022

Abstract: Twin-screw extrusion is a crucial method for the direct inserting of carbon micro- and nanomaterials into a polymer matrix using a dry procedure. The study aimed to determine the influence of the parameters of the twin-screw extruder plasticizing system on the dispersion homogeneity and distribution of graphite filler in the polylactide polymer matrix and overall quality of the composite. As a filler, a graphite micropowder with a 5 μm lateral size of platelets was used at concentration of 1 wt.%. Three configurations of screws with different mixing intensity and various types segments were considered in the extrusion experiments. Morphology and chemical structure of the obtained composites were examined using scanning electron microscopy (SEM), Fourier transform infrared spectroscopy – attenuated total reflectance (FTIR-ATR) and Raman spectroscopy. Differential scanning calorimetry (DSC) and melting flow rate measurements (MFR) were used to asses thermal and rheological properties of the composites. Samples of the polylactide/graphite composites were also subjected to mechanical tests. The results show that the selection of the mechanical parameters of twin-screw extruder plasticizing system plays a key role in the preparation of the homogeneous PLA/graphite composites. Incorrect selection of the screw geometry results in poor mixing quality and a significant deterioration of the mechanical and thermal properties of the composites. Optimised mixing and extrusion parameters can be the starting point for the design of efficient twin-screw extruder plasticizing system for fabrication of PLA composites with carbon nanotube and graphene fillers.

Key words: differential scanning calorimetry, extrusion, graphite, infrared spectroscopy, mechanical properties, melting flow rate, plasticizing system, polylactide, twin-screw extruder

1. INTRODUCTION

Traditional polymers, obtained from crude oil, are nowadays increasingly being replaced by their equivalents produced from renewable sources. Their use reduces environmental pollution, greenhouse gas emissions and the consumption of fossil resources [1–6]. Polylactide (PLA), also known as poly(lactic acid), is the oldest and one of the most interesting and useful biodegradable polymers. Currently, PLA has a principal position on the market of biodegradable polymers [7]. Several applications of PLA-based polymers have been developed in the automotive [8, 9], agricultural [10, 11], medicine [12, 13], electronic [14, 15] and packaging [16, 17] industries.

To improve mechanical, thermal and electrical properties of PLA for industrial and commodity applications, various types of fillers have been added: nanomaterials [18], organic fibres [19], talc [20], montmorillonite [21] and graphite [22]. Carbon nanomaterials such as carbon nanotubes and graphene with superior thermal and electrical properties can be used as a filler that improves some specific properties, such as stiffness, thermal stability, fire retardancy and lower permeability [23].

Due to its high versatility, PLA is processed using the same methods as other popular polymers: injection and compression moulding, spinning, extrusion or 3D printing [24–28].

Extrusion has been widely used in the manufacture of films, sheets, pipes and profiles. This processing technique can be used for preparation of polylactide composites containing a wide range of additives. The advantages of the extrusion include high efficiency, quality and repeatability, and possibility of mass production and of obtaining multi-component composites in one technological process. The quality and thus the properties of polymer composites obtained by extrusion are affected by both the extrusion temperature [29] and processing speed [30]. The configuration of the extruder plasticizing system plays a key role in the dispersion quality of the filler in the polymer matrix and the properties of final composites [31]. High-quality polymer composites are characterised by an excellent dispersion of the filler. Undispersed filler agglomerates exercised a negative effect on mechanical [32], thermal [33] and electrical properties [34] of obtained composites.

Good dispersion can be obtained using plasticizing systems characterised by high mixing and grinding abilities. However, the use of such systems may have a negative effect in terms of change in the degree of polymer degradation [35].

The innovation of work involves the selection of an optimal plasticizing system of a twin-screw extruder with the preferred processing parameters required to obtain PLA composites with an excellent dispersion of graphite fillers and without significant changes in polymer properties. The developed system will be used for further research on composites with carbon nanotubes and graphene as similar fillers. Currently, there is little information on the optimal configuration of screws in the processing of PLA with carbon fillers of this type.

2. MATERIALS AND SAMPLE PREPARATION

Graphite micropowder, MG3096 (3000 mesh), used as a carbon filler, was purchased from Sinograf S.A. Company (Poland). The polylactide (PLA) produced by Total-Corbion (Netherlands), available under the trade name Luminy® LX175 (sample marked as PLA/TC), was used as a matrix in the obtained polymer masterbatches and composites. For obtaining masterbatches, before mixing, PLA was ground into powder form with a particle size of 100–600 µm. Typical properties of used PLA are shown in Table 1 [36, 37].

Tab. 1. Typical properties of Luminy® LX175

Properties	Method	Typical value
Density	Literature value	1.24 g/cm^3
Stereochemical purity	Total-Corbion PLA method	96% (L-isomer)
Residual monomer	Total-Corbion PLA method	≤0.3%
Melting temperature	DSC	155 °C
Glass transition temperature	DSC	60 °C

2.1. Masterbatch preparation

Masterbatch was prepared by mixing 30 g of polylactide with 10 g of graphite powder in a mixer (50 EHT Brabender Plasti-Corder® Lab-Station Germany), at 190 °C and 50 rpm.

Before the mixing process, PLA was dried in the POL-EKO SLW 180 STD dryer at temperature 80 °C for 8 h. Preparation of the masterbatch in the mixer was carried out in two stages. In the first, PLA was melted for 2.5 min; in the second, graphite powder was added and the mixture was stirred for 2 min. The properties of obtained masterbatch are available in our published papers [38, 39].

2.2. Composites preparation

The tested composites containing 1% graphite were extruded using 960 g of pristine PLA with 40 g of masterbatch. The extrusion process was carried out using a twin-screw extruder (Bühler BTSK, Uzwil, Switzerland) with a screw diameter of 20 mm and a screw length of 790 mm. All samples were extruded at the same main drive speed: 150 rpm; and temperature profile: 180 °C, 180 °C, 190 °C, 190 °C or 195 °C (head). The following parameters were registered during the extrusion process: changes of the temperature in each extruder zone, stock temperature, torque of the main drive, power of the main drive and the process efficiency. Before extrusion, polylactide and masterbatch were dried in a dryer for 8 h at 80 °C. Three configurations of screws with different mixing intensities and various types of mixing segments were used to prepare samples.

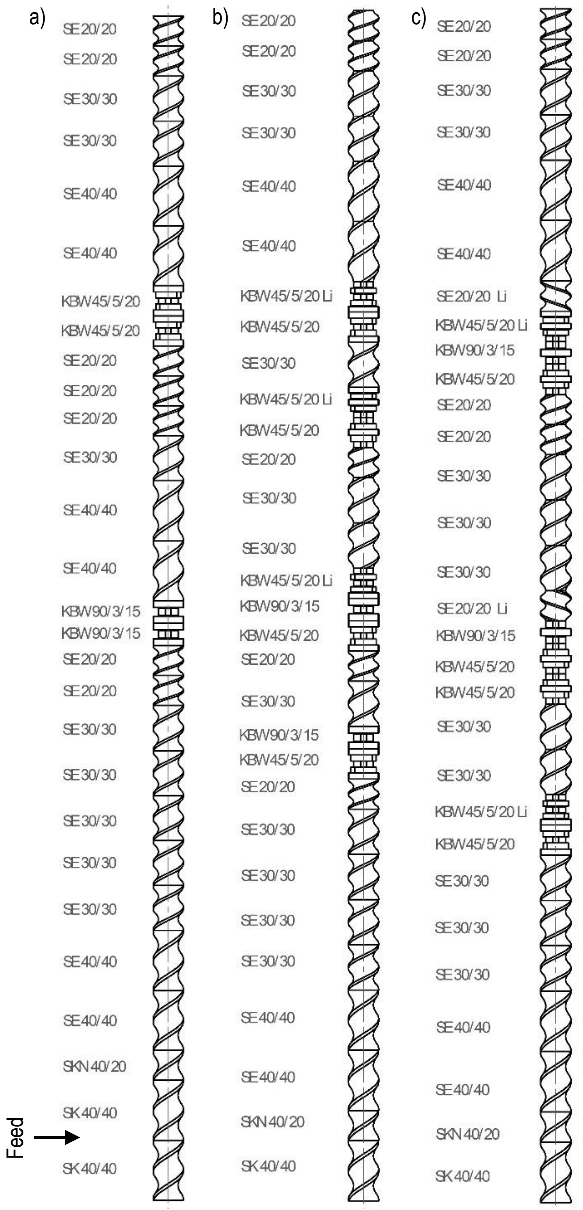
a)
SE20/20
SE20/20
SE30/30
SE30/30
SE40/40
SE40/40
KBW45/5/20
KBW45/5/20
SE20/20
SE20/20
SE20/20
SE30/30
SE40/40
SE40/40
KBW90/3/15
KBW90/3/15
SE20/20
SE20/20
SE30/30
SE30/30
SE30/30
SE30/30
SE30/30
SE40/40
SE40/40
SKN40/20
SK40/40
Feed
SK40/40
b)
SE20/20
SE20/20
SE30/30
SE30/30
SE40/40
SE40/40
KBW45/5/20 Li
KBW45/5/20
SE30/30
KBW45/5/20 Li
KBW45/5/20
SE20/20
SE30/30
SE30/30
KBW45/5/20 Li
KBW90/3/15
KBW45/5/20
SE20/20
SE30/30
KBW90/3/15
KBW45/5/20
SE20/20
SE30/30
SE30/30
SE30/30
SE30/30
SE40/40
SE40/40
SKN40/20
SK40/40
c)
SE20/20
SE20/20
SE30/30
SE30/30
SE40/40
SE40/40
SE20/20 Li
KBW45/5/20 Li
KBW90/3/15
KBW45/5/20
SE20/20
SE20/20
SE30/30
SE30/30
SE30/30
SE20/20 Li
KBW90/3/15
KBW45/5/20
KBW45/5/20
SE30/30
SE30/30
KBW45/5/20 Li
KBW45/5/20
SE30/30
SE30/30
SE30/30
SE40/40
SE40/40
SKN40/20
SK40/40

Fig. 1. Drawings of the screw systems: (A) K1; (B) K3; (C) K5

The K1 system, shown in Figure 1A, is characterised by two zones with low intensity mixing and shearing functions. In the first zone, two neutral kneading elements KBW 90/3/15 were used and in the second zone, two forward kneading elements KBW 45/5/20 were used.

The K3 screw system shown in Figure 1B has a higher intensity than the K1 system, and it includes four mixing and shearing zones. The first zone of the screw system consists of two kneading elements KBW 90/2/15 and KBW 45/5/20. The subsequent zones have forward kneading elements and an additional reverse kneading element KBW 45/5/20. The reverse element holds the polymer in the zone for longer, resulting in more intense mixing, but this can lead to the degradation of PLA.

K5, shown in Figure 1C, is a strong mixing and degrading system. We included this in our study to observe the effect of strong

DOI 10.2478/ama-2022-0038

mixing on PLA matrix. The system includes three mixing–shearing zones. Each one contains a reverse kneading element, which causes a significant increase in mixing.

Neat polymers (PLA/NG) and polylactide-graphite composites (PLA/G) prepared using one of the three plasticizing systems (K1, K3, or K5) are listed in Table 2.

Tab. 2. Labelling and processing methods of PLA/graphite composites

Sample	Graphite content (%)	Plasticizing system
PLA/NG/K1	0	K1
PLA/G/K1	1	K1
PLA/NG/K3	0	K3
PLA/G/K3	1	K3
PLA/NG/K5	0	K5
PLA/G/K5	1	K5

3. MATERIALS CHARACTERISATION

3.1. Phase morphology analysis

To evaluate the dispersion of graphite in the polymer matrix, scanning electron microscopy (SEM, SU8010, Hitachi, Japan) was used. For SEM imaging, samples were deposited on conductive carbon adhesive tape and coated with a nanometrical layer of gold. Gold was used to increase the surfaces' electrical conductivity in the tested samples. All microscopic observations were made at the accelerating voltage of 10 kV and a working distance of 8 mm.

3.2. Chemical structure analysis

Fourier transform infrared spectroscopy – attenuated total reflectance spectra were measured using the Cary 630 FTIR-ATR spectrometer (Agilent Technologies, USA). Measurements were carried out over the spectral range of 400–4000 cm^{-1} with a resolution of 2 cm^{-1}.

Raman spectra were recorded in backscattering geometry, with a Senterra Raman microscope (Bruker Optik, Billerica, MA, USA), using a 2-mW laser beam with a wavelength of 532 nm as an excitation light source.

Both the FTIR-ATR and Raman spectra were acquired at ambient temperatures.

3.3. Thermal behaviour and stability analysis

The Mettler Toledo (Switzerland) DSC1 calorimeter was used to perform differential scanning calorimetry. The calorimeter was calibrated with pure indium and zinc standards. All samples were tested under nitrogen atmosphere, at a gas flow rate of 50 cm^3/min. Each sample of 5–7 mg was sealed in aluminium crucible. DSC analysis was divided into five stages:

- First stage (heating 1): the samples were heated at a constant rate of 10 °C/min from 0 °C to 300 °C.
- Second stage: this was an isothermal stage lasting 5 min.
- Third stage: the samples were cooled at a rate of 10 °C/min to 0 °C.
- Fourth stage: this was an isothermal stage lasting 5 min.
- Fifth stage (heating 2): the samples were heated at a constant rate of 10 °C/min from 0 °C to 300 °C.

The analyses were performed in accordance with the PN-EN ISO 11357-(1-3): 2009 standards [40].

The decomposition temperature of the Luminy® LX175 in nitrogen atmosphere is above 300 °C [41].

The room temperature crystallinity, X_C (1), of PLA composites was evaluated using the following formula:

$$X_C = \left(\frac{\Delta H_m - \Delta H_{cc}}{w \Delta H_m^0}\right) \cdot 100\% \qquad (1)$$

where X_C represents PLA crystallinity, ΔH_m melting enthalpy, ΔH_{cc} cold crystallisation enthalpy (J/g), w fraction of the polymer in the composite materials and ΔH_m^0 melting enthalpy of 100% crystalline PLA (93 J/g) [42].

3.4. Rheological properties

The melt flow rate of the composites was determined according to the PN-EN ISO 1133:2011 standard [43] using a Dynisco (USA) LMI 4003 capillary plastometer. The measurements were carried out under the piston loading of 2.16 kg at 190 C. Samples were dried before measurement for 8 h at 80 °C in a drier.

3.5. Mechanical properties

To perform tensile and Charpy impact tests, normalised dumbbells and bars were prepared using a laboratory injection moulding type Plus 35 (Battenfeld GmbH, Germany). The moulded pieces were made according to PN-EN ISO 294-1 standard [44].

To determine tensile strength (σ_m), stress at break (σ_b), strain at strength (ε_m) and elongation at break (ε_b) according to the PN-EN ISO 527-1:2020 standard [45], a tensile testing machine type TIRAtest 27025 (TIRA Maschinenbau GmbH, Germany) was used. The mechanical properties were measured at a speed of 50.0 mm/min. Tensile modulus (E_t) was determined with the use of the same machine at a speed of 1.0 mm/min.

Charpy impact strength (α_{cN}) was determined in notched samples type 1eU according to the PN-EN ISO 179-1:2010 standard [46] with edgewise impact, using a pendulum impact tester, type IMPats15 (ATS FAAR, Italy), equipped with a 0.5-N pendulum.

All mechanical tests were carried out at 50% relative humidity and 23 °C. The specimens were conditioned in the same conditions as the measurement for 24 h.

4. RESULTS

4.1. Extrusion process analysis

Table 3 shows the values of stock temperature (T_t), torque main drive (M_o), power main drive (W) and efficiency (Y) recorded during extrusion.

Tab. 3. Parameters recorded during extrusion

Sample	PLA/NG/K1	PLA/G/K1	PLA/NG/K3	PLA/G/K3	PLA/NG/K5	PLA/G/K5
T_t (°C)	220	220	217	220	218	218
M_o (Nm)	15.5	16.5	21.5	22.0	25.7	26.4
W (kW)	0.46	0.47	0.65	0.66	0.74	0.76
Y (kg/h)	3.7	3.7	3.7	3.7	3.7	3.7

The K1 system generated low torque in the range of 15.5–16.5 Nm. The increase in mixing intensity resulted in an increase in torque by almost 21.5 Nm (K3) and by as much as 25.7 Nm in the case of K5. Changes in the value of the main drive power supply, which were related to the increased mixing capacity of the plasticizing system, were also observed. The value of this parameter for K1 is lower than for K5 by 62%. No differences between the set and actual extrusion temperature were observed. The addition of 1% graphite did not cause any significant differences in the extrusion process. The only observed differences were a slight increase in the torque and power main drive in samples with graphite filler compared to the neat polymer samples extruded in this same plasticizing system. Addition of graphite and changes in plasticizing system have not resulted in changes in the efficiency of the process.

4.2. Phase morphology analysis

Figure 2 shows SEM images of graphite fillers and PLA graphite composites, and the size of the graphite flakes was found to be 6 ± 2 µm. In the breakthrough of the sample obtained with the K1 plasticizing system, the presence of larger fragments of graphite filler is visible. This means that the graphite introduced into the polymer matrix was not completely ground during extrusion. The graphite filler in the PLA/G/K3 and PLA/G/K5 samples was rubbed into smaller pieces, and this proves that better mixing and grinding properties of screws were utilised in the K3 and K5 systems compared with K1. For the samples obtained with the use of K3 and K5 plasticizing systems, orientation of the graphite flakes in the direction of extrusion can be seen.

No pores or any other types of discontinuity were found in the polymer matrix.

4.2. FTIR-ATR and Raman analyses

Figure 3 shows FTIR-ATR spectra of the composites. The lowest spectrum was obtained for the raw PLA (PLA/TC sample). Recorded absorption spectra contain the bands assigned to the PLA polymer matrix [47, 48]. The crystalline and amorphous polymer phases can be assigned to bands at 753 cm⁻¹ and 865 cm⁻¹. At 1041 cm⁻¹ appear the stretching modes of C–CH₃ group. The symmetric and asymmetric stretching modes of the C–O–C group appear at 1081 cm⁻¹ (symm), 1180 cm⁻¹ and 1266 cm⁻¹, respectively, while 1127 cm⁻¹ is a position of rocking modes of the CH_3 group band. Features characteristic to the CH and CH_3 symmetric bending modes appear at 1358 cm⁻¹ and 1381 cm⁻¹, while the band corresponding to the asymmetric bending modes is found at 1452 cm⁻¹. Ester C=O stretching modes appear at 1746 cm⁻¹. Weak bands (not shown in Figure 4) at 2945 cm⁻¹ and 2994 cm⁻¹ are attributed to the asymmetric modes of the CH_3 group.

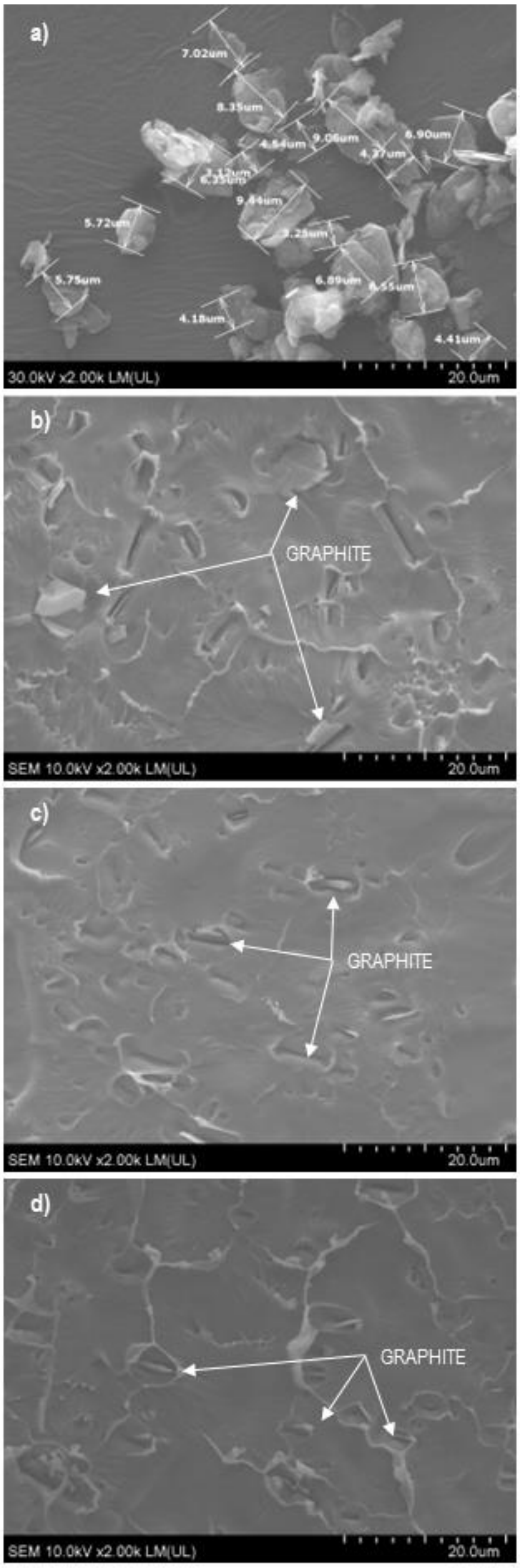

Fig. 2. SEM picture of: (A) graphite filler, samples; (B) PLA/G/K1; (C) PLA/G/K3; (D) PLA/G/K5

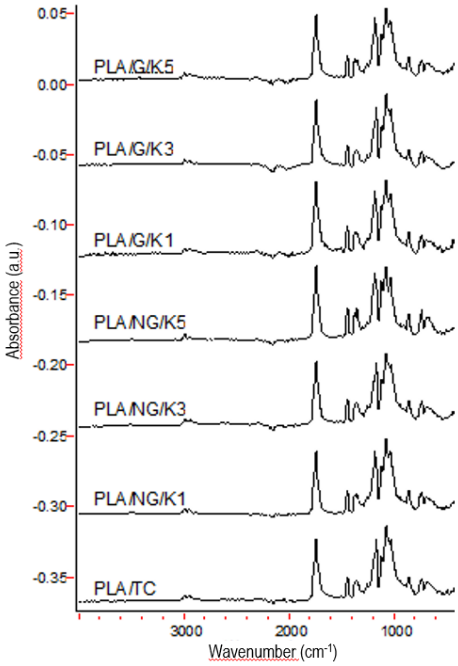

Fig. 3. FTIR-ATR spectra of samples

The plasticizing system used during extrusion did not change the intensity of the bands assigned to the carbonyl (1746 cm^{-1}) and ester (1081 cm^{-1} and 1180 cm^{-1}) groups. The changes in intensity (reduction) of these peaks indicates the shortening of the polymer chains and thus their degradation [49]. Based on this observation, it can be concluded that the used plasticizing systems did not cause polylactide degradation, or caused only a negligibly low amount of degradation.

Graphite filler does not affect the position and relative intensities of the characteristic PLA bands.

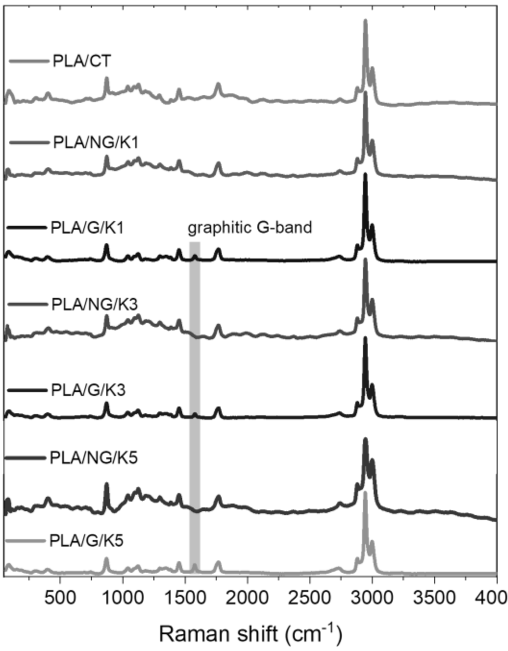

Fig. 4. Raman spectra of neat PLA and PLA/graphite composites

As shown in Figure 4, various oscillation modes visible in FTIR-ATR are also Raman-active. These include the following bands: the stretching modes of the C-CH_3 group at 1042 cm^{-1}, symmetric stretching modes of C-O-C group at 1092 cm^{-1}, the rocking modes of the CH_3 group at 1127 cm^{-1} and the asymmetric bending modes of the CH_3 group at 1452 cm^{-1}. The ester C=O group stretch shows a complex band at around 1770 cm^{-1}. As Qin and Kean [50] have demonstrated, in amorphous PLA, the single C=O stretching mode appears at 1770 cm^{-1}, whereas in crystalline polymer triplet band it is present at 1776 cm^{-1}, 1766 cm^{-1} and 1750 cm^{-1}. Results of the C=O band deconvolution show significant decrease of the 1750 cm^{-1} component intensity in samples subjected to plasticizing process, which indicates reduction of the crystallinity. However, no differences are observed between the proceeded samples of neat polymer and composite. Additionally, the choice of the screw system does not affect the C=O band structure.

Compared to the FTIR-ATR bands, the bands assigned to symmetric stretching of the CH_3 group at 2881 cm^{-1} and 2945 cm^{-1}, and asymmetric stretching of the methyl group at 2998 cm^{-1}, are very strong.

Raman feature at 873 cm^{-1}, attributed to the stretching modes of the C–COO group of PLA, is seen.

Graphitic G-band appears at 1578 cm^{-1} in samples PLA/G/K1, PLA/G/K3 and PLA/G/K5 containing graphite filler.

4.3. Thermal behaviour and stability analysis

To determine the influence of the extruder screws' configuration on the thermal properties of the obtained composites, the DSC technique was used. Thermal data, such as the glass transition temperature (T_g), crystallisation temperature (T_c), cold crystallisation temperature (T_{cc}), melting temperature (T_m), crystallisation enthalpy (ΔH_c), cold crystallisation enthalpy (ΔH_{cc}) and melting enthalpy (ΔH_m), are summarised in Table 4. Thermograms for the first and second heating scans are presented in Figures 5 and 6, respectively.

The heating scan of the pristine PLA (sample PLA/TC) showed an endothermic peak corresponding to the melting of the polymer (T_m^1 = 148.8 °C). This peak was not observed in the second heating scan. This behaviour confirms that the slow crystallisation rate of high molecular weight PLA is not conducive to the development of the crystalline phase during cooling [51]. The rate used during the cooling of the polymer melt (10 °C/min) does not allow for recrystallisation. This speed is too fast for the polylactide chains to reorganise into crystal regions. Since the mobility of the chains is not limited by the presence of crystallites, the glass transition (compared to heating 1) is more pronounced [52]. The absence/large reduction of this peak has also been reported by other researchers [53–55].

For all samples, the glass transition between 57 °C and 64 °C (heating 1) marks the point at which the polymer chains are allowed to move. Reorganisation of amorphous domains into crystalline ones manifest as an exothermic peak at 111 °C in the case of neat polymer and 116–117 °C for PLA/graphite composite. The increase in temperature is related to the restriction of the mobility of the polymer chains by graphite micro-platelets, which hinders the formation of a semi-crystalline phase in the polymer [56]. Melting peak appears near 151–153 °C. There is no correlation between graphite content and melting enthalpy in heating 1 scan results. All samples have amorphous character.

Tab. 4. Thermal parameters obtained by DSC

Sample	**PLA/TC**	**PLA/NG/K1**	**PLA/G/K1**	**PLA/NG/K3**	**PLA/G/K3**	**PLA/NG/K5**	**PLA/G/K5**
Heating 1							
T_m^1 (°C)	148.8	151.4	153.5	151.4	151.8	151.7	153.2
ΔH_m^1 (J/g)	28.7	28.2	24.3	25.8	26.8	26.6	27.1
T_g^1 (°C)	64.3	58.0	60.2	61.5	61.5	58.8	57.6
$T_{cc}1$ (°C)	-	111.5	117.3	111.7	115.9	112.0	117.3
ΔH_{cc}^1 (J/g)	-	27.7	24.1	26.6	26.1	26.6	27.0
X_c^1 (%)	31	0	0	0	0	0	0
Heating 2							
T_m^2 (°C)	-	151.3	151.2	151.5	150.1	151.1	150.0
ΔH_m^2 (J/g)	-	3.1	15.4	2.1	22.7	10.6	24.0
T_g^2 (°C)	57.1	58.7	60.0	59.1	59.0	59.1	59.8
T_{cc}^2 (°C)	-	131.3	128.1	129.8	125.4	129.3	125.3
ΔH_{cc}^2 (J/g)	-	3.0	15.1	1.8	22.5	10.3	23.8
X_c^2 (%)	0	0	0	0	0	0	0

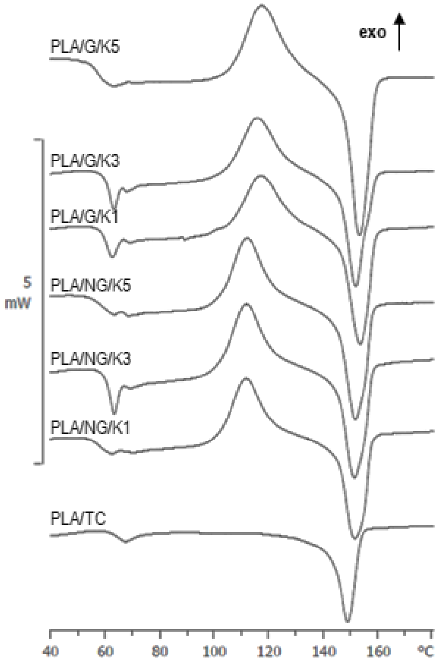

Fig. 5. Heating 1 DSC thermograms of samples

No changes were recorded on the thermograms of the samples during cooling.

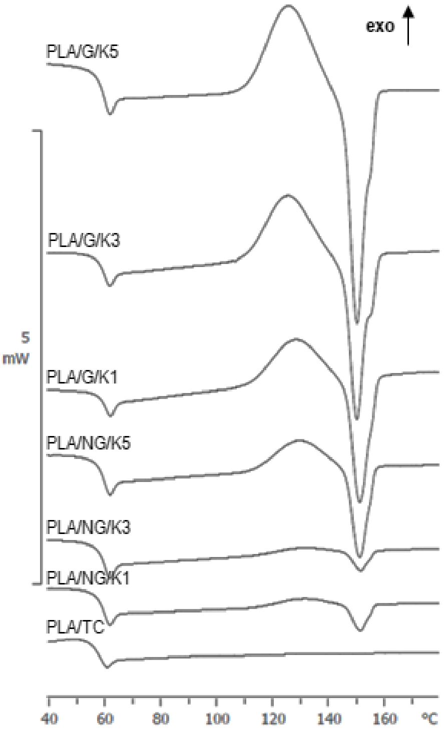

Fig. 6. Heating 2 DSC thermograms of samples

Glass transition temperature in the second heating scan is almost in this same level, near 60 °C, for all samples. The same observation can be made in the case of the melting temperature, where, too, the differences between the samples are small. However, there is a difference in the melting enthalpy between PLA/graphite composites and neat polymers. Samples with graphite filler need much more energy to melt. The same relationship occurs with regard to the enthalpy and temperature of cold crystallisation. For samples with graphite, ΔH_{cc}^2 is higher and T_{cc}^2 lower. Graphite fillers affect the position of the exothermic peak, which is slightly shifted to lower temperatures. As revealed by molecular simulations, local mobility of the polymer chains near the graphite phase are highly anisotropic and drastically reduced in the direction perpendicular to the graphite basal planes. Thus, graphite filler can act as a nucleating agent that promotes the crystallisation process. As a consequence, the T_{cc}^2 decreases [57]. Crystallinity determined from the second heating data for all samples is on a 0% level.

4.4. Rheological properties

Table 5 summarises the MFR values of the obtained samples. An increase in MFR value may be a sign of degradation of the polymer [58]. In the samples without graphite, no significant increase in the value of this parameter was observed. This observation, combined with the conclusions from the FTIR-ATR analysis, allows us to suppose that the used plasticizing system had a negligible effect on the degradation of the used PLA. For samples containing graphite, a slight increase in the melt flow rate can be noticed compared to the samples without this additive, obtained with the same plasticizing system. This may be due to an increase in flow resistance associated with the use of solid filler [59].

Tab. 5. MFR values with standard deviations

Sample	MFR [g/10 min]
PLA/NG/K1	5.8 ± 0.2
PLA/G/K1	5.8 ± 0.1
PLA/NG/K3	6.3 ± 0.1
PLA/G/K3	6.0 ± 0.1
PLA/NG/K5	6.4 ± 0.1
PLA/G/K5	6.0 ± 0.1

4.5. Mechanical properties

The results of mechanical tests of the samples are summarised in Table 6.

Tab.6. Mechanical properties

Sample	PLA/TC	PLA/NG/K1	PLA/G/K1	PLA/NG/K3	PLA/G/K3	PLA/NG/K5	PLA/G/K5
Static tension							
σ_m (MPa)	71.8 ± 0.6	65.3 ± 2.7	64.0 ± 2.9	67.3 ± 2.3	63.3 ± 1.9	67.6 ± 0.7	63.5 ± 1.1
σ_b (MPa)	70.9 ± 1.6	65.2 ± 2.5	63.7 ± 2.7	67.0 ± 2.3	63.0 ± 1.8	67.4 ± 0.7	63.0 ± 1.0
ε_m (%)	4.7 ± 0.2	4.3 ± 0.2	4.1 ± 0.2	4.4 ± 0.4	4.2 ± 0.2	4.7 ± 0.1	4.3 ± 0.1
ε_b (%)	5.1 ± 0.4	4.4 ± 0.2	4.2 ± 0.2	4.4 ± 0.4	4.3 ± 0.2	4.7 ± 0.1	4.4 ± 0.1
E_t (MPa)	3135 ± 82	2024 ± 124	2168 ± 79	2193 ± 125	2101 ± 81	1943 ± 82	2024 ± 156
Charpy impact strength							
α_{cN} (kJ/m^2)	2.9 ± 0.3	3.2 ± 0.4	3.5 ± 0.3	2.8 ± 0.2	2.9 ± 0.1	2.4 ± 0.1	3.3 ± 0.2

During extrusion, the polylactide is partially degraded [58]. This can be observed by comparing the mechanical properties registered during static tension between the pristine polylactide and the samples obtained by a twin-screw extruder without graphite. For these samples, correlations are not observed between the plasticizing system used and changes in mechanical properties. This means that the high temperature associated with the composite extrusion process is mainly responsible for the degradation of the polymer. It should also be taken into account that the samples made of the granulate obtained with the twin-screw extruder were subjected to one thermal treatment more than PLA. An additional process could increase the degradation of the polymer, which is manifested by a greater difference in the values recorded during the static tensile tests.

The addition of graphite caused a slight reduction in value of tensile strength (σ_m) and stress at break (σ_b) for all samples. The same effect was observed by other researchers [60–62].

The results of the Charpy impact test do not show any significant difference between samples. It seems that the configuration of the plasticizing system does not affect the value of this parameter. The addition of graphite microplates slightly increased the value of Charpy impact strength. Polymer degradation can be responsible, among other things, for the decrease in the α_{cN} value [63]. Since the difference between the PLA/TC sample and the others is small, it can be concluded that the polymer degradation during extrusion is insignificant.

5. CONCLUSIONS

The configuration of the plasticizing system of the twin-screw extruder affects the properties of the obtained polymer composites. For efficient mixing of the composite, it is necessary to use a screw with intensive mixing system. The mild configuration makes it impossible to obtain composites with an effective dispersion of graphite in the polymer matrix. The systems equipped with segments responsible for improving mixing, grinding and reversing the material ensure proper grinding of the graphite flakes and prevent the formation of agglomerates.

However, the increase in mixing intensity generates a greater load on the machine (M_o and W); therefore, the mixing and grinding elements in the screw system should be optimally selected to obtain the correct graphite dispersion with the lowest possible load on the machine during processing.

The increase in the intensity of mixing and shear in the screw configuration causes slight degradation in the PLA chain (chain breakage), which is indicated by a decrease in strength properties and an increase in the flow rate. On the other hand, the change of the screw configuration did not affect the oxidative degradation of PLA, which is confirmed by the results of the infrared and Raman analyses.

The addition of graphite has a slight influence on the mechanical properties and the melt flow rate of the obtained composites. For mechanical tests, a slight decrease in the measured values was noticed that is within the standard deviation of the measurement. Graphite filler improves the Charpy impact strength of composites. The MFR value slightly decreased after adding graphite to the polymer matrix.

The addition of graphite and the configuration of the type of extruder plasticizing system used had no effect on the thermal properties of the composites. There were no differences in the melting point and the degree of crystallinity of the tested samples. All samples showed an amorphous nature. The only observation worth noticing is the increase in enthalpy and the decrease in the cold crystallisation temperature of samples containing graphite microplates. This effect is related to the nucleophilic properties of the graphite filler.

The proposed configurations of the plasticizing system did not have a significant impact on the degradation of PLA and thus on the deterioration of the obtained composites' properties. At the same time, the K3 and K5 configurations made it possible to obtain samples with an excellent dispersion of the filler in the polymer matrix.

REFERENCES

1. Taib N-AAB, Rahman MR, Huda D, Kuok KK, Hamdan S, Bakri MKB, Julaihi MRMB, Khan A. A review on poly lactic acid (PLA) as a biodegradable polymer. Polym Bull, 2022.

2. Banerjee R, Ray SS. Sustainability and Life Cycle Assessment of Thermoplastic Polymers for Packaging: A Review on Fundamental Principles and Applications. Macromolecular Materials and Engineering, 2022; 307:2100794.
3. Siracusa V, Blanco I. Bio-Polyethylene (Bio-PE), Bio-Polypropylene (Bio-PP) and Bio-Poly(ethylene terephthalate) (Bio-PET): Recent Developments in Bio-Based Polymers Analogous to Petroleum-Derived Ones for Packaging and Engineering Applications. Polymers, 2020;12:1641.
4. Jenck JF, Agterberg F, Droescher MJ. Products and processes for a sustainable chemical industry: a review of achievements and prospects. Green Chem,2004; 6:544–556.
5. Kaplan DL. Introduction to Biopolymers from Renewable Resources. In: Kaplan DL (ed) Biopolymers from Renewable Resources. Springer, Berlin, Heidelberg, 1998; 1–29.
6. Kümmerer K. Sustainable from the very beginning: rational design of molecules by life cycle engineering as an important approach for green pharmacy and green chemistry. Green Chem, 2007; 9: 899–907.
7. Androsch R, Di Lorenzo ML. Synthesis, Structure and Properties of Poly(lactic acid), 1st ed. 2018.
8. Hu R-H, Ma Z-G, Zheng S, Li Y-N, Yang G-H, Kim H-K, Lim J-K. A fabrication process of high volume fraction of jute fiber/polylactide composites for truck liner. Int J Precis Eng Manuf, 2012;13: 1243–1246.
9. Notta-Cuvier D, Odent J, Delille R, Murariu M, Lauro F, Raquez JM, Bennani B, Dubois P. Tailoring polylactide (PLA) properties for automotive applications: Effect of addition of designed additives on main mechanical properties. Polymer Testing, 2014; 36:1–9.
10. Sevostyanov MA, Kaplan MA, Nasakina EO. Development of a Biodegradable Polymer Based on High-Molecular-Weight Polylactide for Medicine and Agriculture: Mechanical Properties and Biocompatibility. Dokl Chem, 2020; 490:36–39.
11. Tertyshnaya Y, Jobelius H, Olkhov A, Shibryaeva L, Ivanitskikh A. Polylactide Fiber Materials and their Application in Agriculture. Key Engineering Materials. 2022; 910:617–622.
12. Peres C, Matos AI, Conniot J, Sainz V, Zupančič E, Silva JM, Graça L, Sá Gaspar R, Préat V, Florindo HF. Poly(lactic acid)-based particulate systems are promising tools for immune modulation. Acta Biomaterialia, 2017; 48:41–57.
13. Sullivan MP, McHale KJ, Parvizi J, Mehta S. Nanotechnology. The Bone & Joint Journal, 2014; 96-B:569–573.
14. Zhou J, Yu J, Bai D, Lu J, Liu H, Li Y, Li L. AgNW/stereocomplex-type polylactide biodegradable conducting film and its application in flexible electronics. J Mater Sci: Mater Electron, 2021;32:6080–6093.
15. Al-Attar H, Alwattar AA, Haddad A, Abdullah BA, Quayle P, Yeates SG. Polylactide-perylene derivative for blue biodegradable organic light-emitting diodes. Polymer International, 2021; 70:51–58.
16. Ahmed J, Mulla M, Jacob H, Luciano G, T.b. B, Almusallam A. Polylactide/poly(ε-caprolactone)/zinc oxide/clove essential oil composite antimicrobial films for scrambled egg packaging. Food Packaging and Shelf Life, 2019; 21:100355.
17. Ahmed J, Mulla MZ, Al-Zuwayed SA, Joseph A, Auras R. Morphological, barrier, thermal, and rheological properties of high-pressure treated co-extruded polylactide films and the suitability for food packaging. Food Packaging and Shelf Life, 2022; 32:100812.
18. Raquez J-M, Habibi Y, Murariu M, Dubois P. Polylactide (PLA)-based nanocomposites. Progress in Polymer Science, 2013; 38:1504–1542.
19. Malinowski R, Raszkowska-Kaczor A, Moraczewski K, Głuszewski W, Krasinskyi V, Wedderburn L. The Structure and Mechanical Properties of Hemp Fibers-Reinforced Poly(ε-Caprolactone) Composites Modified by Electron Beam Irradiation. Applied Sciences, 2021; 11:5317.
20. Thakur KAM, Kean RT, Zupfer JM, Buehler NU, Doscotch MA, Munson EJ. Solid State 13C CP-MAS NMR Studies of the Crystallinity and Morphology of Poly(l-lactide). Macromolecules, 1996; 29:8844–8851.
21. Sinha Ray S, Yamada K, Okamoto M, Ueda K. New polylactide-layered silicate nanocomposites. 2. Concurrent improvements of material properties, biodegradability and melt rheology. Polymer, 2003; 44:857–866.
22. Fiedurek K, Szroeder P, Macko M, Raszkowska-Kaczor A, Puszczykowska N. Influence of the parameters of the extrusion process on the properties of PLA composites with the addition of graphite. IOP Conf Ser: Mater Sci Eng, 2021 1199:012057.
23. Gonçalves C, Gonçalves IC, Magalhães FD, Pinto AM. Poly(lactic acid) Composites Containing Carbon-Based Nanomaterials: A Review. Polymers,2017; 9:269.
24. Lim L-T, Auras R, Rubino M. Processing technologies for poly(lactic acid). Progress in Polymer Science,2008; 33:820–852.
25. Perepelkin KE. Polylactide Fibres: Fabrication, Properties, Use, Prospects. A Review. Fibre Chemistry, 2002; 34:85–100.
26. Harris AM, Lee EC. Improving mechanical performance of injection molded PLA by controlling crystallinity. Journal of Applied Polymer Science, 2018; 107:2246–2255.
27. Tümer EH, Erbil HY. Extrusion-Based 3D Printing Applications of PLA Composites: A Review. Coatings, 2021; 11:390.
28. Cicala G, Giordano D, Tosto C, Filippone G, Recca A, Blanco I. Polylactide (PLA) Filaments a Biobased Solution for Additive Manufacturing: Correlating Rheology and Thermomechanical Properties with Printing Quality. Materials, 2018; 11:1191.
29. Ghasem N, Al-Marzouqi M, Abdul Rahim N. Effect of polymer extrusion temperature on poly(vinylidene fluoride) hollow fiber membranes: Properties and performance used as gas–liquid membrane contactor for CO2 absorption. Separation and Purification Technology, 2012; 99:91–103.
30. Schweighuber A, Felgel-Farnholz A, Bögl T, Fischer J, Buchberger W. Investigations on the influence of multiple extrusion on the degradation of polyolefins. Polymer Degradation and Stability, 2021; 192:109689.
31. Kosmalska D, Janczak K, Raszkowska-Kaczor A, Stasiek A, Ligor T. Polylactide as a Substitute for Conventional Polymers—Biopolymer Processing under Varying Extrusion Conditions. Environments, 2022; 9:57.
32. Michael FM, Khalid M, Walvekar R, Ratnam CT, Ramarad S, Siddiqui H, Hoque ME. Effect of nanofillers on the physico-mechanical properties of load bearing bone implants. Materials Science and Engineering, 2016; C 67:792–806.
33. Pan J, Bian L. A physics investigation for influence of carbon nanotube agglomeration on thermal properties of composites. Materials Chemistry and Physics, 2019; 236:121777.
34. Tamayo-Vegas S, Muhsan A, Liu C, Tarfaoui M, Lafdi K. The Effect of Agglomeration on the Electrical and Mechanical Properties of Polymer Matrix Nanocomposites Reinforced with Carbon Nanotubes. Polymers, 2022; 14:1842.
35. Canevarolo SV, Babetto AC. Effect of screw element type in degradation of polypropylene upon multiple extrusions. Advances in Polymer Technology, 2002; 21:243–249.
36. Zou D, Zheng X, Ye Y, Yan D, Xu H, Si S, Li X. Effect of different amounts of bamboo charcoal on properties of biodegradable bamboo charcoal/polylactic acid composites. International Journal of Biological Macromolecules, 2022; 216:456–464.
37. Aversa C, Barletta M, Gisario A, Pizzi E, Prati R, Vesco S. Corotating twin-screw extrusion of poly(lactic acid) PLA/poly(butylene succinate) PBS/ micro-lamellar talc blends for extrusion blow molding of biobased bottles for alcoholic beverages. Journal of Applied Polymer Science, 2021 138:51294.
38. Kaczor D, Fiedurek K, Bajer K, Raszkowska-Kaczor A, Domek G, Macko M, Madajski P, Szroeder P. Impact of the Graphite Fillers on the Thermal Processing of Graphite/Poly(lactic acid) Composites. Materials, 2021; 14:5346.
39. Kaczor D, Bajer K, Domek G, Raszkowska-Kaczor A, Szroeder P. The method of obtaining polymer masterbatches based on polylactide with carbon filler. IOP Conf Ser: Mater Sci Eng, 2021; 1199:012058.

40. PN-EN ISO 11357-(1-3):2009 Tworzywa sztuczne - Różnicowa kalorymetria skaningowa (DSC) - Część 1: Zasady ogólne; Część 2: Wyznaczanie temperatury zeszklenia i stopnia przejścia w stan szklisty; Część 3: Oznaczanie temperatury oraz entalpii topnienia i krystalizacji.
41. Silva M, Gomes C, Pinho I, Gonçalves H, Vale AC, Covas JA, Alves NM, Paiva MC. Poly(Lactic Acid)/Graphite Nanoplatelet Nanocomposite Filaments for Ligament Scaffolds. Nanomaterials, 2021; 11:2796.
42. Batakliev T, Georgiev V, Kalupgian C, Muñoz PAR, Ribeiro H, Fechine GJM, Andrade RJE, Ivanov E, Kotsilkova R. Physico-chemical Characterization of PLA-based Composites Holding Carbon Nanofillers. Appl Compos Mater, 2021; 28:1175–1192.
43. PN-EN ISO 1133-1:2011 Tworzywa sztuczne - Oznaczanie masowego wskaźnika szybkości płynięcia (MFR) i objętościowego wskaźnika szybkości płynięcia (MVR) tworzyw termoplastycznych - Część 1: Metoda standardowa.
44. PN-EN ISO 294-1:2017-07 Tworzywa sztuczne - Wtryskiwanie kształtek do badań z tworzyw termoplastycznych - Część 1: Zasady ogólne, formowanie uniwersalnych kształtek do badań i kształtek w postaci beleczek.
45. PN-EN ISO 527-1:2020-01 Tworzywa sztuczne - Oznaczanie właściwości mechanicznych przy statycznym rozciąganiu - Część 1: Zasady ogólne.
46. PN-EN ISO 179-2:2020-12 Tworzywa sztuczne - Oznaczanie udarności metodą Charpy'ego - Część 2: Instrumentalne badanie udarności.
47. Yuniarto K, Purwanto YA, Purwanto S, Welt BA, Purwadaria HK, Sunarti TC. Infrared and Raman studies on polylactide acid and polyethylene glycol-400 blend. AIP Conference Proceedings, 2016; 1725:020101.
48. Kister G, Cassanas G, Vert M. Effects of morphology, conformation and configuration on the IR and Raman spectra of various poly(lactic acid)s. Polymer, 1998; 39:267–273.
49. Amorin NSQS, Rosa G, Alves JF, Gonçalves SPC, Franchetti SMM, Fechine GJM. Study of thermodegradation and thermostabilization of poly(lactide acid) using subsequent extrusion cycles. Journal of Applied Polymer Science, 2014 131, 40023.
50. Qin D, Kean RT. Crystallinity Determination of Polylactide by FT-Raman Spectrometry. Appl Spectrosc, 1998; 52:488–495.
51. Signori F, Coltelli M-B, Bronco S. Thermal degradation of poly(lactic acid) (PLA) and poly(butylene adipate-co-terephthalate) (PBAT) and their blends upon melt processing. Polymer Degradation and Stability, 2009; 94:74–82.
52. Cock F, Cuadri AA, García-Morales M, Partal P. Thermal, rheological and microstructural characterisation of commercial biodegradable polyesters. Polymer Testing, 2013; 32:716–723.
53. Carrasco F, Pagès P, Gámez-Pérez J, Santana OO, Maspoch ML. Processing of poly(lactic acid): Characterization of chemical structure, thermal stability and mechanical properties. Polymer Degradation and Stability, 2010; 95:116–125.
54. Mainil-Varlet P, Hauke C, Maquet V, Printzen G, Arens S, Schaffner T, Jérôme R, Perren S, Schlegel U. Polylactide implants and bacterial contamination: An animal study. Journal of Biomedical Materials Research, 2001; 54:335–343.
55. Usachev SV, Lomakin SM, Koverzanova EV, Shilkina NG, Levina II, Prut EV, Rogovina SZ, Berlin AA. Thermal degradation of various types of polylactides research. The effect of reduced graphite oxide on the composition of the PLA4042D pyrolysis products. Thermochimica Acta, 2022; 712:179227.
56. Mngomezulu ME, Luyt AS, John MJ. Morphology, thermal and dynamic mechanical properties of poly(lactic acid)/expandable graphite (PLA/EG) flame retardant composites. Journal of Thermoplastic Composite Materials, 2019; 32:89–107.
57. Harmandaris VA, Daoulas KCh, Mavrantzas VG. Molecular Dynamics Simulation of a Polymer Melt/Solid Interface: Local Dynamics and Chain Mobility in a Thin Film of Polyethylene Melt Adsorbed on Graphite. Macromolecules, 2005; 38:5796–5809.
58. Mysiukiewicz O, Barczewski M, Skórczewska K, Matykiewicz D. Correlation between Processing Parameters and Degradation of Different Polylactide Grades during Twin-Screw Extrusion. Polymers, 2020; 12:1333.
59. Przekop RE, Kujawa M, Pawlak W, Dobrosielska M, Sztorch B, Wieleba W. Graphite Modified Polylactide (PLA) for 3D Printed (FDM/FFF) Sliding Elements. Polymers, 2020; 12:1250.
60. Murariu M, Dechief AL, Bonnaud L, Paint Y, Gallos A, Fontaine G, Bourbigot S, Dubois P. The production and properties of polylactide composites filled with expanded graphite. Polymer Degradation and Stability, 2010; 95:889–900.
61. Żenkiewicz M, Richert J, Rytlewski P, Richert A. Comparative analysis of shungite and graphite effects on some properties of polylactide composites. Polymer Testing, 2011; 30:429–435.
62. Kim I-H, Jeong YG. Polylactide/exfoliated graphite nanocomposites with enhanced thermal stability, mechanical modulus, and electrical conductivity. Journal of Polymer Science Part B: Polymer Physics, 2010; 48:850–858.
63. Żenkiewicz M, Richert J, Rytlewski P, Moraczewski K, Stepczyńska M, Karasiewicz T. Characterisation of multi-extruded poly(lactic acid). Polymer Testing, 2009; 28:412–418.

This work is supported by the Ministry of Education and Science of the Republic of Poland as part of the 'Implementation doctorate' program (contract No. DWD/4/71/2020) and by the Faculty of Mechatronics of the Kazimierz Wielki University (funds from the subsidy for scientific research).

Daniel Kaczor: https://orcid.org/0000-0002-0291-2121

Krzysztof Bajer: https://orcid.org/0000-0002-4719-5760

Grzegorz Domek: https://orcid.org/0000-0003-3566-9110

Piotr Madajski: https://orcid.org/0000-0002-6995-1643

Aneta Raszkowska-Kaczor: https://orcid.org/0000-0002-6868-6833

Paweł Szroeder: https://orcid.org/0000-0002-4266-4206

sciendo

DOI 10.2478/ama-2022-0039

acta mechanica et automatica, vol.16 no.4 (2022)
Special Issue "Machine Modeling and Simulations 2022"

SELECTION OF THE HEAT TRANSFER COEFFICIENT USING SWARMING ALGORITHMS

Elżbieta GAWROŃSKA*, **Robert DYJA***, **Maria ZYCH***, **Grzegorz DOMEK****

*Faculty of Mechanical Engineering and Computer Science, Czestochowa University of Technology,
ul. Dąbrowskiego 73, 42-201 Częstochowa, Poland
**Faculty of Mechatronics, Kazimierz Wielki University, ul. Kopernika 1, 85-074 Bydgoszcz, Poland

elzbieta.gawronska@icis.pcz.pl, robert.dyja@icis.pcz.pl, maria.zych@icis.pcz.pl, gdomek@ukw.edu.pl

received 24 June 2022, revised 9 August 2022, accepted 10 August 2022

Abstract: The article presents the use of swarming algorithms in selecting the heat transfer coefficient, taking into account the boundary condition of the IV types. Numerical calculations were made using the proprietary TalyFEM program and classic form of swarming algorithms. A function was also used for the calculations, which, during the calculation, determined the error of the approximate solution and was minimalised using a pair of individually employed algorithms, namely artificial bee colony (ABC) and ant colony optimisation (ACO). The tests were carried out to select the heat transfer coefficient from one range. Describing the geometry for a mesh of 408 fine elements with 214 nodes, the research carried out presents two squares (one on top of the other) separated by a heat transfer layer with a κ coefficient. A type III boundary condition was established on the right and left of both edges. The upper and lower edges were isolated, and a type IV boundary condition with imperfect contact was established between the squares. Calculations were made for ABC and ACO, respectively, for populations equal to 20, 40 and 60 individuals and 2, 6 and 12 iterations. In addition, in each case, 0%, 1%, 2% and 5% noise of the reference values were also considered. The obtained results are satisfactory and very close to the reference values of the κ parameter. The obtained results demonstrate the possibility of using artificial intelligence (AI) algorithms to reconstruct the IV type boundary condition value during heat conduction modelling.

Key words: swarm algorithm, ABC algorithm, ACO algorithm, heat transfer coefficient, computer simulation, numerical modelling

1. INTRODUCTION

Artificial intelligence (AI) is a branch of computer science of a practical and cognitive nature, and finds a steadily increasing volume of applications not only in science, technology and engineering but also in everyday life. This section covers re-search on intelligent systems, their modelling, construction and use to support and substitute human mental work and deepen understanding of human reasoning. AI methods are irreplacea-ble in a situation where it is necessary to infer further proce-dures based on incomplete information on a given issue. One of the elements of AI is optimisation issues. Optimisation problems appear in almost every area of science, engineering, economics and other fields of study. In order to solve most of today's optimisation problems, it is necessary to use algorithms that adapt easily to constraints and do not depend on the num-ber of variables and the size of the solution space. Then, vari-ous types of nature-/biology-inspired algorithms come in handy, such as genetic algorithm (GA), differential evolution (DE), ant colony optimisation (ACO) and artificial bee colony (ABC), the rules of which are taken from observation of nature. In recent years, there has been an increase in interest in the class of algorithms called swarms; these algorithms are based on swarm intelligence. Their use has made it possible to signifi-cantly improve the performance of a given activity through its far-reaching optimisation. Even though the first optimisation algorithms were developed in the previous century, research-ers still exhibit great interest in this topic, especially with regard to optimisation of issues related to heat transfer [1,2].

AI algorithms have found many uses in solving various problems. For example, in the problem of image contrast enhancement, the ABC algorithm allowed obtaining better-quality images [3]. The use of the ACO algorithm improved the Elman neural network, thus leading the way for the capability to determine the state of charge of lithium-ion batteries in electric vehicles. Nature-inspired algorithms are also used to navigate mobile robots that have to navigate over uncertain terrain [4].

Karaboga et al. presented a new approach to solving the inverse heat conduction problem and estimating an unknown heat source. The author formulated the problem of physical heat transfer as an optimisation problem. The ABC algorithm, based on the intelligent behaviour of a honey bee swarm, turned out to be very simple and flexible compared to the existing swarming algorithms. The author showed that the algorithm is very stable for testing problems. The proposed algorithm can be used for unimodal and multimodal solving of numerical optimisation problems. The features of the algorithm proposed by Karaboga became the basis for the present authors' work in this article [5,6,7].

Physical problems modelled by mathematical models can be divided into direct and inverse problems [8]. Direct problems refer to a situation when all input data are known, and the problem is solved (mainly numerically) with initial-boundary assumptions [9]. Inverse problems consist of recreating some model parameters based on the experiment, which makes it possible to control its course and the final quality of the product [10,11]. This type of control is becoming more and more desirable in manufacturing processes. Solving the inverse heat conduction problem is more complex than solving the direct problem. Except in the most uncomplicated cases, it is impossible to solve the inverse problem with the help of analytical methods. Moreover, even if such a solution exists, it is neither unequivocal nor stable. Therefore, the approximate method that gives a satisfactory solution is needed [12,13]. Conducting experimental research is laborious, time-consuming and requires additional financial outlays. Such an experiment can be particularly burdensome, for example, when a qualitative analysis of different materials needs to be performed. Using efficient and optimal numerical methods makes it possible to perform an extensive series of tests with relatively lower amounts of effort and cost involved.

Numerical simulation of heat transfer processes is based on solutions to both direct and inverse problems. The second approach has been very popular among researchers in recent years. An example of the use of inverse problems and optimisation algorithms to reconstruct the conditions of the experiment is the study by Matsevityi et al. [14], in which the authors successfully reconstructed the heat transfer coefficient with the environment (Newton boundary condition) and obtained graphs of temperature changes over time that were very consistent with those obtained from experimentation.

In the example presented in this article, selected optimisation swarm algorithms (ABC and ACO) are used to reconstruct the heat transfer coefficient between the cast and the casting mould in numerical modelling of the heat conduction problem.

2. METHODS

2.1. Heat conduction problem

The heat transfer process is divided into: steady-state, when the temperature distribution in the system under consid-eration does not change with time, and the amount of heat is constant (in this case, the only variables are coordinates in space); and transient (unsteady-state), when the temperature distribution and heat change with respect to time. The transient heat flow is considered in this paper.

During the heating and cooling process, unsteady-state heat conduction occurs when both bodies strive to achieve a temperature equilibrium with the environment in which they find themselves. According to Fourier's law, the heat flux conduc-tion density is directly proportional to the temperature gradient. The mathematical formula of heat transfer is defined as follows:

$$c\rho\frac{\partial T}{\partial t} + \nabla \cdot (-\lambda \nabla T) = Q \tag{1}$$

where c is specific heat $\left[\frac{J}{kgK}\right]$, ρ is density $\left[\frac{kg}{m^3}\right]$, T is temperature [K], t is time [s], λ is heat transfer coefficient $\left[\frac{W}{mK}\right]$ and Q represents internal heat sources $\left[\frac{W}{m^3}\right]$. Since the phase transformation was not taken into account, Q was equal to 0.

The problem of transient heat conduction is one of the initial-boundary issues, requiring the setting of appropriate initial and boundary conditions at the commencement of calculations. Initial conditions, called Cauchy conditions, allow giving specified temperature values at the initial instant for t = 0 s.

$$T(\mathrm{r},t)|_{t=0} = T_0(\mathrm{r}) \tag{2}$$

where r is the field vector at a given point. There are four types of boundary conditions that are associated with heat transfer:

- Dirichlet boundary condition (the first type condition) assumes the temperature (T_z) on the Γ boundary of area Ω.

  $$\Gamma: T = T_z. \tag{3}$$

  when the measurement's body surface temperature T_z is known, the boundary conditions can be formulated as Dirichlet boundary conditions.
- Von Neumann boundary condition (the second type condition) assumes the known heat flux (q_z) on the Γ boundary of area Ω.

  $$\Gamma: q = q_z. \tag{4}$$
- Newton boundary condition (the third type condition) assumes the exchanged heat with the environment on the boundary Γ of the area Ω.

  $$\Gamma: q = \propto (T - T_{amb}), \tag{5}$$

  where $\propto$ is the coefficient of heat exchange with the environment, T is the temperature of the body on the boundary Γ, T_{amb} is the ambient temperature and q is the heat flux flowing into the Ω area when $T < T_{amb}$ or flowing from the Ω area when $T > T_{amb}$. In the third boundary condition, the heat transfer coefficient determines the intensity of convection. The $\propto$ coefficient depends on the heat exchange type as well as the speed and direction of the flow to the body surface.
- Continuity condition (the fourth type condition) assumes contact and the heat exchange between two bodies. This contact may be ideal or non-ideal. In the non-ideal case, there is a separation layer with a κ coefficient:

  $$\kappa = \frac{\lambda_p}{\delta}, \tag{6}$$

  where λ_p is the thermal conductivity coefficient of the separation layer and δ is the thickness of this layer.

Using the previously described boundary conditions in the tested model, we find that the results are consistent with Fig. 3, and the area dimensions are given in Fig. 2. All boundaries (numbered from 1 to 8) are 0.02 m long.

This work aims to reconstruct the heat transfer coefficient κ through the layer separating the cast and the casting mould.

2.2. ABC algorithm

The first works on simulating swarming behaviour, using mathematical and numerical modelling, appeared in the 70s and 80s of the previous century. However, they started to be widely used only in the first decade of the 21st century. For example, the ABC algorithm uses the intelligent behaviour of a swarm of honeybees. The algorithm model is based on the search for food by an ABC.

The algorithm ABC consists of three main components: food sources, unemployed bees and employed bees closely related to the food source. The number of solutions in the population equals the number of food sources. The amount of nectar in the food source is the value of the evaluating function associated with the solution. In searching for food, bees have developed various techniques to improve communication with other bees about the location of food sources. Employed bees (scout bees) randomly choose the direction and area to search for the best available food sources. Once such a source is found, the scout becomes an employed bee and returns to the hive. They inform the bees that are spectators about the direction, distance and area of the food.

The information is passed on in the dance. After that, the sources are exploited, and the employed bees become unemployed when exhausted [15].

In the ABC algorithm, the position of the food source is a possible solution to the optimisation problem, and the nectar content of the food source corresponds to the quality (efficiency) of the related solution. The number of employed and unemployed bees equals the number of solutions in the population. In the first step, ABC generates a random initial population P of SN solutions, where SN is the number of the food source. Each solution x_i (i = 1, 2, ..., SN) is a vector of solutions to D. In the algorithm, D denotes the number of optimisation parameters. The determination of the food sources' coordinates is subjected to multiple iterations C = 1, 2, …, C_{max}, where the iterations mean the update of the solutions. The employed bee updates the changes in position (solution) depending on local information (visual information) and tests the amount of nectar (efficiency) of the new source (new solution). If the amount of new nectar is higher than in the previous iteration, the bee remembers the new nectar position and forgets the current one. Otherwise, it retains the previous position in its memory. After the search process is complete, all employed bees share nectar information from the various food sources and their position information with the bees in the dance area. An unemployed artificial bee selects a food source depending on the probability value p_i calculated according to the following formula:

$$p_i = \frac{fit_i}{\sum_{n=1}^{SN} fit_n} \qquad \text{for } i = 1, 2, \dots, P, \tag{7}$$

where fit_i is an efficiency of i^{th} solution, proportional to the nectar amount of food source, and SN equals the number of the employed bees.

In the next step, the update of the coordinates of the food sources is carried out, which is based on the own coordinates of the bee and other employed bees. The above process follows the relationship:

$$v_i = x_{ij} + rand[-1,1] \cdot (x_{ij} - x_{kj}) \tag{8}$$

where v_{ij} is the update of the food sources' coordinates, and i, k = 1, 2, …, SN and j = 1, 2, …, D are randomly selected within the given range. The variable k is determined randomly, too, and it must be different from i. The search for the optimal solution is related to the iterative process of reducing the difference between successive updates of the position of food sources.

The ABC algorithm uses four control parameters: (i) the global selection process used by unemployed bees Eq. (7), (ii) a local selection process carried out by the viewer bees and depends on local information about the adjacent food source Eq. (8), (iii) a local selection process, called sparse, carried out by all bees, and (iv) a random selection process carried out by the scout bees.

The survival and progress of a bee colony depend on the quick discovery and efficient use of the best food resources. Similarly, successful solutions to complex engineering problems are related to finding reasonable solutions relatively quickly, especially for problems that need to be solved in real-time.

2.3. ACO algorithm

The ACO algorithm was presented and developed by Marco Dorigo et al. in the 90s of the previous century and is a part of metaheuristic algorithms. The inspiration comes from the world of ants that can find the shortest route between an anthill and an available food source.

In the beginning, ants walking towards a food source choose the route randomly. They return to the anthill and leave a pheromone trail on their route, which gradually evaporates if other ants do not follow the path. On a shorter route, evaporation is slower than on longer routes, and thus subsequent ants choose this route more willingly than other routes, and by choosing it, they strengthen the pheromone trail. This phenomenon is called positive feedback. In an ACO algorithm, a colony of artificial individuals cooperates to search for optimal solutions to complex combinatorial problems. There is an indirect interaction between ants collecting some kind of experience and using it in further research. Each of the ants follows an identical strategy of finding the shortest path to the goal. Over time, the ants work together to work out a set of shortest paths leading them to their designated food sources. This is a manifestation of collective intelligence [16,17].

Finding the best solution in the classical ACO algorithm is an iterative process, too, similar to finding the best solution in the ABC algorithm. At each iteration, an ant selects a path to a food source depending on the probability value p_{ij} calculated according to the following formula:

$$p_{ij} = \frac{a_{ij}}{\sum_{l \in N_i} a_{il}}, \tag{9}$$

where N_i is the feasible neighbourhood of i^{th} node for k^{th} ant and is the set of nodes that she has not yet visited. At each iteration, a k^{th} ant located in the i^{th} node on the path to a food source chooses the j^{th} node from the nearest neighbourhood [18].

In order to avoid an unlimited increase in the pheromone traces, pheromone pairing is added in each t^{th} iteration in the algorithm. An additional matrix is created for each ant to store the nodes of the current traces. This matrix is called the pheromone array. In the first iteration, in the classic form of an algorithm, for each ant, the nodes on the paths from anthill to food sources are fixed by roulette wheel law after considering the probability determined by the formula in Eq. (9). It allows for the initiation of each ant's trace transition matrices. After going over all the ants, the trace with the best quality index is found for each iteration. Based on this indicator, the trace for each ant is modified. Then, for the best transition path (the superscript of best), new nodes are randomly determined as a particular random deviation from the position of the previous nodes:

$$x_{ij}(\mathrm{t}) = x_{ij}(t-1) + rand[0,1] \cdot \left[x_{ij}^{best}(t-1) - x_{ij}(t-1)\right] \tag{10}$$

The above-mentioned algorithm steps are repeated in each iteration. Consequently, the traces determined in successive iterations get closer to the path characterised by the best quality indicator that all ants follow.

3. IMPLEMENTS AND ASSUMPTIONS

This article deals with a topic that requires the connection of two separate fields: thermomechanics and computer science. The cooling of the aluminium alloy has been selected from the thermomechanics field. The reconstruction of the value of one of the coefficients in the contact boundary condition became the main point of this work. The heat transfer coefficient of the layer separating the cast and the casting mould is selected based on the available literature, as well as according to the discretion of the person performing numerical calculations or the employee responsible for making the cast in the foundry, who makes an ideal decision based on their field experience and the prevalent circumstances. In this study, an attempt was made to fill the gap in this research area by creating a tool enabling the reconstruction of the heat transfer coefficient.

Finite element models and meshes were created in GMSH open source 3D finite element mesh generator [19]. Numerical calculations were made using an in-house software, whose application was combined with that of TalyFEM library, an application developed previously in the literature [20,21,22], as well as using algorithms implemented in the C++ language. The finite element method facilitates the modelling of complex problems, and its wide application allows for easy adaptation of many existing computational techniques. TalyFEM is a library that uses the finite element method to simulate selected physical phenomena, containing many PETSc (the Portable, Extensible Toolkit for Scientific Computation) data structures such as vectors, matrices and ready-made solvers [23]. The tests were performed on a computer with the following parameters – Processor: Intel (R) Core^{TM} i5-4590 CPU @ 3.30 GHz, x86_64 architecture; Manufacturer ID: Genuine Intel; CPU family: 6; CPU clock speed: 3279.890 MHz; Operating system: Linux (in distribution Ubuntu). In the field of AI, optimisation heuristic algorithms were used. These algorithms have been implemented in Python and adapted to the possibility of connecting them with TalyFEM [24].

The functional Eq. (11), determining the error of the approximate solution, and minimised with the use of selected swarming algorithms, assumes the form of the formula:

$$J(\kappa) = \sum_{i=1}^{N_1}\sum_{j=1}^{N_2}\left(T_{ij} - U_{ij}\right)^2, \tag{11}$$

where N_1 is the number of observing, during the experiment, finite element's nodes, N_2 is the number of time steps in the numerical experiment, U_{ij} are the reference temperatures generated with the reference heat transfer coefficient κ and T_{ij} are the temperatures obtained during the numerical experiment. The standard deviation value was used to present the variability of the temperature distribution, i.e. to determine the similarity of the obtained solutions to each other and the deviation from the mean value, taking into account the obtained value of the κ coefficient.

In order to execute a numerical experiment, reconstructing the thermal conductivity of the separating layer, both numerical (using TalyFEM) and optimisation (using ABC and ACO heuristic algorithms) calculations were carried out. The heuristic of the optimisation algorithms used requires the user to run the program several times. In our work, all calculations were run five times for each configuration. During each iteration, the temporary best values of the $\boldsymbol{\kappa}$ coefficient were obtained among all individuals participating in the search for a food source. Finally, the reconstructed coefficient was the mean value of the best values obtained during each program run. The best heat transfer coefficient is the one that is closest to the reference coefficient, and its functional has the lowest value. The general idea of our software is presented in Fig. 1.

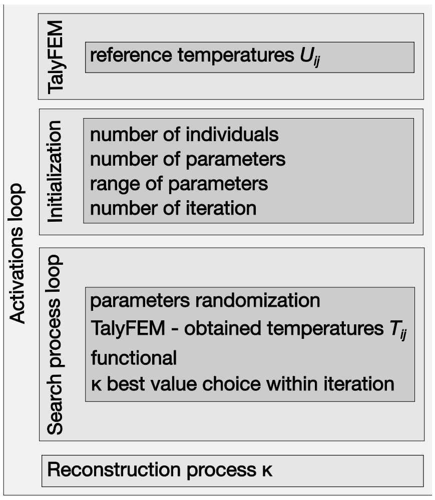

Fig. 1. Scheme of the problem solution

4. RESULTS

The considered geometry and the finite element mesh are presented in Fig. 2.

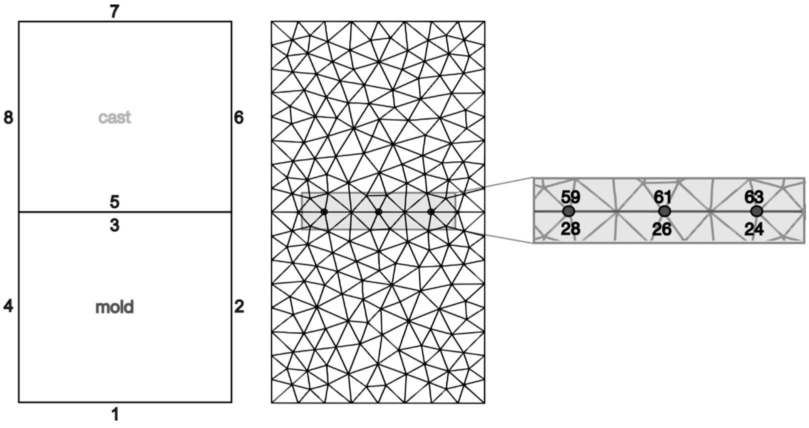

Fig. 2. Geometry and finite element mesh with denoted nodes

However, only one was chosen at a random density of finite element mesh because the differences in the results for all cases were minor. Detailed observations of the temperature course in time and the determined heat transfer coefficient κ were carried out for three pairs of nodes. However, only one middle pair of nodes 26–61 (the first number of the node in a pair belongs to the mould, the other to the casting) was chosen to represent experiment results. The nodes were chosen symmetrically in sensitive (from the point of view of the macroscale) places. The nodes at the interface between the cast and the casting mould have the same spatial coordinates, making finite element meshes easier to automatically generate and separate, which simulates a layer separating two areas with completely different material properties. The mesh was composed of 360 finite triangular elements (214 nodes).

The numerical experiment for the Al-2%Cu alloy and parameter κ from the value range 900–1,500 $\left[\frac{W}{m^2K}\right]$ was carried out, and the reference temperatures U_{ij} were obtained for κ = 100$\left[\frac{W}{m^2K}\right]$. The initial temperatures were T_0 = 960 K for the cast and T_0 = 590 K for the casting mould. Material properties are shown in Tab. 1.

Tab. 1. Material properties to cast and casting mould.

Property	**Symbol**	**Cast**	**Mould**
Density	$\rho,\ \frac{\mathrm{kg}}{\mathrm{m}^3}$	2,824	7,500
Specific heat	$c,\ \frac{\mathrm{J}}{\mathrm{kgK}}$	1,077	620
Heat transfer coefficient	$\lambda,\ \frac{\mathrm{W}}{\mathrm{mK}}$	262	40

The boundary conditions are shown in Fig. 3. In the Newton boundary condition (the third kind of boundary condition), convective heat exchange with the environment was established, assuming that the ambient temperature is 300 K, and the heat exchange coefficient with the environment is 100 $\left[\frac{W}{m^2K}\right]$.

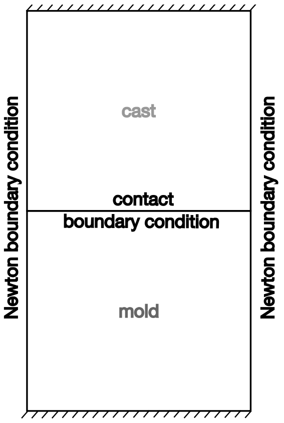

Fig. 3. Boundary conditions

Calculations were performed for the presented finite element mesh for the ABC and ACO algorithms for a population of 20, 40 and 60 bees/ants. A characteristic feature of heuristic algorithms is that they must be run more than once to give the possibility of narrowing down the search area and obtaining reliable calculation results. In this study, the algorithms were run five times in each case. Moreover, in each case, 0%, 1%, 2% and 5% noise of the reference temperatures U_{ij} were also considered. The following part of the article presents the results obtained from a numerical experiment for a given configuration presented in Section 4.

The tables presented in the article contain the results of the calculations (κ represents heat transfer coefficient, σ standard deviation and J the value of the minimised functional) using the ABC and ACO algorithms at 0%, 1%, 2% and 5% noise for 2, 6 and 12 iterations for finite element meshes with 214 nodes. Tab. 2 shows the calculations for 20 individuals (bees/ants) of the population, whereas Tab. 3 shows the calculations for 60 individuals' selected swarming algorithms. After analysing the results presented in the tables, the following conclusions can be drawn:

- the errors in the reconstruction of the κ coefficient are minor and do not exceed a few percent,
- even for disturbed input data, the errors in the reconstruction of the κ coefficient do not exceed the amount of the noise introduced,
- the values of standard deviations decrease for each of the algorithms (grey colour in Figs. 4 and 5) corresponding to an increase in the number of iterations,
- similar to the size of the noise increases, the value of the minimised functional increases, but the values of standard deviations decrease for each of the algorithms,
- a small number of iterations results in a more significant discrepancy between the obtained κ coefficient values and thus a more significant standard deviation,
- regardless of the perturbation value introduced, increasing the number of iterations of the algorithm execution does not significantly reduce the functional value, i.e. it does not significantly improve the reconstructed value of the κ coefficient. However, one could say the best representation of the κ coefficient was obtained for 12 iterations for each noise case.

Summarising, it can be generalised that the error in determining κ coefficient was smaller than the percentage variation in the reference temperature value in all cases. There are no significant differences between the selected algorithms, but the obtained standard deviation and functional results favour the ACO algorithm.

Tab. 2. Calculations for the ABC and ACO algorithm (20 bees/ants) for the κ coefficient with 0%, 1%, 2% and 5% noise of the reference temperature; σ is the standard deviation value expressed as a percentage; J is the functional value

Noise	**Iterations**	κ		σ **%**		J	
		ABC	**ACO**	**ABC**	**ACO**	**ABC**	**ACO**
0%	2	1,005.42	1,002.02	1.720797	0.315057	0.005593	0.001838
	6	999.971	999.982	0.191069	0.003093	0.000811	0.000017
	12	1,000.02	1,000.00	0.021884	0.000049	0.000107	0.000000
1%	2	1,001.568	999.738	1.511249	0.229253	0.159742	0.159514
	6	994.17	997.505	0.680394	0.010121	0.159566	0.159503

	12	997.594	997.65	0.023884	0.011118	0.159503	0.159503
2%	2	996.772	998.459	0.357987	0.405015	0.319783	0.319784
	6	996.797	997.88	0.197866	0.003302	0.319779	0.319776
	12	997.873	998.037	0.004802	0.011228	0.319776	0.319776
5%	2	1,002.746	1,007.952	0.388378	0.446690	0.806145	0.806146
	6	1,005.352	1,005.147	0.106457	0.022512	0.806141	0.806141
	12	1,005.287	1,005.061	0.031364	0.007003	0.806141	0.806141

ABC, artificial bee colony; ACO, ant colony optimisation

Tab. 3. Calculations for the ABC and ACO algorithm (60 bees/ants) for the κ coefficient with 0%, 1%, 2% and 5% noise of the reference temperature; σ is the standard deviation value expressed as a percentage; J is the functional value

Noise	Iterations	κ		σ %		J	
		ABC	ACO	ABC	ACO	ABC	ACO
0%	2	999.772	1,000.119	0.207614	0.043968	0.000982	0.000185
	6	1,000.254	1000.00	0.073764	0.000043	0.000347	0.000000
	12	1000.025	1,000.00	0.009152	0.000000	0.000041	0.000000
1%	2	998.251	998.286	0.6631	0.000064	0.159548	0.159504
	6	996.963	997.609	0.058549	0.000011	0.159504	0.159503
	12	997.649	997.561	0.010208	0.000010	0.159503	0.159503
2%	2	999.058	997.718	0.139638	0.121819	0.319777	0.319777
	6	998.001	997.891	0.012700	0.010942	0.319776	0.319776
	12	998.037	998.008	0.014075	0.014957	0.319776	0.319776
5%	2	1,003.347	1,005.048	0.246709	0.039688	0.806143	0.806141
	6	1,005.028	1,005.061	0.041702	0.005901	0.806141	0.806141
	12	1,005.075	1,005.050	0.019215	0.007564	0.806141	0.806141

ABC, artificial bee colony; ACO, ant colony optimisation

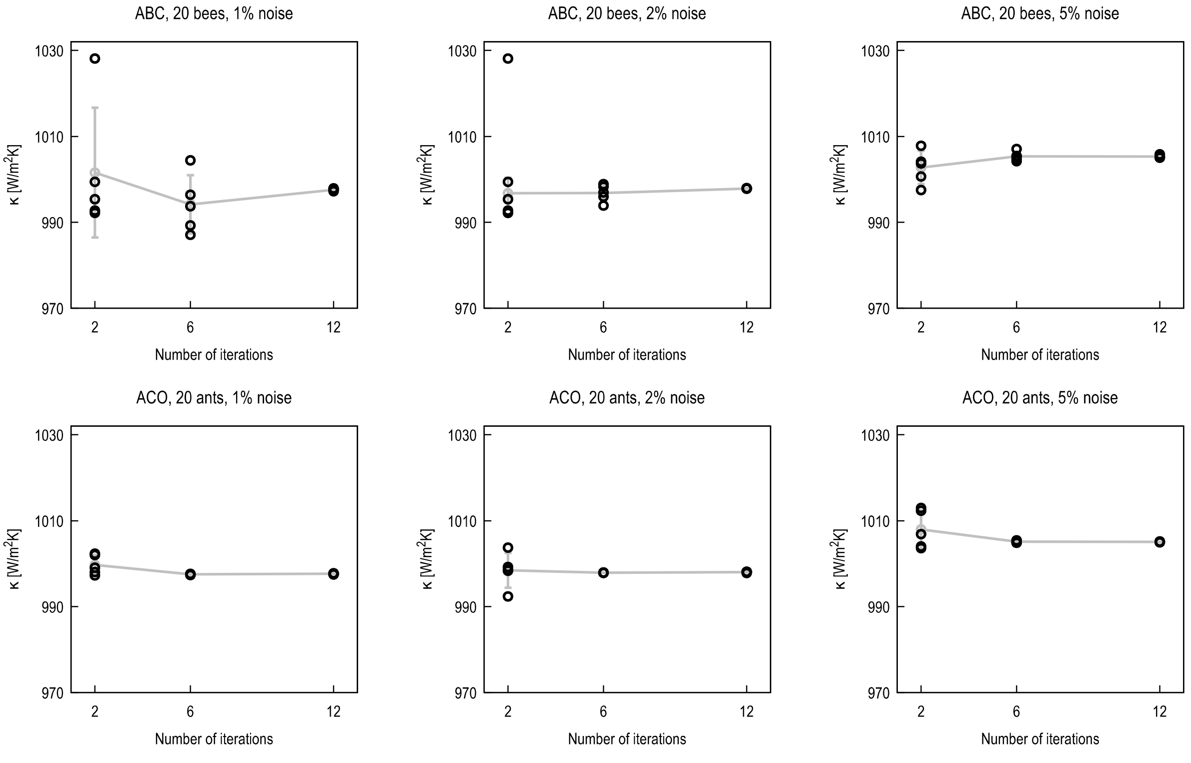

Fig. 4. Value of κ coefficient for ABC (the first row) and ACO (the second row) algorithm, 20 bees/ants, and 2, 6 and 12 iterations. The standard deviation and mean values of the κ coefficient are depicted by the grey color of the line and points. The exact value of the κ coefficient is 1,000.
ABC, artificial bee colony; ACO, ant colony optimisation

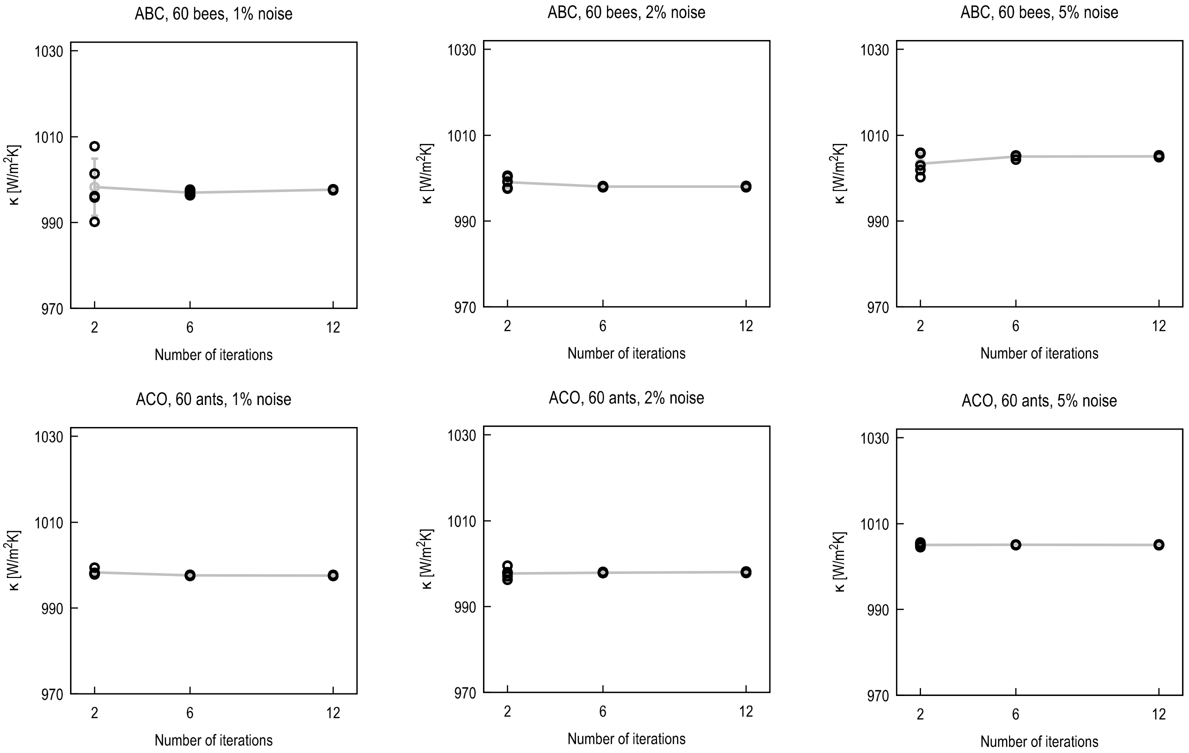

Fig. 5. Value of κ coefficient for ABC (the first row) and ACO (the second row) algorithm, 60 bees/ants, and 2, 6 and 12 iterations. The standard deviation and mean values of the κ coefficient are depicted by the grey colour of the line and points. The exact value of the κ coefficient is 1,000. ABC, artificial bee colony; ACO, ant colony optimisation

4.1. Analysis of the results obtained using the ABC algorithm

Figs. 6–9 show the temperature courses over time for the middle pair of nodes (26–61) in the finite element mesh of the studied geometry. In the case of ABC algorithm this figures visualise 0%, 1%, 2% and 5% disturbance for 20, 40 and 60 bees corresponding to 2, 6, and 12 iterations, respectively. The left panel tallies with the mould, and the right panel with the cast. The temperature distribution is physically correct in each case. The corresponding differences between the values of the temporary temperature T_{ij} and the reference temperature U_{ij} in the last row of each figure are shown. After about 20 s, it can be seen that the temperatures in the cast and the casting mould level out.

Moreover, there are unseen differences in the obtained temperatures, regardless of the ABC algorithm's iteration number. However, these differences do not exceed 1 K in any of the cases. It can be concluded from the graphs that there are no slight visible differences in the obtained temperatures, regardless of the number of individuals in the population and the number of iterations using the ABC algorithm. The time in the figures starts with the first time step, which is 0.05 s.

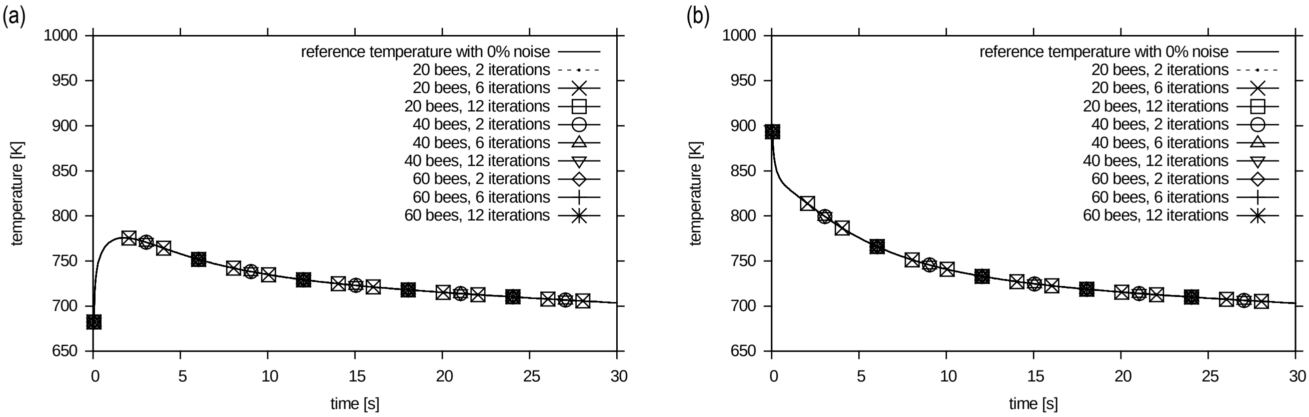

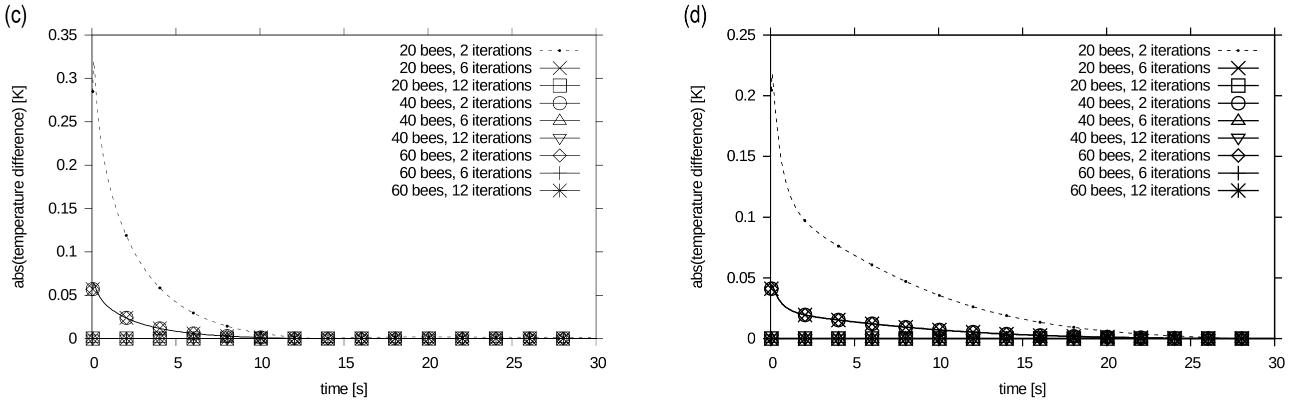

Fig. 6. Temperature over time distribution at 0% disturbance, for the ABC algorithm, with 20, 40 and 60 bees for 2, 6 and 12 iterations, respectively. The left panel depicts data obtained for node number 26 belonging to the mould, whereas the right panel for node no 61 belonging to the cast. Temperature vs. time courses concerning the reference temperature for (a) the mould and (b) the cast are shown. The corresponding difference between values of temporary temperature T_{ij} and the reference temperature U_{ij} for (c) the mould and (d) the cast is depicted. ABC, artificial bee colony

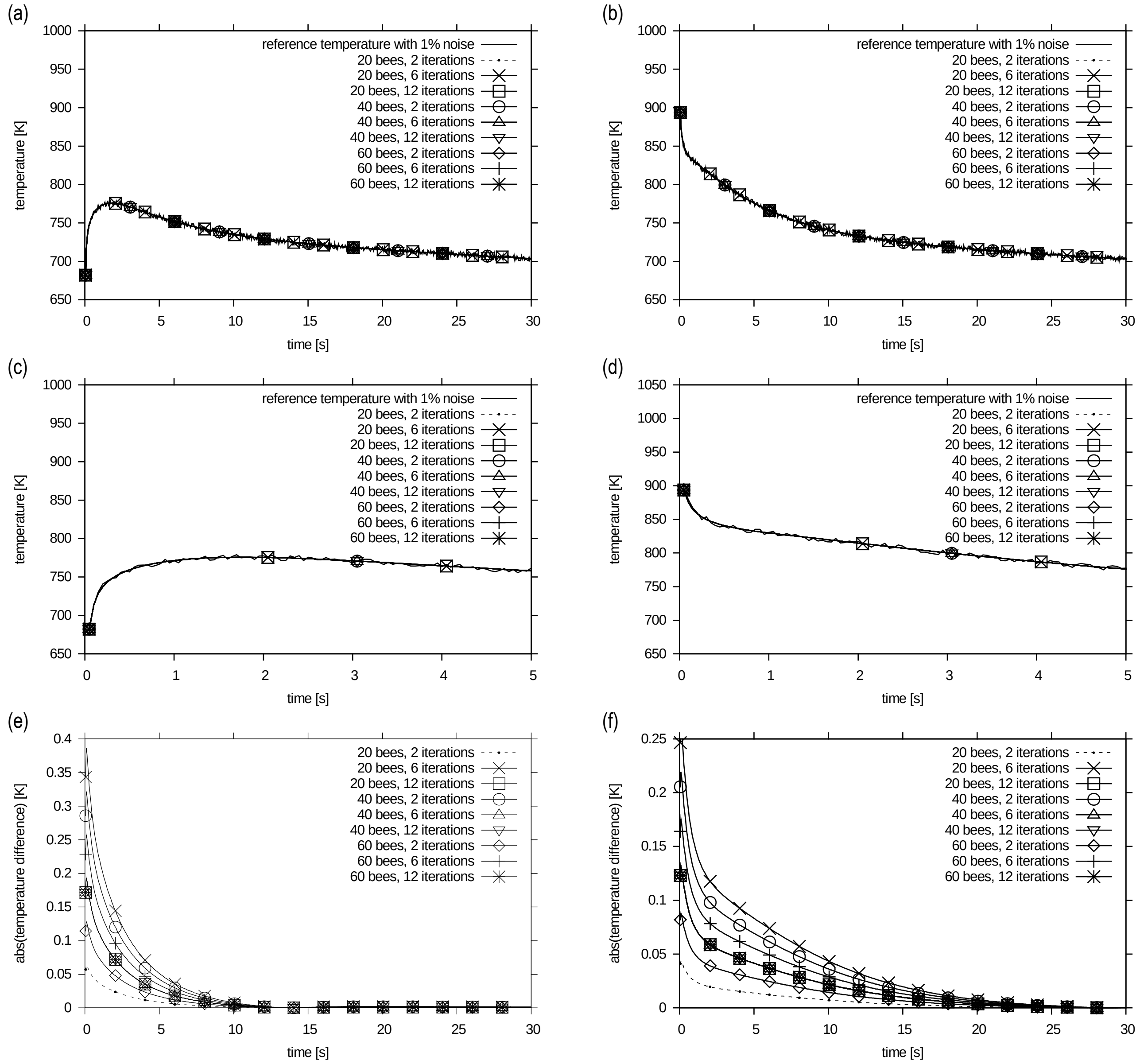

Fig. 7. Temperature over time distribution at 1% disturbance, for the ABC algorithm, with 20, 40 and 60 bees for 2, 6 and 12 iterations, respectively. The left panel depicts data obtained for node number 26 belonging to the mould and the right panel for node number 61 belonging to the cast. Temperature vs. time courses concerning the reference temperature in (a) the mould and (b) the cast for the entire time of the numerical experiment, whereas (c) and (d) for the first 5 s, are shown. Furthermore, the corresponding difference between values of the temporary temperature T_{ij} and the reference temperature U_{ij} for (e) the mould and (f) the cast is depicted. ABC, artificial bee colony.

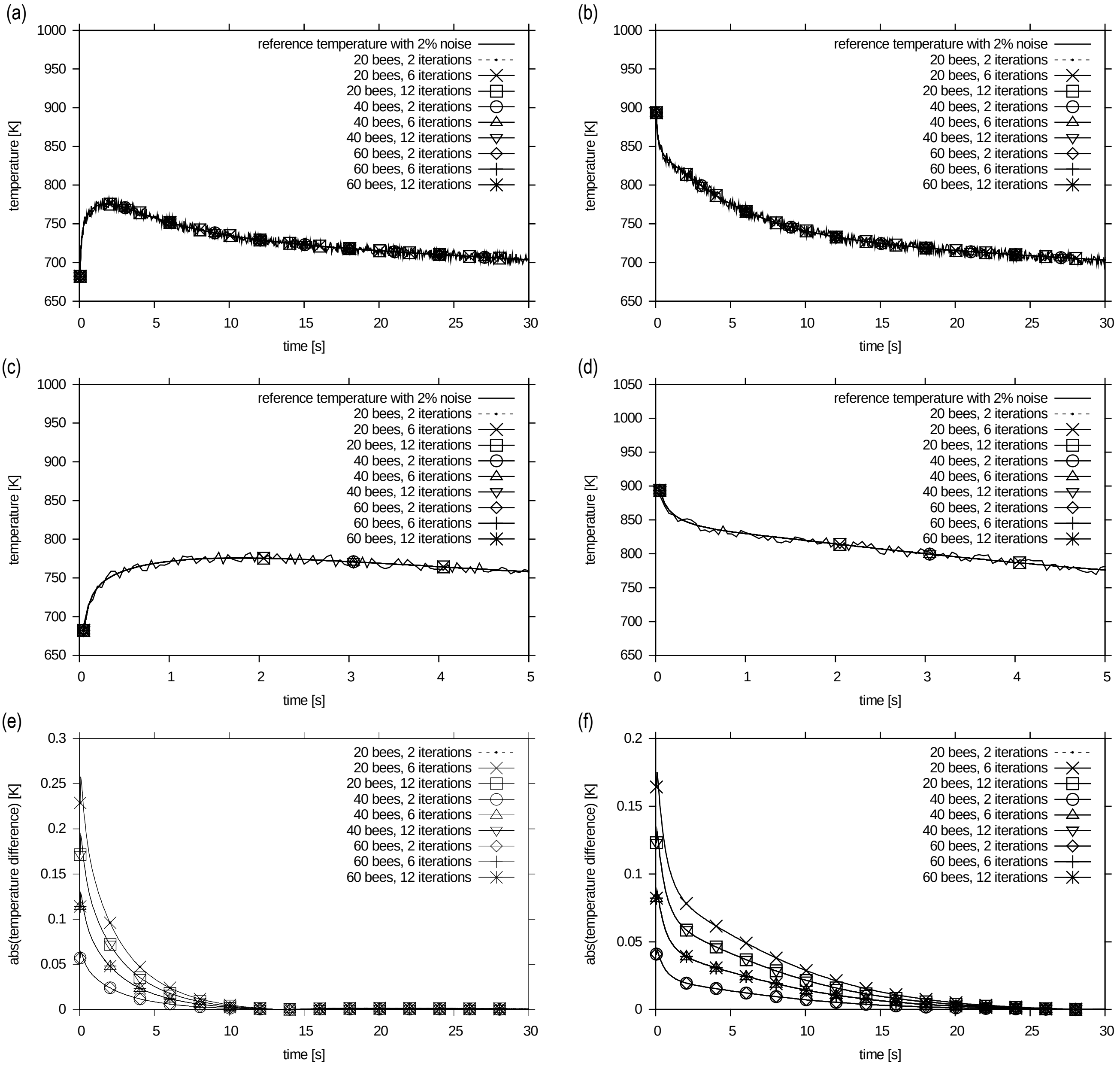

Fig. 8. Temperature over time distribution at 2% disturbance, for the ABC algorithm, with 20, 40 and 60 bees for 2, 6 and 12 iterations, respectively. The left panel depicts data obtained for node number 26 belonging to the mould and the right panel for node number 61 belonging to the cast. Temperature vs. time courses concerning the reference temperature in (a) the mould and (b) the cast for the entire time of the numerical experiment, whereas (c) and (d) for the first 5 s, are shown. Furthermore, the corresponding difference between values of the temporary temperature T_{ij} and the reference temperature U_{ij} for (e) the mould and (f) the cast is depicted. ABC, artificial bee colony

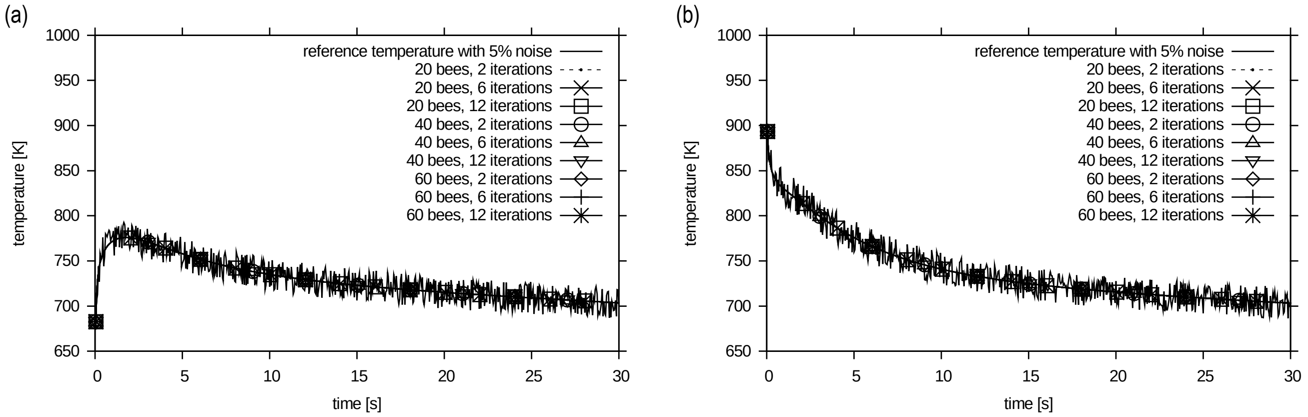

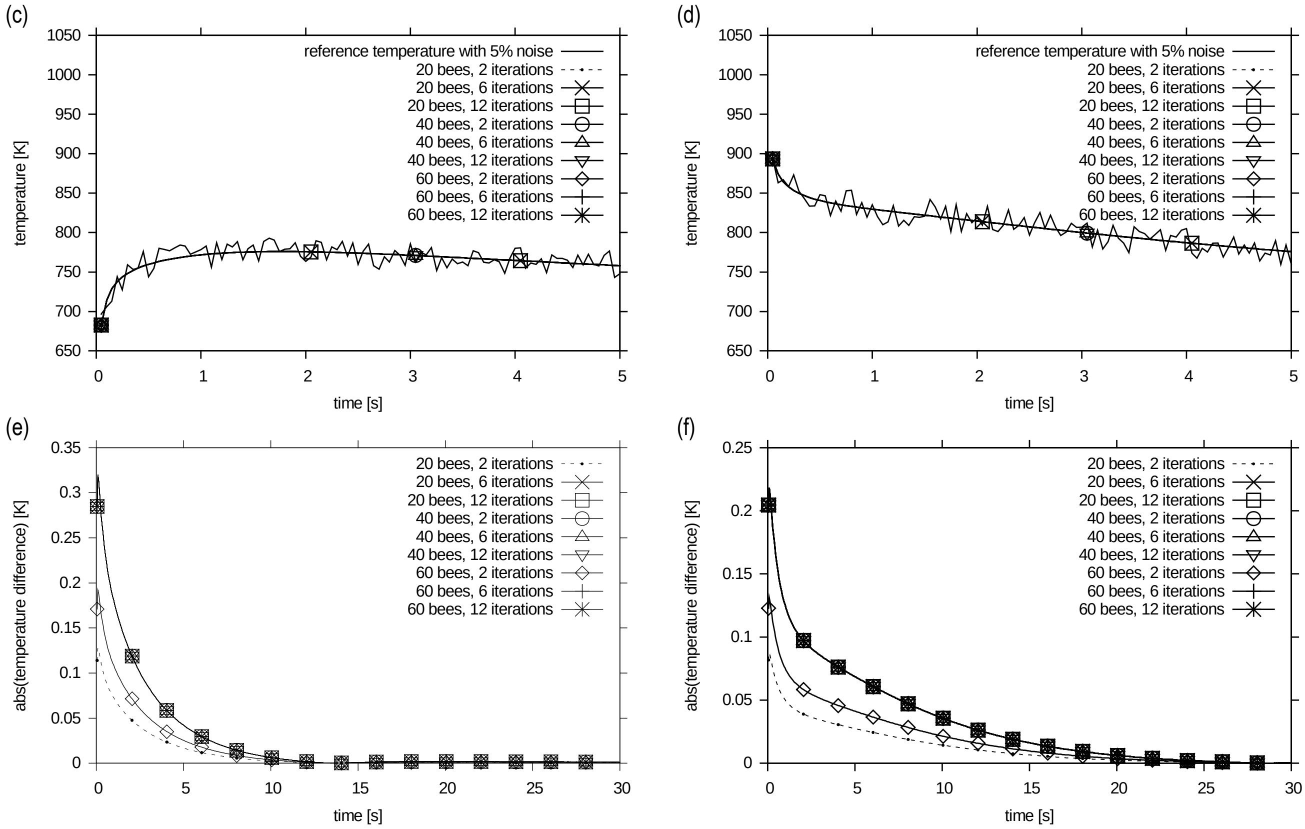

Fig. 9. Temperature over time distribution at 5% disturbance, for the ABC algorithm, with 20, 40 and 60 bees for 2, 6 and 12 iterations, respectively. The left panel depicts data obtained for node number 26 belonging to the mould and the right panel for node number 61 belonging to the cast. Temperature vs. time courses concerning the reference temperature in (a) the mould and (b) the cast for the entire time of the numerical experiment, whereas (c) and (d) for the first 5 s, are shown. Furthermore, the corresponding difference between values of the temporary temperature T_{ij} and the reference temperature U_{ij} for (e) the mould and (f) the cast is depicted. ABC, artificial bee colony

4.2. Analysis of the results obtained using the ACO algorithm

Figs. 10–13 show the temperature courses over time for the middle pair of nodes (26–61) in the finite element mesh of the studied geometry. In the case of ACO algorithm this figures visualise 0%, 1%, 2% and 5% disturbance for 20, 40 and 60 ants corresponding to 2, 6, and 12 iterations, respectively. The left panel tallies with the mould, and the right panel with the cast. The temperature distribution is physically correct in each case. The corresponding differences between values of the temporary temperature T_{ij} and the reference temperature U_{ij} in the last row of each figure are shown. After about 20 s, it can be seen that the temperatures in the cast and the casting mould level out.

Moreover, there are unseen differences in the obtained temperatures, regardless of the ACO algorithm's iteration number. However, these differences do not exceed 1 K in any of the cases. It can be concluded from the graphs that there are no slight visible differences in the obtained temperatures, regardless of the number of individuals in the population and the number of iterations using the ABC algorithm. The time in the figures starts with the first time step, which is 0.05 s.

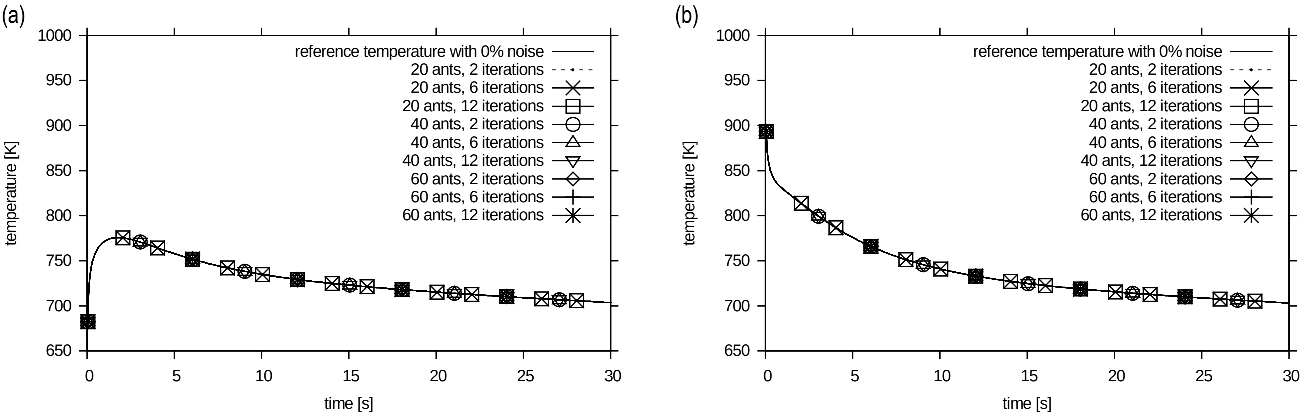

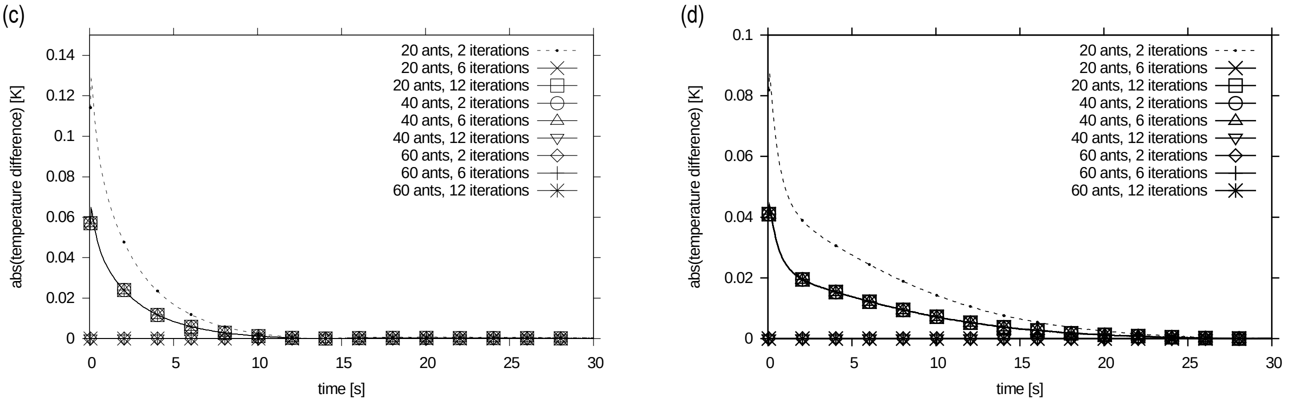

Fig. 10. Temperature over time distribution at 0% disturbance, for the ACO algorithm, with 20, 40 and 60 ants for 2, 6 and 12 iterations, respectively. Left panel depicts data obtained for node number 26 belonging to the mould and right panel for node number 61 belonging to the cast. Temperature vs. time courses with respect to the reference temperature for (a) the mould and (b) the cast. Corresponding difference between values of the temporary temperature T_{ij} and the reference temperature U_{ij} for (c) the mould and (d) the cast. ACO, ant colony optimisation

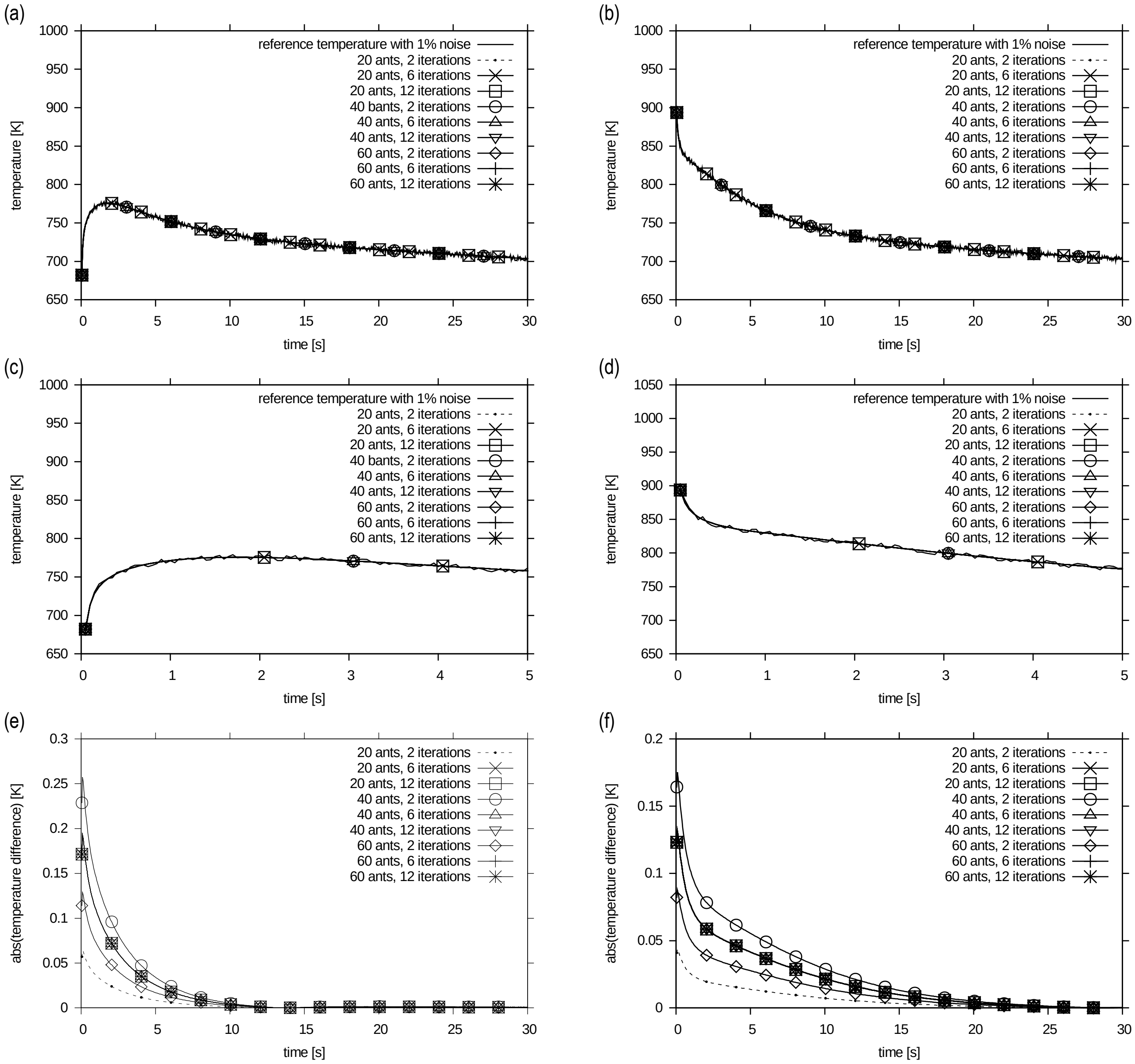

Fig. 11. Temperature over time distribution at 1% disturbance, for the ACO algorithm, with 20, 40 and 60 ants for 2, 6 and 12 iterations, respectively. The left panel depicts data obtained for node number 26 belonging to the mould and the right panel for node number 61 belonging to the cast. Temperature vs. time courses concerning the reference temperature in (a) the mould and (b) the cast for the entire time of the numerical experiment, whereas (c) and (d) for the first 5 s, are shown. Furthermore, the corresponding difference between values of the temporary temperature T_{ij} and the reference temperature U_{ij} for (e) the mould and (f) the cast is depicted. ACO, ant colony optimisation

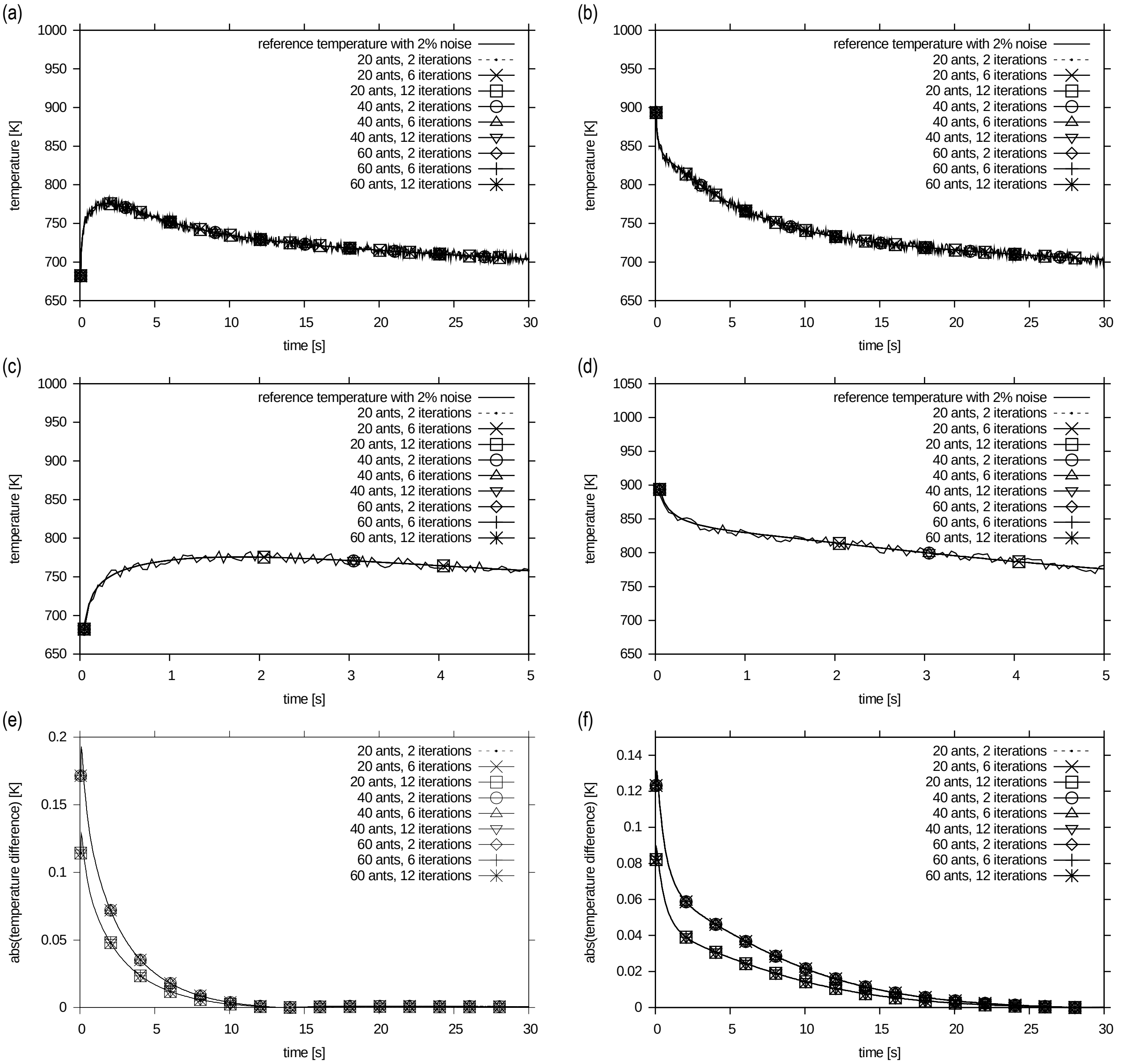

Fig. 12. Temperature over time distribution at 2% disturbance, for the ACO algorithm, with 20, 40 and 60 ants for 2, 6 and 12 iterations, respectively. The left panel depicts data obtained for node number 26 belonging to the mould and the right panel for node number 61 belonging to the cast. Temperature vs. time courses concerning the reference temperature in (a) the mould and (b) the cast for the entire time of the numerical experiment, whereas (c) and (d) for the first 5 s, are shown. Furthermore, the corresponding difference between values of the temporary temperature T_{ij} and the reference temperature U_{ij} for (e) the mould and (f) the cast is depicted. ACO, ant colony optimisation

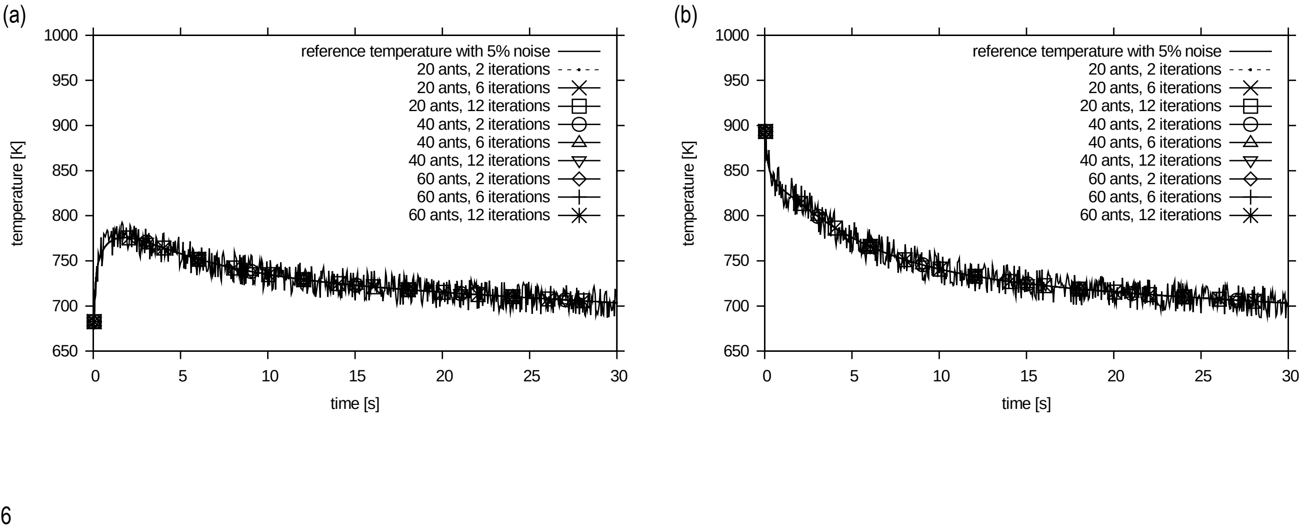

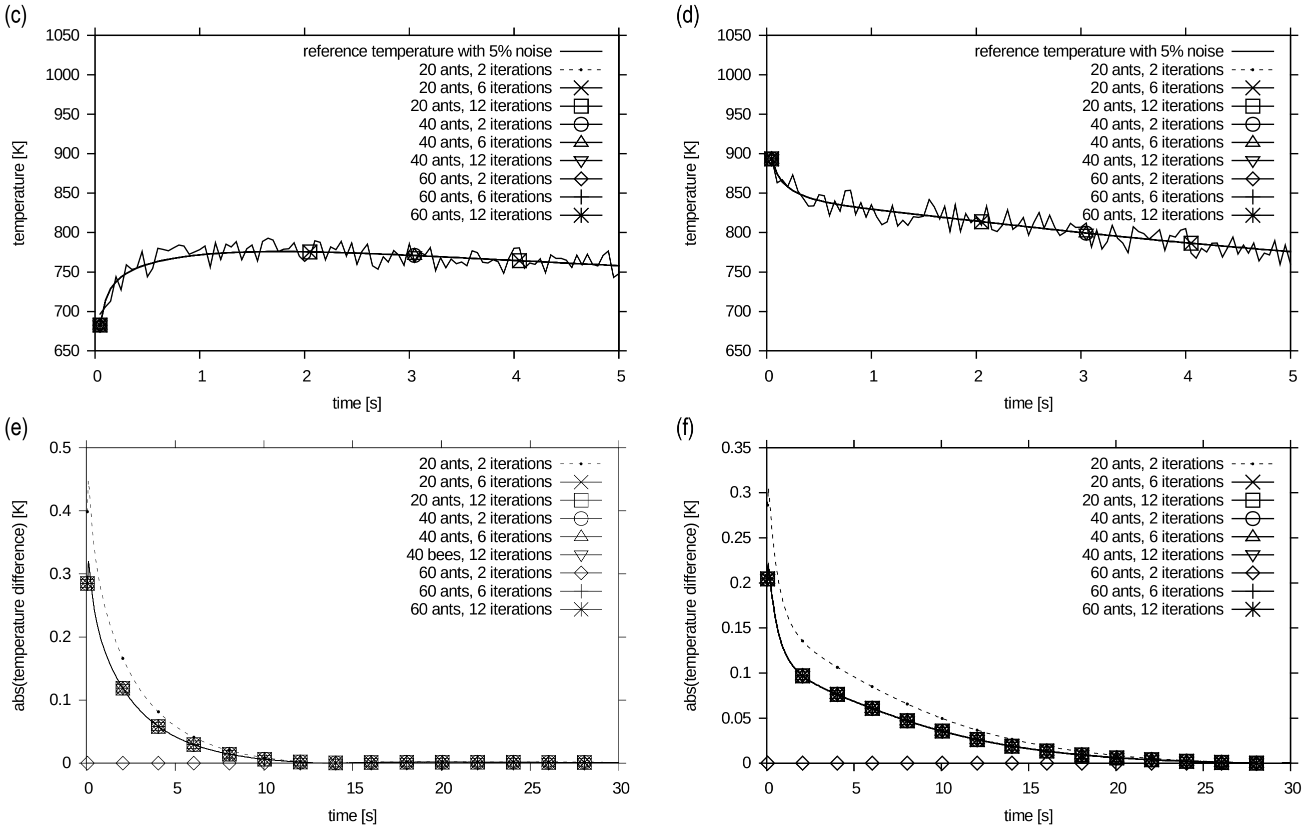

Fig. 13. Temperature over time distribution at 2% disturbance, for the ACO algorithm, with 20, 40 and 60 ants for 2, 6 and 12 iterations, respectively. The left panel depicts data obtained for node number 26 belonging to the mould and the right panel for node number 61 belonging to the cast. Temperature vs. time courses concerning the reference temperature in (a) the mould and (b) the cast for the entire time of the numerical experiment, whereas (c) and (d) for the first 5 s, are shown. Furthermore, the corresponding difference between values of the temporary temperature T_{ij} and the reference temperature U_{ij} for (e) the mould and (f) the cast is depicted. ACO, ant colony optimisation

4.3. Comparative analysis of the results for the ABC and ACO algorithms

Fig. 14 shows the temperature courses over time for the middle pair of nodes (mould-cast) in the finite element mesh of the studied geometry with a 2% disturbance of the temperature reference value for the second, sixth, and twelfth iterations and 60 bees/ants in ABC/ACO algorithm. Similar to the previous figures, after about 20 s, it can be seen that the temperatures in the cast and the casting mould level out. Moreover, the graph shows tiny differences (practically unseen) in the obtained temperatures between the ABC and the ACO algorithms. However, these differences do not exceed 0.2 K.

Both the ABC and the ACO algorithms meet the expectations for the correct determination of the κ coefficient and the correct course of temperature over time, consistent with the physics of the phenomenon.

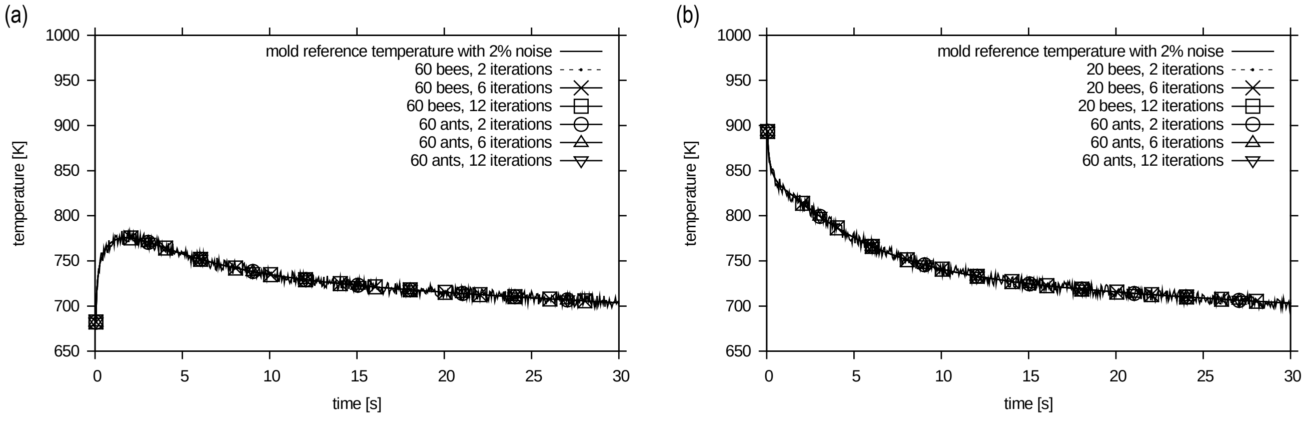

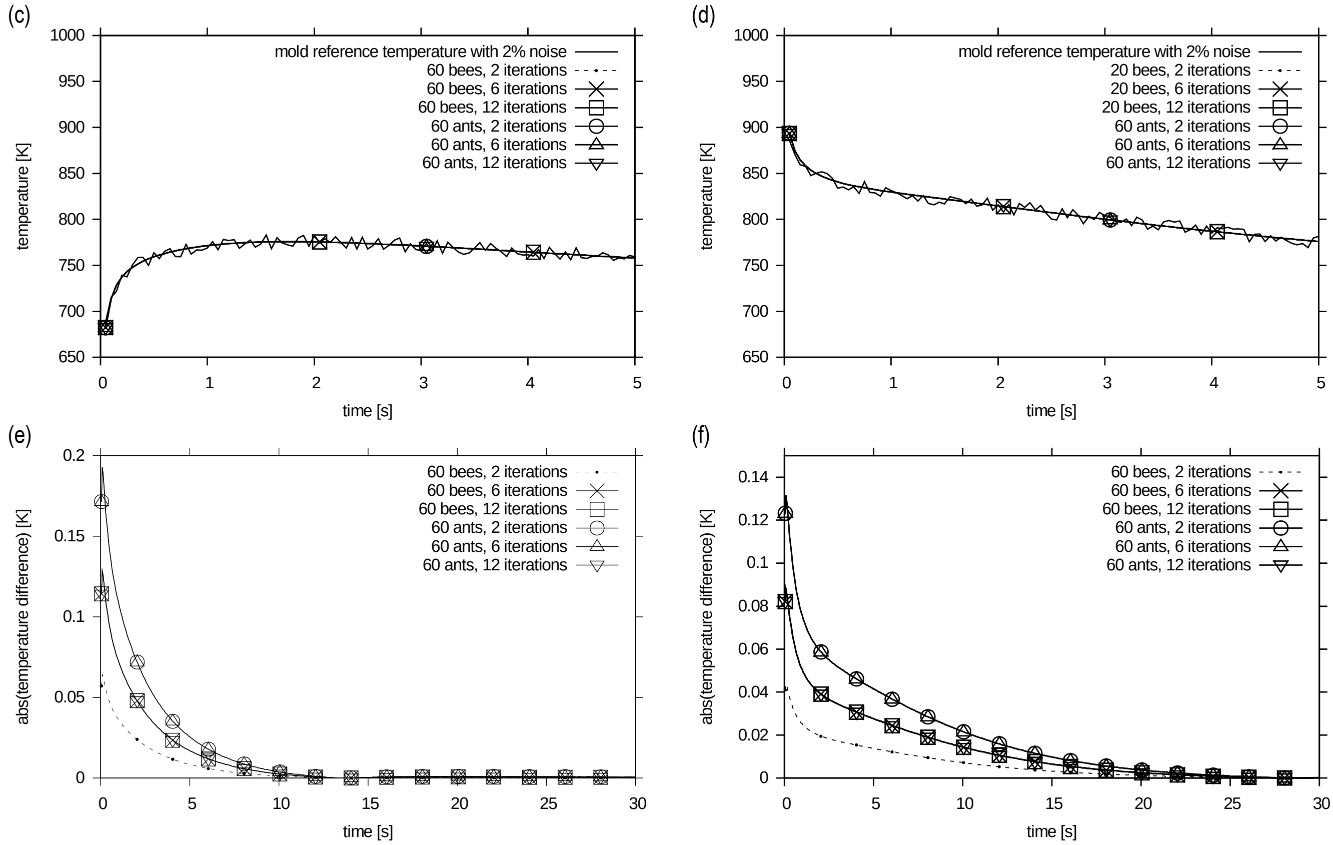

Fig. 14. Temperature over time distribution at 2% disturbance, for the ABC and ACO algorithms, with 60 bees/ants and for 2, 6 and 12 iterations. The left panel depicts data obtained for node number 26 belonging to the mould and the right panel for node number 61 belonging to the cast. Temperature vs. time courses concerning the reference temperature in (a) the mould and (b) the cast for the entire time of the numerical experiment, whereas (c) and (d) for the first 5 s, are shown. Furthermore, the corresponding difference between values of the temporary temperature T_{ij} and the reference temperature U_{ij} for (e) the mould and (f) the cast is depicted. ABC, artificial bee colony; ACO, ant colony optimisation

The possibility of using AI algorithms in problems in the field of thermomechanics was presented. In reconstructing the heat transfer coefficient of the layer separating the cast and the casting mould, no significant difference was observed between the ABC algorithm and the ACO algorithm. The graphs of temperature variability over time show a very good representation of reality for both swarming algorithms. After analysis of the results obtained with the ABC and ACO algorithms, it can be concluded that: for simple geometry and the same number of individuals, slight differences in the obtained values of the κ coefficient and the values of the minimised functional may speak in favour of the ant colony algorithm. The conducted research has shown that both the ABC and ACO algorithms are promising tools that can be successfully used to determine the value of the thermal conductivity coefficient. The errors in the reconstruction of the κ coefficient and the standard deviation are very similar between the algorithms. Equally important, they are smaller, or at worst, comparable to the disturbance of the input data. It has been shown that both algorithms select the desired coefficient at a satisfactory level. For each algorithm, the obtained temperature results were very similar or identical to the values assumed as the standard ones.

5. SUMMARY

The investigated problem consisted of reconstructing the heat transfer coefficient at the interface between the cast and the casting mould based on a numerical experiment using artificial bee and ant colonies algorithms for optimisation. The presented solution has been described and tested to assess its stability and the accuracy of the results obtained. The numerical experiment demonstrated an excellent reconstruction of the sought coefficient as well as perfect and physically similar consistency of temperature distribution over time. In each case of the input data and frequency of measurements taken, the errors in the mapping of the heat conduction coefficient and temperature were lower or comparable with the input data errors. The proposed solution is stable, and the obtained results are satisfactory, which bodes well for the future use of our research to recreate the experimental conditions for the solidification and cooling of non-ferrous metal alloy castings.

It is important to mention the possibility for recreation of the heat conduction coefficient of the layer separating the mould and the casting in the form of several intervals, i.e., by obtaining several numerical values; this is an arena of study that has not been explored in the present article, but it would be interesting to explore it as part of future work. Also, the possibility of obtaining a continuous variation in the value of the heat transfer coefficient through the layer separating the mould and the casting can be mentioned as another potential direction for further research. The suggested study of the impact of the distribution of nodes in which the error value was calculated is also a possible direction for further research.

REFERENCES

1. Gosselin L, Tye-Gingras M, Mathieu-Potvin F. Review of utilization of genetic algorithms in heat transfer problems. International Journal of Heat and Mass Transfer. 2009; 52(9-10):2169-2188.
2. Kot V. Solution of the classical Stefan problem: Neumann condition. Journal of Engineering Physics and Thermophysics. 2017; 90(4): 889-917.
3. Chen J, Yu W, Tian J, Chen L, Zhou Z. Image contrast enhancement using an artificial bee colony algorithm. Swarm and Evolutionary Computation. 2018; 38:287-294.
4. Zhao X, Xuan D, Zhao K, Li Z. Elman neural network using ant colony optimization algorithm for estimating of state of charge of lithium-ion battery. Journal of Energy Storage. 2020; 32:101789.
5. Karaboga D, Gorkemli B, Ozturk C, Karaboga N. A comprehensive survey: artificial bee colony (ABC) algorithm and applications. Artificial Intelligence Review. 2014; 42:21-57.
6. Karaboga D. An idea based on honey bee swarm for numerical optimization. Technical Report. Kayseri/Türkiye: Erciyes University, Engineering Faculty, Computer Engineering Department; 2005. Report No.: TR-06.
7. Karaboga D, Basturk B. On the performance of artificial bee colony (ABC) algorithm. Applied Soft Computing. 2008; 8(1):687-697.
8. Hetmaniok E, Słota D, Zielonka A. Artificial Bee Colo-ny Algorithm Used for Reconstructing the Heat Flux Density in the Solidification Process. In International Conference on Artificial Intel-ligence and Soft Computing; 2014; 363–372.
9. Hetmaniok E, Słota D, Zielonka A, Wituła R. Comparison of ABC and ACO Algorithms Applied for Solving the Inverse Heat Conduction Problem. In International Symposium on Swarm Intelligence and Differential Evolution; 2012; 249–257.
10. Hetmaniok E, Słota D, Zielonka A. Restoration of the cooling conditions in a three-dimensional continuous casting process using AI algorithms. Applied Mathematical Modelling. 2015; 39(16): 4794-4807.
11. Zielonka A, Hetmaniok E, Słota D. Inverse alloy solidification problem including the material phenomenon solved by using the bee algorithm. International Communications in Heat and Mass Transfer. 2017; 87:295-301.
12. Grzymkowski R, Hetmaniok E, Słota D, Zielonka A. Application of the Ant Colony Optimization Algorithm in Solving the Inverse Stefan Problem. In Metal Forming; 2012; 1287-1290.
13. Hetmaniok E, Słota D, Zielonka A. Application of the Swarm Intelligence Algorithm for Investigating the Inverse Continuous Casting Problem. Contemporary Challenges and Solutions in Applied Artificial Intelligence. 2013; 489: 157–162.
14. Matsevityi YM, Alekhina SV, Borukhov VT. Identification of the thermal conductivity coefficient for quasi-stationary two-dimensional heat conduction equations. Journal of Engineering Physics and Thermophysics. 2017; 90(6):1295-1301.
15. Tereshko V, Loengarov A. Collective decision-making in honey bee foraging dynamics. Computing and Information Systems. 2005; 9: 1-7.
16. Colorni A, Dorigo M, Maniezzo V. Distributed Optimization by Ant Colonies. In Proceedings of the European Conference on Artificial Life; 1991; 134-142.
17. Dorigo M, Maniezzo V, Colorni A. Ant system: Optimization by a colony of cooperating agents. IEEE Transactions on Systems, Man and Cybernetics, Part B (Cybernetics). 1996; 26(1):29-41.
18. Dorigo M, Di Caro G. Ant colony optimization: a new meta-heuristic. In Proceedings of the 1999 Congress on Evolutionary Computation-CEC99; 1999;1470-1477.
19. Geuzaine C, Remacle JF. GMSH: a three-dimensional finite element mesh generator with built-in pre- and post-processing facilities. International Journal for Numerical Methods in Engineering. 2009; 79(11):1309-1331.
20. Dyja R, Grosser A. Oblicznia równoległe w symulacji krzepnięcia wykorzystującej model pośredni narstania fazy stałej. Modelowanie Inżynierskie. 2015; 24(55):21-26.
21. Dyja R, Gawronska E, Grosser A, Jeruszka P, Sczygiol N. Estimate the Impact of Different Heat Capacity Approximation Methods on the Numerical Results During Computer Simulation of Solidification. Engineering Letters. 2016; 24(2):237-245.
22. Kodali HK, Ganapathysubramanian B. A computational framework to investigate charge transport in heterogeneous organic photovoltaic devices. Computer Methods in Applied Mechanics and Engineering. 2012; 247:113-129.
23. Balay S, Gropp WD, McInnes LC, Smith BF. Efficient Management of Parallelism in Object-Oriented Numerical Software Libraries. In Arge E,BAM,LHP. Modern Software Tools for Scientific Computing. Boston. 1997;163–202.
24. Dyja R. Comparison of Results from In-House Solidification Convection Model with Standard Benchmark. Acta Physica Polonica. 2021; 139(5):525-528.

Elżbieta Gawrońska: https://orcid.org/0000-0003-1060-3641

Robert Dyja: https://orcid.org/0000-0001-6941-4728

Maria Zych: https://orcid.org/0000-0002-0406-6053

Grzegorz Domek: https://orcid.org/0000-0003-3566-9110

DOI 10.2478/ama-2022-0040

THE USE OF THERMOGRAPHY TO DETERMINE THE COMPACTION OF A SADDLE-SHAPED BRIQUETTE PRODUCED IN AN INNOVATIVE ROLLER PRESS COMPACTION UNIT

Michał BEMBENEK*, Andrzej UHRYŃSKI**

*Department of Manufacturing Systems, Faculty of Mechanical Engineering and Robotics,
AGH University of Science and Technology, Al. Adama Mickiewicza 30, 30-059 Kraków , Poland
**Department of Machine Design and Operation, Faculty of Mechanical Engineering and Robotics,
AGH University of Science and Technology, Al. Adama Mickiewicza 30, 30-059 Kraków, Poland

bembenek@agh.edu.pl, uhrynski@agh.edu.pl

received 25 June 2022, revised 11 September 2022, accepted 12 September 2022

Abstract: The unit compacting pressure in the fine-grained material consolidation process in the roller press can reach >100 MPa and is a parameter that results, among other things, from the properties of the consolidated material and the compaction unit geometry. Achieving the right pressure during briquetting is one of the factors that guarantee the proper consolidation and quality of briquettes. The distribution of the temperature on the surface of the briquettes correlates with locally exerted pressure. The present work aimed to analyse the briquetting process of four fine-grained materials in a roller press equipped with saddle-shaped briquette-forming rollers based on images obtained from the thermography conducted immediately after their consolidation. The tests were carried out in a roller press that was equipped with forming rollers of 450-mm diameter and having a cavity with a volume of 4 cm^3, as described by patent PL 222229 B1. Two mixtures of hydrated lime with 9.1 wt% and 13.0 wt% water, a mixture of scale and a mixture of electric arc furnace (EAF) dust were used for the tests. In most mixtures, the highest temperatures were achieved in the middle-upper part of the briquettes. The briquettes from the EAF dust mixture heated locally the most on the surface up to 37.7 °C. The difference between the maximum briquette temperature and the ambient temperature was 20.2 °C.

Key words: roller press, thermography, thermovision, saddle-shaped briquettes, briquetting

1. INTRODUCTION

Many phenomena can be correlated with the temperature change of a tested object; therefore, it is important to obtain a precise picture of the distribution and increase of its surface temperature. The technique that makes it possible is thermography (it is based on measuring the radiation in the infrared range). Thermographic research finds increasingly wider possibilities of application, and it is used increasingly often; and this is a consequence, among other things, of the fact that the devices used for it allow for a set of steadily improving capabilities for measuring possibilities at lower costs of production and progressive miniaturisation. The decisive advantage of non-contact measurements is their non-invasiveness, which is often the basic criterion for selecting them.

Thermovision was originally used by the army to observe aeroplanes and detect the movement of military units. Until now, it has been successfully used for military purposes or the research related to, for example, the detection of defects in graphite nozzles used in missile propulsion systems [1] or to assess the technical condition of elements of military bridges [2]. Thermal imaging is widely used by the construction industry. It is useful for testing the energy efficiency of buildings, detecting defects in installation systems and verifying the effects of modernisation [3], as well as testing the thermal properties of walls [4], or detecting delamination of structural elements of buildings [5]. This technique, mainly due to its non-invasiveness, has been playing a special role in medicine for many years. It is used as a quick and precise tool to collect information necessary to diagnose rare diseases [6] or to evaluate the effectiveness of medical treatments [7]. It was also used to assess the impact of the body's reaction to low temperatures [8], vibrations [9] or workload [10].

However, it seems that the greatest spectrum of possibilities of using thermovision is provided by mechanical and electrical engineering. Thermography is very useful in the removal and treatment of material so as to control the increase and distribution of temperature in the tool working zone [11] and on the chip surface [12]. Its advantages were used in the assessment of welded joints and in the diagnosis of the course of the welding process itself [13, 14]. It should also be mentioned that this technique is used in the widely understood diagnostics of machines, ranging from numerically controlled machine tools [15], through rotating machines [16], belt conveyors [17], brakes [18] and rolling bearings (there is no way to measure the temperature of moving rolling elements and cage other than the contactless method) [19], up to electrical machines and devices [20, 21, 22]. The attempts to link strength and stress measurements in a material with the amount of heat energy produced are very interesting [23]. The methodology of measuring ropes has also been described, including the relation between temperature increase and stress increase in the rope [24]. The relations between the mechanical properties of polypropylene stretching were analysed [25]; a system was suggested to analyse the thermomechanical properties and heat release in the stretching process [26]. Experiments have been carried out confirming the thesis that the analysis of temperature distribution in strength tests is the basis for the qualitative assessment of the stresses in the tested samples [27].

In addition to passive thermography (described above), we can also discuss active thermography, which is to be distinguished from the former variant in that it is a method of stimulating (arousing) the subject of research, e.g. by delivering an impulse in the form of thermal energy [28] or causing this effect by means of an acoustic wave [29], including ultrasounds [30] or microwaves [31], and then observing its path propagation and the effects that they have caused in the material using a thermograph on the surface of the tested object. This type of thermovision is particularly applicable in defectoscopy [32, 33].

Thermal phenomena are a rich source of information about technological processes and changes or irregularities taking place during these processes [34], which allows us to control the parameters of the process and to introduce the necessary modification so that the process runs properly and the product is of high quality. Thermography was used, among other purposes, for process control: casting and cooling of cast iron [35], production of casting moulds in order to form turbocharger blades [36], extrusion of poly (vinyl chloride) [37], production of tires [38] and the production of textiles [39, 40]. The quality of compacts made of loose materials leaving the compaction zone was also checked. Online monitoring of the powder flow during compaction helps to locate the areas of greatest pressure and identify the influence of the roller force on the powder temperature [41]. Recently, a study has been published that proposes a methodology to ascertain the extent to which the share material on the raking face undergoes wear during deployment in soil. The temperature distribution on the tool during operation was measured. Then, a hypothesis was made that the amount of heat emitted in a given area of the share surface correlates with the intensity of tribological processes [42].

An interesting issue is the use of thermography studies for agglomeration processes of fine-grained materials in a roller press [43]. During the production of a briquette in a roller briquetting press, the pressure exerted on its external surface is not uniform [44]. Depending on the place on the surface, it may have a variable value [45, 46]. The resulting compacting pressure distribution depends not only on the material properties but also on the geometry of the compaction unit and the briquette volume. The local compacting pressure exerted can be related to the temperature at the surface of the briquette. The higher the temperature at a given point in the briquette, the higher the compacting pressure exerted in this place. The results presented in this article are a continuation of previous research published in the literature that present a simultaneous study of the temperature distribution and the compacting pressures in various compacting units of the roller press.”. In previous works, the temperature distributions on the surface of classic saddle-shaped [47] and pillow-shaped briquettes [48] were presented. The tests presented in this article were carried out on four different mixtures of fine-grained materials in the innovative roller press compaction unit described by the PL 222229 B1 patent [49], in which the saddle-shaped cavities are distributed along the forming rollers. Compared with other compaction units, its geometry enables, among other utilities, self-synchronisation of working rollers, without the need for an additional gearbox.

2. MATERIALS AND METHODS

2.1. Briquetting process

The thermographic research of the briquetting process in the roller press was performed using a roller press (Fig. 1) with a 450-mm roller-pitch diameter with an installed PL 222229 B1 patented compaction unit for the production of pillow-shaped briquettes with dimensions of 31 mm × 24 mm × 11 mm and a rated capacity of 4 cm^3 (Fig. 2). There were 30 forming cavities in each of the two rows on the surfaces of the forming rollers. The roller press was equipped with a 22-kW motor with a cycloidal gear and a frequency converter that enabled infinitely variable control of the rotation speed of the rollers. A gravity feeder was used when all materials were consolidated. The rollers' rotation speed was 0.85 RPM, which gave a peripheral speed of the rollers equal to 0.02 m/s. It caused each briquette in the forming row to fall out at approx. 2.0 s. The inter-roller gap was set to 1 mm.

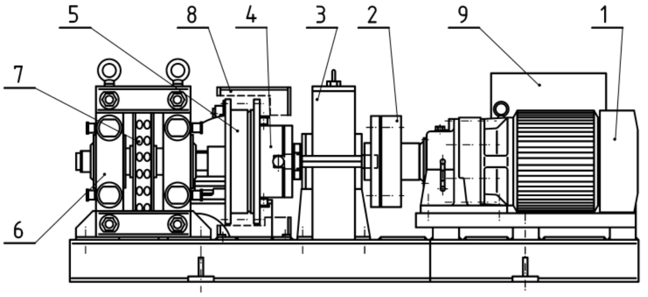

Fig. 1. The scheme of laboratory roller press (LPW 450): (1) gear motor with a cycloidal transmission, (2) flexible clutch, (3) gearbox, (4) Oldham clutch, (5) friction clutch, (6) moulding rollers cage, (7) forming rollers, (8) safety cover and (9) hydraulic system of sliding roller support

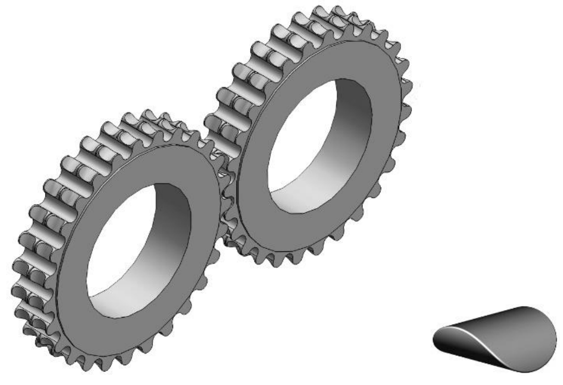

Fig. 2. The patented rollers PL 222229 B1 used in roller press compaction unit with a saddle-shaped briquette

Before the agglomeration process, four mixtures were prepared with the materials. They were thoroughly mixed in a Z-blade mixer with four rectangular mixing elements with dimensions of 190 mm × 90 mm and a shaft rotating speed of 55 RPM and brought to proper moisture, enabling them to be consolidated in a roller press, and the binders were added. The moisture content was determined using the weight method at 105 °C until a constant weight was obtained. The Vibra AJH 420 CE (Tokyo, Japan) scale was used.

2.2. Mixtures

2.2.1. Mixtures 1 (M1)

Its composition was 90.9 wt% calcium hydroxide manufactured by Lhoist (EN 459-1 CL 90-S) (Limelette, Belgium) and 9.1 wt% water. The average grain diameter was 19.9 µm. The mixture was mixed for about 30 min. The moisture content of the mixture was 9.4 wt%.

2.2.2. Mixture 2 (M2)

Its composition was 87.0 wt% calcium hydroxide manufactured by Lhoist (EN 459-1 CL 90-S) (Limelette, Belgium) and 13.0 wt% water. The average grain diameter was 19.9 µm. The mixture was mixed for about 30 min. The moisture content of the mixture was 13.2 wt%.

2.2.3. Mixture 3 (M3)

The mixture consisted of pre-compacted 92.6 wt% mill scale, with a grain size of ≤5 mm being obtained after the addition of water and molasses, each to an extent of 3.7 wt%. The mixture was mixed for about 10 min. Its moisture content was 5.2%. The pre-compacted process involved briquetting and crushing the consolidated briquettes to a size <10 mm.

2.2.4. Mixture 4 (M4)

The mixture contained 47.7 wt% of electric arc furnace dust (EAFD), 36.7 wt% of scale, 7.3 wt% fine coke breeze, 5.5 wt% 80° Bx molasses and 2.8 wt% calcium hydroxide. The last two ingredients were added as binders. The mixture was mixed for about 10 min. Its moisture content was 4.6%.

2.3. Thermography tests

The FLIR T1020 28° thermal imaging camera (Wilsonville, OR, USA) was used for the tests. The whole operating temperature range of the camera was from –40°C to +650°C, while the temperature range of −40°C to +150°C was used, for which the temperature measurement error was ±2°C or ±2% of the measurement value. The camera was equipped with a microbolometric matrix with a resolution of 1024 × 768 pixels, a 28° × 21° lens and a <0.0025 °C noise equivalent temperature difference (NETD) sensor. Before the tests, it was necessary to calibrate the camera. The ambient temperature during tests was 21.3 °C. The measuring station was prevented from having access to daylight and artificial light, since these were eliminated beforehand in the laboratory environment. In addition, a special shield was made (Fig. 3) to block the inflow of the light to the working area of the thermal imaging camera, and the purposes of this exercise were: (1) to eliminate the possibility of the reflection of radiation disturbing the test result and (2) to ensure repeatability of the distance measurement between the camera and the tested briquette.

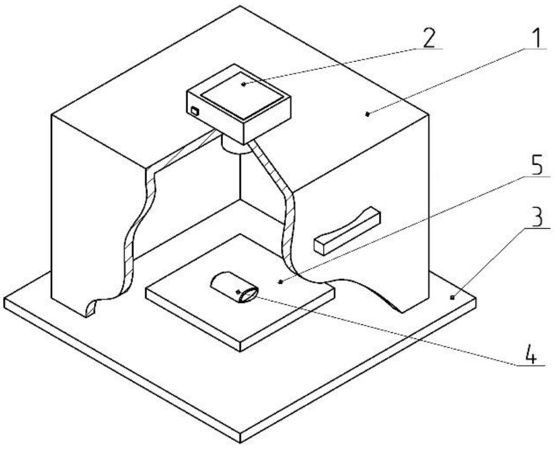

Fig. 3. A specially constructed station for capturing images of briquettes, which eliminates the effects of external radiation [48]: (1) cover; (2) thermal imaging camera; (3) base; (4) briquette; and (5) plywood pad

Each time the briquette was produced in a roller press, it was caught and transferred to a plywood plate, using heat-insulating gloves, immediately after leaving the compaction unit. Then, the briquettes and the pad were placed in a measuring station, and thermal images were captured. The time between catching the briquettes and capturing the photo was about 3 s. After each test, the plywood pad was changed to make the test conditions reproducible as the pads got hotter. The pads got hotter from the briquettes as time went on. It was possible to transfer the briquette to the plywood pad directly after it was removed from the compaction unit, while maintaining precise control of the briquette top-bottom, front-back orientation due to the low peripheral speed of the rollers (0.02 m/s). The tests of briquetting with the higher peripheral speed were unsuccessful due to the lack of possibility of controlled catching of the briquettes in the right orientation [47,48]. The images of the briquettes were captured in such a way that their 'top' (Fig. 4) was always located up the top edge of the image. Two briquettes were placed on the pads in two positions: 'front' and 'back', as shown in Fig. 4b.

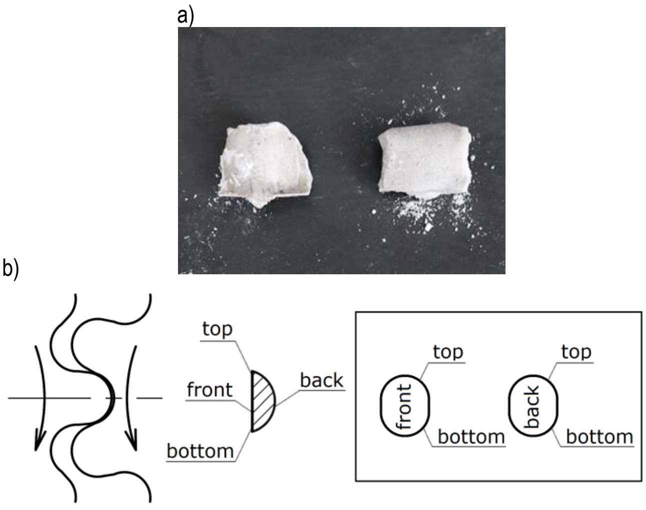

Fig. 4. The briquettes arrangement: (a) on the plywood pad (b) in the compacting unit

From each mixture, five thermal images of the briquettes were captured for further analysis. The FLIR Thermal Studio program (Wilsonville, OR, USA) was used to analyse the images. First, the maximum and minimum temperatures were determined for each type of briquette, and its measurements were averaged.

To examine the temperature distribution on the briquette surface, a special grid (shown in Fig. 5) was fitted into the thermograms. The measuring points were spaced 4.0 mm from each other. For each image in the vertical axis of the briquette at seven points, temperature values were read.

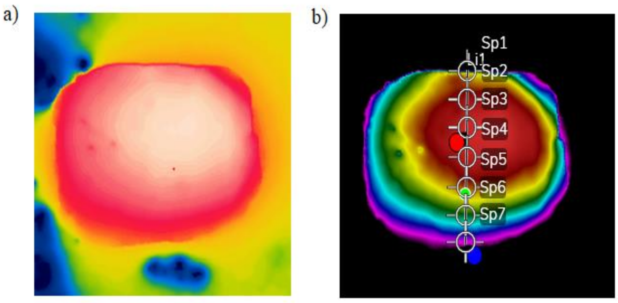

Fig. 5. Thermal image of the briquette: (a) thermal image from the camera, (b) thermal image processed in the FLIR Thermal Studio program with seven temperature measurement points superimposed

The emissivity of the integrated materials was determined according to previously developed procedures [48] with the use the FLIR Thermal Studio program. Pilot batches of briquettes, from each of the mixtures, were prepared. The briquettes were then seasoned at ambient temperature for 24 h. Then, briquettes were deposited in a SPT-200 furnace (ZUT Colector, Kraków, Poland), which had been previously heated to 59 °C for 20 min to ensure that the temperature prevailing in them would be higher than the ambient temperature. The temperature of the furnace was measured using a Kyoritsu KEW 1011 multimeter and K-type 8216 thermocouple (Kyoritsu, Tokyo, Japan). After removing the briquettes from the furnace, their thermal images were captured and processed in the FLIR Thermal Studio program.

3. RESULTS AND DISCUSSION

From all the materials used in the tests, high-quality briquettes that did not crumble were obtained.

3.1. Emissivity

The emissivity results of individual materials are presented in Tab. 1. All tested materials showed high emissivity, which is a desirable feature. This allows us to perform thermographic measurements with minimal measurement errors. Mixture M2 showed the highest emissivity. The difference between the highest and the lowest emissivity is 0.17. The above cases of emissivity were taken into account appropriately for each type of briquette in the images analysed.

Tab. 1. Emissivity of briquettes

Mixture	Emissivity, ε -
M1	0.81
M2	0.98
M3	0.86
M4	0.85

3.2. Differences in temperature on the surface of briquettes

The results of the minimum and maximum temperature for each type of briquette on the front and back sides are presented in Fig. 6. The research showed that the temperature on the surface of the briquettes differed depending on the mixture used for consolidation.

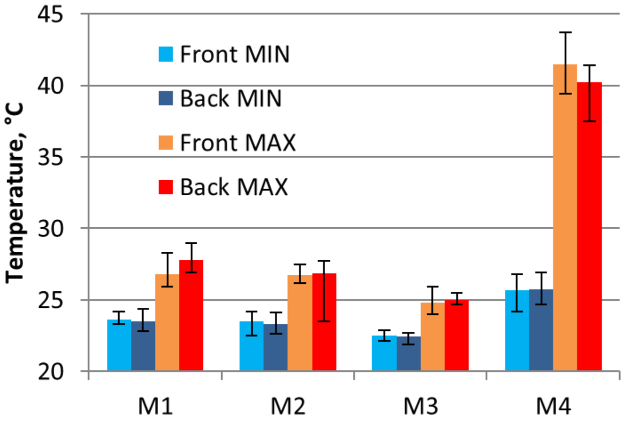

Fig. 6. The graphs of average minimum and maximum temperature measurements on the surface

The highest temperature on the whole surface of the briquettes was obtained for mixture M4 (EAFD mixture). It amounted to 41.5 °C and was 20.2 °C higher than the ambient temperature. The lowest maximum temperature was obtained for mixture M3. The difference in maximum temperatures between the materials was 16.5 °C. The lowest minimum temperature was obtained for mixture M3. It was still higher than the ambient temperature by 1.1 °C. In this case, a relatively low unit compacting pressure during compaction can be expected.

3.3. Temperature distribution on briquette surfaces

The results of the temperature distribution on the briquette front surfaces for each type of briquette are presented in Fig. 7. As in the case of other compaction units, the temperature on the surface of the briquettes turned out to be non-uniform. The highest temperature is obtained in the upper middle part of the briquette. In this part of the briquette from the front side, one can therefore expect the greatest packing of the material, resulting from the greatest compacting pressure acting at this point [46]. These results coincide with the simulation tests carried out for briquetting of fine-grained materials using the discrete element method [50]. The temperature distribution curve for material M4 differs from the other curves. In point 2, the temperature is not higher than in point 1, which is the case with other curves. It can

DOI 10.2478/ama-2022-0040

be assumed that the volume of the moulding cavities used for this mixture is too small. The mixture is overpressed, the structure of the briquettes is destroyed and defects appear in the briquettes. This can be seen in Fig. 8.

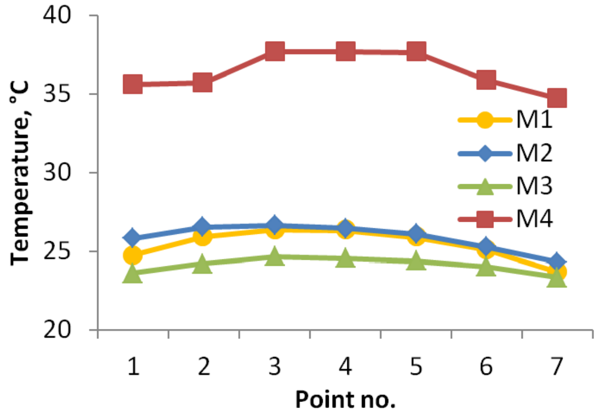

Fig. 7. The temperature distribution on the front side of the briquette surfaces

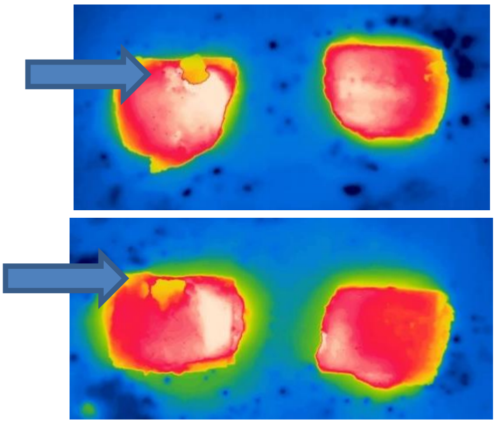

Fig. 8. Thermographic image with the damaged structure of the briquette from M4 mixture

The results of the temperature distribution on the briquette back surfaces are presented in Fig. 9.

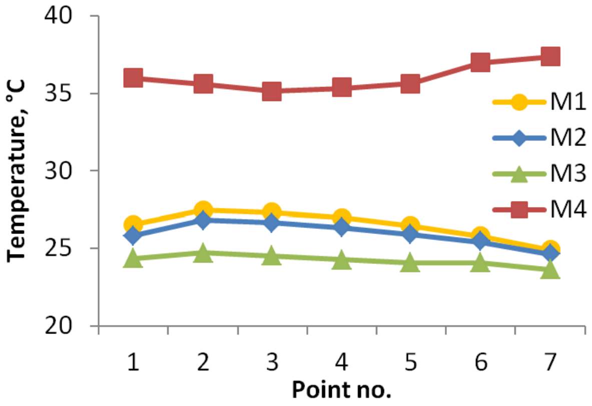

Fig. 9. The temperature distribution on the back side of briquette surfaces

For M1, M2 and M3 mixtures, the highest temperature on the back side of the briquette was obtained in point 2. The temperature distribution for these materials takes the form of a parabola directed downwards. This means that the minimum temperatures are at the top and bottom of the briquette. The M4 material, in turn, has the highest recorded temperatures in the upper and lower parts of the briquette, differently for the remaining mixtures. This is probably owing to the volume of the cavity being too small for this type of mixture, and its overpressing is caused by the exertion of excessive pressure on the material, which was also noticed on the front side of the briquette. No defects were noticed on this side of the briquettes. The difference in the temperature distribution between the M1 and M2 mixes, i.e. mixes with the same composition but with different moisture content, proved that the moisture had an influence on the unit pressure during briquette formation [51].

4. CONCLUSION

The conducted research proved that thermographic methods can be indirectly used to describe the phenomena occurring in the roller press compacting unit as described by the patent PL 222229 B1. As experience shows, the method requires special preparation of the test stand to eliminate the influence of undesirable external factors, such as radiation sources, that may prevent the reliable processing of the obtained results.

For M1, M2 and M3 mixtures, similar results of temperature distributions were obtained as in the case of the classic compaction system for the production of saddle-shaped and pillow-shaped briquettes. The highest obtained temperature was obtained in the middle-upper part of the briquette. For the EAFD mixture, the temperature distribution curves turned out to be different. This is probably due to the volume of the forming cavities being too small for this type of material. Additionally, thermographic tests showed defects in briquettes made of M4 mixture. This confirms the hypothesis that thermography as an indirect method can be used to test the correctness of the selection of the type of the roller press compaction unit and the volume of briquettes.

In the authors' opinion, the tests are utilitarian, as they show the possibility of using thermographic tests to assess the quality of briquettes in industrial conditions.

Further research is planned to determine the correlation between the local temperature of the material and the compacting pressure exerted there. A special stand has been developed for this purpose.

REFERENCES

1. Świderski W, Miszczak M, Szabra D. Zastosowanie pomiarów termowizyjnych w badaniach dysz grafitowych stosowanych układach napędowych przeciwlotniczych pocisków rakietowych krótkiego zasięgu. Biuletyn Wojskowej Akademii Technicznej. 2008;57(3): 285-293.
2. Duchaczek A, Mańko Z. Próba zastosowania termowizji w badaniach zmęczeniowych dźwigarów stalowych w mostach wojskowych. Zeszyty Naukowe / Wyższa Szkoła Oficerska Wojsk Lądowych im. gen. T. Kościuszki. 2009;(3): 125-135.
3. Al-Habaibeh A, Hawas A, Hamadeh L, Medjdoub B, Marsh J, Sen A. Enhancing the sustainability and energy conservation in heritage buildings: The case of Nottingham Playhouse. Frontiers of Architectural Research. 2022;11(1): 142-160. https://doi.org/10.1016/j.foar.2021.09.001

4. Silva GP, Batista PIB, Povóas YV. The usage of infrared thermography to study thermal performance of walls: a bibliographic review. Revista ALCONPAT. 2019;9(2): 117-129. https://doi.org/10.21041/ra.v9i2.341
5. Tomita K, Chew MYL. A Review of Infrared Thermography for Delamination Detection on Infrastructures and Buildings. Sensors. 2022;22(2): 423. https://doi.org/10.3390/s22020423
6. Branco JHL, Branco RLL, Siqueira TC, de Souza LC, Dalago KMS. Andrade A. Clinical applicability of infrared thermography in rheumatic diseases: A systematic review. Journal of Thermal Biology, 2022, 104, 103172 https://doi.org/10.1016/j.jtherbio.2021.103172
7. Kaźmierska B, Sobiech KA, Demczuk-Włodarczyk E, Chwałczyńska A. Thermovision assessment of temperature changes in selected body areas after short-wave diathermy treatment. Journal of Thermal Analysis and Calorimetry. 2021: 1-8 https://doi.org/10.1007/s10973-021-11136-z
8. Damijan Z, Uhryński A. Systemic cryotherapy influence of low temperatures on selected physiological parameters. Acta Physica Polonica A 2012;121(1-A): 38-41. http://dx.doi.org/10.12693%2FAPhysPolA.121.A-38
9. Damijan Z, Uhryński A. The effect of general low frequency vibration on energy balance of a human being. Acta Physica Polonica A. 2013;123(6): 970-973. doi: 10.12693/APhysPolA.123.970
10. Damijan Z, Uhryński A. The influence of driver's working environment on thermical changes of their organism. Acta Physica Polonica A. 2010;118(1): 35-40. doi: 10.12693/APhysPolA.118.35
11. Molenda J, Charchalis A. Using thermovision for temperature measurements during turning process. Journal of KONES Powertrain and Transport. 2018;25(4): 293-298. https://doi.org/10.5604/01.3001.0012.4803
12. Bartoszuk M. Thermovision measurements of temperature on the tool-chip upper side in turning of aisi 321 steel. Technical Sciences. 2020;23(1): 69-80. https://doi.org/10.31648/ts.5177
13. Piecuch G, Madera M, Żabiński T. Diagnostics of welding process based on thermovision images using convolutional neural network. IOP Conf. Series: Materials Science and Engineering. 2019;710(1): 012042. doi: 10.1088/1757-899X/710/1/012042
14. Nowacki J, Wypych A. Application of thermovision method to welding thermal cycle analysis. The Journal of Achievements in Materials and Manufacturing Engineering. 2010;40(2): 131-137.
15. Struzikiewicz G, Sioma A. Application of infrared and high-speed cameras in diagnostics of CNC milling machines: case study. Photonics Applications in Astronomy, Communications, Industry, and High-Energy Physics Experiments. 2019;11176: 111760c. https://doi.org/10.1117/12.2536679
16. Fidal M. Identification of machine technical state on the basis of fourier analysis of infrared images. Diagnostics And Structural Health Monitoring. 2011;2(58): 25-30.
17. Michalik P, Zajac J. Use of thermovision for monitoring temperature conveyor belt of pipe conveyor. Applied Mechanics and Materials. 2014;683: 238-42. https://doi.org/10.4028/www.scientific.net/AMM.683.238
18. Baranowski P, Damaziak K, Malachowski J, Mazurkiewicz L, Polakowski H, Piatkowski T, Kastek M. Thermovision in the validation process of numerical simulation of braking. Metrology and Measurement Systems. 2014;21(2): 329-340. http://dx.doi.org/10.2478%2Fmms-2014-0028
19. Jakubek B, Grochalski K, Rukat W, Sokol H. Thermovision measurements of rolling bearings. Measurement. 2022;189: 110512. https://doi.org/10.1016/j.measurement.2021.110512
20. Janura R, Gutten M, Korenciak D, Sebok M. Thermal processes in materials of oil transformers. Diagnostic of Electrical Machines and Insulating Systems in Electrical Engineering (DEMISEE). 2016: 81-84. doi: 10.1109/DEMISEE.2016.7530470
21. Simko M, Chupac M, Gutten M. Thermovision measurements on electric machines. International Conference on Diagnostics in Electrical Engineering (Diagnostika). 2018: 1-4. doi: 10.1109/DIAGNOSTIKA.2018.8526033
22. Wylecial T, Urbaniak D. Research on thermal contact resistance in a bed of steel square bars using thermovision. Acta Physica Polonica A. 2019;135(2): 263-269. doi: 10.12693/APhysPolA.135.263
23. Sharkeev Y, Vavilov V, Skripnyak V.A, Belyavskaya O, Legostaeva E, Kozulin A, Chulkov A, Sorokoletov A, Skripnyak VV, Eroshenko A, Kuimova M. Analyzing the deformation and fracture of bioinert titanium, zirconium and niobium alloys in different structural states by the use of infrared thermography. Metals. 2018; 8(9): 703. https://doi.org/10.3390/met8090703
24. Heinz D, Halek B, Krešák J, Peterka P, Fedorko G Molnár V. Methodology of measurement of steel ropes by infrared technology. Engineering Failure Analysis. 2022;133: 105978. https://doi.org/10.1016/j.engfailanal.2021.105978
25. Pawlak A, Rozanski A, Galeski A. Thermovision studies of plastic deformation and cavitation in polypropylene. Mechanics of Materials. 2013;67: 104-118. https://doi.org/10.1016/j.mechmat.2013.07.016
26. Koštial P, Ružiak I, Jonšta Z, Kopal I, Hrehuš R, Kršková J. Experimental method for complex thermo-mechanical material analysis. International Journal of Thermophysics. 2010;31: 630–636. https://doi.org/10.1007/s10765-010-0745-5
27. Pieklak K, Mikołajczyk Z. Strength tests of 3D warp-knitted composites with the use of the thermovision technique. Fibres & Textiles in Eastern Europe. 2011;19(5 (88)): 100-105.
28. Grochalski K, Peta K. Diagnostic methods of detecting defects within the material with the use of active infrared thermovision. Archives of Mechanical Technology and Materials. 2017:37(1): 41-44. doi: 10.1515/amtm-2017-0006
29. Bazaleev NI, Bryukhovetskij VV, Klepikov VF, Litvinenko VV. Thermovision acoustic thermography construction materials defectoscopy. Voprosy Atomnoj Nauki i Tekhniki. Fizika Radiatsionnykh Povrezhdenij i Radiatsionnoe Materialovedenie. 2011;2(97/72): 178-185.
30. Wierzbicki Ł, Stabik J, Wróbel G, Szczepanik M. Efficiency of two non-destructive testing methods to detect defects in polymeric materials. Journal of Achievements in Materials and Manufacturing Engineering 2010;38(2): 163-170.
31. Durka T, Stefanidis G, Van Gerven T, Stankiewicz A, On the accuracy and reproducibility of fiber optic (FO) and infrared (IR) temperature measurements of solid materials in microwave applications. Measurement Science and Technology. 2010;21(4): 045108. http://dx.doi.org/10.1088/0957-0233/21/4/045108
32. Lahiri BB, Bagavathiappan S, Reshmi PR, Philip J, Jayakumar T, Raj B. Quantification of defects in composites and rubber materials using active thermography. Infrared Physics & Technology. 2012;55(2-3): 191-199. https://doi.org/10.1016/j.infrared.2012.01.001
33. Różański L, Ziopaja K. Detection of material defects in reinforced concrete slab using active thermography. Measurement Automation Monitoring. 2017;63(3): 82-85.
34. Miękina W, Madura H. Podstawy teoretyczne pomiarów termowizyjnych. Pomiary termowizyjne w praktyce. Agenda Wydawnicza Paku. 2004: 10-26.
35. Lepiarczyk D, Uhryński A. Thermo-Vision Analysis of Iron Foundry Production Process Concerning Secondary Usage of Heat. Polish Journal of Environmental Studies. 2014;23(3): 1017-1023.
36. Żaba K, Nowak S, Kwiatkowski M, Nowosielski M, Kita P, Sioma A. Application of non-destructive methods to quality assessment of pattern assembly and ceramic mould in the investment casting elements of aircraft engines. Archives of Metallurgy and Materials. 2014;59(4): 1517-1525. doi: 10.2478/amm-2014-0250
37. Tor-Świątek A, Samujło B. Use of thermo vision research to analyze the thermal stability of microcellular extrusion process of poly(vinyl chloride). Maintenance and Reliability. 2013;15(1): 58–61.
38. Hynek M, Votapek P. Thermal analysis of tyre curing process. Engineering mechanics, 17th international conference. Prague. 2011: 223-226.
39. Kašiković N, Novaković D, Milić N, Vladić G, Zeljković Ž, Stančić M. Thermovision and spectrophotometric analysis of ink volume and material characteristics influence on colour changes of heat treated printed substrates. Technical Gazette. 2015;(22)1: 33-41. doi: 10.17559/TV-20130928115500
40. Michalak M. Non-contact tests of thermal properties of textiles, Part 1. (Bezkontaktowe badania właściwości cieplnych wyrobów włókienniczych. Cz. 1.) Przegląd Włókienniczy - Włókno, Odzież, Skóra. 2010; 2: 31-33.

41. Litstera JD, Omara C, Salman AD, Yua M, Weidemannb M, Schmidt A. Roller compaction: Infrared thermography as a PAT for monitoring powder flow from feeding to compaction zone. International Journal of Pharmaceutics. 2020;578: 119114. https://doi.org/10.1016/j.ijpharm.2020.119114
42. Kostencki P, Stawicki T, Królicka A. Wear of Ploughshare Material With Regards to the Temperature Distribution on the Rake Face When Used in Soil. *Journal of Tribology*. 2022;144(4): 041704. https://doi.org/10.1115/1.4053586
43. Yu M, Omar C, Weidemann M, Schmidt A, Litster JD, Salman AD. Roller compaction: Infrared thermography as a PAT for monitoring powder flow from feeding to compaction zone. Int J Pharm [Internet]. 2020;578(119114):119114. Available from: https://www.sciencedirect.com/science/article/pii/S0378517320300983
44. Bembenek M, Krawczyk J, Pańcikiewicz K. The wear on roller press rollers made of 20Cr4/1.7027 steel under conditions of copper concentrate briquetting. Materials (Basel) [Internet]. 2020 [cited 2022 Jun 14];13(24):5782. Available from: https://www.mdpi.com/1996-1944/13/24/5782
45. Bembenek M. Exploring efficiencies: Examining the possibility of decreasing the size of the briquettes used as the batch in the electric arc furnace dust processing line. Sustainability [Internet]. 2020 [cited 2022 Jun 14];12(16):6393. Available from: https://www.mdpi.com/2071-1050/12/16/6393
46. Bembenek M, Krawczyk J, Frocisz Ł, Śleboda T. The analysis of the morphology of the saddle-shaped bronze chips briquettes produced in the roller press. Materials (Basel) [Internet]. 2021 [cited 2022 Jun 14];14(6):1455. Available from: https://www.mdpi.com/1996-1944/14/6/1455
47. Bembenek M, Uhryński A. Analysis of the temperature distribution on the surface of saddle-shaped briquettes consolidated in the roller press. Materials (Basel) [Internet]. 2021 [cited 2022 Jun 14];14(7):1770. Available from: https://www.mdpi.com/1996-1944/14/7/1770
48. Uhryński A, Bembenek M. The thermographic analysis of the agglomeration process in the roller press of pillow-shaped briquettes. Materials (Basel) [Internet]. 2022 [cited 2022 Jun 14];15(8):2870. Available from: https://www.mdpi.com/1996-1944/15/8/2870
49. Hryniewicz M., Janewicz A . Briquetting device. Polish patent, PL 222229 B1, July 29, 2016
50. Bembenek M, Buczak M, Baiul K. Modelling of the Fine-Grained Materials Briquetting Process in a Roller Press with the Discrete Element Method. Materials. 2022; 15(14):4901. https://doi.org/10.3390/ma15144901
51. Bembenek M. Exploring Efficiencies: Examining the Possibility of Decreasing the Size of the Briquettes Used as the Batch in the Electric Arc Furnace Dust Processing Line. Sustainability. 2020; 12(16):6393. https://doi.org/10.3390/su12166393

We would like to thank Mr. Gabriel Grzebinoga for his help during the research.

Michał Bembenek: https://orcid.org/0000-0002-7665-8058

Andrzej Uhryński: https://orcid.org/0000-0001-8832-7873

sciendo

DOI 10.2478/ama-2022-0041

VORTEX-TYPE GRANULATION MACHINES: TECHNOLOGICAL BASIS OF CALCULATION AND IMPLEMENTATION ROADMAP

Artem ARTYUKHOV[*], **Jan KRMELA**[**], **Vladimíra KRMELOVÁ**[***], **Dastan OSPANOV**[****]

[*]Academic and Research Institute of Business, Economics and Management, Department of Marketing,
Sumy State University, 2, Rymskogo-Korsakova St., 40007 Sumy, Ukraine
[**]Faculty of Industrial Technologies in Púchov, Department of Numerical Methods and Computational Modeling,
Alexander Dubček University of Trenčín, Ivana Krasku 491/30, 02001 Púchov, Slovakia
[***]Faculty of Industrial Technologies in Púchov, Department of Materials Technologies and Environment,
Alexander Dubček University of Trenčín, Ivana Krasku 491/30, 02001 Púchov, Slovakia
[****]Faculty of Engineering, Department of Transport Engineering and Technology,
Saken Seifullin Kazakh Agrotechnical University, Zhengis Ave 62, 010000, Nur-Sultan, Kazakhstan

a.artyukhov@pohnp.sumdu.edu.ua, jan.krmela@tnuni.sk, vladimira.krmelova@tnuni.sk, d.ospanov@kazatu.kz

received 1 July 2022, revised 18 September 2022, accepted 18 September 2022

Abstract: This work is devoted to describing the technological foundations and the main stages of calculating granulation machines with active hydrodynamic modes. The optimisation criterion is substantiated when choosing the design of the granulation machine. The work uses methods of analysis and synthesis, search for cause-and-effect relationships, theoretical and computer modelling, and experimental studies. The nodes of the vortex granulator directly influence the formation of a vortex fluidised bed, and the directional movement of granules of various sizes are determined. A technique for carrying out a computer simulation of the hydrodynamic operating conditions of a granulation machine in various operating modes with an assessment of the quality of granulated products (e.g., the production of porous ammonium nitrate) is proposed. The results of a computer simulation of the process of formation of a vortex fluidised bed are presented. A variant of the solution for developing an automation scheme for a vortex-type granulation machine is shown. A roadmap for introducing granulation technology in vortex-type granulation machines is described with details of the main stages. The prospects for improving the design of a vortex-type granulation machine and optimising the operation of a granulation plant to produce porous ammonium nitrate are outlined.

Key words: granulation machine, optimisation criterion, computer simulation, automation scheme, roadmap

1. INTRODUCTION

The production of granular products in various industries (chemical, pharmaceutical, food, mining, etc.) is implemented in various ways [1–3] in devices with several designs [4–7]. The choice of a method for obtaining a granulated product and the instrumentation of this process depend on the type of product, the productivity of the granulation plant, and the scientific justification for the use of one design solution or another [8]. Before starting production, a comparative analysis of methods and devices for granulation is carried out, which encompasses a computation of their technical and economic aspects, an assessment of the energy efficiency and environmental safety concerns involved, and ascertainment of the degree up to which the approach to granulation in question is in compliance with sustainable development goals.

One of the most versatile non-pressure granulation methods is implementing the process in a fluidised bed [9, 10] with a wide range of granulation devices [11]. Considering the effectiveness of such a hydrodynamic system in obtaining a wide range of granular products, fluidised bed granulators are a reliable solution for many industries. At the same time, it is necessary to constantly improve the design of granulators to stabilise the granulation process and create conditions for controlling the movement of granules in the working space of the device [12]. The second factor allows, with a high degree of accuracy, to calculate the residence time of the granules in the working space of the apparatus and, due to the variation in the design of the granulator, achieve optimisation according to the criterion 'minimum residence time of the granules in the device'.

One way to effectively control the directional movement of granules in the working space of the granulator is to use specific configurations of the fluidised bed. The vortex granulators [13] have shown their effectiveness and the ability to create a directional movement of the fluidised bed [14].

The use of fluidised bed granulators requires constant hardware design improvement and increased specific productivity. One of the methods of reducing the size of granulation equipment is to increase the relative velocity of the continuous and dispersed phases. This can be achieved by using vortex and highly turbulent flows in the devices of the suspended layer. The increase in productivity (phase load) for devices with such flow organisation leads to a smaller relative increase in their overall size and energy consumption for granulation.

Determination of the structure of the fluidised bed and hydrodynamic characteristics of the flow in vortex granulators, development of recommendations and methods of engineering calculation, and design of devices with predictable parameters taking into account the prospects for low-capacity and small-scale production of granular products and the implementation of new methods and equipment for granulation constitute an urgent scientific and practical task.

Creating a reliable calculation algorithm for vortex granulators is an essential step in their wide industrial implementation. It is possible to control the residence time of the granules in the working space of the vortex apparatus based on a description of the hydrodynamic conditions for the movement of flows [15]. The approach to the control process takes into account the technological characteristics of the process (the main characteristic is the velocity of the gas flow, which determines the range of stable existence of the fluidised bed), as well as the design features of the granulator, which determine the law of distribution of the gas flow velocity. This work aims to analyse the influence of the design of some nodes of the vortex granulator on the features of the movement of single-phase and two-phase flows.

2. DESCRIPTION OF THE VORTEX GRANULATOR'S DESIGN AND THE CONDITIONS FOR DESIGNING ITS INDIVIDUAL UNITS

The design of the vortex granulator is shown in Fig. 1. The principle of its action is as follows.

A heat transfer agent is fed through the pipe into the device in the lower cylindrical section of the granulator. It flows to the vortex gas-distributing unit. The heat transfer agent is twisted around the vertical axis of the device and acquires a spiral motion. The vortex axisymmetrical flow of the heat transfer agent moves up the inner cone space towards the material. Simultaneously the fluid material (solution or fusion) is fed into the formed vortex flow of the heat transfer agent through the pipe in the upper part of the outing case into the spray unit. The fusion jet flows out of the spraying unit and is broken into the spheric granules. The created granules make contact with the axisymmetric vortex flow of the heat transfer agent, become cool, are crystallised and come to the internal surface of the inner cone. Depending on the obtained size, granules are classified into large and small fractions due to the whirl and axis velocity changes in the axisymmetric vortex flow of the heat transfer agent, and these changes take place only as a function of the variation in the height of the inner cone. Small fraction granules are taken by the vortex flow of the heat transfer agent, move to the upper internal cone intersection and discharge from the active volume of the device through the annular space. In the annular space, the small fraction granules move down under the gravity force and get down to the lower intersection of the outing case. In the lower part of the outing case, these granules come to the depression zone. It is formed around the gas flow jet, which is fed through the pipe in the central part of the granulator (it is not shown on the scheme). Granules are picked up by this jet and thrown to the central part of the inner cone workspace into the vortex weighted layer core. The fusion that falls on the surface of the small granules is crystallised. Therefore, the size of the granules increases. The large fraction does not leave the device's workspace, and granules circulate in the inner cone and move along its intersection, as far as they are growing and increasing. When the intended size is achieved, granules fall on the surface of the inner cone, pass through the vortex gas-distributing unit and are output from the device. The spent heat transfer agent is driven from the inner cone through the proper pipe [16].

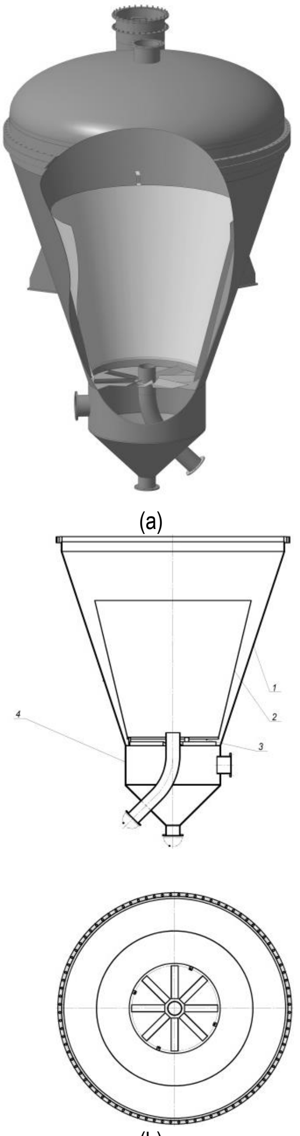

(a)

(b)

Fig. 1. The design of the vortex granulator (authors' elaboration): (a) schematic diagram (with cover and connectors); (b) elements of the workspace (granulation zone with cover and connectors); 1 – main body; 2 – inner case; 3 – gas flow distributor; 4 – swirler

A practical interest that the present research is concerned with is the nodes of the working space of the vortex granulator, which directly impact the distribution of the gas flow velocity in the apparatus. According to Yang [17], the range of stable existence of a fluidised bed is limited by two critical velocities:

- gas flow rate, which corresponds to the beginning of the fluidisation of the granules; and
- gas flow rate, which corresponds to the mode of entrainment of granules from the working space of the vortex granulator.

It should be noted that the vortex fluidised bed is a polydisperse system, and design solutions should be used in the working space of the vortex granulator, which will provide a different force effect on granules of various sizes. The simplest solution is to create a granulator with a variable cross-sectional area. Due to such a constructive solution, an efficient separation of granules into fractions is ensured (with the possibility of creating different heat treatment conditions for each fraction), as well as the movement of a specific fraction to the required point in the working space of the granulator. The scheme of the internal circulation of small granules (seeding agent) and the distribution of granules by size (classification) is shown in Fig. 2.

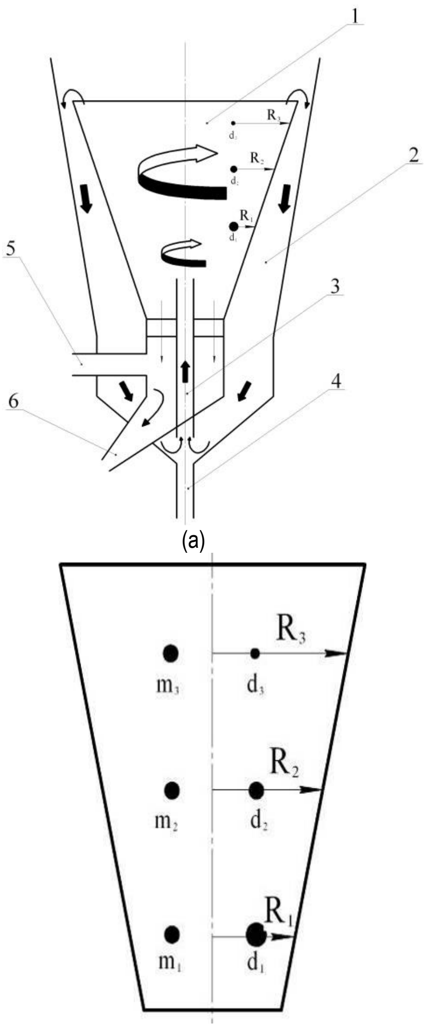

(a)

(b)

$R_1 > R_2 > R_3$

$m_1 > m_2 > m_3$

Fig. 2. Scheme of the working space of the vortex granulator (authors' elaboration): (a) organization of flows' motion (b) physical model of classification; 1 – zone of granulation and classification of granules; 2 – zone of internal circulation of the seeding agent; 3 – input of internal recycle; 4 – heat carrier for ejection; 5 – heat carrier for creating a vortex fluidised bed; 6 – withdrawal of commercial fraction granules; R_i – radius of granule; m_i – mass of granule

The distribution of fractions in the working space of the vortex granulator is significantly affected by the swirl mode of the gas flow and the degree of uniformity of the distribution of the gas flow under the swirler.

After the coolant passes through the supply pipe, it does not have time to be evenly distributed under the swirler; as a result of this, the coolant does not pass the entire cross-section of the swirler, and not all overclocking elements of the swirler take part in the vortex motion of the coolant. This causes uneven spiral motion of the granules, which causes uneven application of the film solution or melt.

This pattern/phase of the granules' motion is characterised/accompanied by the emergence of stagnant zones in the lower part of the working space (mainly on the periphery) and the lack of intense lateral mixing in the same part of the device. The presence of stagnant zones and the absence of lateral mixing lead to temperature inhomogeneities in the suspended layer, which reduce the uniformity of solid film formation from solution or melt on the granule surface and degrades the strength of the finished product and its monodispersity [16].

A constructive solution is proposed that allows the formation of a stable vortex gas flow (Fig. 3).

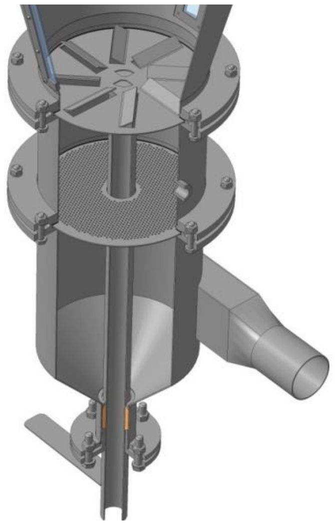

Fig. 3. The design of the swirler and gas flow distributor (authors' elaboration)

When installing the distribution element in the form of a failed perforated lattice in the middle part of the annular pellet trap, it becomes possible to redistribute the coolant throughout the cross-section of the annular pellet trap until it enters the vortex gas distribution unit. In this case, the coolant enters the vortex gas distribution node throughout its cross-section, reducing the likelihood of stagnant zones in the lower part of the working space and significantly intensifying the granules' lateral mixing. Reduction of stagnant zones and intensification of lateral mixing of granules lead to equalisation of temperature fields of the material in the suspended layer, which allows applying a film of solution or melt and granulation under the same thermodynamic conditions for all granules. On the other hand, the presence, in the design of the claimed device, of the distribution element in the form of a failed perforated lattice in the middle part of the annular pellet trap simplifies the removal of granules due to their uniform redistribution in the annular granules space.

This optimisation of the device for granulation in a fluidised bed reduces the equipment's size and energy consumption. It increases the degree of monodispersion of the particle size distribution of the resulting product [16].

3. COMPUTER SIMULATION OF THE PROCESS OF A VORTEX FLUIDISED BED FORMATION

Computer modelling has become a widespread means of studying the main processes and apparatuses of chemical production [18–20]. The use of computer simulation makes it possible to reduce the cost of experimental research and select the optimal equipment design before creating a scientific sample. Another advantage of computer simulation involves fixing the dynamics of changes in a particular parameter over time. Based on the choice of the optimal design of the nodes of the vortex granulator, computer simulation clearly shows the process of formation of the vortex fluidised bed. The distribution of granules in the working space of the vortex granulator, the intensity of the swirl of the gas flow (significant: evolution in time) and the presence of stagnant zones are determined by analysing computer simulation data.

The simulation of hydrodynamic processes in modern software products is based on the numerical solution of a system of equations that describe the most general case of the movement of a liquid medium. These are the Navier–Stokes and flow continuity equations [21].

Computer simulation of flow motion with the help of software products is based on the finite-volume method of solving the system of equations of the hydrodynamics of solid and dispersed phases and the use of a rectangular adaptive mesh with local grinding depending on the initial conditions for modelling.

Direct modelling of turbulent flows by numerically solving the Navier–Stokes equations written for instantaneous velocities is still complicated, and in addition, as a rule, not instantaneous but time-averaged values of velocities are of interest. Thus, the Reynolds equations are used for the analysis of turbulent flows instead of the Navier–Stokes equations.

Thus, computer simulation of the movement of single-phase and two-phase flows is based on solving the system of differential Reynolds equations and the continuity of the flow [21], and the system of differential equations of particle motion [22], considering the constraint of the flow of granules in a vortex fluidised bed. The modelling process consists of the following steps [21]:

– creation of a geometric (three-dimensional solid) model of the working area, where it is planned to study the hydrodynamics of flow movement;
– construction of the computational grid;
– choice of the mathematical model of calculation; and
– carrying out the calculation.

The dynamics of a vortex fluidised bed formation are shown in Fig. 4.

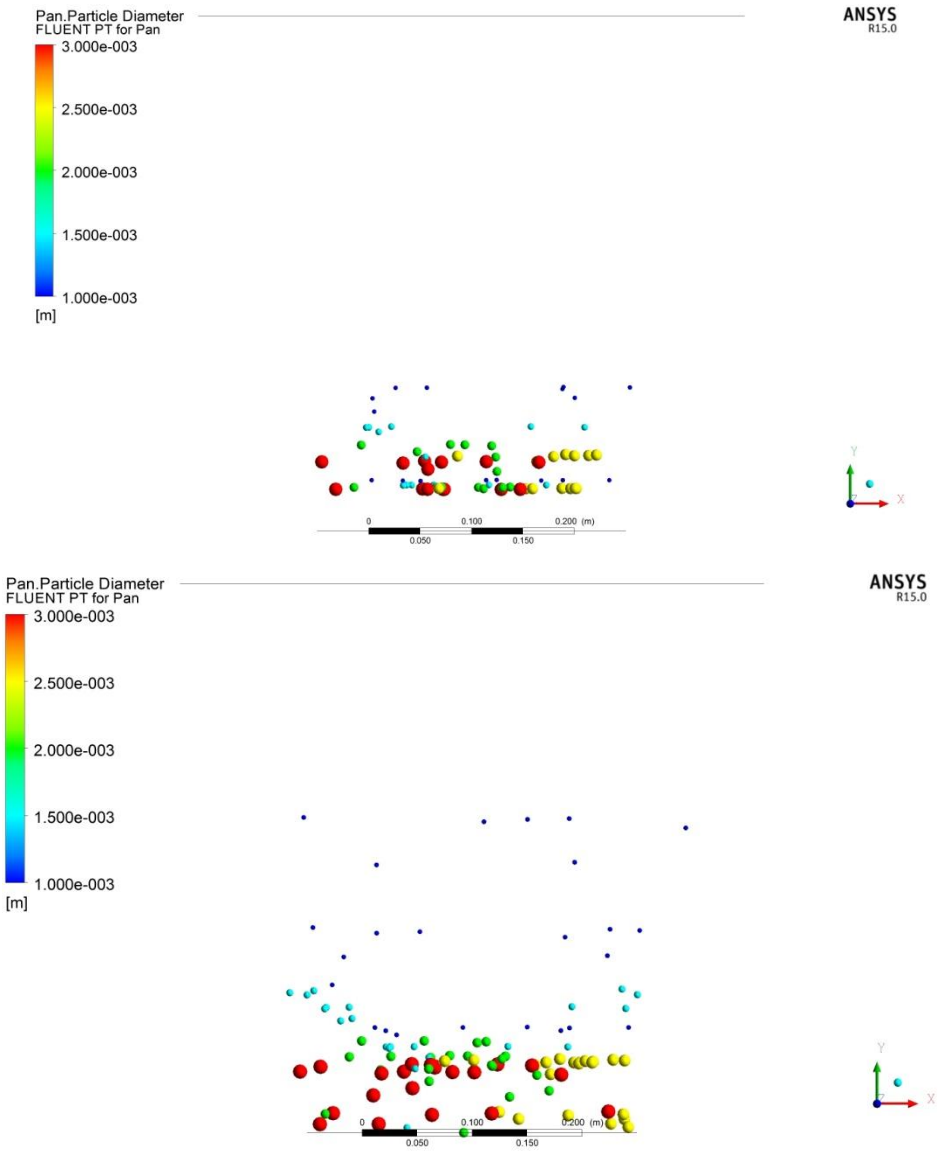

Fig. 4a. Dynamics of a vortex fluidised bed formation (authors' simulation results): formation of a vortex fluidised bed

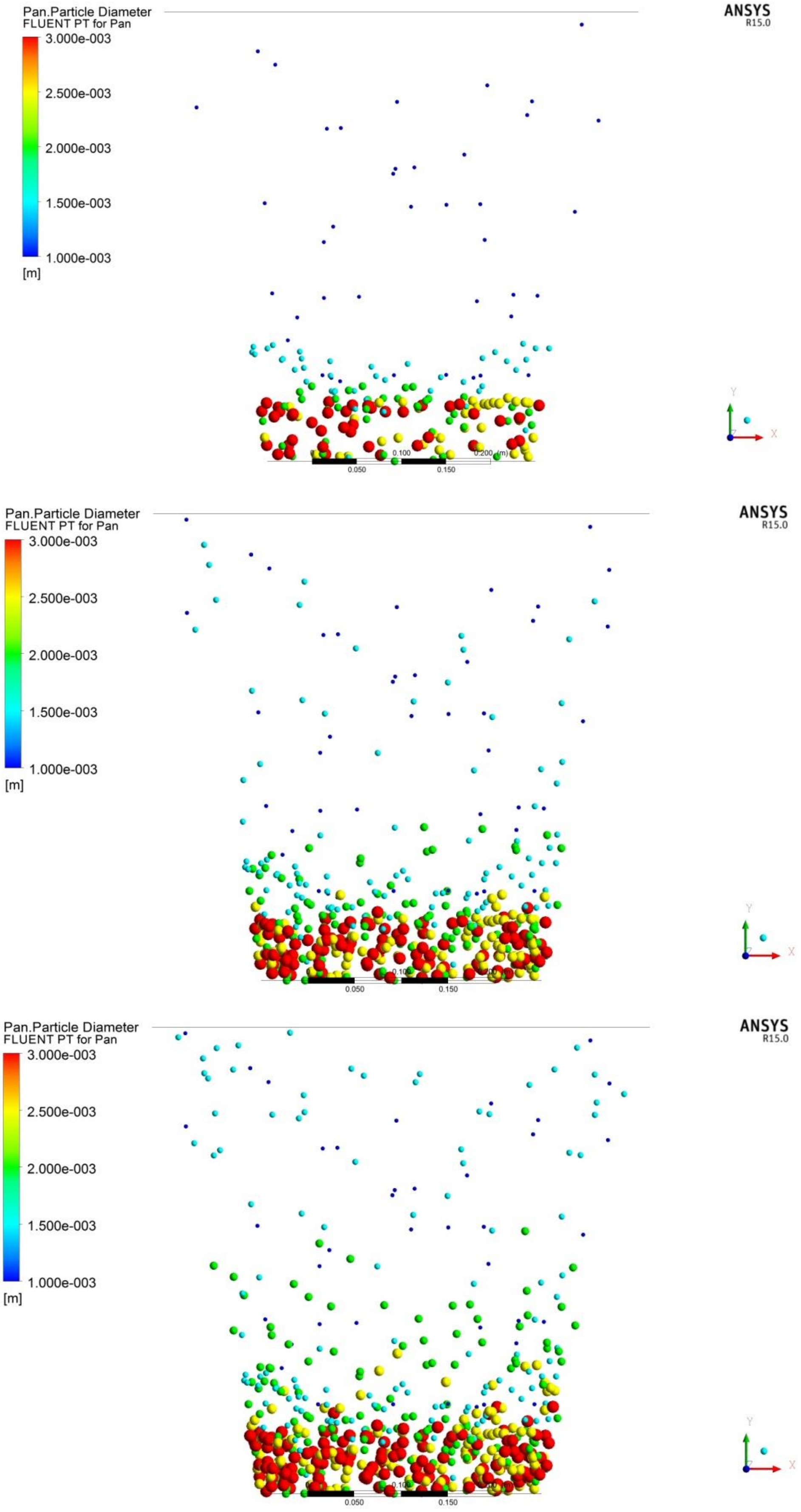

Fig. 4b. Dynamics of a vortex fluidised bed formation (authors' simulation results): creation of an 'active' zone above the gas distribution device

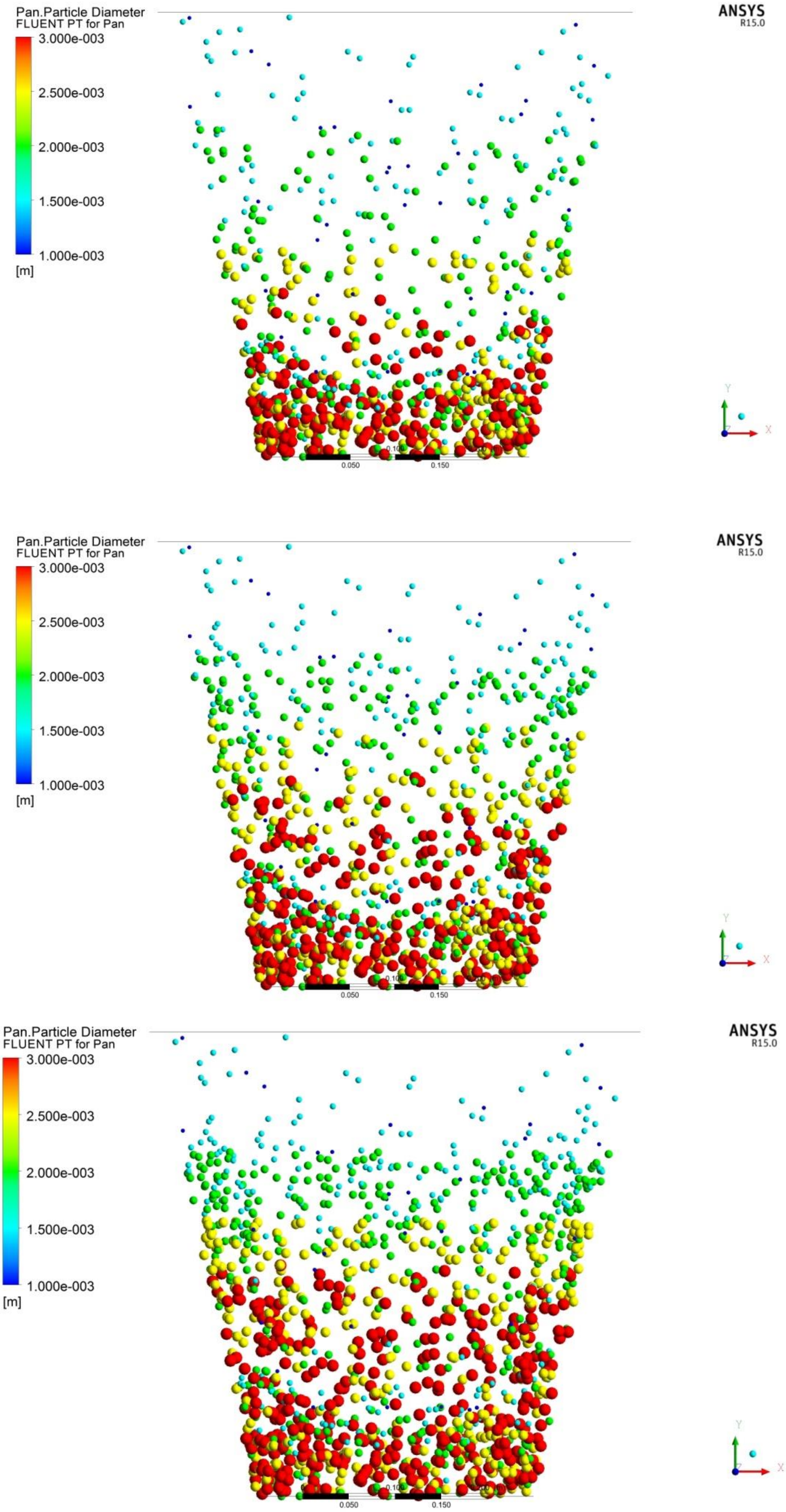

Fig. 4c. Dynamics of a vortex fluidised bed formation (authors' simulation results): developed vortex fluidised bed mode

Analysis of simulation results allows the authors to draw the following conclusions:

- with an increasing degree of compression of the flow, there is a broader range of fractions at a certain height;
- with increasing degree of compression of the flow, the number of the main (corresponding to this calculated height) fraction increases; and
- the height of the vortex granulator decreases the content of the fraction from another range.

4. INDUSTRIAL IMPLEMENTATION OF THE RESULTS OF SIMULATION AND OPTIMISATION OF THE VORTEX GRANULATOR'S DESIGN

The process of introducing a vortex granulator based on the optimisation calculation of the design of its main units can be represented as the following algorithm, developed by the present authors:

- creation of a roadmap for the implementation of equipment;
- layout of the main components of the granulator;
- layout of the main equipment of the unit;
- development of a scheme for automated control of the unit; and
- product testing.

The vortex granulator implementation roadmap evaluates various aspects of a product's entry into the market. The use of the Technology & Commercialization Readiness Level Calculator [23] as an evaluation tool (Fig. 5 a) is suggested. Sequential selection of the development readiness level according to various criteria enables construction of the resulting analysis diagram (Fig. 5 b).

A set of activities is identified, which are intended to be carried out in the future to ensure that the desired level of readiness is achieved for each of the criteria. Below is an example of such activities for the criterion 'Product development'.

Their layout completes the choice of the design of individual nodes of the vortex granulator into a common assembly unit (Figs. 1 and 6). All corners and transitions between the nodes of the structure, where possible, are rounded, which gives a plastic and aesthetic appearance to the whole complex shape of the vortex granulator. The proportionality of each of the nodes of the vortex granulator infuses its appearance with integrity and conciseness. To ensure the correct functioning of the technological departure, it has been ensured that all units incorporate the minimum necessary requirements, are located in easily accessible places and do not interfere with the inspection and repair of industrial design.

When placing the equipment, it is necessary to consider the following technological requirements: ease of maintenance of the equipment and the possibility of dismantling the apparatus and its parts during repairs; ensuring the shortest pipelines between devices; a rational solution for in-plant transport. At the same time, building codes, requirements for natural light, rules and regulations on safety and labour protection, and sanitary and fire restrictions should be observed.

When choosing a layout option for technological equipment, it is necessary to consider the features of the technological process and the properties of the feedstock and the production product. The layout of the main technological equipment of the granulation plant is shown in the example of the production of porous ammonium nitrate (Fig. 7).

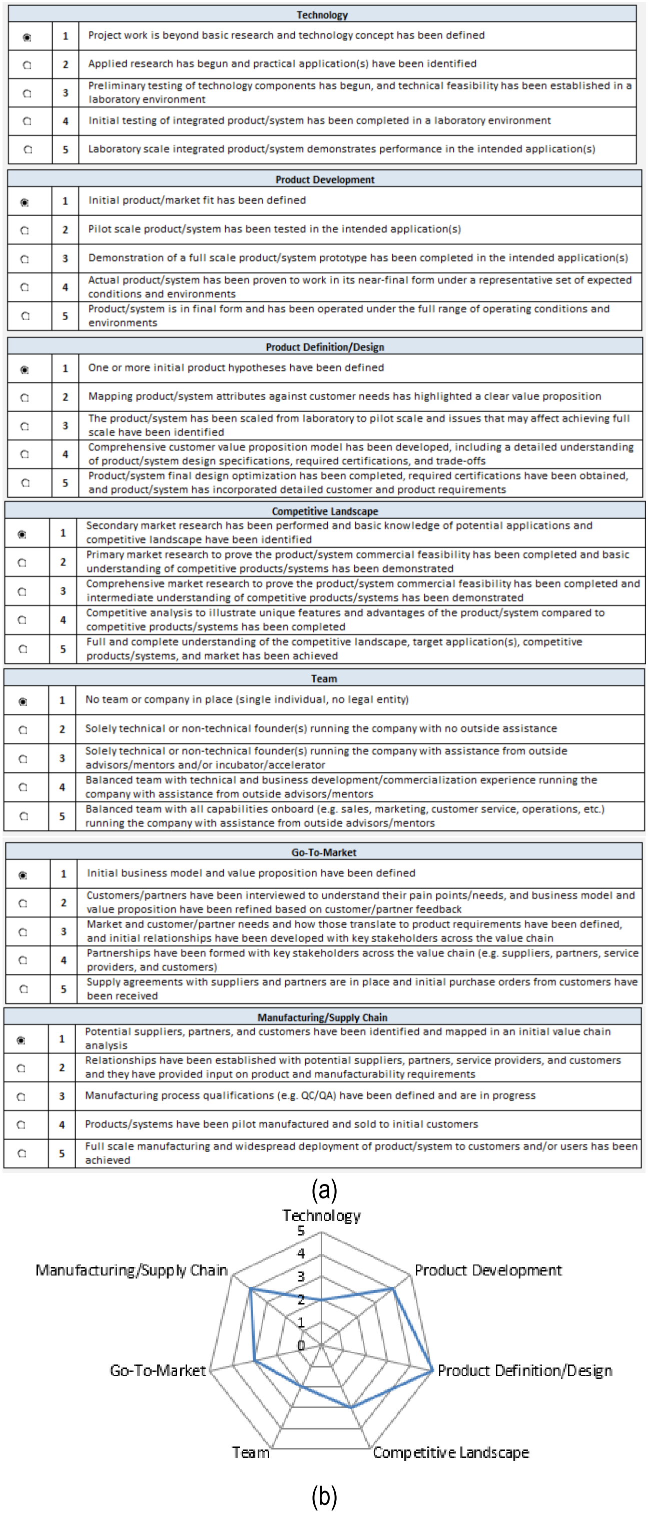

		Technology
●	1	Project work is beyond basic research and technology concept has been defined
○	2	Applied research has begun and practical application(s) have been identified
○	3	Preliminary testing of technology components has begun, and technical feasibility has been established in a laboratory environment
○	4	Initial testing of integrated product/system has been completed in a laboratory environment
○	5	Laboratory scale integrated product/system demonstrates performance in the intended application(s)

		Product Development
●	1	Initial product/market fit has been defined
○	2	Pilot scale product/system has been tested in the intended application(s)
○	3	Demonstration of a full scale product/system prototype has been completed in the intended application(s)
○	4	Actual product/system has been proven to work in its near-final form under a representative set of expected conditions and environments
○	5	Product/system is in final form and has been operated under the full range of operating conditions and environments

		Product Definition/Design
●	1	One or more initial product hypotheses have been defined
○	2	Mapping product/system attributes against customer needs has highlighted a clear value proposition
○	3	The product/system has been scaled from laboratory to pilot scale and issues that may affect achieving full scale have been identified
○	4	Comprehensive customer value proposition model has been developed, including a detailed understanding of product/system design specifications, required certifications, and trade-offs
○	5	Product/system final design optimization has been completed, required certifications have been obtained, and product/system has incorporated detailed customer and product requirements

		Competitive Landscape
●	1	Secondary market research has been performed and basic knowledge of potential applications and competitive landscape have been identified
○	2	Primary market research to prove the product/system commercial feasibility has been completed and basic understanding of competitive products/systems has been demonstrated
○	3	Comprehensive market research to prove the product/system commercial feasibility has been completed and intermediate understanding of competitive products/systems has been demonstrated
○	4	Competitive analysis to illustrate unique features and advantages of the product/system compared to competitive products/systems has been completed
○	5	Full and complete understanding of the competitive landscape, target application(s), competitive products/systems, and market has been achieved

		Team
●	1	No team or company in place (single individual, no legal entity)
○	2	Solely technical or non-technical founder(s) running the company with no outside assistance
○	3	Solely technical or non-technical founder(s) running the company with assistance from outside advisors/mentors and/or incubator/accelerator
○	4	Balanced team with technical and business development/commercialization experience running the company with assistance from outside advisors/mentors
○	5	Balanced team with all capabilities onboard (e.g. sales, marketing, customer service, operations, etc.) running the company with assistance from outside advisors/mentors

		Go-To-Market
●	1	Initial business model and value proposition have been defined
○	2	Customers/partners have been interviewed to understand their pain points/needs, and business model and value proposition have been refined based on customer/partner feedback
○	3	Market and customer/partner needs and how those translate to product requirements have been defined, and initial relationships have been developed with key stakeholders across the value chain
○	4	Partnerships have been formed with key stakeholders across the value chain (e.g. suppliers, partners, service providers, and customers)
○	5	Supply agreements with suppliers and partners are in place and initial purchase orders from customers have been received

		Manufacturing/Supply Chain
●	1	Potential suppliers, partners, and customers have been identified and mapped in an initial value chain analysis
○	2	Relationships have been established with potential suppliers, partners, service providers, and customers and they have provided input on product and manufacturability requirements
○	3	Manufacturing process qualifications (e.g. QC/QA) have been defined and are in progress
○	4	Products/systems have been pilot manufactured and sold to initial customers
○	5	Full scale manufacturing and widespread deployment of product/system to customers and/or users has been achieved

(a)

(b)

Fig. 5. (a) Criteria for assessing the level of development readiness (authors' simulation results based on Technology & Commercialization Readiness Level Calculator); (b) Resulting analysis diagram: principal image, arbitrary choice of criteria level

During the layout of the equipment, several technological solutions were used [24], which were adapted by the authors for the conditions for the production of porous ammonium nitrate. Porous ammonium nitrate is highly hygroscopic (the ability to absorb moisture from the air), which is one of the reasons for its caking. The caking of ammonium nitrate is usually understood as the chemical losing its flow ability during storage. Due to its high

DOI 10.2478/ama-2022-0041

hygroscopicity, pure ammonium nitrate is capable of caking during storage due to a significant change in its solubility and modification transformations with temperature changes. At the same time, the strength of the granules also decreases. Therefore, the main and auxiliary technological equipment for the granulation process will be placed indoors, which will ensure its isolation from the effects of precipitation. The absorption column for off-gas cleaning will be located in an open area, as the impact of atmospheric precipitation does not affect the conduct of the gas purification process. The open layout of the device will reduce capital costs for construction, improve conditions for the repair and installation of the column and reduce the impact of harmful and hazardous production factors (heat generation, explosion and fire hazard) on workers' plots.

To ensure the transportation of bulk materials without additional equipment and the creation of normal conditions for the cooling process of the obtained ammonium nitrate granules, the technological equipment will be located on two floors, one above the other.

The building is designed as a rectangle. The main dimensions of the designed building are taken from the standard range of dimensions. The column spacing (location of centre axes) is 6 m, and the span width is 18 m. Thus, for the designed building, a grid of columns having dimensions of 18 m x 6 m was adopted. The height of the first floor is assumed to be 6 m, the second 4.8 m. For the organisation of inter-floor overlap, we accept standard prefabricated reinforced concrete beam ceilings consisting of crossbars and floor slabs. Standard floor slabs 6 m long are laid on crossbars. The beamed ceiling is laid on the shelves of the columns. The columns of the outer rows (wall) have one-sided consoles, and the middle rows have two-sided consoles for supporting the crossbars. In the extreme columns, embedded metal flights are provided for fastening walls and crossbars. Link columns have embedded metal flights for attaching crossbars. For the building being designed, we accept panel walls. The building is heated, and emergency heating is provided in case of plant shutdown. The panels are a flat single-layer structure for a heated building made of expanded clay concrete and perlite concrete. The panel thickness is given as 200 mm. Ordinary panels are designed for blind sections of walls; and lintel panels are installed above and below window openings.

The projected building provides for the installation of sagging equipment. It is installed not on the ceiling but on special beams. To do this, we use crossbars of the rectangular cross-section with a special selection. The main beams are laid on them. Auxiliary beams are installed on the main beams, on which a metal ring is laid. The device supports are stationed on this ring as the apparatus is being installed.

A service ladder with a span of 1 m and an inclination angle of 60° is installed on the second floor to service the technological equipment located on this floor. We make the flight of stairs from steel reinforcement and the landing of the stairs from sheet punched material.

To organise the covering of the designed building, we use reinforced concrete truss beams for a span of 18 m of a gable profile. The beams are attached to the columns with anchor bolts, released from the columns and supporting metal sheets, and welded to the embedded parts of the beams. Coating slabs made of reinforced concrete are laid directly on the truss structures (beams). To fasten the roof slabs to the rays, steel-embedded parts are provided for, at the end of whose longitudinal ribs the embedded parts of the slabs are positioned, and thereafter welded. The seams between the plates are sealed with cement-sand mortar. The composition of the enclosing part of the coating, which is laid on the slabs, includes a vapour barrier layer, a waterproofing layer and a layer of gravel embedded in the mastic that makes up the roof. The roof protects the coating, as well as the building as a whole, from moisture penetration. The floor construction is chemically resistant. The foundations of the designed building and equipment are reliably isolated from the action of aggressive environments.

A need was felt to attenuate the pressure that the blast waves (from the bulk chemical processes associated with ammonium nitrate processing) are expected to impose on the main building structures; accordingly, all buildings located in the industrial area were designed with windows larger than are usually necessary (for ensuring adequate ventilation and natural lighting); additionally, working platforms for the maintenance of technological equipment were partially covered with steel gratings.

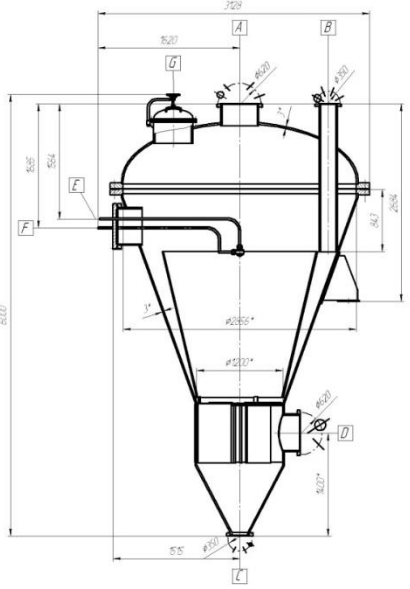

Symbol	Function
A	Outlet of gas
B	Inlet of seeding agent
C	Outlet of granular product
D	Inlet of drying air
E	Air inlet for spraying of the liquid material
F	Inlet of melt
G	Hatch

Fig. 6. The industrial design of vortex granulator (authors' elaboration)

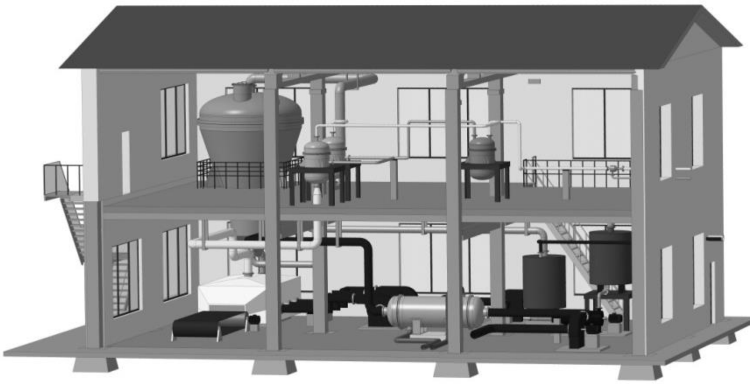

Fig. 7. Layout of the main equipment for the production of porous ammonium nitrate (authors' elaboration)

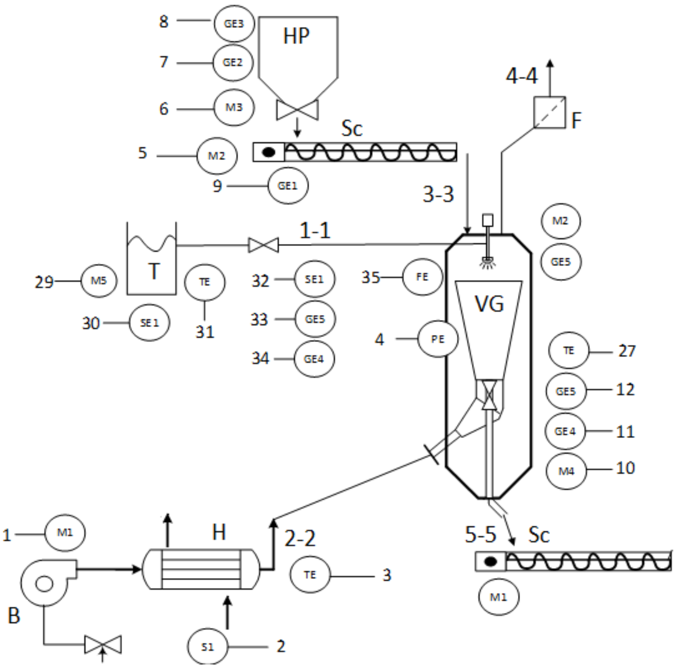
8
GE3
HP
7
GE2
6
M3
4-4
F
Sc
5
M2
9
GE1
3-3
1-1
M2
GE5
T
29
M5
TE
32
SE1
35
FE
30
SE1
31
33
GE5
VG
4
PE
34
GE4
TE
27
GE5
12
GE4
11
M4
10
1
M1
H
2-2
5-5
Sc
TE
3
B
M1
S1
2

Fig. 8. Functional diagram of the control object (authors' elaboration)

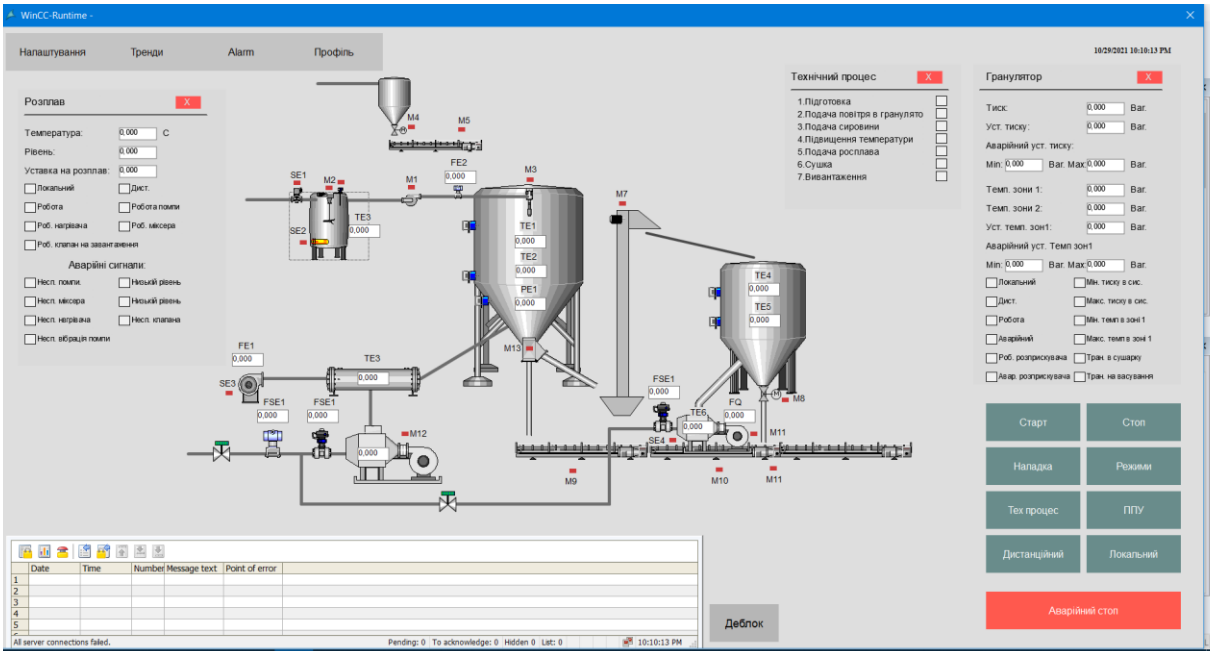
WinCC-Runtime -
Налаштування
Тренди
Alarm
Профіль
M4
M5
SE1
M2
M1
FE2
M3
M7
SE2
TE3
TE1
TE2
PE1
TE4
TE5
M13
M8
FE1
TE3
SE3
FSE1
FSE1
M12
FSE1
FQ
TE6
SE4
M11
M9
M10
M11
Старт
Стоп
Наладка
Режими
Тех процес
ППУ
Дистанційний
Локальний
Деблок
Аварійний стоп

10/29/2021 10:10:13 PM

Розплав

Температура: 0,000 C
Рівень: 0,000
Уставка на розплав: 0,000

☐ Локальний ☐ Дист.
☐ Робота ☐ Робота помпи
☐ Роб. нагрівача ☐ Роб. міксера
☐ Роб. клапан на завантаження

Аварійні сигнали:

☐ Несп. помпи. ☐ Низький рівень
☐ Несп. міксера ☐ Низький рівень
☐ Несп. нагрівача ☐ Несп. клапана
☐ Несп. вібрація помпи

Технічний процес

1.Підготовка ☐
2.Подача повітря в гранулято ☐
3.Подача сировини ☐
4.Підвищення температури ☐
5.Подача росплава ☐
6.Сушка ☐
7.Вивантаження ☐

Гранулятор

Тиск: 0,000 Bar.
Уст. тиску: 0,000 Bar.
Аварійний уст. тиску:
Min: 0,000 Bar. Max: 0,000 Bar.
Темп. зони 1: 0,000 Bar.
Темп. зони 2: 0,000 Bar.
Уст. темп. зон1: 0,000 Bar.
Аварійний уст. Темп зон1
Min: 0,000 Bar. Max: 0,000 Bar.

☐ Локальний ☐ Мін. тиску в сис.
☐ Дист. ☐ Макс. тиску в сис.
☐ Робота ☐ Мін. темп в зоні 1
☐ Аварійний ☐ Макс. темп в зоні 1
☐ Роб. розприскувача ☐ Тран. в сушарку
☐ Авар. розприскувача ☐ Тран. на васування

	Date	Time	Number	Message text	Point of error
1					
2					
3					
4					
5					

All server connections failed. Pending: 0 To acknowledge: 0 Hidden 0 List: 0 10:10:13 PM

Fig. 9. Dispatching system for vortex granulator control (authors' elaboration)

The dispatching system for controlling the vortex granulator (Fig. 8) based on Wincc (Fig. 9) was decomposed.

At the final stage of implementation, an analysis is made of the quality indicators of the finished product, namely porous ammonium nitrate. The product is evaluated with reference to the characteristics of the porous structure of the granule and the specific characteristics inherent in the ANFO (ammonium nitrate/fuel oil) industrial explosive component. An example of the structure of a porous ammonium nitrate granule is shown in Fig. 10.

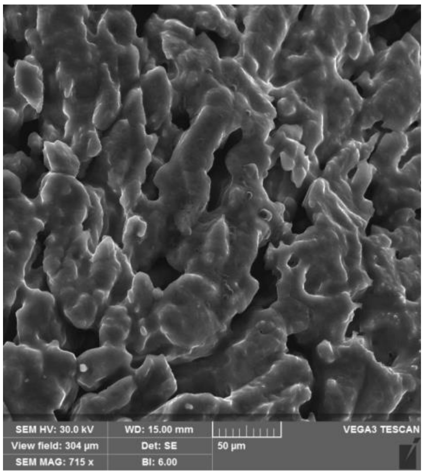

Fig. 10. Sample of porous ammonium nitrate granule (authors' photo based on the results of scanning electron microscopy)

5. CONCLUSIONS

Obtaining a consistent solution for tasks formulated for implementation via an optimised granulation function along the chain 'optimisation calculation of apparatus units – computer simulation – creation of a test sample of the granulator – installation equipment layout – provision of installation control – testing of the finished product' ensures a successful transfer of granulation technology using whirl granulators. The algorithm proposed in the present study can be applied to other equipment in engineering. Evaluation of the effectiveness of solutions at each stage of considering the level of developmental readiness for implementation allows the creation of a roadmap for the development of technology and improvement of the main equipment of the installation.

REFERENCES

1. Stahl H. Comparing Different Granulation Techniques. Pharmaceutical Technology Europe. 23–33.
2. Parikh D. Handbook of Pharmaceutical Granulation Technology. 3rd ed. Informa Healthcare; 2009.
3. Muralidhar P, Bhargav E, Sowmya C. Novel techniques of granulation: a review. Int Res J Pharm. 2016; 7(10): 8–13.
4. Solanki HK, Basuri T, Thakkar JH, Patel CA. Recent advances in granulation technology. Int J Pharm Sci. 2010; 5(3): 48–54.
5. Saikh MA. A technical note on granulation technology: a way to optimise granules. Int J Pharm Sci. 2013; 4: 55-67.
6. Artyukhov AE, Artyukhova NO. Technology and the main technological equipment of the process to obtain N_4HNO_3 with Nanoporous Structure. Springer Proc Phys. 2019; 221: 585–594.
7. Artyukhov A., Artyukhova N, Krmela J, Krmelová V. Complex designing of granulation units with application of computer and software modeling: Case "Vortex granulator". IOP Conf Ser: Mater Sci and Eng. 2020; 776(1): 012016.
8. Litster J, Ennis B. The science and engineering of granulation processes. Springer-Science+Business Media; 2004.
9. Srinivasan S. Granulation techniques and technologies: recent progresses. BI. 2015; 5(1): 55–63.
10. Kunii D, Levenspiel O: Fluidization engineering. Butterworth-Heinemann: 1991.
11. Salman AD, Hounslow MJ, Seville, JPK. Granulation. Amsterdam: Elsevier Science Ltd; 2006.
12. Artyukhov A, Artyukhova N, Krmela J, Krmelová V. Granulation machines with highly turbulized flows: Creation of software complex for technological design. IOP Conf Ser: Mater Sci and Eng. 2020; 776(1): 012018.
13. Artyukhov AE, Sklabinskyi VI. Experimental and industrial implementation of porous ammonium nitrate producing process in vortex granulators. Nauk Visnyk Natsionalnoho Hirnychoho Universytetu. 2013; 6:42-48.
14. Artyukhov A, Artyukhova N: Utilization of dust and ammonia from exhaust gases: new solutions for dryers with different types of fluidized bed. J Environ Health Sci Eng. 2018; 16(2):193-204.
15. Obodiak V, Artyukhova N, Artyukhov A. Calculation of the residence time of dispersed phase in sectioned devices: Theoretical basics and software implementation. Lect Notes Mech Eng. 2020: 813–820.
16. Artyukhov A, Krmela J, Artyukhova N, Ostroha R. Modeling of the Aerodisperse Systems Hydrodynamics in Devices With Directional Motion of the Fluidized Bed. Encyclopedia of Information Science and Technology, Fifth Edition. IGI Global; 2020. – 1289-1307.
17. Yang WC. Handbook of fluidizaition and fluid-particle systems. New York: Marcel Dekker; 2003.
18. Shi DP, Luo ZH, Guo AY. Numerical Simulation of the Gas−Solid Flow in Fluidized-Bed Polymerization Reactors. Ind Eng Chem Res. 2010; 49(9):4070–4079.
19. Pandaba P, Sukanta, KD. Numerical Simulation for Hydrodynamic Analysis and Pressure Drop Prediction in Horizontal Gas-Solid Flows. Part Sci Technol. 2014; 32(1): 94–103.
20. Feldmann F, Hagemann B, Ganzer L, Panfilov M. Numerical simulation of hydrodynamic and gas mixing processes in underground hydrogen storages. Environ. Earth Sci. 2016; 75: 1165–1172.
21. Crowe C. Multiphase flow handbook. Boca Raton, Taylor & Francis Group; 2006.
22. Rybalko M, Loth E, Lankford D. A Lagrangian particle random walk model for hybrid RANS/LES turbulent flows. Powder Technol. 2012; 221: 105-113.
23. Technology & Commercialization Readiness Level Calculator. Available from: https://portal.nyserda.ny.gov/servlet/servlet.FileDownload?file=00Pt000000ASeCMEA1.
24. Cussler EL, Moggridge GD. Chemical Product Design (Cambridge Series in Chemical Engineering). Cambridge University Press; 2011.

Funding: This research work was supported by the Ministry of Science and Education of Ukraine under the project 'Technological bases of multistage convective drying in small-sized devices with utilization and heat recovery units,' project No. 0120U100476, and by the Cultural and Educational Grant Agency of the Slovak Republic (KEGA), project No. 003TnUAD-4/2022.

Artem Artyukhov: https://orcid.org/0000-0003-1112-6891

Jan Krmela: https://orcid.org/0000-0001-9767-9870

Vladimíra Krmelová: https://orcid.org/0000-0002-3822-3416

Dastan Ospanov: https://orcid.org/0000-0003-0401-180X

DOI 10.2478/ama-2022-0042

acta mechanica et automatica, vol.16 no.4 (2022)

A METHOD OF INCREASING THE ACCURACY OF LOW-STIFFNESS SHAFTS: SINGLE-PASS TRAVERSE GRINDING WITHOUT STEADY RESTS

Paweł SUŁKOWICZ*, Robert BABIARZ*, Jan BUREK*, Jarosław BUK*, Kamil GANCARCZYK*

*Faculty of Mechanical Engineering and Aeronautics, Rzeszow University of Technology,
al. Powstańców Warszawy 12, 35-959 Rzeszów, Poland

sulkowicz@prz.edu.pl, robertb@prz.edu.pl, jburek@prz.edu.pl, jbuk@prz.edu.pl, kamilgancarczyk@prz.edu.pl

received 8 June 2022, revised 4 August 2022, accepted 12 August 2022

Abstract: The article presents a method of increasing the shape and dimensional accuracy of low-stiffness shafts manufactured in a single pass of a grinding wheel in traverse grinding. One-pass manufacturing is one of the ways for reducing machining time and increasing efficiency, thus lowering production costs. However, maintaining the necessary accuracy proves to be a challenge because the whole machining allowance has to be removed at once, leaving no room for errors that could be fixed in additional passes of the tool. It is especially true in finishing operations, such as traverse grinding. In addition, grinding the workpiece in a single pass of a grinding wheel leads to high forces, which cause elastic deformation of the part. The lower the stiffness of the part, the more difficult it is to achieve the required accuracy. As a result, there are many methods of improving the accuracy of grinding such parts, but they tend to be either expensive or reduce the machining efficiency. Thus, it is important to seek new methods that would allow improving the accuracy of the machining without reducing its efficiency. The proposed method does not require using steady rests and is based on the measurement of the normal grinding force component. Knowing the value of the grinding force when grinding with a set grinding depth, the elastic deformation of the machine tool–tool–workpiece system is calculated in each position of the grinding wheel. Based on the calculated deformation, the additional infeed of the grinding wheel is implemented in order to stabilise real grinding depth and to increase the accuracy of the produced part. The experimental tests were conducted to prove the effectiveness of the proposed method.

Key words: traverse grinding, low-stiffness shafts, single-pass grinding, cylindricity error

1. INTRODUCTION

Grinding is a machining process traditionally used to achieve high accuracy and surface quality of the workpiece with low cutting volume. The developments in the field of abrasive materials as well as in the design and technological capabilities of modern grinding machines enable the implementation of many new processes and machining strategies. High-efficiency grinding (HEG) processes are used in order to reduce machining time and lower production costs. The methods that allow achieving such task are collectively named high-performance grinding (HPG) or HEG [1]. Two directions of the development in high-performance grinding processes can be distinguished, namely, deep grinding methods and grinding processes with high grinding wheel peripheral speeds. In the case of deep-cut grinding (DCG) processes, high machining efficiency is achieved as a result of using high values of grinding wheel infeed (grinding depth ae), relatively low feed rates of the workpiece and low peripheral speed of a grinding wheel. An alternative solution is to increase the peripheral speed of the grinding wheel, which, in turn, allows improving machining efficiency while maintaining the required surface quality due to a significant increase in grinding speed (e.g., high-speed grinding, HSG) [2–4]. Most high-performance grinding methods, however, are based not on increasing the grinding speed but on the use of high grinding depth values in many cases, allowing the workpiece to be machined with a single pass of a grinding wheel [5].

There are three main grinding processes that can be executed in a single pass of a grinding wheel. The first one is the creep feed grinding (CFG), in which a highly porous, conventional grinding wheel machines the workpiece with very high depths of cut (in some cases, up to even 20 mm) and low feed rates. The process is used in the aerospace and automotive industry in machining difficult-to-cut materials such as superalloys and refers mainly to surface grinding, although can also be used in cylindrical grinding [6, 7]. The second one-pass method – known as traverse contour grinding or continuous path-controlled grinding (CPCG) – is recognised as an alternative to hard turning and consists of using a narrow cylindrical grinding wheel (cBN), which follows the shape of the workpiece [8–10]. The last method involves outside or inside cylindrical traverse grinding with high grinding infeed and electro-corundum grinding wheels, which may be cylindrical or cylindrical with a conic zone for rough grinding, or have a zone-diversified structure [9].

Grinding is a finishing operation, so the influence of elastic deformations of a machine tool–tool–workpiece system is of great importance. Elastic deformations of a workpiece, grinding wheel and machine tool components affect the contact zone between the wheel and the workpiece, thus impacting the shape and dimensional accuracy of the machined part. The types of typical deviations observed after grinding depend on the type of machining process. In the case of traverse grinding of a part mounted between centres, shape deviations depend mostly on the machine tool–tool–workpiece system stiffness and on the accuracy of setting up the workpiece. In low-stiffness shafts machining, the greatest challenge in achieving the needed accuracy is reducing the cylindricity error resulting from the elastic deformation of the system. Cylindricity errors are dependent on deviations in the straightness of a cylindrical surface [11]. There are two main types of errors produced during traverse grinding. The first one is taper error, which is a result of the elastic deformation of the machine tool centres and is dependent on the difference between the stiffness of a headstock centre and the stiffness of a tailstock centre (Fig. 1a). The second type of error is called barrel error, which results from the elastic deformation of the workpiece (Fig. 1b).

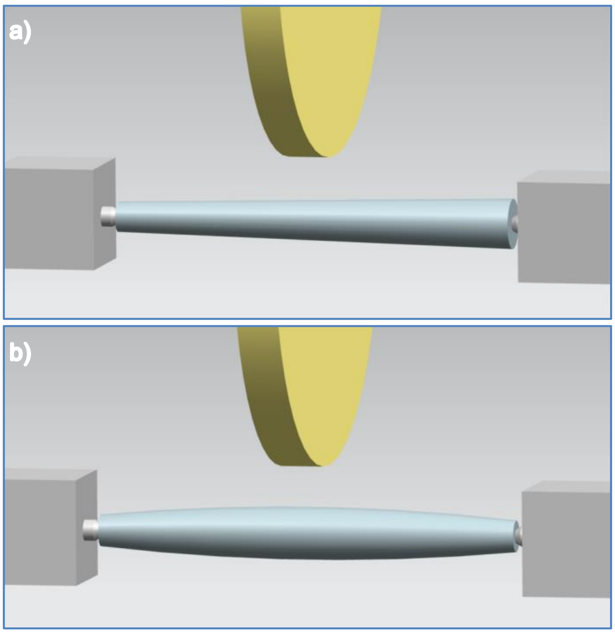

Fig. 1. Typical errors in traverse grinding: (a) taper error, (b) barrel error

The values of errors depend on kinematics and the design of the grinding machine, dimensions of the workpiece, technological parameters, among others,. The higher the grinding force and the lower the stiffness of the workpiece, the higher the values of the cylindricity error. Thus, the task of machining a low-stiffness workpiece in a single grinding pass proves to be especially difficult [12].

Conventional methods of reducing the shape and size errors of parts machined in traverse grinding aim to reduce the elastic deformation of a machine tool–tool–workpiece system. One way to achieve that goal is by increasing the rigidity of the system by the application of grinding steady rests. However, a proper setting of steady rests on a grinding machine is time-consuming and in many cases requires the skill of an operator. The application of steady rests also involves the risk of damaging the machined surface. The elastic deformation is reduced, but it still can be significant, especially in places distant from the rest and machine centres. One can use a computer numerical controlled CNC-steady rest, but it is expensive and requires changes in the design of a grinding machine. The second way to reduce machining errors is by lowering the grinding force by reducing the values of technological parameters, in particular the axial feed fa and the grinding depth ae. However, this solution is not very practical due to a significant increase in machining times.

Considering the aforementioned limitations, many researchers tried to develop new strategies in traverse grinding of low-stiffness shafts. Porzycki et al. [13] obtained a significant improvement in the quality of the ground surface, accuracy of the shape of the workpiece and a decrease in the wear of the grinding wheel as a result of the application of the adaptive control system of the axial feed based on the grinding force measurement. Amitay et al. [14] developed an adaptive feed rate control system based on the grinding wheel spindle power signal in order to improve the accuracy of ground workpieces. Gao and Jones [15] designed a test stand for traverse grinding of shafts supported with adaptively controlled steady rests based on the measurement of the diameter of the workpiece during machining. Park et al. [16] developed a model that predicts cylindrical errors resulting from traverse grinding of low-stiffness shafts with steady rests. Choi and Lee[17] proposed a strategy for optimising the position of steady rests to reduce elastic deformation of the workpiece as well as a method for measuring and compensating for thermal deformations during traverse grinding of low-stiffness shafts. Kruszyński and Lajmert [18] developed a system for optimising the traverse grinding process with the use of a neural network. Swic and Taranenko [19] described a method of adaptive control in machining accuracy of axial-symmetrical low-rigidity parts in an elastic-deformable state. The method consisted of additional positive feedback relative to the machining force, and the errors were decreased due to the control of axial feed. Parenti and Bianchi[20] presented a method for improving the surface quality of ground shafts due to the application of a process parameter control system based on the measurement of vibration amplitude and the use of artificial intelligence.

The analysis of the literature revealed that previous studies focused on improving the shape and dimensional accuracy of traverse ground low-stiffness shafts mainly based on the control of technological parameters during the process (resulting in lower machining efficiency), the use of adaptively controlled steady rests or required the use of additional, efficient computational systems and interference in the grinding machine control systems (which limits their use chiefly to laboratory solutions).

2. METHOD

In order to achieve accurate and efficient single-pass traverse grinding without the use of steady rests, the following method has been developed. Instead of trying to lower the elastic deformation of the machine tool–tool–workpiece system, a different approach has been undertaken. The method is based on introducing an additional grinding wheel infeed calculated on the basis of the analysis of the cut-layer cross-section and the measurement of the grinding force. During traditional traverse grinding, due to the grinding force exerted on the workpiece, it elastically deforms, resulting in real grinding depth a_{er} being lower than the set grinding depth a_e and thus leading to machining errors. In order to obtain low cylindrical deviations, the real grinding depth a_{er} ought to be as close to the set grinding depth a_e as possible. The real grinding depth a_{er} is dependent on many factors, such as stiffness of the machine, workpiece material and its dimensions, type of a grinding wheel and its condition and technological parameters. Many of the factors influencing grinding depth a_{er} are constant and can be determined before the machining.

Previous research indicates that in traverse grinding of low-stiffness shafts, elements with lowest stiffness, such as workpiece and machine centres, have a crucial impact on the elastic deformation of the part [10, 21–23]. Depending on the workpiece geometry, they are responsible for up to over 90% of the compliance of the entire system. Taking that into account, one can calculate total elastic deformation at any given place of the workpiece during grinding as a sum of the deformations of machine centres (x_1), workpiece deflection (x_2) and the deformation of other elements of the system (x_3). The elastic deformation of the workpiece due to the deformation of centres can be calculated from the following equation:

$$x_1 = \left(1-\frac{z}{l}\right)^2 \cdot \frac{F_n}{k_h} + \left(\frac{z}{l}\right)^2 \cdot \frac{F_n}{k_t} \tag{1}$$

where z is the position of the grinding wheel along the axis of the workpiece, F_n is the normal component of the grinding force, l is the length of the workpiece, k_h is the stiffness of the headstock centre and k_t is the stiffness of the tailstock centre. For a straight shaft with no steps, the deflection of the workpiece can be calculated as follows:

$$x_2 = \frac{F_n \cdot z^2 \cdot (l-z)^2}{3 \cdot E \cdot I \cdot l} \tag{2}$$

where E is Young's modulus and I is the area moment of inertia. The elastic deformation of the remaining components of the system x_3 can be described as follows:

$$x_3 = \frac{F_n}{k_m} \tag{3}$$

where k_m is the total stiffness of other components of the grinding machine determined experimentally.

The aforementioned equations present simple linear relations between deflections and forces and as such will not describe the deformations resulting from the grinding process as accurately as finite element method (FEM) calculations. However, their simplicity allows for easy and fast calculation and thus may be of use in industrial practice. Considering this, total elastic deformation at any given place of the workpiece during grinding can be calculated from the following equation:

$$x = \left(1-\frac{z}{l}\right)^2 \cdot \frac{F_n}{k_h} + \left(\frac{z}{l}\right)^2 \cdot \frac{F_n}{k_t} + \frac{F_n \cdot z^2 \cdot (l-z)^2}{3 \cdot E \cdot I \cdot l} + \frac{F_n}{k_m} \tag{4}$$

From the stated relationships, it can be concluded that the deformation of the workpiece during grinding is a function of the normal grinding force component F_n and the position of the grinding wheel z. Therefore, the measurement of the normal grinding force F_n during machining allows for calculating the deformation and for calculating the additional grinding wheel infeed to improve the accuracy of the process. The described method is based on the open-loop control and thus does not require introducing online adaptive systems into machine control systems and can be adopted into any CNC-controlled grinding machine equipped with a force sensor. It is based on the measurement of the normal grinding force component F_n during grinding of a test part with constant grinding wheel infeed a_e. Then, the additional infeed in each position of the grinding wheel alongside the workpiece is applied when grinding the following parts.

Increasing the grinding depth a_e results in the increase in the grinding force and, as a consequence, in the increase of the elastic deformation of the workpiece. Therefore, applying the additional infeed based on the elastic deformation calculated from the measured force would decrease the machining errors, but to achieve the lowest values of deviations, the additional deformation ought to be considered.

Fig. 2 presents a simplified view of the ground layer cross-section depending on the grinding wheel infeed.

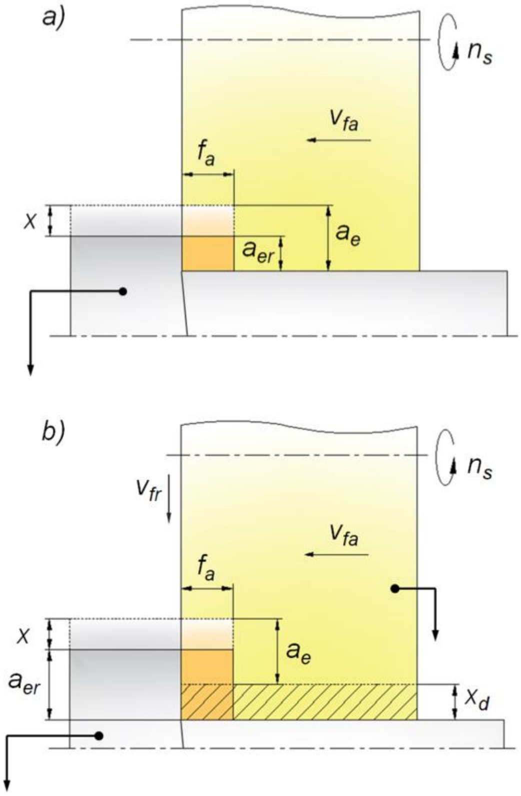

Fig. 2. A view of the ground layer cross-section: (a) with constant grinding wheel infeed, (b) with additional grinding wheel infeed

Considering this, a relationship describing the real grinding depth can be formulated as follows:

$$a_{er} = a_e - x + x_d \tag{5}$$

where x_d is the value of the additional infeed at a given grinding wheel position. As follows from Eq. (5), the real grinding depth a_{er} will be equal to the set grinding depth a_e when the value of the total elastic deformation x is equal to the value of the additional grinding wheel infeed x_d. Therefore, the value of the additional infeed of the grinding wheel at any given place during machining can be determined from the following relationship:

$$x_d = F_n \left[\left(1-\frac{z}{l}\right)^2 \cdot \frac{1}{k_h} + \left(\frac{z}{l}\right)^2 \cdot \frac{1}{k_t} + \frac{z^2 \cdot (l-z)^2}{3 \cdot E \cdot I \cdot l} + \frac{1}{k_m}\right] \tag{6}$$

Considering this, in order to calculate the additional infeed of the grinding wheel, it is necessary to determine, besides geometrical and material parameters of the workpiece and stiffness coefficients of the machine, the value of the normal grinding force F_n applied to the workpiece when grinding with $a_e = a_{er}$. Thus, in the presented method, it is necessary to grind a test part with a constant grinding wheel infeed in order to measure the normal grinding force value. The method is best suited for parts with low variations in machining allowance because adopted equations assume the allowance is constant, and thus, any significant change in the shaft diameter between parts will influence the accuracy of produced parts. In addition, due to the wear of a grinding wheel, the grinding force should be measured during each grinding pass to recalculate the values of the infeed and thus to ensure high accuracy for all the parts.

In addition, in traverse grinding, due to the abrupt change in the machining load at the beginning and at the end of each grinding pass, cylindrical deviations, which often surpass the deviations resulting from the deflection of a workpiece, tend to occur. In order to reduce these errors, the presented method involves a strategy of gradual entry and exit of the grinding wheel from the workpiece, thus allowing to avoid sudden increases and decreases in the machining load. The strategy consisted of moving the grinding wheel linearly in both X and Z axes from the depth of a_e = 0 μm up to the set a_e at the grinding length that was equal to a quarter of the grinding wheel width.

3. EXPERIMENTAL SETUP

In order to check the effectiveness of the proposed method, experimental tests were performed. The experimental setup was designed based on a three-axis CNC cylindrical grinding machine by Geibel & Hotz (Fig. 3). The measurement of the grinding force was conducted with two dynamometers of type 9601A31 by Kistler. The signal from the dynamometers was amplified and registered with an A/D converter type NI USB-6009 by National Instruments and a computer equipped with LabVIEW SignalExpress software.

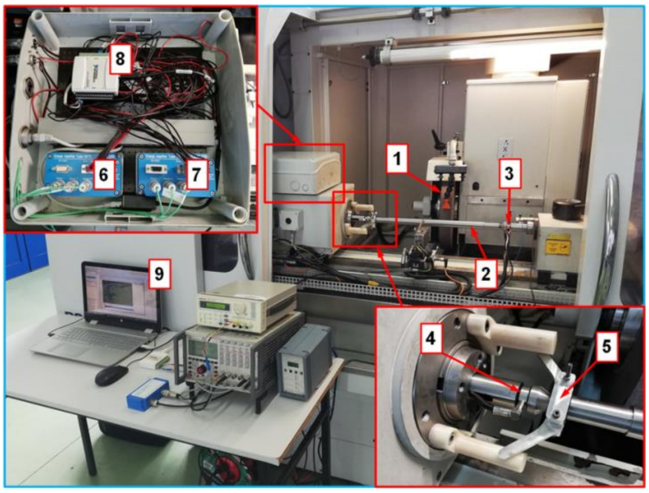

Fig. 3. Test stand: 1 – grinding wheel; 2 – workpiece; 3,4 – dynamometers; 5 – grinding carrier; 6,7 – signal amplifiers; 8 – A/D converter; 9 – computer with LabVIEW SignalExpress software

The measurement of the accuracy of the grinded workpiece was conducted on the grinding machine, with the use of an inductive sensor type GT 21 by TESA (Fig. 4). The sensor mounted on the grinding wheel spindle unit allowed recording the profiles of grinded shafts. The cylindricity error ΔC was calculated as a difference between the maximum Δr_{wmax} and minimum Δr_{wmax} values recorded by the sensor during the measurement. The measurement of the diameter of a workpiece was conducted with the Micromar 8 control gauge by Marposs. Such a measuring setup was investigated in previous works and proved to be accurate [24]. The values of the stiffness coefficients were determined experimentally by loading the respective part of the machine and measuring the resultant deflection with the inductive sensor. The determined values were as follows: k_h = 7.12 kN/mm, k_t = 5.03 kN/mm and k_m = 21.43 kN/mm.

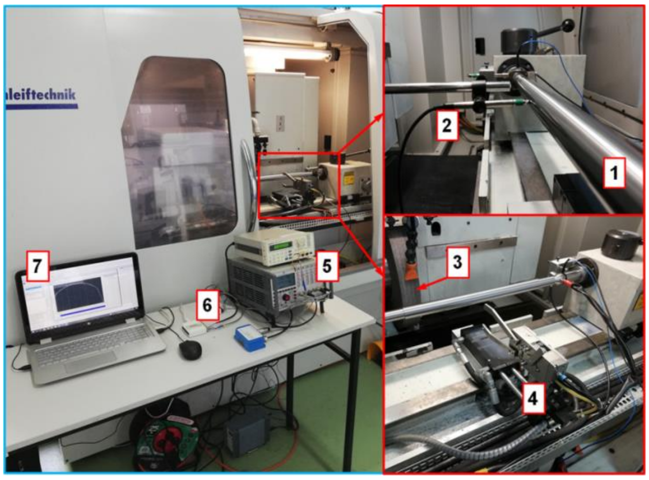

Fig. 4. Test stand: 1 – workpiece; 2 – inductive sensor; 3 – grinding wheel; 4 – control gauge; 5 – amplifier; 6 – A/D converter; 7 – computer

The M60H12VEPI electro-corundum grinding wheel by Andre Abrasives was used in the tests. The width of the grinding wheel was equal to b_s = 50 mm. The workpieces in the shape of straight shafts with the length of l = 500 mm and the diameter of d_w = 30 mm were machined from the 100Cr6 steel and underwent thermal treatment in order to achieve a hardness of approx. 60 HRC. On both sides of the shafts, there was a step with a diameter of 25 mm so as to enable entry and exit of the grinding wheel, as well as to allow mounting of the grinding carrier. Thus, the grinding length was equal to l_s = 375 mm. The workpieces were grinded in a single pass of a grinding wheel with constant infeed and with the variable infeed. The direction of grinding was from the headstock to the tailstock. After each machining pass, the grinding wheel was dressed in order to restore its cutting capabilities. For the experimental tests, such a range of technological parameters was assumed, which allowed utilising the capabilities of the grinding machine and simultaneously did not cause the loss of stability of the machining. The technological parameters are presented in Table 1.

Tab. 1. Values of set technological parameters for the grinding tests

Technological parameter	Value
Grinding wheel speed v_s (m/s) Grinding wheel infeed a_e (μm) Grinding feed f_a (mm/obr)	35 20, 40, 60, 80, 100, 120 1
Workpiece speed v_w (m/s)	0.44
Dressing infeed a_{ed} (μm)	10
Dressing feed f_{ad} (mm/obr)	0.1

4. RESULTS

Fig. 5 presents recorded deviations of the grinded workpiece profiles after tests with the variable infeed and with the constant infeed.

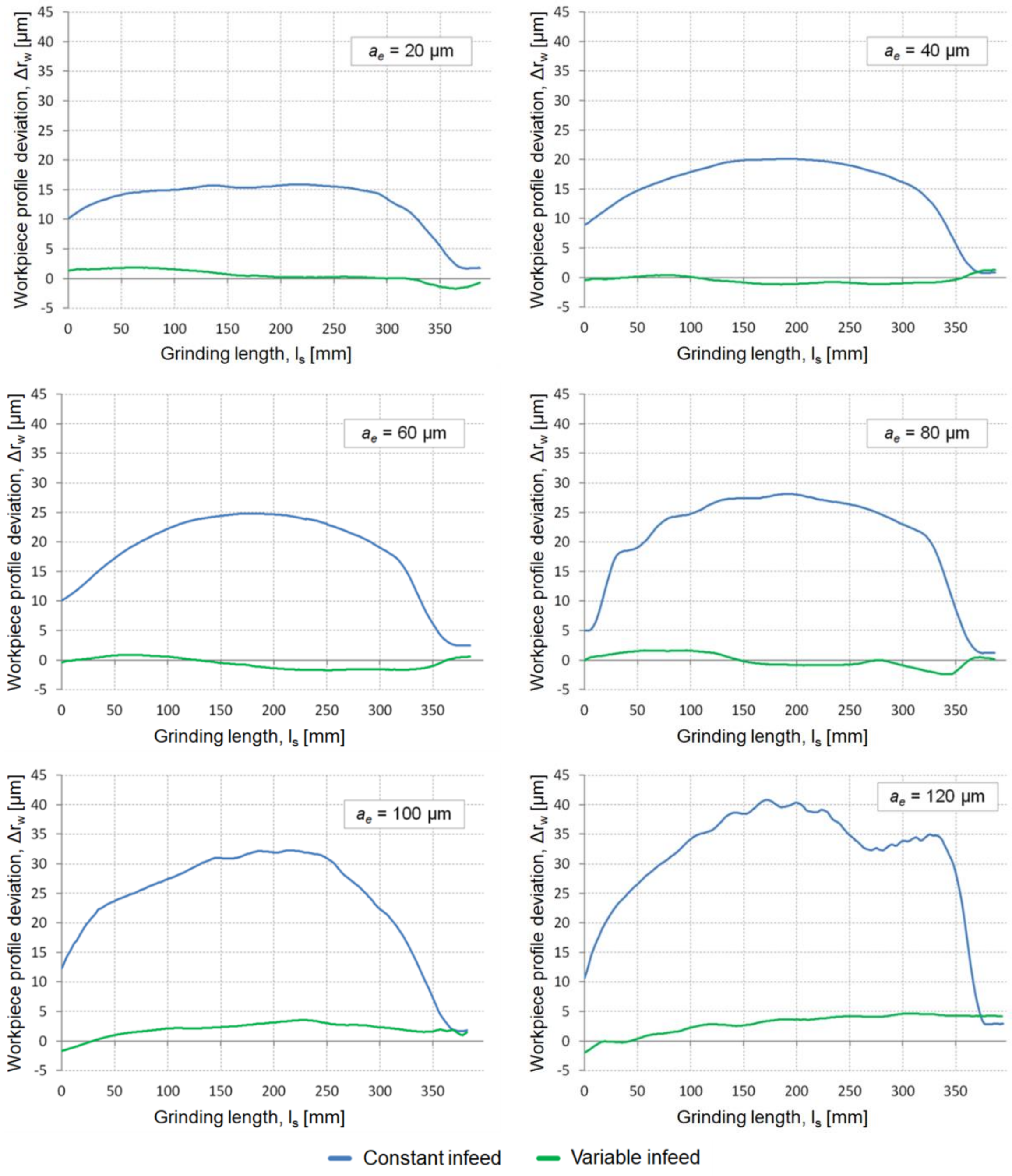

Fig. 5. Deviations of the grinded workpiece profiles

Analysing the deviations recorded after grinding tests with constant grinding infeed, one can observe that with the increase in the grinding length, due to elastic deformation of the machining system, the values of the deviations increase until they reach a maximum, which is situated usually near the lowest stiffness point of the system. Then, the deviations gradually decrease until the grinding wheel exits the workpiece, where a sudden decrease in errors can be observed due to the reduction in elastic deformations of the system. The difference in the rate of the deviation increase and decrease results from the difference in the stiffness of the machine tool centres.

The analysis of the presented graphs leads to the conclusion that grinding with variable infeed can significantly decrease the deviations of the grinded profiles in the tested range of the grinding depths. For grinding with constant infeed, the biggest variations in recorded deviations were observed at the start and the end of the grinding, especially with lower grinding depths, where the deflection of the workpiece is comparably low. The increase in grinding depth resulted in an increase in the strain of the machine tool–tool–workpiece system and thus in the increase in recorded deviations. The local decrease in deviation values of the workpiece grinded with a_e = 120 μm indicates the loss of stability of the machining. For the selected geometry of shafts, trying to grind with a_e > 120 resulted in the sudden increase in forces and vibrations, resulting in chipping of the grinding wheel. On the other hand, the deviations of the grinded profiles recorded after grinding with variable infeed were close to linear. For the grinding depths of a_e = 100 μm and a_e =120 μm, one can observe an increase in deviation values with an increase in grinding length. For other grinding depths, the errors did not show a clear tendency of changes. For all the grinding tests with variable infeed, the measured deviations were in the range of –3 μm to +5 μm.

In addition, the local decrease in deviations recorded after grinding with a constant infeed of a_e =120 μm indicate the loss of stability of the machining. On the other hand, when grinding with the additional infeed, the loss of stability was not observed.

Fig. 6a presents the values of calculated cylindricity errors` Fig. 6b presents the maximum dimensional error recorded after grinding. As can be seen from the graph, for the tests with constant grinding infeed, there was a monotonous and almost linear dependence between the grinding depth and cylindricity deviation. For the tests conducted with variable infeed, the recorded values of cylindrical deviation were equal to approximately 5 μm for all the analysed grinding depths. The higher the set grinding depth, the higher the obtained deviations.

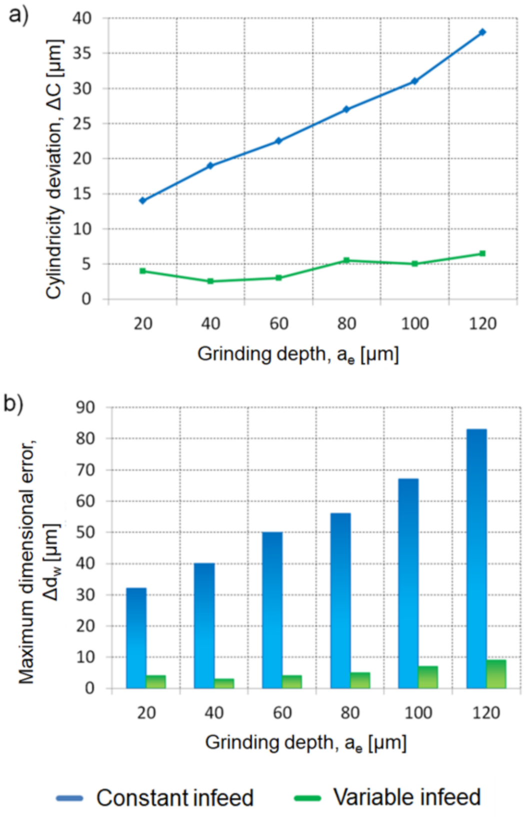

Fig. 6. Deviations of the workpieces grinded with various set grinding depths: (a) cylindricity error, (b) maximum dimensional error

The analysis of the recorded cylindricity deviations leads to a conclusion that applying the variable infeed can decrease the cylindricity deviations up to 87%, on average approx. 82%. In addition, the maximum dimensional error was reduced by approx. 90% in comparison to grinding with constant grinding infeed.

Fig. 7 presents the values of the normal component of grinding force recorded during grinding tests.

As can be observed from the presented graphs, the use of the additional infeed resulted in the increase in the normal grinding force component for all set grinding depths. The values of force measured when grinding with constant infeed increase with the increase in grinding time due to the wear of the grinding wheel and the increase in the system stiffness resulting from the grinding wheel getting closer to the tailstock centre. On the other hand, the course of F_n changes recorded during grinding indicates stabilisation of its value. During grinding with variable infeed, the average values of the normal cutting force component were higher than those when grinding with constant infeed, with an increase of approximately 11%.

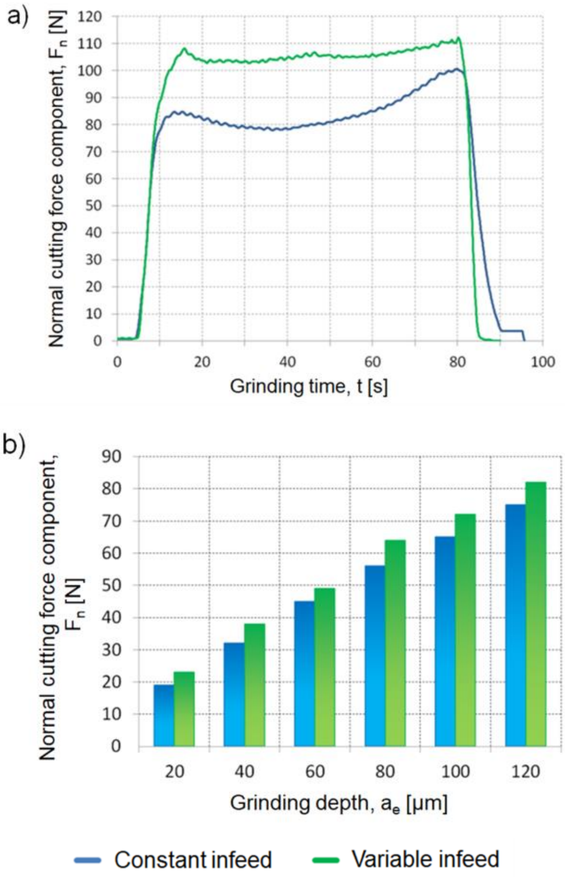

Fig. 7. Normal grinding force component: (a) courses of changes (b) average values

One of the most important indicators of the effectiveness of the grinding process is the quality of the manufactured surface. In order to assess the influence of the proposed method on the surface roughness of grinded parts, Ra surface roughness parameter was measured after each grinding test. Fig. 8 presents the results of the measurements conducted at the start, in the middle and at the end of the workpiece.

Analysing the roughness of the parts, one can observe that the higher the grinding depth, the lower the quality of the manufactured surface, which is true for both grinding with constant and with variable infeed, especially at the beginning and at the end of the workpiece. At the beginning, in the case of grinding with constant infeed, every increase in the grinding depth a_e of 20 μm results in a significant increase in Ra parameter, approximately 13%. On the other hand, surface roughness measured at the start of the part grinded with variable infeed did not show such clear increasing tendency and was equal approx. Ra 0.2–0.25 μm for all the grinding depths. A significant difference between surface roughness measured at the end of the workpiece after grinding with constant and variable infeed was observed as well. The values of surface roughness Ra decreased on average by approximately 26% when grinding with variable infeed. However, increasing the infeed during grinding did not result in a significant increase in Ra parameters measured in the middle of the workpiece (on average approx. 4% increase). No significant increase in surface roughness of grinded parts was measured in the middle of the workpiece, even though the machining load was higher, which may result from the higher stability of the machining with the additional grinding infeed. The reduction in surface roughness Ra measured at the beginning and at the end of the workpiece may result from the gradual entry and exit of the grinding wheel, which allowed for reducing the loading impact and thus improving the quality of the surface at those parts of the workpiece.

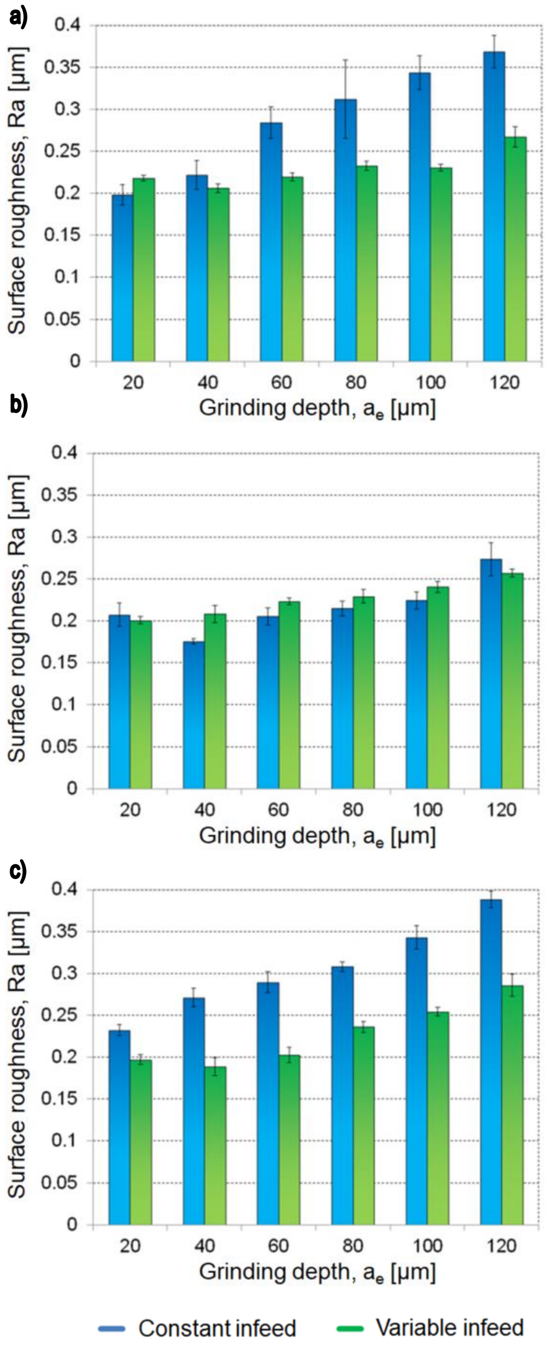

Fig. 8. Surface roughness Ra of the test parts: (a) at the beginning (b) in the middle (c) at the end

5. CONCLUSIONS

The article presents a method of increasing the shape and dimensional accuracy of low-stiffness shafts manufactured in a single pass of a grinding wheel in traverse grinding. The method consisted of applying additional infeed calculated in each position of the grinding wheel based on the measurement of the normal component of the grinding force. In order to prove its effectiveness, experimental tests were conducted. Low-stiffness shafts were grinded in a single pass of a grinding wheel with constant and variable infeed. The results showed that grinding with the use of the proposed method can significantly improve the quality of manufactured workpieces. For the analysed range of set grinding depths, grinding with variable infeed allowed reducing the cylindricity deviations to a few micrometres, which constitutes a decrease of, on average, approximately 82%. In addition, the maximum dimensional error was reduced by approx. 90% in comparison to grinding with constant grinding infeed. Grinding tests with the use of the method resulted in increasing the normal grinding force component, on average approximately by 11%. However, the increased load did not correspond with the increase in surface roughness. The measurements of Ra surface roughness parameter showed that at the beginning and at the end of the workpiece, grinding with variable infeed improved the quality of the surface. Thus, the presented method may constitute a viable option when grinding low-stiffness shafts in a single pass of a grinding wheel without the use of steady rests.

REFERENCES

1. Han X., Wu T. Analysis of acoustic emission in precision and high-efficiency grinding technology. Int J Adv Manuf Tech. 2013; 67(9):1997-2006.
2. Oczoś K. Characteristics of development trends in grinding with grinding wheels. Materials of XXIII Scientific Abrasive Conference .2000; 13-62.
3. Kopac J., Krajnik P. High-performance grinding – A review..J Mater Process Tech. 2006;175:278-284.
4. Klocke F., Barth S., Mattfeld P. High Performance Grinding. Procedia CIRP. 2016;46:266-271.
5. Klocke F., Soo L., Karpuschewski B., Webster J., Novovic D., Elfizy A., Axinte D., Tönissen S. Abrasive machining of advanced aerospace alloys and composites. CIRP Annals – Manufacturing Technology. 2015;64(2):581-604.
6. Kalchenko V., Pogiba N., Kalchenko D. Determination of Cutting Force Components in Creep-Feed Grinding of Revolution Surfaces Using an Oriented Elbor Wheel. J Superhard Mater. 2012;34(2): 118-130.
7. Żyłka Ł., Babiarz R. Dressing process in the grinding of aerospace blade root. J Mech Sci Technol. 2017;31(9): 4411-4417.
8. Webster J., Tricard M. Innovations in Abrasive Products for Precision Grinding. CIRP Annals. 2004;53(2):597-617.
9. Nadolny K. A review on single-pass grinding processes.. J Cent South Univ. 2013;20:1502-1509.
10. Burek J., Sułkowicz P., Babiarz R., Płodzień M. Cylindrical Continuous Path Controlled Grinding with Profile Grinding Wheel Type 1F1. Reszow Uniwersity of Technology Scientific Letters, Mechanics. 2017;89(4):449-456.
11. Marinescu I. D., Hitchiner M. P., Uhlmann E., Rowe W. B., Inasaki I. Handbook of Machining with Grinding Wheels. CRC Press,. 2016.
12. Urbicain G., Olvera D., Fernandez A., Rodriguez L., Tabernero L.N. Stability Lobes in Turning of Low Rigidity Components. Adv Mat Res. 2012;498:576-585.
13. Porzycki J., Batsch A., Oczoś K. A two-parameter adaptive control system for the traverse cylindrical grinding process. IFAC Proceedings Volumes. 1980;13(10):151-154.
14. Amitay G. Malkin S., Koren Y. Adaptive Control Optimization of Grinding. . J Eng Ind. 1981;103(1):103-108.

15. Gao Y., Jones B. Control of the traverse grinding process using dynamically active workpiece steadies. . Int J Mach Tool Manu. 1993;33(2):231-244.
16. Park C., Kim D., Lee S. Shape prediction during the cylindrical traverse grinding of a slender workpiece. J Mater Process Tech. 1999;88:23-32.
17. Choi H., Lee S. Machining error compensation of external cylindrical grinding using thermally actuated rest. Mechatronics. 2002;12: 643-656.
18. Kruszyński B., Lajmert W. An intelligent system for online optimization of the cylindrical traverse grinding operation. Int J Eng Manu. 2006;3:355-363.
19. Świć A., Taranenko W. Adaptive control of machining accuracy of axial – symmetrical lowrigidity parts in elastic – deformable state. Maintenance and Reliability. 2012;3:215-221.
20. Parenti P., Bianchi G. Model-based adaptive process control for surface finish improvement in traverse grinding. Mechatronics. 2016;36:97-111.
21. Saljẻ E., Mushardt H. Aufbau einer Optimierregelung für einen mehrstufigen Schleifprozess. Werkstattstechnik. 1975;65:335-338.
22. Burek J. Stabilization of normal grinding force component in multistage plunge grinding. PhD thesis (Rzeszow University of Technology). 1985.
23. Onishi T., Kodani T., Ohashi K., Sakakura M., Tsukamoto S. Study on the Shape Error in the Cylindrical Traverse Grinding of a Workpiece with High Aspect Ratio. Adv Mat Res. 2014;10(17):78-81.
24. Burek J., Sułkowicz P., Babiarz R. Cylindricity error measurement and compensation in traverse grinding of low-stiffness shafts. Mechanik. 2018;91(11):970-972.

Paweł Sułkowicz: https://orcid.org/0000-0003-4604-7683

Robert Babiarz: https://orcid.org/0000-0002-3418-6670

Jan Burek: https://orcid.org/0000-0003-2664-5248

Jarosław Buk: https://orcid.org/0000-0002-8997-4877

Kamil Gancarczyk: https://orcid.org/0000-0002-5938-6636

DOI 10.2478/ama-2022-0043

ANALYSIS OF THE DETERMINATION OF THE ACCURACY PARAMETER FOR DUAL RECEIVERS BASED ON EGNOS SOLUTION IN AERIAL NAVIGATION

Kamil KRASUSKI*, Janusz ĆWIKLAK*, Mieczysław BAKUŁA*, Magda MROZIK**

*Institute of Navigation, Polish Air Force University, ul. Dywizjonu 303 nr 35, 08-521 Dęblin, Poland
**Faculty of Transport and Aviation Engineering, Silesian University of Technology,
ul. Krasińskiego 8, 40-019 Katowice, Poland.

k.krasuski@law.mil.pl, j.cwiklak@law.mil.pl, m.bakula@law.mil.pl, magda.mrozik@polsl.pl

received 6 July 2022, revised 21 August 2022, accepted 22 August 2022

Abstract: The paper presents the results of research on the determination of the accuracy parameter for European Geostationary Navigation Overlay System (EGNOS) positioning for a dual set of on-board global navigation satellite system (GNSS) receivers. The study focusses in particular on presenting a modified algorithm to determine the accuracy of EGNOS positioning for a mixed model with measurement weights. The mathematical algorithm considers the measurement weights as a function of the squared inverse and the inverse of the position dilution of precision (PDOP) geometrical coefficient. The research uses actual EGNOS measurement data recorded by two on-board GNSS receivers installed in a Diamond DA 20-C airplane. The calculations determined the accuracy of EGNOS positioning separately for each receiver and the resultant value for the set of two GNSS receivers. Based on the conducted tests, it was determined that the mixed model with measurement weights in the form of a function of the inverse square of the PDOP geometrical coefficient was the most efficient and that it improved the accuracy of EGNOS positioning by 37%–63% compared to the results of position errors calculated separately for each GNSS receiver.

Keywords: SBAS, EGNOS, accuracy, GNSS receivers, position errors

1. INTRODUCTION

Satellite-based augmentation system (SBAS) positioning systems enable the determination of the four main parameters of global navigation satellite system (GNSS) positioning in aviation, i.e. of the accuracy, continuity, availability and integrity parameters [1, 2]. Accuracy is understood as the comparison of the determined coordinates of the aerial vehicle with the reference trajectory of the flight. Thus, it may be stated that the accuracy of SBAS positioning in aerial navigation is the difference between the coordinates of the aerial vehicle determined using the SBAS solution and the reference position of the flight [3]. The availability parameter defines the period during which the SBAS system was functioning and enabled a navigation solution of the position of the aircraft without any interruptions or failures [4]. The continuity of SBAS positioning is defined as the capacity of the system to function without any unplanned failures on the route of the flight [5]. Finally, the integrity as a quality parameter of GNSS positioning is, in fact, a measure of the trust that can be placed on the measurement results obtained from the navigation solution [6]. If this definition is referred directly to aviation, integrity describes the level of trust in navigating both in the horizontal and vertical planes. Among the parameters of the quality of SBAS positioning, the accuracy is the most important, and it requires continuous tests and analyses for specific types of aviation operations.

2. SCIENTIFIC KNOWLEDGE ANALYSIS

The accuracy of SBAS positioning has been studied and analysed in numerous aviation experiments. In our part of the globe, these analyses focussed mainly on the functioning and operation of the European Geostationary Navigation Overlay System (EGNOS) system [7]. The institutions that have been actively involved in the research on the application of the EGNOS support system in Polish aviation since the beginning include the Polish Air Force University in Dęblin and the University of Warmia and Mazury in Olsztyn. In Poland, the first tests with use of the EGNOS system were started in 2003. At that time, the EGNOS system was in the EGNOS System Test Bed (ESTB) test phase [8]. The research determined the accuracy of EGNOS positioning for on-board GNSS receivers. The coordinates of the aerial vehicle from the EGNOS solution were compared to the reference position of the flight calculated with the RTK-OTF (Real Time Kinematic – On The Fly) differential technique [9]. It should be added that, during the realisation of test flights, numerous breakdowns in the functioning of the EGNOS system were noted, which also led to the deficiencies in the determination of the accuracy of EGNOS positioning in measurement epochs. Further aviation tests were conducted in 2007, when the accuracy of EGNOS positioning was analysed as part of the Open Service (OS) system of the EGNOS system [10]. The flight experiment analysed the accuracy of EGNOS positioning for various classes of GNSS navigation receivers. During the analyses, once again, interruptions in receiving the corrections from the EGNOS system were noted, which resulted in a deteriorated accuracy of EGNOS positioning. The subsequent aviation experiments conducted with the use of the EGNOS system took place in the years 2010–2011, when a new service was introduced in EGNOS positioning, i.e. the Safety of Life (SoL) service [11]. For example, Grzegorzewski et al. [12] presented the results of the accuracy of EGNOS positioning for test flights conducted in south-eastern Poland. The analysis of the results revealed a low accuracy of EGNOS positioning for flights performed in the area of Chełm. Additionally, the results for EGNOS positioning were worse than those for automated GPS (Global Positioning System) positioning. Further flight experiments with the EGNOS system are described in Fellner and Jafernik [13] and Fellner et al. [14]. These studies present the results of EGNOS positioning as part of the SBAS (Satellite Based Augmentation system) APV (Approach with Vertical Guidance) landing procedures for the airports in Katowice and Mielec.

Later, more studies were conducted to assess the accuracy of EGNOS positioning, for the GNSS reference station installed at the Olsztyn-Datki airport in north-eastern Poland [15]. The present research project aimed to present the selection of the best location and the manner of stabilising the station to monitor GNSS signals at the airport. A station that locally monitors the signal from GPS and EGNOS satellites will, in consequence, improve the safety during the landing of aerial vehicles that sue the GNSS approach procedures and will allow determining the quality of GPS/EGNOS positioning in aviation. Other research experiments with the use of the EGNOS system in aerial navigation were conducted in Dęblin and Olsztyn, where physical reference GNSS stations were installed in order to monitor the quality of GPS/EGNOS data [16, 17]. The studies involved calculating the accuracy and integrity of EGNOS positioning in real time. Similar research works were described in the studies of Felski and Nowak [18] and Jafernik [19]. These articles also presented the results of the accuracy of EGNOS positioning for GNSS reference stations installed in Polish airports. The calculations were performed in real time and in post-processing mode. The next reproach experiment is described in the research of Ciećko and Grunwald [20]. It comprised the analysis of the accuracy of EGNOS positioning in a trial flight test for the purposes of checking the requirements of en-route navigation and precise landing approach PA category I.

As far as research conducted in Europe is concerned, there is a significant body of research that deserves mention [21–26]. In these studies, the accuracy of EGNOS positioning was determined for the given landing approach procedure, mainly precise procedure PA (Precision Approach) category I or SBAS APV.

The analysis of the state of knowledge reveals the following:
- Since the beginning of research with the use of the EGNOS system in aviation, the accuracy parameter was the essential parameter to be determined in aerial navigation;
- The determined values of the accuracy parameter have changed with the development, modernisation and introduction of the new EGNOS positioning services, e.g. based on data from EGNOS satellites: PRN123, PRN126 and PRN136;
- The accuracy of EGNOS positioning in flight experiments was determined and calculated for the EGNOS solution from a single receiver;
- The analysis of the state of knowledge shows that the topic of analysing the accuracy of EGNOS positioning was very important, which is reflected in the number of research projects.

In reference to the analysis of the state of knowledge, the existing scope of research may be extended to include the following elements:
- The accuracy of EGNOS positioning in flight tests should be determined based on a multi-receiver EGNOS solution;
- The research on the accuracy of EGNOS positioning in flight tests should use at least two GNSS receivers with the EGNOS tracking function;
- If at least two GNSS receivers are used, various mathematical models should be applied to enable the determination of the resultant EGNOS positioning accuracy.

This article presents the strategy of determining the parameter of accuracy for EGNOS positioning for two GNSS receivers. For this purpose, two different models of determining the EGNOS positioning accuracy were presented and applied in practice. The numerical calculations were based on a mixed model for various measurement weights to determine the accuracy for a set of two GNSS receivers. The obtained research results revealed that the application of the mixed model in calculations significantly improved the accuracy of EGNOS positioning.

Summarising, the main author's contribution to the work is as follows:
- development of an integration model of the EGNOS solution for two GNSS receivers,
- implementation of a linear combination model based on weighting factors,
- application of selected different weighting factors,
- demonstration of the effectiveness of the proposed model for determining the accuracy of the EGNOS solution for two GNSS receivers,
- implementation of the developed algorithm for GPS and EGNOS kinematic data from an aviation experiment.

The forthcoming portions of the article are classifiable as follows: The third section presents the research method, the fourth the research test, the fifth the research results, the sixth discusses the results and the final section presents the conclusions.

3. RESEARCH METHOD

The research methodology was based on two mathematical models that enable the determination of the accuracy parameter of EGNOS positioning for a measurement system consisting of two GNSS receivers. The first mathematical model concerns the determination of the accuracy of EGNOS positioning for the mixed model that is based on the measurement weights (α, β), as shown in Eq. (1):

$$\begin{cases} dB = \alpha \cdot dB_{Rx1} + \beta \cdot dB_{Rx2} \\ dL = \alpha \cdot dL_{Rx1} + \beta \cdot dL_{Rx2} \\ dh = \alpha \cdot dh_{Rx1} + \beta \cdot dh_{Rx2} \end{cases} \tag{1}$$

where (dB, dL, dh) are position errors, resultant value of the accuracy of EGNOS positioning, $Rx1$ is GNSS receiver 1, $Rx2$ is GNSS receiver 2, α is measurement weight for receiver $Rx1$, $\alpha = \frac{1}{PDOP_{Rx1}^2}$, $PDOP_{Rx1}$ is value of the position dilution of precision (PDOP) geometrical coefficient [27] for receiver $Rx1$, β is measurement weight for receiver $Rx2$, $\beta = \frac{1}{PDOP_{Rx2}^2}$, $PDOP_{Rx2}$ is value of the PDOP geometrical coefficient for receiver $Rx2$, $(dB_{Rx1}, dL_{Rx1}, dh_{Rx1})$ are position errors [28], positioning accuracy determined from a single EGNOS solution for receiver $Rx1$, and $(dB_{Rx2}, dL_{Rx2}, dh_{Rx2})$ are position errors [28], positioning accuracy determined from a single EGNOS solution for receiver $Rx2$.

Eq. (1) describes an algorithm of the mixed model for the determination of the accuracy parameter of EGNOS positioning. In Eq. (1), measurement weights (α, β) are used for the model of integrating the values of accuracy of EGNOS positioning for a single GNSS receiver. The measurement weights (α, β) were calculated as a function of the inverse square of the PDOP geometrical coefficient determined for a single EGNOS solution from a single GNSS receiver. The mathematical model (1) ensures a linear combination of the position errors $(dB_{Rx1}, dL_{Rx1}, dh_{Rx1})$ determined for receiver $Rx1$ and the position errors $(dB_{Rx2}, dL_{Rx2}, dh_{Rx2})$ determined for receiver $Rx2$. As a result, Eq. (1) will finally enable the determination of the resultant accuracy of EGNOS positioning for two GNSS receivers.

The second mathematical solution comprises a mixed model that uses measurement weights (γ, δ) to determine the accuracy of EGNOS positioning, as shown in Eq. (2):

$$\begin{cases} dB = \gamma \cdot dB_{Rx1} + \delta \cdot dB_{Rx2} \\ dL = \gamma \cdot dL_{Rx1} + \delta \cdot dL_{Rx2} \\ dh = \gamma \cdot dh_{Rx1} + \delta \cdot dh_{Rx2} \end{cases} \tag{2}$$

where γ is measurement weight for receiver $Rx1$, $\gamma = \frac{1}{PDOP_{Rx1}}$, δ is measurement weight for receiver $Rx2$ and $\delta = \frac{1}{PDOP_{Rx2}}$.

Eq. (2) describes an algorithm of the weighted average model for the determination of the accuracy parameter of EGNOS positioning. In Eq. (2), measurement weights (γ, δ) are used for the model of integrating the values of accuracy of EGNOS positioning for a single GNSS receiver. The (γ, δ) measurement weights were calculated as the inverse of the PDOP geometrical coefficients determined for a single EGNOS solution and a single GNSS receiver. Similarly to Eq. (1), the mathematical model (2) provides a linear combination of the position errors $(dB_{Rx1}, dL_{Rx1}, dh_{Rx1})$ determined for receiver $Rx1$ and the position errors $(dB_{Rx2}, dL_{Rx2}, dh_{Rx2})$ determined for receiver $Rx2$. Based on that, Eq. (2) enables the determination of the resultant accuracy of EGNOS positioning for two GNSS receivers in another way.

4. RESEARCH TEST

The presented algorithm for the determination of the value of accuracy of EGNOS positioning with the use of two GNSS receivers has been verified and tested during a flight experiment. The experiment was conducted in north-eastern Poland in the autumn of 2020. The flight experiment comprised a test flight with a Diamond DA 20-C aircraft. Figs. 1 and 2 present the horizontal and vertical trajectories of the flight of the aircraft, respectively. The test flight on the route Olsztyn-Suwałki-Olsztyn lasted approximately 4 h. Two geodesic receivers (one manufactured by Septentrio (manufactory: Belgium) and another by Trimble (manufactory: USA) were installed on board the aircraft. For the Septentrio receiver, the AT1675-29 PolaNt* GG satellite antenna was used, and for the Trimble receiver, the GA830 type antenna was used [29]. These receivers recorded GNSS data at 1-s intervals. The collected GNSS data enabled determining the coordinates of the airplane from the EGNOS solution for each of the receivers separately [30] and then computation of the position errors, i.e. in this case, the parameters $(dB_{Rx1}, dL_{Rx1}, dh_{Rx1})$ and $(dB_{Rx2}, dL_{Rx2}, dh_{Rx2})$. The position errors $(dB_{Rx1}, dL_{Rx1}, dh_{Rx1})$ and $(dB_{Rx2}, dL_{Rx2}, dh_{Rx2})$ were determined based on the comparison of the coordinates of the aircraft obtained from GPS solution with EGNOS corrections and the reference position of the flight calculated with the use of the RTK-OTF differential technique [8, 10]. The aircraft position was estimated based on GPS data as a GNSS system and also EGNOS corrections as a SBAS system [31, 32].

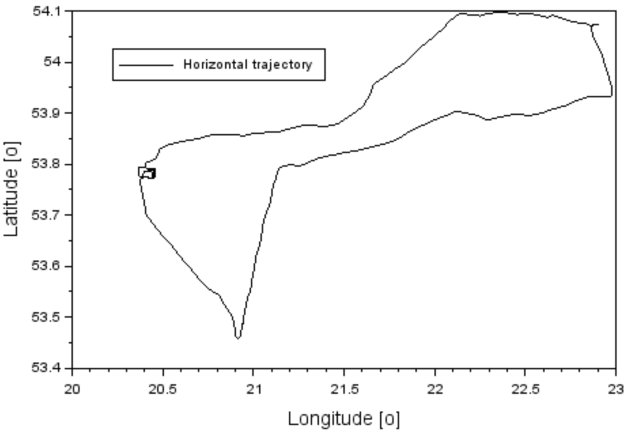

Fig. 1. The horizontal trajectory of aircraft (own study)

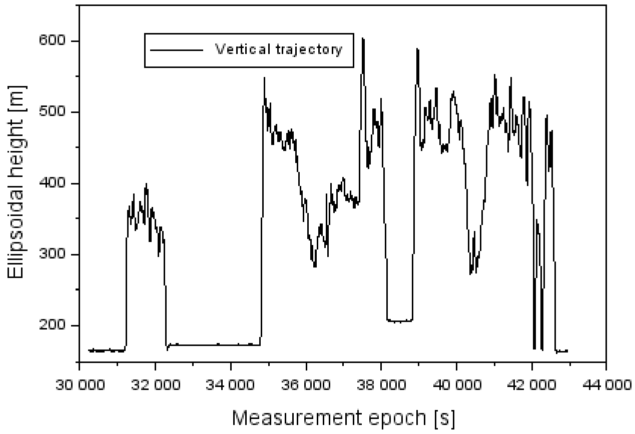

Fig. 2. The vertical trajectory of aircraft (own study)

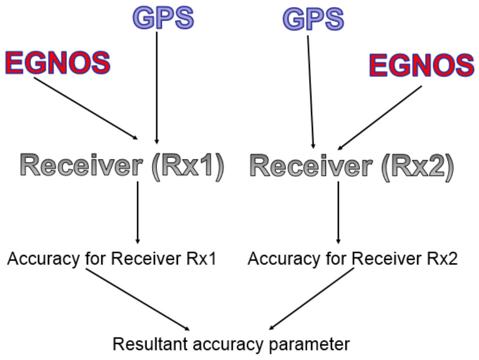
GPS
EGNOS
GPS
EGNOS
Receiver (Rx1)
Receiver (Rx2)
Accuracy for Receiver Rx1
Accuracy for Receiver Rx2
Resultant accuracy parameter

Fig. 3. The flowchart of presented mathematical algorithm (own study). EGNOS, European Geostationary Navigation Overlay System

The final parameters $(dB_{Rx1}, dL_{Rx1}, dh_{Rx1})$ and $(dB_{Rx2}, dL_{Rx2}, dh_{Rx2})$ define the accuracy of GPS + EGNOS positioning for each GNSS receiver separately. The subsequent stage consisted in the development and practical application of the algorithms (1) and (2) for the purposes of determining the resultant accuracy of GPS + EGNOS positioning for a set of two GNSS receivers. For this purpose, a digital application was developed in the Scilab v.6.0.0 programming language [33], which was developed by writing the source codes for Eqs (1) and (2). As a result, the positioning accuracy was calculated for the mixed model, the weighted average model and the arithmetic average model. The results of the conducted numerical analyses are presented in Section 5. Fig. 3 shows the final flowchart of the computational algorithm developed for Eqs (1) and (2).

5. RESEARCH RESULTS

The presentation of the test results begins with presenting the values of position errors $(dB_{Rx1}, dL_{Rx1}, dh_{Rx1})$ and $(dB_{Rx2}, dL_{Rx2}, dh_{Rx2})$ obtained separately for each GNSS receiver. Fig. 4 presents the values of the parameters $(dB_{Rx1}, dL_{Rx1}, dh_{Rx1})$. In the presented diagrams, the Trimble receiver is referred to as $Rx1$. The values of the position errors are as follows: for the B (Latitude) component, from –2.37 m to +1.15 m; for the L (Longitude) component, from –2.08 m to +1.88 m; and for the h (ellipsoidal height) component, from –2.47 m to +5.64 m. It is worth noting that since the epoch of 36,000 s the positioning accuracy for the *Rx*1 receiver has been decreasing. This is due to a decrease in the number of tracked GPS satellites, which in turn affects the availability of EGNOS corrections for GPS satellites. From the epoch of 30,000 s to 36,000 s, the number of GPS satellites ranged from 6 to 13, and from the epoch of 36,000 s to the end of the experiment, it dropped sharply from 10 to 7. The smaller the number of tracked GPS satellites, the larger the increase in the PDOP geometric coefficient, as shown in Fig. 6.

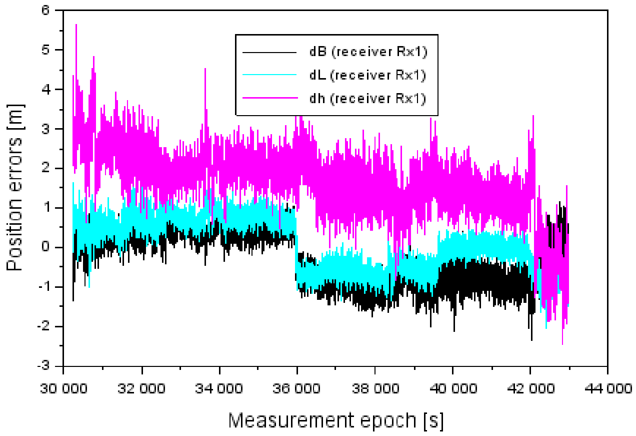

Fig. 4. The position errors of EGNOS positioning for receiver Rx1 (own study)

Fig. 5 presents the results of the values of the parameters $(dB_{Rx2}, dL_{Rx2}, dh_{Rx2})$. In the presented diagrams, the Septentrio receiver is referred to as $Rx2$. The values of the position errors are as follows: for the B component, from –12.65 m to +2.08 m; for the L component, from –9.63 m to +7.22 m; and for the h component, from –1.38 m to +14.34 m. The comparison of the position error results for the receivers $Rx1$ and $Rx2$ reveals that the divergence in position errors is significantly higher for the Septentrio receiver. This is particularly visible in the initial phase of the flight, when the accuracy of EGNOS positioning for receiver $Rx2$ falls below ±10 m. This is due to the low number of GPS satellites being tracked, i.e. only five satellites. This, in turn, affects the deterioration of the positioning conditions, hence the high values of the PDOP coefficient.

Fig. 6 presents the values of PDOP parameter for both GNSS receivers. In the initial measurement epochs, the values of the $PDOP$ coefficient for receiver $Rx2$ amount to almost 8.7, which results in a low accuracy of EGNOS positioning. For the other measurement epochs, the values of the $PDOP$ coefficient are lower than 2.5. In turn, the PDOP values for the $Rx1$ receiver range from 1.6 to 8.4. As for the $Rx2$ receiver, the highest PDOP values for the $Rx1$ receiver are visible in the initial phase of the experiment, where the number of GPS satellites is five. This means that the accuracy of EGNOS positioning decreases with the increase in the PDOP coefficient.

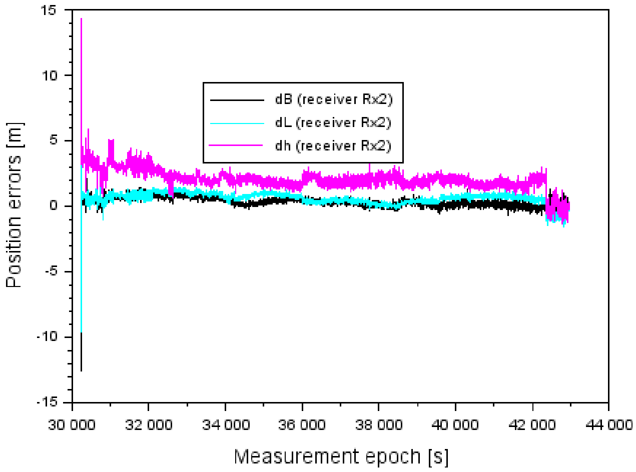

Fig. 5. The position errors of EGNOS positioning for receiver Rx2 (own study). EGNOS, European Geostationary Navigation Overlay System

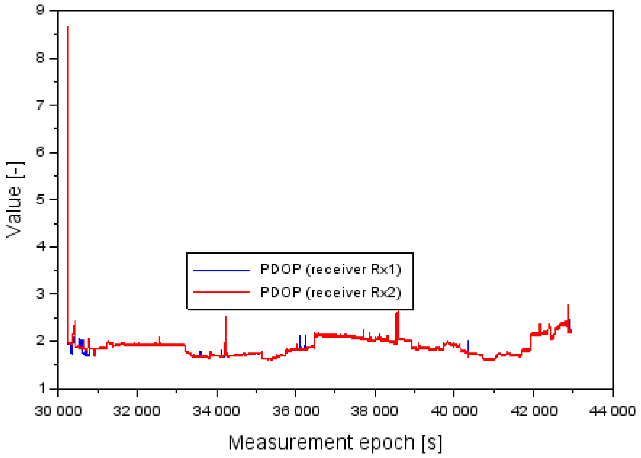

Fig. 6. The values of PDOP parameters (own study). PDOP, position dilution of precision

The further analyses of the obtained results included the values of the weight coefficients (α, β) for Eq. (1), which are presented in Fig. 7. The values of the α coefficient range from 0.014 to 0.394, while the values of the β coefficient range from 0.013 to

0.395. One may notice that the values of these coefficients (α,β) decrease with the increase in the value of the $PDOP$. These relations may also be reversed: as the $PDOP$ geometrical coefficient decreases, the weight coefficients (α, β) increase.

Fig. 8 presents the determined values of the accuracy of EGNOS positioning for two receivers, calculated from Eq. (1). The values of the positioning errors for component B ranged from –0.58 m to +0.64 m while the values of positioning errors for the L component ranged from –0.62 m to +1.07 m; and finally, the values of the positioning error for the h component ranged from–0.54 m to +2.69 m. The results presented in Fig. 8 demonstrate that the best accuracy results were obtained for the B component, while the worst ones for the vertical component h.

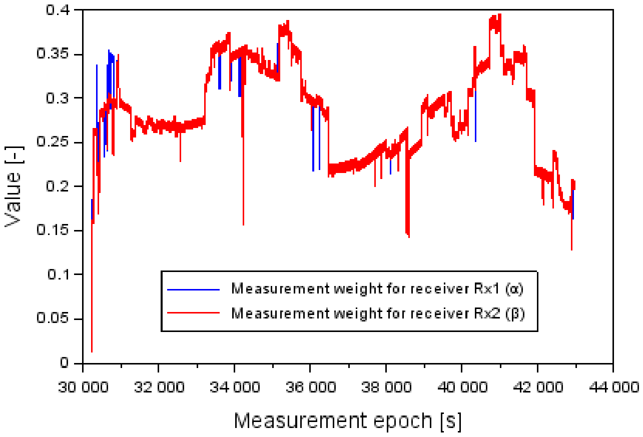

Fig. 7. The values of measurement weights (α, β) (own study)

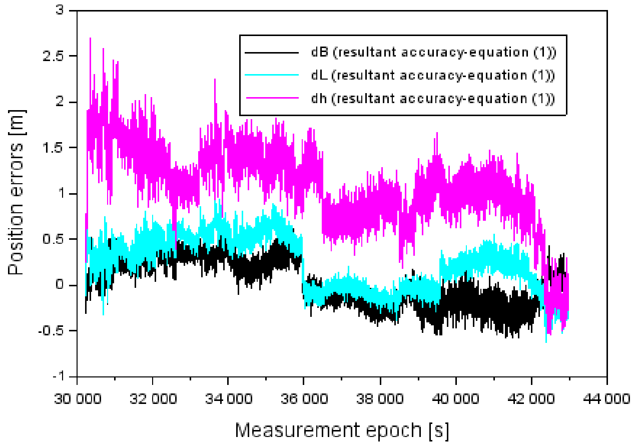

Fig. 8. The resultant accuracy of EGNOS dual receivers' solution based on Eq. (1) (own study). EGNOS, European Geostationary Navigation Overlay System

Fig. 9 presents the values of the weight coefficients (γ, δ) for Eq. (2). The values of the γ coefficient ranged from 0.019 to 0.628, while those of the δ coefficient ranged from 0.015 to 0.628. It should be noted that the change in the (γ, δ) coefficient depends on the value of the $PDOP$ parameter.

Fig. 10 presents the determined values of the accuracy of EGNOS positioning for two receivers, calculated from Eq. (2). The values of the positioning errors for component B ranged from –1.58 m to +1.22 m while the values of positioning errors for the L component ranged from –1.46 m to +1.80 m; and finally, the values of the positioning error for the h component ranged from –1.18 m to +5.07 m. The results presented in Fig. 10 demonstrate that the best accuracy results were obtained for the B component, while the worst ones for the vertical component h.

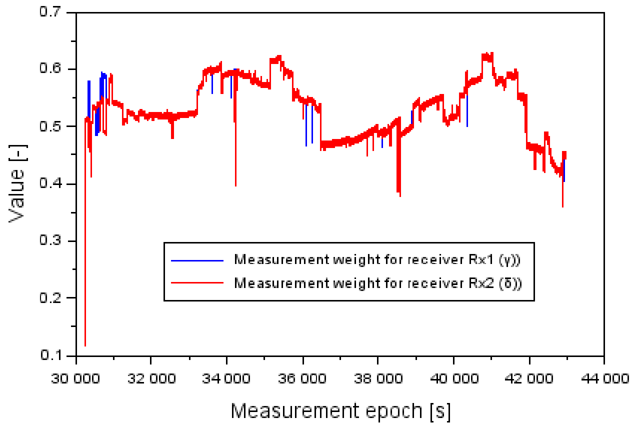

Fig. 9. The values of measurement weights (γ, δ) (own study)

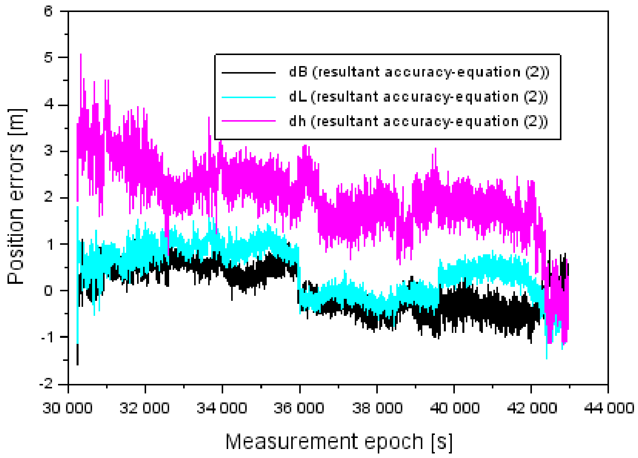

Fig. 10. The resultant accuracy of EGNOS dual receivers' solution based on Eq. (2) (own study). EGNOS, European Geostationary Navigation Overlay System

6. DISCUSSION

The discussion has been divided into two topics. In the first part, the authors present the influence of the algorithms (1) and (2) on the improvement of the accuracy of EGNOS positioning for a dual set of GNSS receivers. Later, in the second part, the obtained research results are compared with the existing state of knowledge.

Fig. 11 presents the results of the comparison of the obtained average positioning errors dB for receivers $Rx1$ and $Rx2$, based on Eqs (1) and (2). As one may notice, the highest positioning accuracy for the B component was obtained from Eq. (1). On the other hand, the lowest accuracy along the B axis is noticeable for the $Rx1$ receiver. The average accuracy values for the B coordinate are 0.62 m for receiver $Rx1$, 0.40 m for receiver $Rx2$, 0.23 m for Eq. (1) and 0.43 m for Eq. (2). It is worth adding that the mathematical model (1) improved the positioning accuracy along the B axis by 63% compared to the results for receiver $Rx1$, 42% compared to the results for receiver $Rx2$ and 46% compared to the results for the mathematical model (2). On the other hand, the application of Eq. (2) only improved the accuracy of positioning along the B axis by 31% compared to the results obtained for receiver $Rx1$.

Fig. 12 presents the results of the comparison of the obtained average positioning errors dL for receivers $Rx1$ and $Rx2$, based on Eqs (1) and (2). As one may notice, the highest positioning accuracy for the L component was obtained from Eq. (1). On the other hand, the lowest accuracy along the L axis was noticeable for the $Rx2$ receiver. The average accuracy values for the L coordinate are as follows: 0.57 m for receiver $Rx1$, 0.67 m for receiver $Rx2$, 0.30 m for Eq. (1) and 0.55 m for Eq. (2). It is worth adding that the mathematical model (1) improved the positioning accuracy along the L axis by 48% compared to the results for receiver $Rx1$, 55% compared to the results for receiver $Rx2$ and 45% compared to the results for mathematical model (2). On the other hand, the application of Eq. (2) improved the positioning accuracy along the L axis by 5% compared to the results for receiver $Rx1$ and 18% as compared to those for receiver $Rx2$.

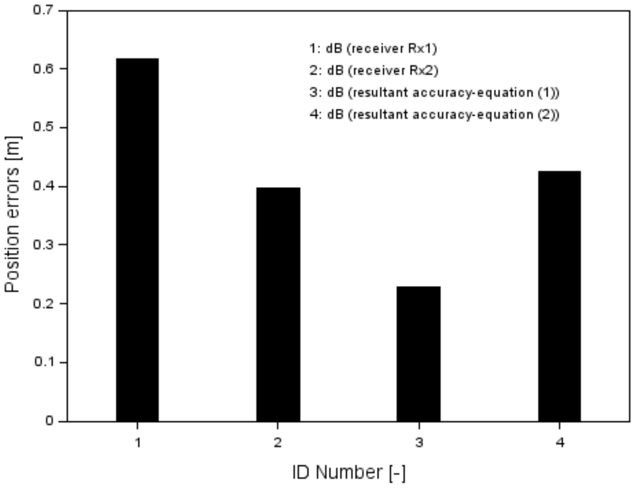

Fig. 11. The comparison of average value of accuracy of latitude (own study)

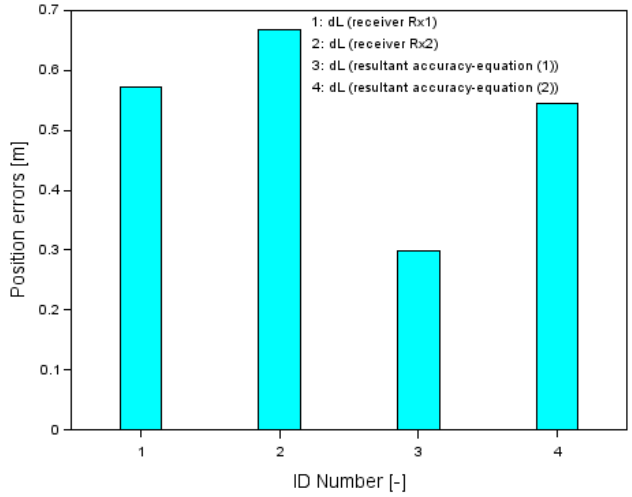

Fig. 12. The comparison of average value of accuracy of longitude (own study)

Fig. 13 presents the results of the comparison of the obtained average positioning errors dh for receivers $Rx1$ and $Rx2$, based on Eqs (1) and (2). As one may notice, the highest positioning accuracy for the h component was obtained from Eq. (1). On the other hand, the lowest accuracy along the h axis was noticeable for the $Rx2$ receiver. The average accuracy values for the h coordinate are as follows: 1.75 m for receiver $Rx1$, 2.06 m for receiver $Rx2$, 1.10 m for Eq. (1) and 2.04 m for Eq. (2). It is worth adding that the mathematical model (1) improved the positioning accuracy along the h axis by 37% compared to the results for receiver $Rx1$, 47% compared to the results for receiver $Rx2$ and 46% compared to the results for the mathematical model (2). On the other hand, the application of Eq. (2) improved the positioning accuracy along the h axis by 16% compared to the results for receiver $Rx1$ and 1% compared to those for receiver $Rx2$.

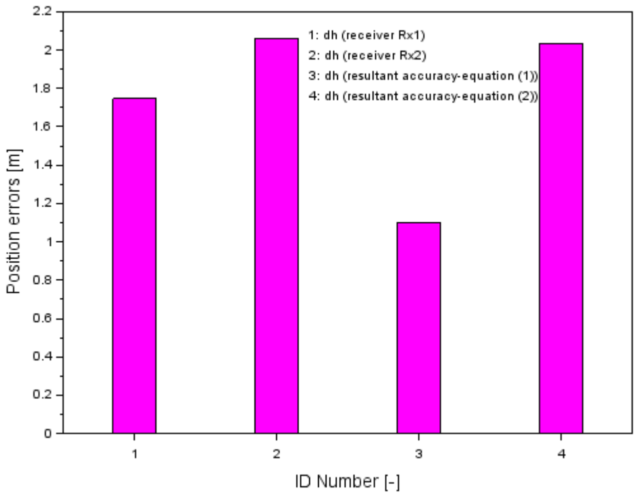

Fig. 13. The comparison of average value of accuracy of ellipsoidal height (own study)

The further part of the discussion shows the effectiveness and efficiency of the research method presented in the paper. Specifically, the mathematical algorithm for Eqs (1) and (2) has been changed with new weighting factor values as described below:

$$\begin{cases} dB = \rho \cdot dB_{Rx1} + \sigma \cdot dB_{Rx2} \\ dL = \rho \cdot dL_{Rx1} + \sigma \cdot dL_{Rx2} \\ dh = \rho \cdot dh_{Rx1} + \sigma \cdot dh_{Rx2} \end{cases} \tag{3}$$

where ρ is measurement weight for receiver $Rx1$, $\rho = \frac{1}{NS_{Rx1}}$, σ is measurement weight for receiver $Rx2$, $\sigma = \frac{1}{NS_{Rx2}}$, NS_{Rx1} is the number of GPS satellite with EGNOS corrections for receiver $Rx1$ [34] and NS_{Rx2} is the number of GPS satellite with EGNOS corrections for receiver $Rx2$.

Eq. (3) uses a different weighting factor calculated as a function of the number of GPS satellites for which EGNOS corrections were determined. The number of GPS satellites represents the satellites tracked by the GNSS receivers during the flight experiment [35]. Fig. 14 shows the test results for the mathematical algorithm used (3). The values of the positioning errors for component B ranged from –2.69 m to +0.26 m while the values of positioning errors for the L component ranged from –1.94 m to +1.64 m; and finally, the values of the positioning error for the h component ranged from –0.36 m to +3.41 m.

The obtained results of the EGNOS positioning accuracy for the mathematical model (3) show high efficiency in relation to the results obtained from algorithms (1) and (2). It is worth noting that the average dB accuracy was 0.08 m for algorithm (3), while 0.23 m for Eq. (1) and 0.43 m for Eq. (2). This shows the improvement of the EGNOS positioning accuracy from Eq. (3) by 65% over mathematical model (1) and 81% over mathematical model (2). In addition, the average dL accuracy was 0.10 m for algorithm (3), while 0.30 m for Eq. (1) and 0.55 m for Eq. (2). This shows the improvement of the EGNOS positioning accuracy from Eq. (3) by 67% over mathematical model (1) and 82% over mathematical model (2). Moreover, the average dh accuracy was 0.38 m for algorithm (3), while 1.10 m for Eq. (1) and 2.04 m for Eq. (2). This shows the improvement of the EGNOS positioning accuracy from Eq. (3) by 65% over mathematical model (1) and 81% over mathematical model (2).

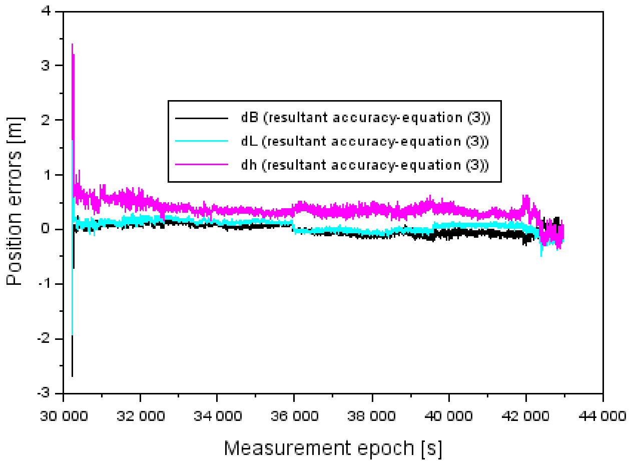

Fig. 14. The resultant accuracy of EGNOS dual receiver solution based on Eq. (3) (own study). EGNOS, European Geostationary Navigation Overlay System

To conclude the discussion, the obtained research results were compared to the analysis of the state of knowledge. The comparison included tests conducted during flight. The obtained positioning accuracy was better than that presented in several studies encountered in the literature [8, 10, 12, 20], all of which involve research works conducted in Poland. On the other hand, the results are comparable to those published in other studies [21, 23, 24, 26].

7. CONCLUSIONS

The paper presents the algorithms that enable an improvement in the accuracy of EGNOS positioning for a dual set of GNSS receivers. In particular, the study presents a computational diagram of a mixed model to improve the accuracy of EGNOS positioning in aerial navigation. In order to achieve it, various measurement weights were applied, which depended on the value of the PDOP geometrical coefficient. The weights were calculated as the inverse square of the PDOP coefficient and the inverse of the PDOP coefficient itself. This enabled performing a linear combination of single position error results from the EGNOS solution for a single GNSS receiver. This was the basis for developing an algorithm to determine the resultant accuracy of EGNOS positioning for two on-board GNSS receivers. The calculations were conducted with the use of actual navigation data from the EGNOS solution obtained from two GNSS receivers installed on board the Diamond DA 20-C aircraft. The final algorithm to improve the accuracy of EGNOS positioning was written in the Scilab v.6.0.0 language environment. The obtained results demonstrated the following:

- The application of Eq. (1) improved the positioning accuracy along the B axis by 63% compared to the results for receiver $Rx1$, 42% compared to the results for receiver $Rx2$ and 46% compared to the results for the mathematical model (2);
- The application of Eq. (2) only improved the accuracy of positioning along the B axis by 31% compared to the results obtained for receiver $Rx1$;
- Mathematical model (1) improved the positioning accuracy along the L axis by 48% compared to the results for receiver $Rx1$, 55% compared to the results for receiver $Rx2$ and 45% compared to the results for the mathematical model (2);
- The application of Eq. (2) improved the positioning accuracy along the L axis by 5% compared to the results for receiver $Rx1$ and 18% compared to those for receiver $Rx2$;
- The mathematical model (1) improved the positioning accuracy along the h axis by 37% compared to the results for receiver $Rx1$, 47% compared to the results for receiver $Rx2$ and 46% compared to the results for the mathematical model (2);
- The application of Eq. (2) improved the positioning accuracy along the h axis by 16% compared to the results for receiver $Rx1$ and 1% compared to those for receiver $Rx2$.

The results of research demonstrated that the mathematical model developed to improve the accuracy of EGNOS positioning that used measurement weights as a function of the inverse square of the PDOP coefficient proved to be the most effective and yielded the best results in navigation calculations.

REFERENCES

1. Felski A, Banaszek K, Woźniak T, Zakrzewski P. Accuracy of EGNOS service in airport operations. Zeszyty Naukowe Marynarki Wojennej. 2011;LII, 1(184): 31-44. (In Polish)
2. Kaleta W. EGNOS Based APV Procedures Development Possibilities In The South-Eastern Part Of Poland. Ann. Navig. 2014;21: 85–94.
3. International Civil Aviation Organization. ICAO Standards and Recommended Practices (SARPS), Annex 10, Volume I (Radio Navigation Aids), 2006. Available at: http://www.ulc.gov.pl/pl/prawo/prawomi%C4%99dzynarodowe/206-konwencje.
4. Specht C. Availability and reliability of the navigation systems - structure modeling. TTS Technika Transportu Szynowego. 2013; 20(10): 2539-546. (In Polish)
5. Malarski M, Banaszek K. Effect of aircraft precision navigation on airport capacity. Prace Naukowe Politechniki Warszawskiej. Transport. 2011;80: 49-74. (In Polish)
6. Zalewski P. SBAS integrity data in e-navigation systems. WUT Journal of Transportation Engineering. 2016;113: 495-506.
7. Specht M. Determination of Navigation System Positioning Accuracy Using the Reliability Method Based on Real Measurements. Remote Sens. 2021;13: 4424.
8. Grzegorzewski M. Navigating an aircraft by means of a position potential in three dimensional space. Ann. Navig. 2005;9: 111.
9. Grzegorzewski M, Jaruszewski W, Fellner A, Oszczak S, Wasilewski A, Rzepecka Z, Kapcia J, Popławski T. Preliminary results of DGPS/DGLONASS aircraft positioning in flight approaches and landings. Ann. Navig. 1999;1: 41–53.
10. Grzegorzewski M, Ciećko A, Oszczak S, Popielarczyk D. Autonomous and EGNOS Positioning Accuracy Determination of Cessna Aircraft on the Edge of EGNOS Coverage. In: Proceedings of the 2008 National Technical Meeting of The Institute of Navigation, San Diego, CA, USA, 28–30 January 2008;407–410.
11. Filip A, Bažant L, Mocek H. The experimental evaluation of the EGNOS safety-of-life services for railway signalling. WIT Transactions on The Built Environment. 2010;114: 735-745.
12. Grzegorzewski M, Światek A, Ciećko A, Oszczak S, Ćwiklak J. Study of EGNOS safety of life service during the period of solar maximum activity. Artif. Satell. 2012;47: 137–145.

DOI 10.2478/ama-2022-0043

13. Fellner A, Jafernik H. Airborne measurement system during validation of EGNOS/GNSS essential parameters in landing. Rep. Geod. Geoinf. 2014;96: 27–37.
14. Fellner A, Fellner R, Piechoczek E. Pre-flight validation RNAV GNSS approach procedures for EPKT in “EGNOS APV Mielec project”. Sci. J. Sil. Univ. Technol. Series Transp. 2016;90: 37–46.
15. Ciećko A, Grunwald G, Kaźmierczak R, Tanajewski D, Bakuła M, Oszczak S, Zazula M. GNSS - EGNOS reference station in the implementation process of landing procedures using satellite technology. Logistyka. 2014;6: 2774-2781. (In Polish)
16. Grunwald G, Bakuła M, Ciećko A. Study of EGNOS accuracy and integrity in eastern Poland. Aeronaut. J. 2016, 1230: 1275–1290.
17. Ciećko A, Grunwald G. The comparison of EGNOS performance at the airports located in eastern Poland. Tech. Sci. 2017;20: 181–198.
18. Felski A, Nowak A. Accuracy and availability of EGNOS—Results of observations. Artif. Satell. 2011;46: 111–118.
19. Jafernik H. Assessment of the Usefulness of EGNOS Differential Corrections in Conducting GPS Static Measurements. Int. J. Eng. Res. Appl. 2016;6: 25–30.
20. Ciećko A, Grunwald G. Examination of Autonomous GPS and GPS/EGNOS Integrity and Accuracy for Aeronautical Applications. Periodica Polytechnica Civil. Eng. 2017;61:920–928.
21. Oliveira J, Tiberius C. Landing: Added Assistance to Pilots on Small Aircraft Provided by EGNOS. In: Proceedings of the Conference 2008 IEEE/ION Position, Location and Navigation Symposium, Monterey, CA, USA, 5–8 May 2008; 321–333.
22. Breeuwer E, Farnworth R, Humphreys P, Mcgregor A, Michel P, Secretan H, Leighton SJ, Ashton KJ. Flying EGNOS: The GNSS-1 Testbed, Paper Galileo’s World, January 2000; 10–21. Available at: http://www.egnos-pro.esa.int/Publications/navigation.html
23. Fonseca A, Azinheira J, Soley S. Contribution to the operational evaluation of EGNOS as an aeronautical navigation system. In: Proceedings of the 25th International Congress of the Aeronautical Sciences (ICAS 2006), Hamburg, Germany, 3–8 September 2006; 1–10.
24. Veerman HPJ, Rosenthal P. EGNOS Flight Trials, Evaluation of EGNOS Performance and Prospects. In: Proceedings of the 2006 National Technical Meeting of The Institute of Navigation, Monterey, CA, USA, 18–20 January 2006; 358–367.
25. Soley S, Farnworth R, Breeuwer E. Approaching nice withthe EGNOS system test bed. In: Proceedings of ION NTM 2002, San Diego, CA, USA, 28–31 January 2002; 539–550.
26. Muls A, Boon F. Evaluating EGNOS augmentation on a military helicopter. In: Proceedings of the 14th International Technical Meeting of the Satellite Division of The Institute of Navigation (ION GPS 2001), Salt Lake City, UT, USA, 11–14 September 2001; 2458–2462.
27. Specht C, Mania M, Skóra M, Specht M. Accuracy of the GPS positioning system in the context of increasing the number of satellites in the constellation. Pol. Marit. Res. 2015;22: 9–14.
28. Specht C, Pawelski J, Smolarek L, Specht M, Dąbrowski P. Assessment of the Positioning Accuracy of DGPS and EGNOS Systems in the Bay of Gdansk Using Maritime Dynamic Measurements. J. Navig. 2019;72:575–587.
29. NGS NOAA website. Available at: https://www.ngs.noaa.gov/ANTCAL/LoadFile?file=ngs14.atx.
30. Fellner R. Analysis of the EGNOS/GNSS parameters in selected aspects of Polish transport. Transp. Probl. Int. Sci. J. 2014;9: 27–37.
31. Krasuski K, Mrozik M, Wierzbicki D, Ćwiklak J, Kozuba J, Ciećko A. Designation of the Quality of EGNOS+SDCM Satellite Positioning in the Approach to Landing Procedure. Appl. Sci. 2022;12:1335.
32. Krasuski K, Wierzbicki D. Monitoring Aircraft Position Using EGNOS Data for the SBAS APV Approach to the Landing Procedure. Sensors. 2020;20:1945.
33. Scilab website. Available at: https://www.scilab.org/.
34. Krasuski K., Wierzbicki D. Application the SBAS/EGNOS Corrections in UAV Positioning. Energies. 2021;14:739.
35. Krasuski K, Wierzbicki D, Bakuła M. Improvement of UAV Positioning Performance Based on EGNOS+SDCM Solution. Remote Sens. 2021;13:2597.

Kamil Krasuski: https://orcid.org/0000-0001-9821-4450

Janusz Ćwiklak: https://orcid.org/0000-0001-5538-0440

Mieczysław Bakuła: https://orcid.org/0000-0002-7180-8483

Magda Mrozik: https://orcid.org/0000-0003-4496-8331

DOI 10.2478/ama-2022-0044

COMPUTATIONAL INVESTIGATION OF VIBRATION CHARACTERISTICS ANALYSIS FOR INDUSTRIAL ROTOR

Noureddine AIMEUR*, **Noureddine MENASRI***

*Laboratory of Materials and Structural Mechanics, University of Mohamed BoudiafM'sila,
B.P 166 Ichbilia, M'sila, 28000, Algeria

noureddine.aimeur@univ-msila.dz; noureddine.menasri@univ-msila.dz

received 14 April 2022, revised 24 August 2022, accepted 25 August 2022

Abstract: During the operation of a rotor, various types of vibrations appear in this mechanical system and often limit the performance and endanger the safety of the operation. Therefore, dynamic analysis is essential because precise knowledge of the vibration behaviour is essential to ensure proper operation. This article presents a set of scientific techniques for the modelling and simulation of rotor vibrations. To work out the equations of the vibratory movement of the rotor, we used the energy approach of Lagrange. To achieve this, a model with one blading wheel carried by a shaft supported by two hydrodynamic bearings is chosen basedon the characteristics of the rotor studied (Fan 280 cement draft fan). It is an arduous task to manually ascertain the analytical resolution of the differential equations that characterise the vibratory behaviour of the rotor. The numerical approach employing the finite element method, programmed on the ANSYS software, made it possible to perform the vibration analysis of the rotor. First, the FAN 280 cement draft fan rotor is modelled using SolidWorks 3D software and reverse design using the coordinate measuring machine (CMM) for the design of the fins. Then, the modal characteristics of the fan rotor model were analysed using the finite element analysis (FEA) software ANSYS Workbench. Also, to study the effect of blade wear on critical speeds, the Campbell diagram was obtained. Finally, harmonic analysis was performed to determine the amplitude of the rotor vortex at critical speeds obtained with and without blade wear.

Key words: rotor dynamic, finite element method,reverse design (CMM), unbalanced,blade wear, simulation (ANSYS)

1. INTRODUCTION

Humanity is surrounded by rotating machines such as fans, pumps, compressors and gas turbines, whose successful operation depends on the behaviour of these machines and their components under dynamic conditions. Excessive vibration of rotating machines may in some cases not only harm the health of their operators but also result in a significant loss of productivity and/or product quality, and in consequence, a reduction in the reliability of machine components. Thus, to avoid these problems, it is essential to determine the excessive operating conditions for each machine operating under critical conditions [1-3].

The analysis of the dynamic characteristics of a machine mainly adopts the methods of experimental modal analysis and (FEM) modal analysis [4-10].

In recent years, there has been much research carried out in the field of the vibratory behaviour of rotors supported by bearings, resultant to which several theoretical and experimental developments and research findings have emerged.

Nan et al. [11] analysed the vibration characteristics of a horizontal machining centre.

By employing experimental modal tests, reliable modal parameters and dynamic characteristics can be obtained for the machining centre. Khan et al. [12], Khamari et al. [13] and Bai et al. [14] performed modal analysis to ascertain the natural frequencies and harmonic analysis using which to plot the stress and deflection at critical speeds. Accordingly, dynamic analysis of the rotor was performed in ANSYS APDL and Workbench to ascertain the natural frequencies and critical speeds.

Several papers have dealt with the study of the dynamic behaviour of the unbalanced rotor [15-18]. The results show that the sudden unbalance in the operating system will cause larger oscillations, which are increased with the advance of the sudden unbalance; and the impact effect will be induced as a result, while the critical speed frequency is excited in the frequency spectrum.

Shuming and Yujia [19] have investigated the damping optimisation of high-pressure rotor support based on harmonic response analysis. The simulation results show that the parametric design of the supporting damping of the high-pressure rotor can effectively reduce the vibration of a high-pressure rotor passing the critical speed. Khamari et al. [13] and Nagaraj et al.[20] have presented the rotordynamic analysis of the rotor using the commercial finite element analysis (FEA) software ANSYS. Several authors in their contributions comprising the literature opine that the detailed (FEA) will be quite useful for researchers around the world. From the modal and harmonic analysis, it was seen that the turboexpander model is safe to operate at its designed rotational speed.Xu and Wang [21] propose an efficient method for free vibration analysis of rotating beams under elastic boundary conditions.

This paper presents a dynamic study of an industrial rotor (FAN280 cement draft fan). First, the FAN 280 cement draft fan rotor is modelled using SolidWorks 3D software and reverse design (CMM, for blade design). Then the modal characteristics of the fan rotor model are analysed using the (FEA) software ANSYS Workbench. Also, to study the effect of blade wear on critical speeds, Campbell's diagram is obtained. Finally, harmonic analy-

DOI 10.2478/ama-2022-0044

sis is performed to determine the magnitude of the rotor vortex at critical speeds obtained with and without blade wear.

2. MODELING OF THE FAN (FN 280)

2.1. Draft fan description

The FN 280 type fans are designed to transport hot gases with limited non-abrasive dust content,and may be categorised under suction type fans that are not accompanied by a suction box.

The fan consists of an impeller with an assembly shaft, 16 blades with a front flange and a rear flange, the shaft and two bearings. The bearings are ball bearings for the thrust roller. The basic designation is 22,332 with a C3 sail for bearing 1 and 22,328 with a C3 sail for bearing 2. It is upturned over the shaft. One of them, designed as a steering bearing, is installed near the engine.The other bearing is designed to move with reference to the body of this bearing, and the shaft is constructed of steel; both of these bearings are mounted in cast FLS bearing housings and mounted on the stool. A cooling turbine is mounted on the shaft close to the casing since the fans have to work at temperatures above 125 °C. The components of the fan casing are the casing itself, the front flange, the rear flange and the suction roof. The casing of the fan, sealed by stuffing rope, is fitted with an inspection hatch. The front flange is bolted to the casing. The technical data of the fan are shown in Tab. 1:

Tab. 1. The technical data of fan

Type	FN280	
Numbers of blades	16	
Temperature	84 C°	
velocity	985 RPM	
Bearing 1	K11= 32000[k/mm]	C11= 3.3[N. s/mm]
	K22 =12000[k/mm]	C22 =1.5 [N. s/mm]
Bearing 1	K11 =38900[k/mm]	C11= 2.6[N. s/mm]
	K22 =16000[k/mm]	C22 =1.5 [N. s/mm]

2.2. Geometric model

The data for the FN 280 fan were taken from the industries and all the parts were designed with SolidWorks program except the blade; since there were no data available for the blade, it was necessary to rely on the reverse design using the coordinate measuring machine (CMM) to obtain point cloud data through the PC-DMIS program, as shown in Fig. 1.

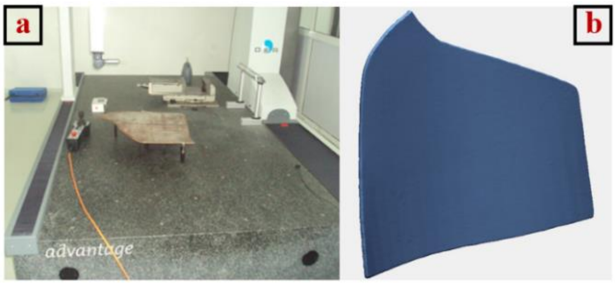

Fig. 1. (a) Impeller Blade; (b) Cloud data from.(CMM)coordinate measuring machine

These data were then exported to Geomagic Design X to obtain a final CAD model, and the fan parts were assembled using the SolidWorks software, as shown in Fig. 2. The model was then converted to a file (x_t) and imported into the ANSYS Workbench program for modal analysis and harmonic response analysis.

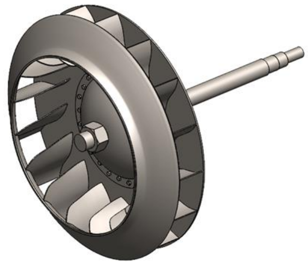

Fig. 2. CAD model of FN 280

2.3. Rotor dynamics equation

For modal analysis of multi DOF rotor bearing system, the equation of motion may be written as under:

$$\left[M\right]\{\ddot{u}\}+(\left[D\right]+[G])\{\dot{u}\}+(\left[S\right]+[H])\{u\}=\left\{F\left(t\right)\right\} \quad (1)$$

The positive definite, but not necessarily diagonal, matrix M is called the mass (inertia) matrix, the skew symmetric matrices G and H are referred to as the gyroscopic and circulatory matrices, respectively, and the indefinite non-symmetric matrices D and S are called the damping and the stiffness matrices, respectively. The matrices M, G, D and H are general rotational speed (Ω) dependent. For a given Ω, Eq. (1) can be written as:

$$\left[M\right]\{\ddot{u}\}+\left[C\right]\{\dot{u}\}+\left[K\right]\{u\}=\left\{f\left(t\right)\right\} \quad (2)$$

where the generalised damping and stiffness matrices, C and K, are now neither positive (negative) definite nor symmetric. We can assume, however, without loss of generality that M, C and K are real[22-23], and thus.

Either wouldbe a solution of the type:

$$\begin{aligned} W &= Xe^{\lambda t} \\ A\lambda X + BX &= 0 \end{aligned} \quad (3)$$

The gyroscopic effect is turned in software.

For harmonics response the equations of forced vibration are:

$$\left[M\right]\{\ddot{u}\}+\left[C\right]\{\dot{u}\}+\left[K\right]\{u\}=\left\{f\left(t\right)\right\} \quad (4)$$

$$f\left(t\right)=f_0\sin\omega t \quad (5)$$

3. BOUNDARY CONDITIONS

3.1. For modal analysis:

We apply a remote displacement condition for each bearing, constraining rotation and translation about the Z axis (bearings are in X–Y plane). We created bearings with the bearings' body-ground on the connection's context tab, their respective positions on the shaft and with stiffness and damping as indicated in Tab. 1.The Fig. 3. shows the position of the boundary conditions applied to the rotor.

Considering that the maximum operating speed of the rotor is 985 rpm, a modal analysis was carried out at three different speeds in both cases; the first speed is 100 rpm, the second 600 rpm and the third 1,200 rpm.

3.2. For harmonic response analysis:

We apply the condition of remote displacement to the bearing locations, and the rotational and transition degrees of freedom are restricted about theZ axis at the bearing sites. Due to the possibility of resonance, and because the mass is asymmetric at the blades, it is converted into a point mass located in the position of the centre of mass, and the range of variance is determined. The frequency for harmonic response analysis is 0–70 Hz, and 2.333 Hz is set as one step for a total of 30 steps.

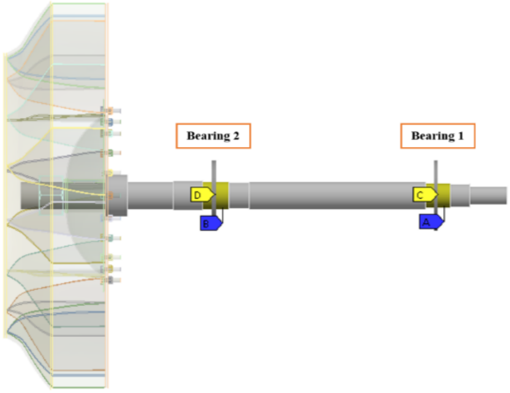

Fig. 3. Rotor boundary conditions

4. MESHING

One of the most important operations of ANSYS is the meshing process, which must be done correctly to enable an accurate simulation using (FEA). The mesh consists of elements containing nodes representing the shape of the geometry and can vary according to the element type. Based on the principle of performing calculations at a finite number of elements and then interpolating the results to the full size, any continuous object can have a large number of degrees of freedom, which makes it difficult to solve for (FEA), and by usingdivision or entanglement, (FEA)reduces degrees of freedom from unlimited to limited. For meshing, there are several methods in the ANSYS workbench, including the mechanical method, the tetrahedral method and the hexahedral dominance method [24-25].

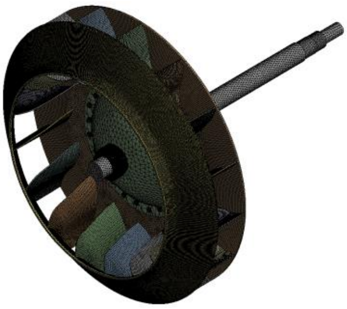

Fig. 4. Rotor mesh

The shaft components have been meshed with element SOLID185, which has the ability to be used in mixed forging, thus enabling the simulation of deformations of elastic materials that are almost incompressible. For blade modelling, the contact surfaces are first constructed at the parts' locations connected individually by the elements CONTA174 and TARGE170, and the bearings mesh with the COMBI214 element.

A total of 531,890 elements have been created and 239,491 nodes are shown in the meshing. Fig. 4 shows the figure of a meshed model.

5. RESULTS

5.1. Modal analysis

The model analysis was carried out at three different speeds: 100 rpm, 600 rpm and 1200 rpm. Additionally, a maximum of four modes was reckoned as ideal for carrying out the model analysis. Based on these parameters, the natural frequencies were calculated and a Campbell diagram was drawn to calculate the critical velocities of the rotor. The natural frequencies obtained from the typical analysis of the rotor are shown in Tab. 2. We note that values close to each other are obtained for the natural frequencies recorded in modes 1–3 at different speeds. As for mode 4, the natural frequency recorded at 1,200 rpm was greater than those at other speeds.

Tab.2. Natural frequencies rotor

Mode N°	Rotational Velocity [RPM]	Natural Frequency [Hz]
1	100	12.775
2		16.857
3		27.826
4		30.153
1	600	12.712
2		16.677
3		23.338
4		36.52
1	1200	12.448
2		15.911
3		19.959
4		45.71

5.1.1. Campbell diagram

The model analysis allows us to extract the Campbell diagram, as shown in Fig. 5, to analyse the evolution of frequencies at the speed of rotation and to determine the critical velocities and stability threshold.

We note that there are three critical speeds: 758.54 rpm, 972.12 rpm and 1,198.2 rpm, at frequencies of 12.775 Hz, 16.677 Hz and 19.959 Hz, respectively, and the following Tab. 3 represents the different rotational speeds obtained, together with values indicating the stability and rotation characterising each mode.

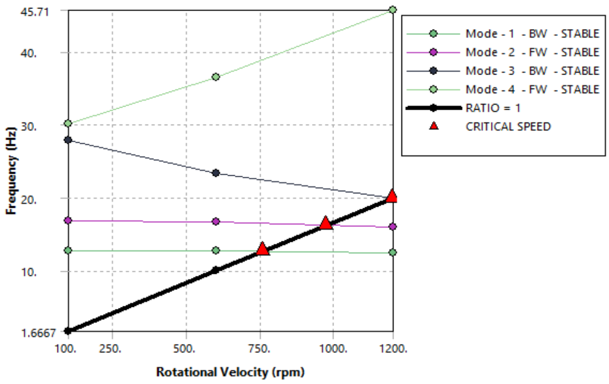

Fig. 5. Campbell diagram

Tab.3. Critical speeds for different rotational speeds

Mode	Whirl Direction	Mode Stability	Critical Speed	100. rpm	600. rpm	1200. rpm
1	BW	STABLE	758.54 rpm	12.775 Hz	12.712 Hz	12.448 Hz
2	FW	STABLE	972.12 rpm	16.857 Hz	16.677 Hz	15.911 Hz
3	BW	STABLE	1198.2 rpm	27.826 Hz	23.338 Hz	19.959 Hz
4	FW	STABLE	NONE	30.153 Hz	36.52 Hz	45.71 Hz

5.1.2. Mode Shapes

Fig. 6. shows the modes of vibrations obtained at a rotational speed of 100 rpm.

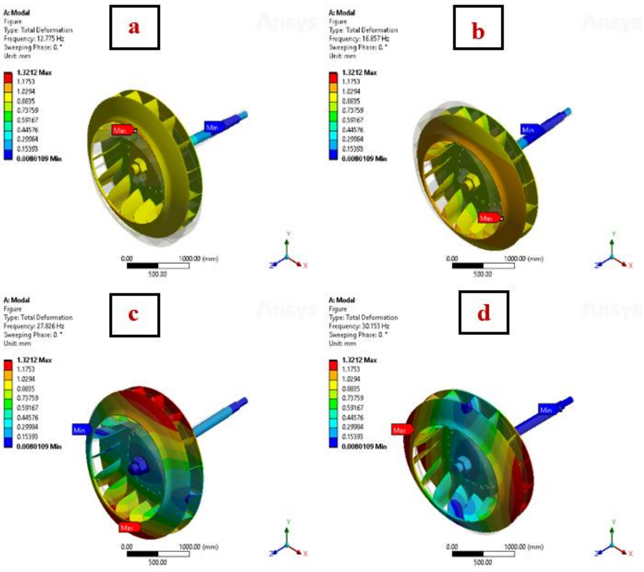

Fig. 6. The mode shapes of vibrations for speeds at 100 rpm: (a) mode 1; (b) mode 2; (c) mode 3; (d) mode 4

Fig. 7. shows the modes of vibrations obtained at a rotational speed of 600 rpm.

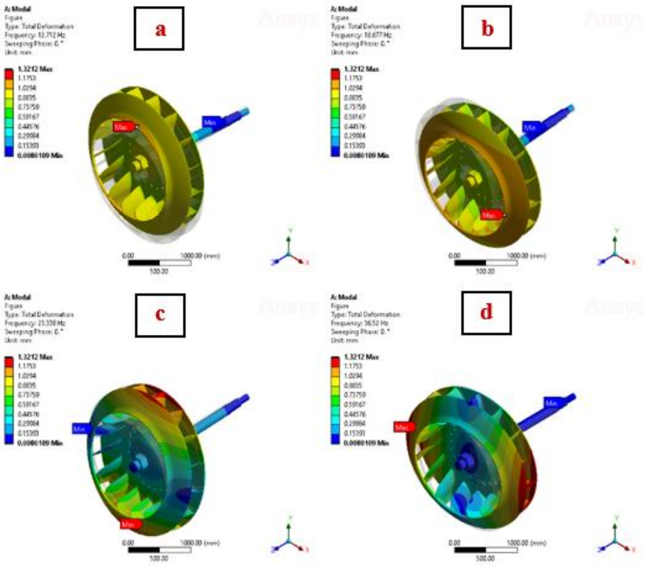

Fig. 7. The mode shapes of vibrations for speeds at 600 rpm: (a) mode 1; (b) mode 2; (c) mode 3; (d) mode 4

Fig. 8. shows the modes of vibrations obtained at a rotational speed of 1,200 rpm.

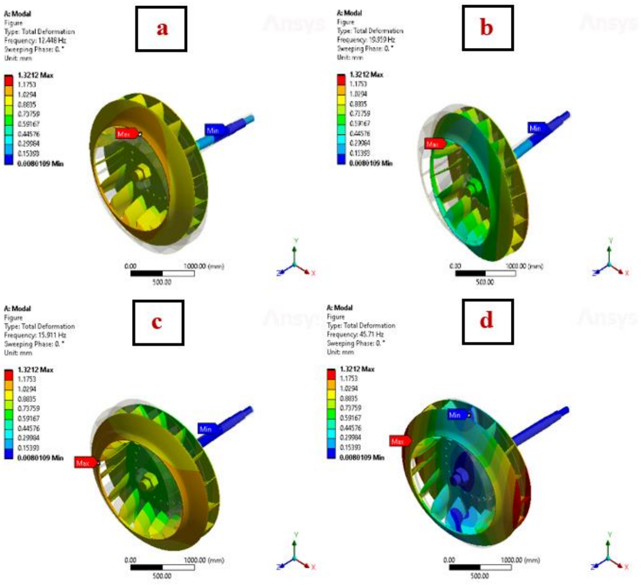

Fig. 8. The mode shapes of vibrations for speeds at 1,200 rpm: (a) mode 1; (b) mode 2; (c) mode 3; (d) mode 4

As for the form of vibration mode, it was found that the maximum distortion at different speeds is almost the same, where the maximum distortion at the first speed is 100 rpm, and the maximum distortion from the first to the fourth positions is in the range of 1.0418–1.5014 mm.

As for the second rotational speed of 600 rpm, the maximum distortion from the first to the fourth positions is in the range of 1.0506–1.338 mm.

As for the third rotational speed of 1200 rpm, the maximum deformation from the first to the fourth positions is in 1.0816–1.3212 mm.

5.2. Harmonic analysis

The harmonic response analysis of the rotor allows us to determine the deformation, stresses and effect of phase angle due to balanced and unbalanced forces acting on the shaft system. The harmonic analysis was carried out to show the frequency response arising pursuant to the application of an unbalanced force of 12,192 kg. mm at the centre of the disc in the two study cases.

5.2.1. Frequency response

Figs. 9–11 represent the severity of the deformation in the three directions.

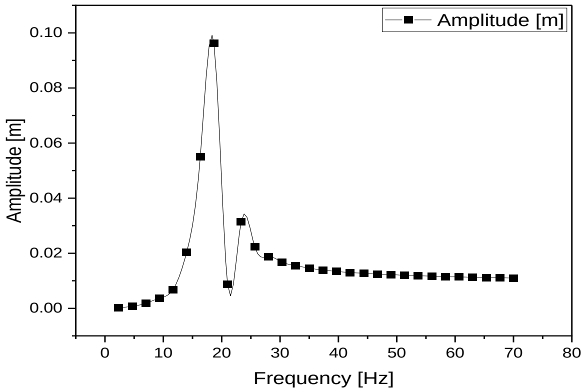

Fig. 9. Frequency response for X-direction

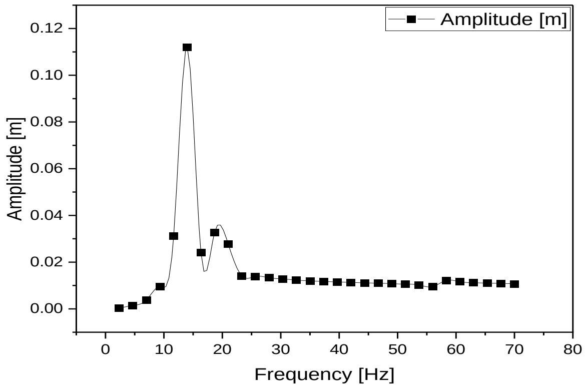

Fig. 10. Frequency response for Y-direction

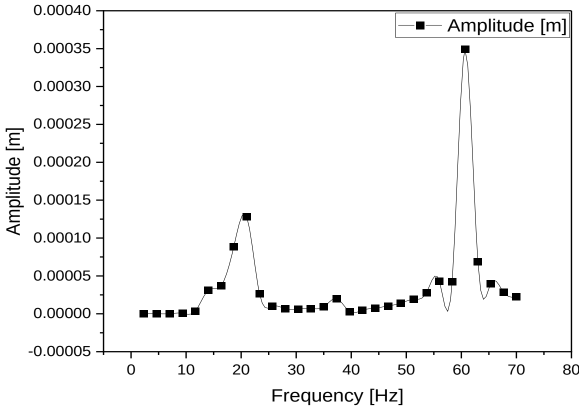

Fig. 11. Frequency response for Z-direction

In Fig. 9, we notice that the maximum amplitude of deformation in the X-direction is 9.6346e–005 m and it appears near 18.667 Hz, which is a value close to the natural frequencies of order 3.In the Y-direction, the maximum amplitude of deformation is 1.1213e–004 m, as shown in Fig. 10, and it appears that the frequency is approximately 14 Hz, which is close to the natural frequencies of the first order, while in the Z-direction, the maximum amplitude of deformation is 3.4939e–007 m, as shown in Fig. 11.

5.2.2. Phase angle effect on deformation

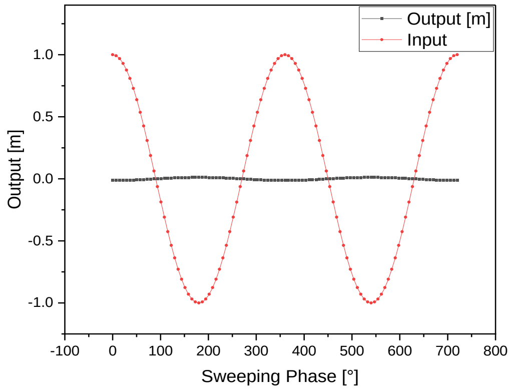

Fig. 12. Phase Angle Directional Deformation X-direction

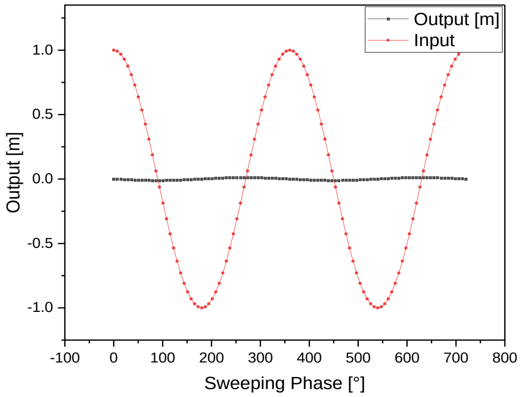

Fig. 13. Phase Angle Directional Deformation Y-direction

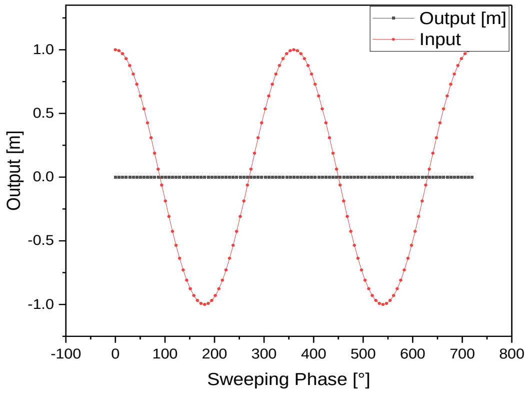

Fig. 14. Phase Angle Directional Deformation Z-direction

The maximum phase angle is –179.78° at 45.71 Hz frequency in the X-direction, 90.25° at 45.71 Hz frequency in Y-direction and 129.02° at 45.71 Hz frequency in Z-direction.

6. FAN WITH WORN BLADES

As the FN280 fan conveys hot gases with limited dust content (cement) over time, the fan blades erode over time. We wanted to simulate this tendency of the blades to undergo wear over time, as well as the worn condition of the blades, in our modelling process, and accordingly, in performing the modal analysis and harmonic response, we tried to design the blades in the form in which they would present after wear, the intent being to achieve a shape for the blades that would approximately correspond to their actual shape in reality post the expected duration of wear. Considering these requirements, the parts were assembled using SolidWorks software, as shown in Fig. 15.

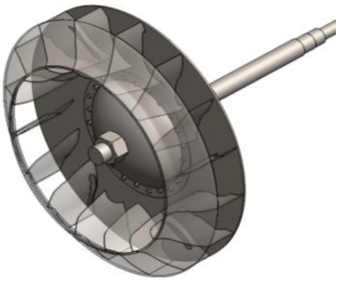

Fig. 15. CAD model of FN 280 with a worn blade

For the boundary conditions of the modal analysis, the same conditions are used as in the first case, with three different speeds: 100 rpm, 600 rpm and 1,200 rpm. The same conditions are applied for the harmonic response analysis, and the range of variance is determined. Thefrequency for harmonic response analysis is 0–70 Hz, and 2.333 Hz is set as one step for a total of 30 steps.

6.1. Meshing with a worn blade

Shaft components have been meshed with element SOLID185, which has the ability to be applied in mixed forging, thus enabling simulation of the deformations of elastic materials thatare almost incompressible. For blades' modelling, the contact surfaces are first constructed at the parts' locations connected individually by the elements CONTA174 and TARGE170, and the bearings mesh with the COMBI214 element.

A total of 531,210 elements have been created and 238,299 nodes are shown in the meshing, Fig 16 shows the figure of a meshed model.

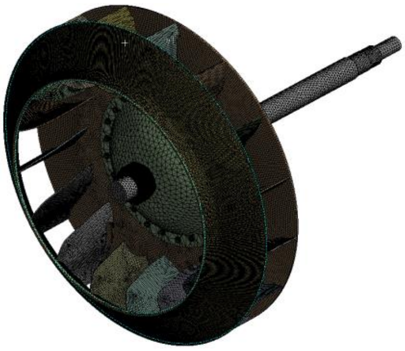

Fig. 16. Rotor mesh with a worn blade

6.2. Results

6.2.1. Modal Analysis

The model analysis was carried out at three different speeds: 100 rpm, 600 rpm and 1200 rpm, and a maximum of four nodes was used to perform the model analysis. Then, the natural frequencies were calculated and a Campbell diagram was drawn to calculate the critical velocities of the rotor. The natural frequencies obtained from the typical analysis of the rotor are shown in Tab. 4.We note that values close to each other are obtained for the natural frequencies recorded in modes 1–3 at different speeds. As for mode 4, the natural frequency recorded at 1200 rpm was greater than those at other speeds.

Tab. 4. Natural frequencies rotor with a worn blade

Mode N°	Rotational Velocity [RPM]	Natural Frequency [Hz]
1	100	13.501
2		18.155
3		30.945
4		33.399
5	600	13.478
6		18.071
7		26.252
8		39.62
9	1200	13.39
10		17.677
11		22.077
12		48.477

6.2.1.1. Campbell diagram

The model analysis allows us to extract the Campbell diagram, as shown in Fig. 17, to analyse the evolution of frequencies at the speed of rotation and to determine the critical velocities and stability threshold.

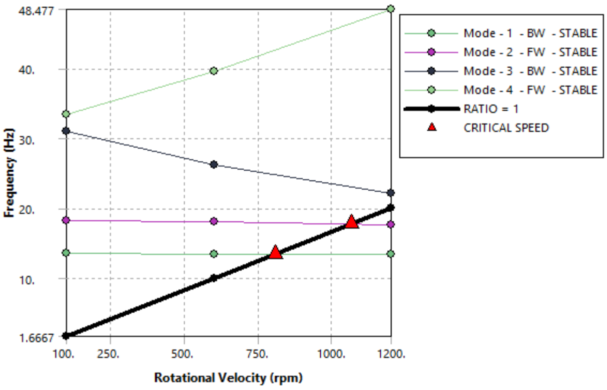

Fig. 17. Campbell diagram with a worn blade

We note that there are two critical speeds, 806.88 rpm and 1065.9 rpm, at frequencies 13.478 Hz and 18,071 Hz, respectively, and Tab. 5 represents the different rotational speeds obtained, together with values indicating the stability and rotation characterising each mode.

Tab.5. Critical speeds for different rotational speeds with a worn blade

Mode	Whirl Direction	Mode Stability	Critical Speed	100. rpm	600. rpm	1200. rpm
1	BW	STABLE	806.88 rpm	13.501 Hz	13.478 Hz	13.39 Hz
2	FW	STABLE	1065.9 rpm	18.155 Hz	18.071 Hz	17.677 Hz
3	BW	STABLE	NONE	30.945 Hz	26.252 Hz	22.077 Hz
4	FW	STABLE	NONE	33.399 Hz	39.62 Hz	48.477 Hz

6.2.1.2. Mode shapes

Fig. 18. shows the modes of vibrations obtained at a rotational speed of 100 rpm.

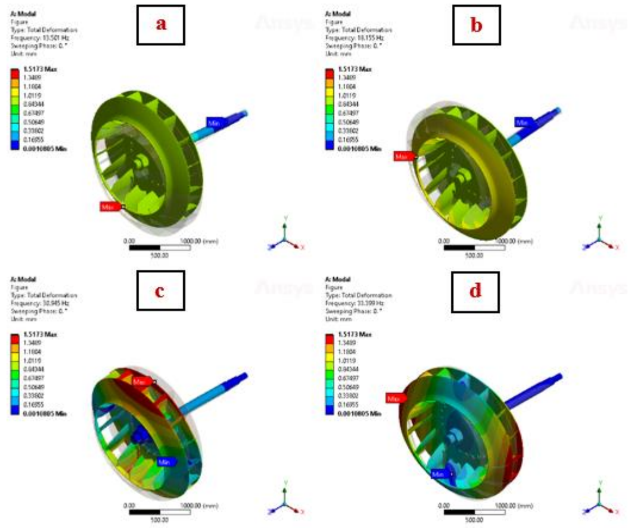

Fig. 18. The mode shapes of vibrations for speeds at 100 rpm: (a) mode 1; (b) mode 2; (c) mode 3; (d) mode 4

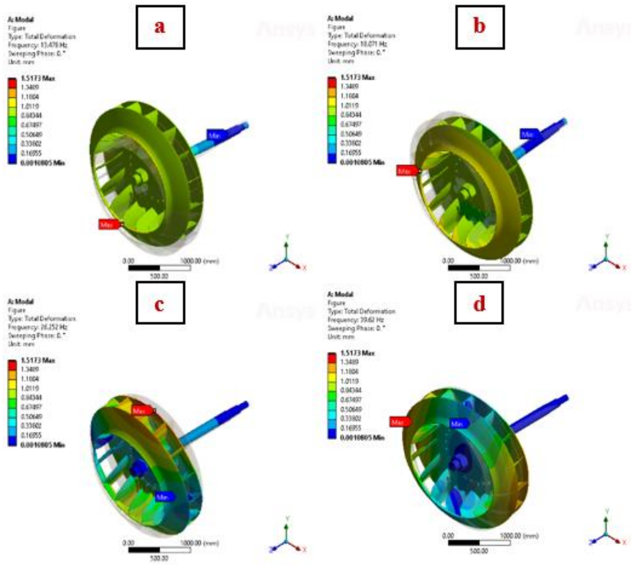

Fig. 19. The mode shapes of vibrations for speeds at 600 rpm: (a) mode 1; (b) mode 2; (c) mode 3; (d) mode 4

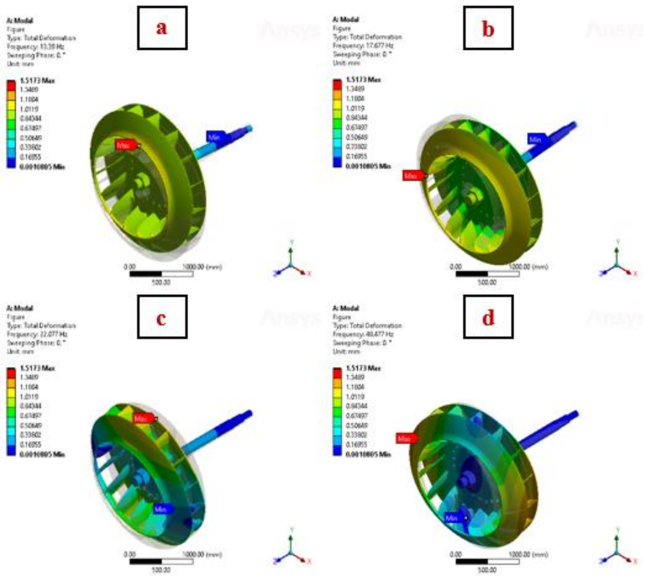

Fig. 20. The mode shapes of vibrations for speeds at 1,200 rpm: (a) mode 1; (b) mode 2; (c) mode 3; (d) mode 4

Fig. 19. shows the modes of vibrations obtained at a rotational speed of 600 rpm.

Fig. 20. shows the modes of vibrations obtained at a rotational speed of 1,200 rpm.

As for the form of vibration mode, it was found that the maximum distortion at different speeds is almost the same, where the maximum distortion at the first speed is 100 rpm, and the maximum distortion from the first to the fourth positionsin the range of 1.0184–1.7757 mm.

As for the second rotational speed of 600 rpm, the maximum distortion from the first to the fourth positions is in the range of 1.0228–1.5448 mm.

As for the third rotational speed of 1,200 rpm, the maximum deformation from the first to the fourth positions in the range of 1.0395–1.5173 mm.

6.2.2. Results of harmonic response analysis

6.2.2.1. Amplitude vs frequency

Figs. 21–23 represent the severity of the deformation in the three directions.

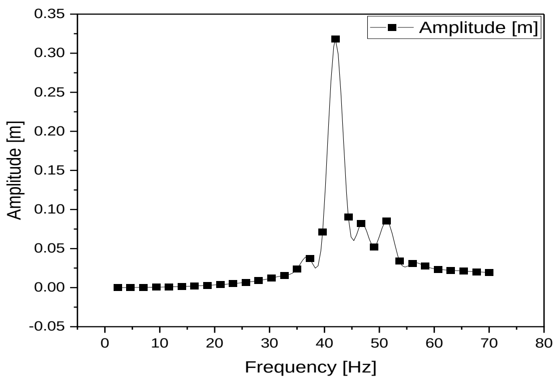

Fig. 21. Frequency response for X-direction

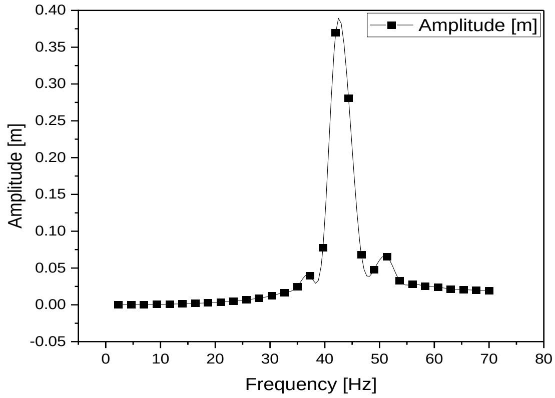

Fig.2 2. Frequency response for Y-direction

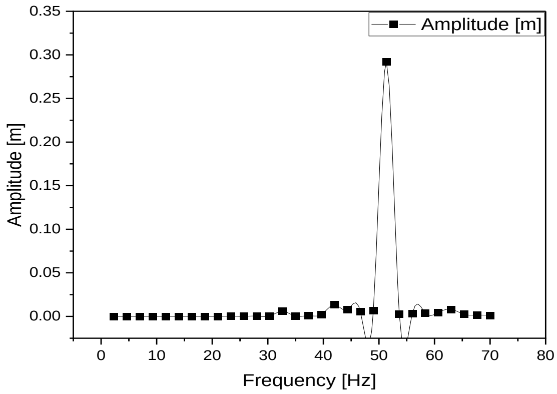

Fig. 23. Frequency response for Z-direction

In Fig. 21, we note that the maximum amplitude of deformation in the X-direction is 2.1737e–003 m, and it appears near the frequency of 16.33 Hz Fig. 21 and is close to the natural frequencies of the order 2. In Fig. 22, we note that the maximum amplitude of deformation in the Y-direction is 5.3828e–004 m, and it appears near the frequency 44.33 Hzand is close to the natural frequencies of order 4, while in Fig. 23, we note that the maximum amplitude of deformation in the Z-direction is 6.8784e–005 m, and it appears near the frequency 51.33 Hz and is close to natural frequencies of order 4.

6.2.2.2. Phase angle effect on deformation

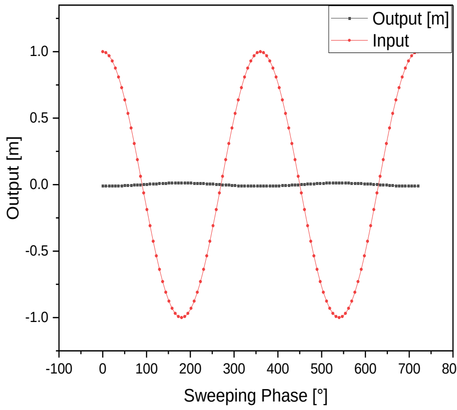

Fig. 24. Phase Response Directional Deformation X-direction

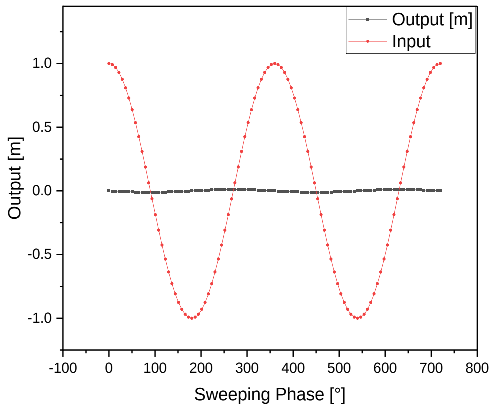

Fig. 25. Phase Response Directional Deformation Y-direction

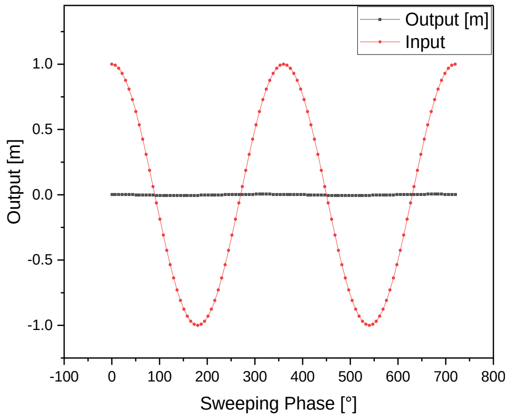

Fig. 26. Phase Response Directional Deformation Z-direction

The maximum phase angle is 179.57° at 49 Hz frequency in X-direction, 89.82°at 49 Hz frequency in Y-direction and 40.241° at 49 Hz frequency in Z-direction.

7. CONCLUSIONS

In the present study, a rotating dynamic analysisof fan blades (FN 280 cement draft fan), in their normal state and in the state after corrosion, was performed using the finite element software ANSYS workbench, to ascertainnatural frequencies and critical speeds after obtaining Campbell's diagram in each case, and the following conclusions were drawn:

- The natural frequencies in the case of the natural fan are less than the value of the natural frequencies in the case after corrosion of the fan blades in all modes, and the maximum deformation in all vibration modes in the first case is less than in the case after corrosion of the fan blades.
- After the Campbell diagram was obtained in the case of the natural fan, three critical speeds were found at 758.54 rpm, 972.12 rpm and 1,198.2 rpm and these occurred in the operating range, but in the case of the fan after corrosion of the fan blades, two critical speeds were found at 806.88 rpm and 1,065.9 rpm.
- In the harmonic analysis, as a result of the unbalanced force of 12,192 kg.mm acting on the disk, the intensity of vibrationwas very high. In the case of a normal fan in the X-direction the system resonates when the excitation frequency reaches 18.667 Hz and 23.33 Hz and the vibration response reaches a

maximum at a frequency of 18.66 Hz; in the Y-direction it resonates at frequencies of 14 Hz and 18.667 Hz and reaches its maximum at 14 Hz; and in the Z-direction it resonates at frequencies of 21 Hz and 60.667 Hz, and reaches its maximum at 60.667 Hz. In the case of the fan after corrosion of the fan blades, the system resonates and reaches its maximum at a frequency of 16.33 Hz in the X- and Y-directions, in the Z-direction, resonates and reaches its maximum at an excitation frequency of 55.33 Hz.

REFERENCES

1. Kushwaha N, Patel V. Modelling and analysis of a cracked rotor: a review of the literature and its implications. Arch Appl Mech. 2020;90(6):1215-45.
2. Xie F, Aly A-M. Structural control and vibration issues in wind turbines: A review. Eng Struct. 2020;210:110087.
3. Gunter E. Critical speed analysis of offset jeffcott rotor using english and metric units. RODYN Vib Inc, Charlottesville, VA. 2004.
4. Cao H, Niu L, Xi S, Chen X. Mechanical model development of rolling bearing-rotor systems: A review. Mech Syst Signal Process. 2018;102:37-58.
5. Huaitao S, Jizong Z, Yu Z, Gang H, editors. Calculation and analysis of critical speed of high speed motor spindle rotor system. IOP Conf Ser Mater Sci Eng; 2018: IOP Publishing.
6. Lee C-W. Vibration analysis of rotors: Springer Science & Business Media; 1993.
7. Wang C, Zhang D, Ma Y, Liang Z, Hong J. Theoretical and experimental investigation on the sudden unbalance and rub-impact in rotor system caused by blade off. Mech Syst Signal Process. 2016;76:111-35.
8. Cardillo L, Corsini A, Delibra G, Rispoli F, Sheard AG, Venturini P. Predicting the performance of an industrial centrifugal fan incorporating cambered plate impeller blades. Period Polytech Mech Eng. 2014;58(1):15-25.
9. Krishna BRV, Mudgala S, Seth D. A comparative dynamic analysis of rotor involving three engineering materials applying finite element analysis (FEA) simulation. Mater Today Proc. 2021;47:4003-14.
10. Hnin MT, Htike TM. Investigation of natural frequency and critical speed for Jeffcott rotor system. J Res Appl Mech Eng. 2021;9(1).
11. Nan JY, Wang M, Zan T, Zhang JX, editors. Vibration Characteristics Analysis of a High-Speed Horizontal Machining Center. Adv Mater Res; 2012: Trans Tech Publ.
12. Khan MM, Shailesh P, Prasad M. Rotor Dynamic Analysis Of Driving Shaft Of Dry Screw Vacuum Pump. 2019.
13. Khamari DS, Kar PS, Jena S, Kumar J, Behera SK, editors. Rotordynamic Analysis of High-Speed Rotor Used in Cryogenic Turboexpander Using Transfer Matrix Method. Proceedings of the 6th National Symposium on Rotor Dynamics; 2021: Springer.
14. Bai B, Zhang L, Guo T, Liu C. Analysis of dynamic characteristics of the main shaft system in a hydro-turbine based on ANSYS. Procedia Eng. 2012;31:654-8.
15. Sinha JK, Lees A, Friswell M. Estimating unbalance and misalignment of a flexible rotating machine from a single run-down. J Sound Vib. 2004;272(3-5):967-89.
16. Yadav H, Upadhyay S, Harsha S. Study of effect of unbalanced forces for high speed rotor. Procedia Eng. 2013;64:593-602.
17. Fegade R, Patel V, Nehete R, Bhandarkar B. Unbalanced response of rotor using ansys parametric design for different bearings. Int J Eng Sci Emerg Technol. 2014;7(1):506-15
18. Khawaja H, Andleeb Z, Moatamedi M. Multiphysics based Modal and Harmonic Analysis of Axial Turbines. Int J Multiphysic. 2022;16(1):81-94.
19. Shuming L, Yujia W, editors. Damping Optimization of High Pressure Rotor Support Based on Harmonic Response Analysis. J Phys Conf Ser; 2021: IOP Publishing.
20. Nagaraj B, Patil L, Kamanat PK, Dhuri K, Azam MS. Rotordynamic Analysis of Bolted Disk-Drum Rotor with Contact Nonlinearity.
21. Xu H, Wang YQ. Differential transformation method for free vibration analysis of rotating Timoshenko beams with elastic boundary conditions. Int J Appl Mech. 2022;14(6):21.
22. Chong-Won L. Vibration analysis of rotors. SOLID Mech ITS Appl. 1993;21:156.
23. Ansys. Rotordynamic Analysis Guide. 2021:158.
24. Grunwald B. Vibration analysis of shaft in SolidWorks and ANSYS. 2018.
25. Mansoora HI, Al-Shammari M, Al-Hamood A, editors. Theoretical Analysis of the Vibrations in Gas Turbine Rotor. IOP Conf Ser Mater Sci Eng; 2020: IOP Publishing.

Noureddine Aimeur: https://orcid.org/0000-0003-0293-8417

Noureddine Menasri: https://orcid.org/0000-0002-7373-684X

INVESTIGATION OF STRUCTURE FORMATION AND TRIBOTECHNICAL PROPERTIES OF STEEL PLASMA COATINGS AFTER CHEMICAL-HEAT TREATMENT AND LIQUID-PHASE IMPREGNATION

Roman MEDIUKH*, Vira MEDIUKH*, Vasyl LABUNETS**
Pavlo NOSKO, Oleksandr BASHTA**, Irina KONDRATENKO***

*Fratsevich Institute for Problems in Materials Science NAS of Ukraine, Department of Functional Materials for Medical Application,
Krzhizhanovsky Str., 3, 03142, Kyiv, Ukraine
**Aerospace Faculty, Department of Applied Mechanics and Materials Engineering, National Aviation University,
Lubomyr Husar Ave., 1, 03058, Kyiv, Ukraine

roman.mediukh@gmail.com, vira.mediukh@gmail.com, nau12@ukr.net,
nosko_p@ukr.net, oleksandr.bashta@npp.nau.edu.ua, irina.kondratenko@gmail.com

received 26 June 2022, revised 2 September 2022, accepted 6 September 2022

Abstract: The paper is focused on the studies of the microstructure development and physical and mechanical properties of metal-matrix composite coatings based on steel 11Cr18MoWCu deposited using plasma and galvanoplasma methods. The expediency of combining gas-thermal spraying processes of plasma coatings with open porosity up to 16%–18%, with their subsequent thermodiffusion saturation (chromium plating) or liquid-phase impregnation with eutectic alloys of previously applied Ni–B galvanic layer, is shown. The study of the tribotechnical properties of the proposed coatings showed a significant improvement in their performance under conditions of various types of intensive wear, as well as in corrosive environments.

Key words: plasma coatings, steel 11Cr18MoWCu, composite electrolytic coatings, impregnation, galvanic plasma coatings, chemical-thermal treatment, structure formation, wear resistance

1. INTRODUCTION

In the current conditions of industrial production in different branches of industry, the problems of inadequate reliability and durability of machines and mechanisms are of particular importance. The solution to these problems is determined mainly by enhancing the effectiveness of the parts that provide surface protection from various types of contact damage. The formation of heterogeneous surface coatings possessing a specific set of functional properties is the most economically feasible solution to these problems [1–3].

Uvarova [4] and Rinaldi and Ferravante [5] suggest that one of the ways to achieve this goal is to develop a technology for multifunctional heterogeneous coatings by combining different deposition methods, and this would allow the physical, mechanical and operational properties of coatings to be altered pursuant to changes made in the ratio of phase components.

The deposition of protective metallic coatings by thermal spraying is technologically simple and allows the formation of a variety of coatings varying in their composition and purpose. Their thickness may vary in a wide range, which has been reported to be from 0.1 mm to ≥5 mm in the literature [6–12]. The strength of adhesion of such coatings to the substrate is in the range of 20–100MPa, which is usually insufficient for most of the tribotechnical applications. Therefore, they require further heat or chemical-heat treatment (CHT), which promotes high adhesion and formation of required composition and heterogeneous structure in the surface, thereby significantly improving the coating properties [13–16].

The functional purpose of gas-thermal coatings can be significantly expanded with the use of galvanic plasma coatings (GPCs).The technology of their deposition consists of two stages. The first stage is the pre-deposition of a galvanic interlayer of eutectic composition, such as Ni–B or Fe–B. The second stage is deposition of gas-thermal coating with total porosity up to 16%–24%. Later, when heating such a composition to the temperature of interlayer eutectic transformation, the gas-thermal coating is impregnated with liquid metal melt during liquid-phase sintering [17–21].

In this work, the 11Cr18MoWCu ferritic steel was used as a material for coating. It is able to work in aggressive environments (acidic or alkaline), and is heat-resistant at operating temperatures up to 900 °C. Molybdenum and copper additives in its composition increase resistance to corrosion in acids [22, 23], whereas tungsten promotes heat resistance [24]. Depending on the type of heat treatment, chromium (Cr23C6), molybdenum (Mo2C) and tungsten (WC) carbides may form in this steel.

For the impregnation of the plasma coating of the 11Cr18MoWCu steel, a Ni–B composite electrolytic coating (CEC) was used. At the eutectic temperature (1080 °C) it fills the pores of the steel with a Ni–Ni3B liquid phase. Upon solidification, the eutectic mixture has the structure of a soft nickel matrix with solid Ni3B particles. This helps to increase the tribotechnical properties of the obtained coatings.

The present work aims to study new steel 11Cr18MoWCu plasma coatings after CHT (chromising) or after impregnation with liquid metal phase Ni–Ni3B.

In particular, the paper addresses the study of:
- process of such coatings' structure formation,
- phase composition, and
- tribotechnical properties under various conditions of their contact interaction.

2. MATERIALS AND THE METHODS

To conduct the experiment, two fundamentally different series of samples were made, and the abbreviated schemes of their preparation are given below:
1. Substrate of steels 0.45C/0.20C + CEC Ni–B + plasma coating 11Cr18MoWCu + vacuum heat treatment;
2. Substrate of steels 0.45C/0.20C + plasma coating 11Cr18MoWCu + diffusion chromium saturation.

Before spraying, the substrate surface was treated with steel crumbs with a particle size of 0.5–1.0 mm at a pressure of 3.4–4.0 × 10^5 Pa. Such pre-treatment of the surface is necessary to give it a developed relief and energy-active state to improve the adhesion of the coating to the substrate.

The Ni–B CEC were obtained from nickel chloride electrolyte [25] by co-precipitation of nickel with dispersed particles of amorphous boron with a diameter of about 3–5 μm in the concentration of 80 g/L. With such a boron content in the electrolyte, the eutectic composition of CEC Ni–B, with amorphous boron content of 3.5%–4% in it, is achieved. During the subsequent heat treatment at a temperature of 1080–1100 °C, the Ni–Ni$_3$B eutectic is formed. The coating deposition rate is 70–80 μm/h at a current density of 10 A/m^2.

The next coating layer was applied by plasma spraying of 11Cr18MoWCu steel. The vacuum heat treatment was performed according to the following regime: heating to 1110 °C, holding for 2–3 min and cooling simultaneously with the furnace. Under such conditions, eutectic melting of CEC occurs and the Ni–Ni$_3$B metal melt is drawn into the pores due to capillary pressure and good wetting of the 11Cr18MoWCu steel by the liquid phase. As a result of such impregnation, GPC Ni–B+11Cr18MoWCu is formed.

11Cr18MoWCu stainless chromium–molybdenum steel wire with a diameter of 1.6 mm was used for spraying plasma coatings on the steel 0.45C substrate.

Plasma spraying was performed on an UPU-3D machine in air using argon as a transporting and plasma-forming gas. Spraying parameters were changed to ensure adhesion and to obtain the maximum open porosity of the coating, which is appropriate for the further CHT [17]. The optimal parameters of spraying are as follows: I = 450 A, U = 35 V, distance from the plasmatron nozzle to the sample is 140 mm, gas consumption is 21 L/min, and wire feed rate is 1.5–1.7 kg/h.

The porosity of plasma coatings was measured by mercury porosimetry under ISO 15901-1: 2016.

Heat treatment of samples and parts was performed in the laboratory vacuum electric furnace SShVL 1.25/25 at a residual gas pressure of 5 x 10^{-3} Pa in the temperature range 1080–1100 °C.

Diffusion saturation by chromium was performed in an electric furnace SNOL-2.3.2/13 in containers made of heat-resistant steel Cr18Ni9Ti with a fusible cover of sodium silicate glass, under controlled temperature and duration of the process. Saturation was performed in powder mixture containing (%wt.): 50 – Fe–Cr (in the ratio 40:60), 47 – Al$_2$O$_3$, 3 – NH$_4$Cl [15].

To determine the Vickers microhardness and thickness of coating (ISO 6507), we used a microhardness tester PMT-3.The microstructure of the coating was studied on standard metallographic samples (sections) after etching in a nital solution (5% HNO$_3$ + 95% C$_2$H$_5$OH) for 5–15 s at T = 20 °C. For microstructural examinations we used an optical microscope MIM-7.

XRD-studies were performed on a DRON-2.0 diffractometer in filtered Co–K$_\alpha$ radiation. Exposure was performed from the surface of the coatings, and to reduce the surface roughness, the samples were polished.

The distribution of elements in the coating was studied using a microanalyser MS-46 'Cameca'. Electronic scanning was performed in the direction perpendicular to the coating.

The adhesion of the coating to the substrate before and after heat treatment was determined by the shear method (see Fig. 1.) The coating is deposited to one-half of the sample (cylinder) surface. The coating-free end of the sample fits into the matrix. So, the coating leans on the end face of the matrix. Adhesion shear strength was calculated as the ratio of the shear load to the area of the coated cylindrical surface.

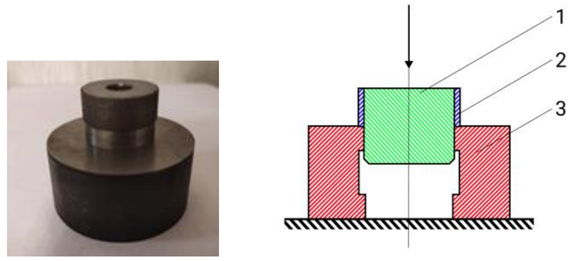

(A) (B)

Fig.1. Device (A) and its scheme (B) for testing of the coating adhesion strength by the shear method: 1 – sample, 2 – coating, 3 – matrix

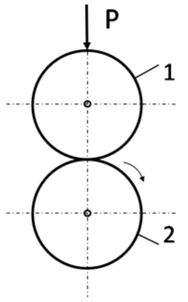

Fig. 2. Scheme of the friction-sliding: 1 – stationary sample with coating, 2 – rotated sample (counterbody)

Tests of coatings' wear resistance under sliding friction were performed on a computerised friction machine 2070 SMT-1 using the disk–disk scheme. Simultaneously, one disk rotated (counterbody), and the other was stationary (see Fig. 2); this simulated friction-sliding. The coating was applied to a stationary disk. Steel 0.45C hardened to HRC 50-52 hardness was used as a counterbody. The sliding speed was constant and equal to 1 m/s, and the specific load was 1 MPa. The tests were performed in air (dry friction) and lubricants TsIATIM-203 and AMG-10 [26] were used. In this case, the 11Cr18MoWCu and Ni–B + 11Cr18MoWCu thermal-spray coating were applied to the generatrix surface of the rings made of 0.45C carbon steel with an outer diameter of 50 mm, an inner diameter of 16 mm and a width of 10 mm. The coated sample was fixed, and the rotating counterbody was made of 0.45C steel, hardened to a hardness of 48–52 HRC. The tests were performed at a load of 1 MPa and a sliding speed of 1 m/s. The wear rate was determined by the weight reduction method.

Investigations of cavitation-erosion wear of coatings were performed on an installation with a magnetostrictive vibrator at an oscillation frequency of 22 kHz, an amplitude of 40 μm and a distance between the sample and the end of the concentrator of 0.5 mm [27]. The sample weight loss was used as a basis for assessing the wear intensity during 1 h, 2 h and 4 h of tests in a working medium of 5% aqueous solution of HCl at a temperature of 18–20 °C.

Tests of the coatings and the 0.45C steel samples under abrasive wear conditions were performed on samples in the form of plates having a size of 20x15x5 mm. Quartz sand with a particle size of 0.1–0.3 mm was used as an abrasive material. Wear resistance was assessed by the sample weight loss per 1 kg of abrasive powder supplied to the friction area.

Hydroabrasive wear of the coatings was investigated on a hydraulic test rig according to the method described by Burda et al. [28]; as an abrasive material we used quartz sand with a particle size of 0.1–0.3 mm, the concentration of solid particles was 5 wt.% and the pulp flow rate was 30 m/s.

The wear of the samples was determined based on the measured weight loss, which was ascertained using electronic balances VLA-200 with an accuracy of 0.1 mg.

3. RESULTS AND DISCUSSION

Depending on the modes of plasma spraying, a certain porous structure of coatings is created, which is one of their essential characteristics. This can play a positive role, increasing the tribotechnical properties of parts during their operation in the oil, when the pores play the role of oil cups and lubrication grooves. Thus, the microstructure of 11Cr18MoWCu steel plasma coating (Fig. 3A) has a layered structure. The layers mainly consist of particles in the form of thin curved plates and many spherical and irregular round-shaped particles. In Fig. 3C and 3D, there is better visibility of an internal structure of the coating layers, and it is seen that spherical particles are located not only along the boundaries of the layers but also in their middle. The coating has a fairly high porosity. Under the optimal modes of spraying the steel 11Cr18MoWCu, the total porosity of the coating is 20%–24%, and the maximum open porosity is 16%–18%.

According to the microstructure analysis, after chromium plating at a temperature of 1100 °C during 3 h, the coating density increases and the porosity decreases significantly.

The boundaries between the layers and particles become less clear and smoother, the structure becomes more homogeneous (Fig. 3B and 3D) and the coating integrity increases. A chromium coating with a thickness of 10 μm and a hardness of 4–4.5 GPa is formed on the surface. To a depth of 50 μm, the structure of the coating is fine-grained with a microhardness of 8.10 GPa. In the coating towards the substrate one can see thin and narrow layers, which differ significantly in size from the plasma coating without heat treatment and have a microhardness of 4.9 GPa.

Fig. 4 presents the X-ray patterns of plasma coating before (Fig. 4B) and after heat treatment (Fig. 4C). For comparison, the X-ray patterns of 11Cr18MoWCu steel wire (see Fig. 4A) show that it has a ferritic structure, and after spraying (see Fig. 4B) it consists of both austenite and ferrite. The probable explanation for its formation may be the following. In the process of melting steel at high temperature for a short time there is a complete homogenisation of the alloy. During the subsequent high-speed solidification and high-rate cooling, a high-temperature fine-crystalline phase is formed, firstly austenite, with carbon, chromium, molybdenum, tungsten and copper dissolved in it. This state is thermodynamically unstable at low temperatures, but the driving force of γ → α transformations is small. Therefore, the very fine grain formed during quenching from the liquid prevents the γ → α transformation.

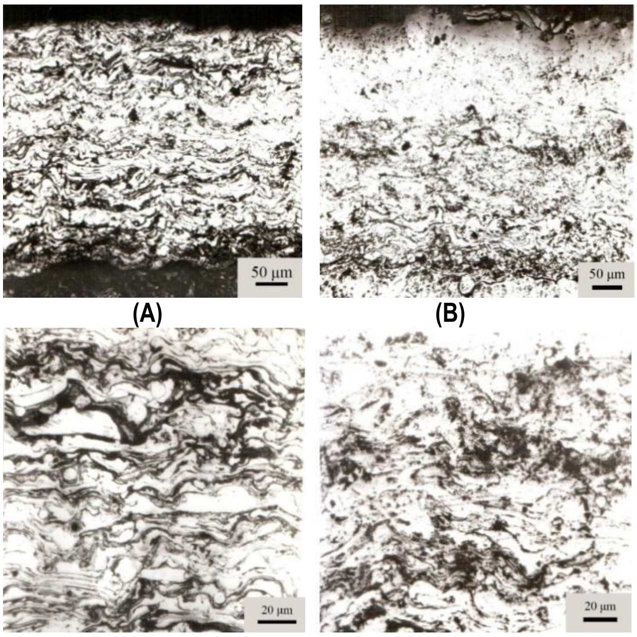

(A) **(B)**
(C) **(D)**

Fig. 3. Microstructure of 11Cr18MoWCu steel plasma coating before (A, C) and after (B, D) CHT chromium plating. (A) and (B) – magnification ×70; (C) and (D) – magnification ×200. CHT, chemical-heat treatment

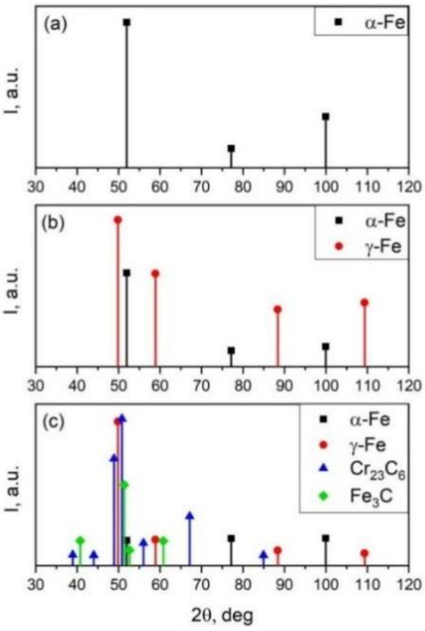

Fig. 4. X-ray patterns: (A) 11Cr18MoWCu steel wire; (B) 11Cr18MoWCu plasma coating before heat treatment; (C) 11Cr18MoWCu plasma coating after CHT chromium plating

Analysis of the bar X-ray pattern of the steel coating after CHT (chromium plating) (see Fig. 4C) showed Fe3C and Cr23C6 phase lines' appearance and a decrease in the intensities of the γ-phase lines and an increase in the α-phase. Obviously, during CHT, there is a partial decomposition of the γ-phase into ferrite and the carbide precipitation.

A deeper understanding of the processes that take place during CHT can be obtained by studying the distribution of chemical elements through the thickness of the coating and the transition zone formed by the diffusion of elements and consisting of a solid solution of relevant components. Fig. 5 represents the concentration profiles of Fe and Cr at the boundary of the coating and the substrate after CHT.

Analysis of profiles allows us to make the following conclusions: In the substrate of 0.45C steel the iron content towards the separation surface gradually decreases and the chromium content increases accordingly. A gradual change of concentrations is observed in the area of the steel coating at a distance of up to 10 μm from the separation surface. The thickness of the transition zone is 18–20 μm. At greater distances from the transition zone we have a significant deviation from uniformity, and a rapid increase of chromium concentration corresponds to the same sharp drop in iron content. The reason for this is the formation of a concentrated substitutional solid solution of chromium in iron, and thus chromium replaces a portion of iron atoms. Also, chromium carbides may be formed. X-ray structural analysis revealed the inclusions of Cr23C6 carbide. The width of the peaks on the curves can be used to estimate the dimensions of these inclusions, and it is ascertained that they vary in a range of 3–5 μm.

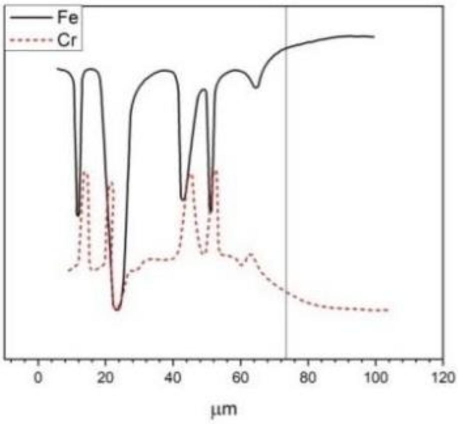

Fig. 5. Profiles of Fe and Cr concentrations at the boundary of 11Cr18MoWCu steel plasma coating and substrate after CHT. The distance from the surface of the coating is plotted along the x-axis. A solid vertical line marks the visible boundary between the coating and the base. The concentration values are given in conventional units. CHT, chemical-heat treatment

The pore size in the plasma coatings is several microns, and their developed surface leads to the formation of a capillary system. The behaviour of capillary system is determined mainly by the properties of the separation margins, specifically their surface energy. Since, to effectively wet the contact surface during further heat treatment and further accelerate the diffusion processes, a liquid phase would be required, it is considered that the impregnation of a structure of coatings characterised by a porous system needs such a phase. Experimental studies of microsections showed that the impregnation of a porous plasma coating with a metal melt of Ni–Ni3B, with eutectic composition of 20%–25% of the total coating thickness, provides a dense coating with a characteristic metallic lustre. In addition, melt impregnation fills open pores and cavities between layers of plasma coating (see Fig. 6), and also provides high adhesion to the substrate due to the formation of a transition zone during mutual diffusion of coating and steel substrate elements.

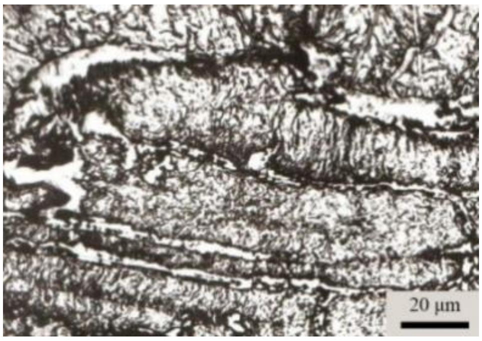

Fig. 6. Microstructure of GPC Ni–B+11Cr18MoWCu after heat treatment at T = 1110 °C, t = 2 min, 500×. GPC, galvanic plasma coating

According to the results of experiments, the adhesion of plasma coatings after CHT increases in the order of 1.7 compared to untreated plasma coating (see Fig. 7).

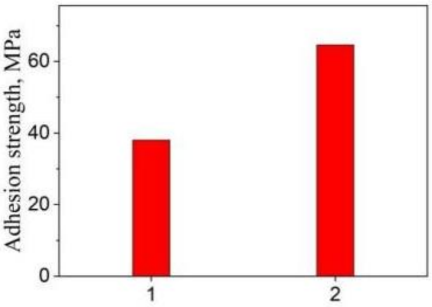

Fig. 7. Adhesion of the plasma coating to the substrate during shear: 1 – as deposited, 11Cr18MoWCu steel; 2 – 11Cr18MoWCu steel after chromium plating

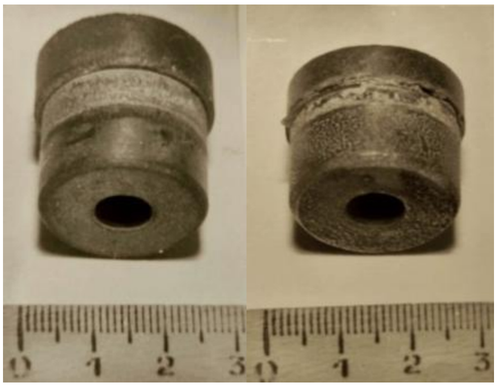

(A) **(B)**

Fig. 8. Samples with plasma coating 11Cr18MoWCu after shear test: (A) as-fabricated; (B) after chromium plating

Figure 8 shows samples with coatings after shear test. As-fabricated plasma coating without CHT (Fig. 8A) is sheared from the substrate, smoothing its rough surface, and the coating after

CHT (Fig. 8B) is cut in the place of mutual diffusion between the coating and the substrate.

11Cr18MoWCu plasma coatings after impregnation with liquid-phase Ni–Ni3B are cut as a solid cast material, which indicates the high strength of adhesion of the GPC to the substrate.

The results of tests under conditions of cavitation-erosion wear (see Fig. 9) showed a slight increase in the stability of carbon steels 0.20C and 0.45C after plasma spraying (curves 3 and 4).

Additionally, due to insufficient adhesion of the coating to the substrate and the presence of a zone with high concentration of defects between them, the coating sometimes delaminates.

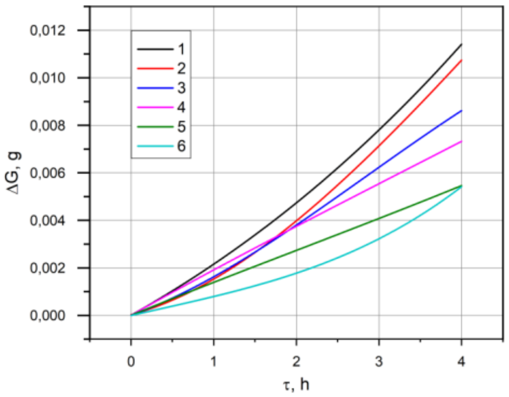

Fig. 9. Dependence of weight loss (ΔG) of 0.20C steel (curves 1, 3, 6) and 0.45C steel (curves 2, 4, 5) in cavitation-erosion wear: 1, 2 – without coating; 3, 4 – with plasma coating; 5, 6 – with plasma coating after CHT. CHT, chemical-heat treatment

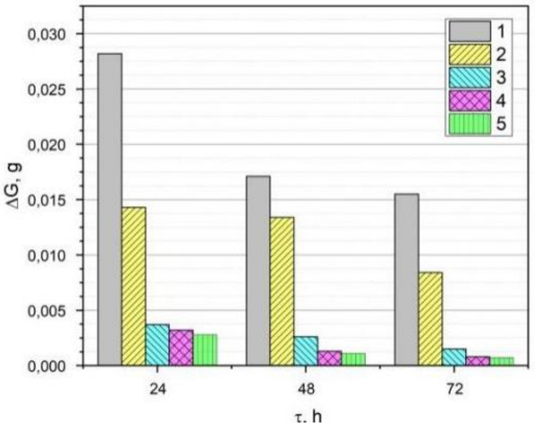

Fig. 10. Dependence of weight loss (ΔG) on the tests' duration (τ) in corrosion-abrasive wear of 11Cr18MoWCu steel plasma coating before and after CHT and impregnation with liquid eutectic phase Ni–Ni3B: 1 – standard 0.45C steel; 2 – plasma coating; 3 – plasma coating after CHT; 4 – plasma coating after impregnation; 5 – plasma coating after CHT and impregnation. CHT, chemical-heat treatment

Thermodiffusion chromium plating of plasma coatings significantly reduces porosity, and heals a defective transition zone with the formation of a transition layer between the coating and substrate, which increases the protective properties of such coatings (see Fig. 9, curves 5 and 6). Studies show that plasma coatings after CHT are 1.5 times superior to untreated coating and, accordingly, 2 times superior to the uncoated 0.20C and 0.45C steels under conditions of cavitation-erosion wear.

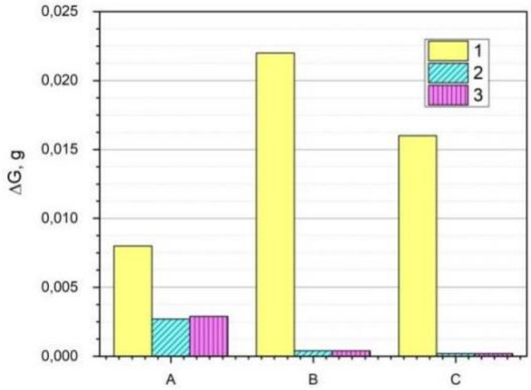

Fig. 11. Dependence of weight loss (ΔG) of the standard 0.45C steel (A), plasma coating 11Cr18MoWCu (B) and GPC Ni–B + 11Cr18MoWCu (C) under sliding friction conditions: 1 – dry friction; 2 – in TsIATIM-203 oil; 3 – in AMG-10 oil. GPC, galvanic plasma coating

Studies of coatings under conditions of corrosion and abrasive wear have shown (see Fig. 10) that steel plasma coatings after different types of heat treatment have much better results compared to the standard 0.45C steel, especially after 72 h of testing, and five times less wear than as-fabricated coating.

The results of friction and wear studies showed high wear resistance of plasma coatings 11Cr18MoWCu and GPC Ni–B + 11Cr18MoWCu, especially in lubricants (see Fig. 11). Coatings running-in effectively resist the phenomena of adhesion and have a high relaxation ability.

4. CONCLUSIONS

Research into the features of structure formation and tribotechnical properties of composite 11Cr18MoWCu steel plasma and galvanoplasmic coatings showed the feasibility of combining the processes of gas-thermal spraying of plasma coatings with open porosity up to 16%–18% and liquid phase of the eutectic composition of the pre-applied Ni–B galvanic layer.

The technology of combined steel plasma coating deposition is proposed. It is proved that after chromium plating at a temperature of 1100 °C and exposure for 3 h, the density of the coating increases, and the number of microcavities in it decreases significantly. The boundaries between the layers and particles become less clear and smoothened, and the structure becomes more homogeneous, increasing the continuity of the coating. Impregnation of porous plasma coatings with the liquid phase of the eutectic composition from the previously applied Ni–B galvanic layer fills open pores and cavities between the layers of the plasma coating with Ni–Ni3B eutectic. The formation of a transition zone as a result of mutual diffusion of the coating and substrate elements contributes to a significant increase in adhesion.

Investigation of physical and mechanical properties of the studied coatings showed a significant improvement in their performance under different types of wear and corrosive environments.

The results of experimental tests prove the following indications concerning plasma coatings after CHT: In conditions of cavitation-erosion wear, it is 1.5 times superior to as-fabricated coating, and 2 times superior to the results obtained when the uncoated 0.20C and 0.45C steel are used; under conditions of corrosion-abrasive wear, it yields much better results than those obtained with standard 0.45C steel, especially after 72 h of testing, and five times less wear than plasma coating without heat treatment.

REFERENCES

1. Hetmanczyk M, Swadzba L, Mendala B. Advanced Materials and Protective Coatings in Aero-Engines Application. Journal of Achievements in Materials and Manufacturing Engineering. 2007; 24(1):372–81.
2. Uvarova I, Babutina T, Kostenko V, Cavyak M. From Nanophased Powders to Composite Coatings. Functional Materials. 2001;8(1): 185–8.
3. Vijayanand P, Kumar A, Vijaya Kumar KR, Vinod A, Kumaran P, Arungalai Vendan S. Characterizations of Plasma Sprayed Composite Coatings Over 1020 Mild Steel. Journal of Mechanical Science and Technology. 2017;31(10):4747–54.
4. Uvarova I. Ultrafine and Nanophased Powders as the Fillers in Composite Coatings. Journal of Advanced Materials. 2000 Apr; 32(2):26–31.
5. Rinaldi C, Ferravante L. An Innovative Shrouded Plasma Technique Producing Clean Coatings with Good Hot Corrosion Resistance for Gas Turbine Blades. EUROMAT 2001 Conf. Proc. Rimini. 2001.
6. Gill BJ, Ridding FL. Argon Shrouded Plasma Spray Technology for Production Applications. Surface Engineering, 1986;2(3):169–76.
7. Brezinová J, Guzanová A, Draganovská D, Egri M. Assessment Tribological Properties of Coatings Applied by HVOF Technology. Acta Mechanica et Automatica. 2013 Sep 1;7(3):135–9.
8. Fauchais P, Vardelle M. Understanding the Formation of D.C. Plasma Sprayed Coatings. Materials Science Forum. 2003 Aug;426–432:2459–66.
9. Coddet C, Verdy C, Dembinski L, Grosdidier T, Cornu D, García JC. High Properties Metallic Alloys Obtained through the Thermal Spray Route. Materials Science Forum. 2003 Aug;426–432:2467–72.
10. Hardwicke CU, Lau Y-C. Advances in Thermal Spray Coatings for Gas Turbines and Energy Generation: A Review. Journal of Thermal Spray Technology. 2013 Feb 28;22(5):564–76.
11. Thorpe ML. Thermal Spray, Industry in Transition. Advanced Mat. and Proc. 1993;143(5):50–61.
12. Bresinova J, Gubanova F, Draganovska D, Marushchak PO, Landova M. Spray Coatings Containing WC and WB Particles. Acta Mechanica et Automatica. 2016;10(4):296–299.
13. Smagorinski ME, Tsantrizos PG. Sprayed Metals and their Thermal Treatment. EUROMAT 2001 Conf. Proc. Rimini. 2001.
14. Kabatova M, Medukh R, Kostenko V, Mihalik J, Seveikova J. Improvement of Corrosion and Wear Resistance of Sintered Steels by Coatings. In Vienna; 2004. p. 423–6.
15. Medyukh RM, Medyukh VK, Uvarova IV. Diffusion Chromizing of Molybdenum-Based Plasma Coatings. Powder Metallurgy and Metal Ceramics. 2018 Jan;56(9–10):535–40.
16. Staia MH, Ramos E, Carrasquero A, Roman A, Lesage J, Chicot D, et al. Effect of substrate roughness induced by grit blasting upon adhesion of WC-17% Co thermal sprayed coatings. Thin Solid Films. 2000 Dec;377–378:657–64.
17. GuslienkoYu, MediukhR, TikhonovichT, ChudovskiV, PavlenkoN. Structure and Wear Resistance of Composite Galvanoplasma Coatings. Powder Metallurgy.1989;1:31–4.
18. Guslienko Yu, Kostenko V, Medukh R, Uvarova I, Kabatova M, Dzubinsky M, Dudrova E. Structure and Properties of Boride Composite Coatings. Functional Materials. 2001;8(1):193–5.
19. Meidukh R, Kabatova M, Parilak L, Kostenko V, Dzubinsky M, Dudrova E. Microstructure and Properties of Ni-B and Ni-B-WC Coating Layers on Sintered Steels. 11 Int. Symposium of Metallography. Slovak Republic; 2001. p. 536–8.
20. Medukh R, Kabatova M, Parilak L, Kostenko V, Dzubinsky M, Dudrova E. Microstructure and Properties of Layers Produced on Sintered Steels by Electrolitic Coatings and Diffusion Chroming. Int. Conference “Protective Coating 2002”. Slovak Republic; 2002.
21. Odhiambo JG, Li W, Zhao Y, Li C. Porosity and Its Significance in Plasma-Sprayed Coatings. Coatings. 2019 Jul 23;9(7):460.
22. Yang B, Shi C, Li Y, Lei Q, Nie Y. Effect of Cu on the corrosion resistance and electrochemical response of a Ni–Co–Cr–Mo alloy in acidic chloride solution. Journal of Materials Research. 2018 Oct 2;33(22):3801–8.
23. Hou Y, Li Y, Wang F, Zhang C, Koizumi Y, Chiba A. Influence of Mo concentration on corrosion resistance to HF acid solution of Ni–Co–Cr–Mo alloys with and without Cu. Corrosion Science. 2015 Oct;99:185–93.
24. Jung S, Jeon C, Jo YH, Choi W-M, Lee B-J, Oh Y-J, et al. Effects of tungsten and molybdenum on high-temperature tensile properties of five heat-resistant austenitic stainless steels. Materials Science and Engineering: A. 2016 Feb;656:190–9.
25. Guslienko Y, Luchka M, Savakin V, Buray M. Patent of Ukraine. 1283, 28.02.1997.
26. Pašečko MÌ, Kìndačuk MV, Labunec' VF, Dziedzic K, Rad'ko OV, Korbut ÊV. Tribologia. Lublin: Politechnika Lubelska; 2017.
27. Kluk A, Medukh R, Nekoz A, Stetsishin M, Dzub A. Increasing of Cavitation-Erosion Resistance of Carbon Steels by Plasma Spraying and Subsequent Thermal-Diffusion Chromium Plating. Problems of Frictions and Wear. 1987;31:66–8.
28. Burda M, Dovzinshiky I, Burda Yu. Patent of Ukraine. 92234, 11.10.2010.

Roman Mediuk: http://orcid.org/0000-0003-2176-9321

Vira Mediukh: http://orcid.org/0000-0003-1592-193X

Vasyl Labunets: http://orcid.org/0000-0002-7860-8468

Pavlo Nosko: https://orcid.org/0000-0003-4792-6460

Oleksandr Bashta: https://orcid.org/0000-0001-7914-897X

Irina Kondratenko: http://orcid.org/0000-0001-7970-2248

DOI 10.2478/ama-2022-0046

NUMERICAL CRITERION FOR THE DURATION OF NON-CHAOTIC TRANSIENTS IN ODEs

Ryszard SZCZEBIOT*, **Roman KACZYŃSKI****, **Leszek GOŁDYN***

*Faculty of Computer Science and Technology, Lomza State University of Applied Sciences,
ul. Akademicka 14, 18-400 Lomza, Poland
**Faculty of Mechanical Engineering, Bialystok University of Technology, ul. Wiejska 45C, 15-351 Bialystok, Poland

rysbiot@ansl.edu.pl, r.kaczynski@pb.edu.pl, lgoldyn@ansl.edu.pl

received 10 August 2022, revised 10 October 2022, accepted 10 October 2022

Abstract: The paper proposes an original numerical criterion for the duration analysis of non-chaotic transients based on the Euclidean norm of a properly defined vector. For this purpose, transient trajectories, prior to their entering a small neighbourhood of the limit cycle, are used. The vector has been defined with its components constituting the lengths of the sections, which connect the origin of the coordinate system with appropriately determined transient trajectory points. The norm of the vector for the analysis of non-chaotic transients has also been applied. As an assessment criterion of transients, the convergence of the norm to small neighbourhood of the limit cycle with the assumed accuracy is used. The paper also provides examples of the application of this criterion to the Van der Pol oscillators in the case of periodic oscillations.

Key words: numerical criterion, non-chaotic transients, limit cycle, ODEs systems, Van der Pol oscillator

1. INTRODUCTION

An exact assessment of transient behaviour in physical systems is very important for many practical reasons. For example, in real-time digital simulators, which are applied in the power industry, the exact assessment of transients is also essential for practical implementations in short-circuit protection systems. The transient behaviour analysis is also essential when dealing with short circuits in the power grid. Control systems, especially the ones used in nonlinear systems, must account not only for the transient phenomena that occur in them but also for their duration. In the analyses of nonlinear systems, neither the superposition principle can be used nor can the transient component be separated. It can be said that the transient phenomenon is fully integrated into the mathematical model of the system and constitutes an inseparable problem to be solved. This is the source of additional difficulties of transient analysis. In addition, the transient dynamics in nonlinear systems depends not only on the parameters of the system but also on the choice of initial conditions. Additionally, it should be emphasised that chaotic systems are particularly sensitive to the latter, where small changes in the initial conditions can cause great differences in the nature of the final solution. An example of this is the system of Lorenz equations [1, 2].

After the introduction of state variables, nonlinear differential equations are transformed into a system of the first-order ordinary differential equation (ODEs), called the state equations. The purpose of these transformations is to simplify the equations so as to be able to use numerical methods to solve them [3, 4]. A great number of physical systems are modelled by second-order ODEs, for example, the Duffing or Van der Pol equations [3, 5, 6, 7, 8, 9]. These equations, after their transformation into a system of equations, are analysed on the phase plane. As a result, for stable systems, it is possible to obtain specific phase portraits whose trajectories are convergent to the limit cycle. In the transients, these trajectories are irregular lines that turn into periodic cycles after the transient time ttr [10].

In contrast to the paper [10], in which the non-chaotic transients in the Duffing equations were examined on the basis of the analyses of cycle fields, in this paper, the Euclidean norm of a properly defined vector was applied to the analyses of the Van der Pol's non-chaotic transients.

The literature available on the subject is very extensive. We will now present a brief description of the selected studies regarding the analysis of the transient behaviour occurring in nonlinear systems [11-17].

Paper [11] presents a general overview of works on transient behaviour in chaotic systems, while monograph [12] and dissertation [18] discuss in detail the physical phenomena taking place in the Duffing and Van der Pol systems including the methods of their analyses.

Specific transient behaviour is discussed in Zumdieck et al. [13]. Long chaotic transients occur in complex networks of pulse-coupled oscillators. It has been shown that small changes in the structure of the system have a decisive influence on its dynamics. The paper [2] presents an interesting analysis of the impact of initial conditions on the course of transient trajectories. To this end, a system of three Lorenz equations has been used. Chaotic transients and super transients in spatially extended systems have been described in Tél and Lai [14]. These specific states occur in the systems described by PDEs (partial differential equations), e.g., the Navier-Stokes equations. Also, the noteworthy results on transient analysis are presented in Cooper et al. [15] and Sabarathinam et al. [16]. In the former one, several methods of controlling an autonomous Van der Pol oscillator have been analysed. It presented transient trajectories using different control methods and non-zero initial conditions, entering the limit cycle of the system. The latter work discusses an original Duffing system with smooth cubic nonlinearity in the form of a memristor. It shows a phase portrait and time evolutions of state variables for non-zero initial conditions and selected system parameters. In the paper by Vahedi et al. [17], the Duffing oscillator has been used for the analyses of distributed-generation (DG) units. The paper analyses an oscillator operating in both chaotic and periodic vibrations under an appropriate control mode. It presents a characteristic phase portrait of the system with transient trajectories of the system and characteristic phase portraits. In the case of periodic vibrations, transient trajectories enter the limit cycle. Papers [19, 20] make use of the transients to estimate encoded parameters of the Duffing and Van der Pol nonlinear systems.

The paper proposes an original criterion for determining the duration of the non-chaotic transient in ODEs, based on the Euclidean norm of a properly defined vector.

The criterion is illustrated by example analyses for the duration of transient processes in physical systems described by the Van der Pol's nonlinear equations.

In our paper, we consider nonlinear systems with a stable small neighbourhood of the limit cycle and the temporal length of the non-chaotic transient time denoted by ttr. The proposed method of estimating the transient time ttr is illustrated by analysing the Van der Pol equations [8, 21]. The above equations were developed in the first half of the 20th century. They have been a subject of many scientific studies, and the phenomena described in them have been frequently discussed. The computations have been made using a proprietary program written in C++. The fourth-order Runge-Kutta method was applied in the numerical calculations. Some selected results were compared with the computations obtained by applying the Wolfram Mathematica software.

2. NUMERICAL CRITERION FOR THE DURATION OF NON-CHAOTIC TRANSIENTS IN ODEs

An accurate time definition for the duration of the non-chaotic transients in nonlinear systems, considering its practical applications, is very important. It can be applied in the analysis of the operation of automation systems, the evaluation of the power systems security and the analysis of the operation of electronic systems.

The time t_{tr}, in which the transient trajectory enters a small neighbourhood of the limit cycle, is assumed as the end of the duration of the non-chaotic transients. For further considerations, a constant number of N points was assumed for each cycle loop of the cycle for determining Euclidean norms (Fig. 1). In this case, the assumed N coincides with the step of numerical calculations.

Each point in N corresponds to the section OP_i $(i = 1,2,\dots,N)$. Thus, we define vector, Y:

$$Y = [y_1, y_2, \dots, y_N] \tag{1}$$

wherein:

$$y_i = OP_i = ({x_{1,i}}^2 + {x_{2,i}}^2)^{1/2}, \quad (i = 1,2,\dots,N) \tag{2}$$

where x_1 and x_2 are the values of state variables in the resulting time intervals

The Euclidean norm is assigned to vector Y:

$$\|Y\| = \left(\Sigma_{i=1}^{N} y_i^2\right)^{\frac{1}{2}} \tag{3}$$

where N is the assumed constant number points for each cycle loop.

In interval time, we have a series of $\|Y\|_k$ norms:

$$\|Y\|_k = \left(\left(\Sigma_{i=1}^{N} y_i^2\right)^{\frac{1}{2}}\right)k, \ (k = 1,2,\dots,L) \tag{4}$$

where L is the total number of cycles investigated.

For stable systems, the series of norms $\|Y\|_k$ $(k = 1,2,\dots,L)$ converges to a stable norm, which represents a small neighbourhood of the limit cycle.

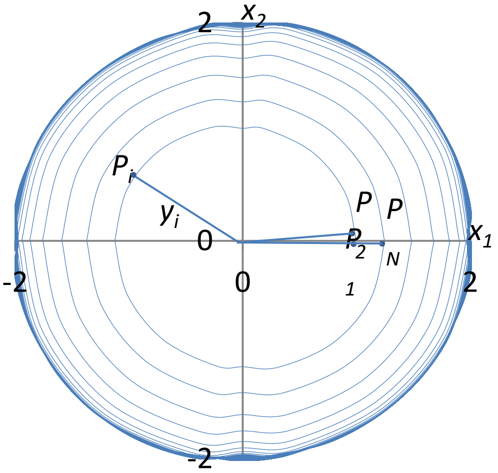

Fig. 1. Phase portrait with non-chaotic transients of the Van der Pol system Eq. (6), $\mu = 0.1$, $x_1(0) = 1$, $x_2(0) = 0$

Considering the above-mentioned facts, a definition of the duration of non-chaotic transients in nonlinear systems can be presented as follows.

In a stable system, described by the system of equations $\dot{x} = f(x(t), u(t), t)$, where $x(t) \in R^n$ and $u(t) \in R^n$, the duration of non-chaotic transients is determined by time t_{tr}, in which the transient trajectory tends to a small neighbourhood of the limit cycle with the condition:

$$\frac{|\|Y\|_k - (\|Y\|_m)_k|}{(\|Y\|_m)_k} \geq \varepsilon, k = L-1, L-2, \dots \tag{5}$$

where for each k, $(\|Y\|_m)_k$ represents the mean value of the norms calculated for cycles $L, \dots, k+1$ and ε is a sufficiently small number.

It should be noted that the non-chaotic transients last as long as the standard deviations $\|Y\|_k$ in criterion (5) are greater by ε than the mean value of $(\|Y\|_m)_k$. The condition is checked cyclically from the end of the integration interval, i.e., from small deviations of the norm $\|Y\|_k$ for a more precise determination of the mean value of $(\|Y\|_m)_k$. The first cycle satisfying the condition (5) determines the last cycle of the non-chaotic transients and therefore its duration t_{tr}.

3. APPLICATION OF THE PROPOSED CRITERION FOR THE VAN DER POL EQUATION

The Van der Pol equation without the driving force is very often presented after the application of the Liénard transformation:

$$\dot{x}_1 = -x_2$$

$$\dot{x}_2 = x_1 + \mu\left(x_2 - \frac{{x_2}^3}{3}\right). \tag{6}$$

The Van der Pol equation applies to systems in which there is a nonlinear damping $\mu(1 - x^2)$, where μ is a small parameter.

Using the $\mu = 0.1$ to solve the system (6) with initial conditions $x_1(0) = 1, x_2(0) = 0$, it is possible to obtain a typical phase portrait shown in Fig. 1. The convergence of $\|Y\|_k$ to $(\|Y\|_m)_k$ is illustrated in Fig. 2. Assuming $\varepsilon = 0.005$, the transient time t_{tr} is found to be $t_{tr} = 52.06$.

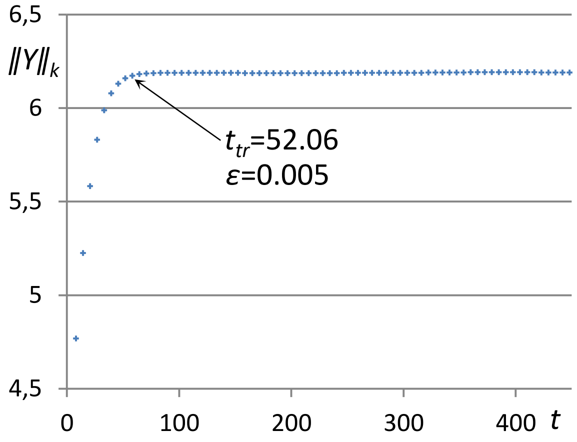

Fig. 2. Chart of $\|Y\|_k = f(t)$, $\mu = 0.1$, $x_1(0) = 1$, $x_2(0) = 0$

An example application of the proposed criterion for the dependence of the transient time on the value of the damping coefficient μ is given for the driven Van der Pol equation.

This equation is most often used to describe electronic vibration generators, although it can be found in other fields of knowledge [21, 22].

The Van der Pol equation with a driving function b1cos(b2t) has the following form:

$$\frac{d^2z}{dt^2} + \frac{\mu(1-z^2)dz}{dt} + z = b_1\cos(b_2t), \tag{7}$$

where μ is the parameter of the electronic circuit, while b_1 and b_2 are the driving parameters.

Eq. (7) can be represented as a system of equations, taking $z(t) = x_1(t)$, $dz/dt = x_2(t)$:

$$\dot{x}_1 = x_2$$

$$\dot{x}_2 = -\mu(1 - {x_1}^2)x_2 - x_1 + b_1\cos(b_2t). \tag{8}$$

In further considerations, we adopt damping parameter values μ changing in the range 0.01÷0.2 and take:

$$b_1 = 1.0, b_2 = 250. \tag{9}$$

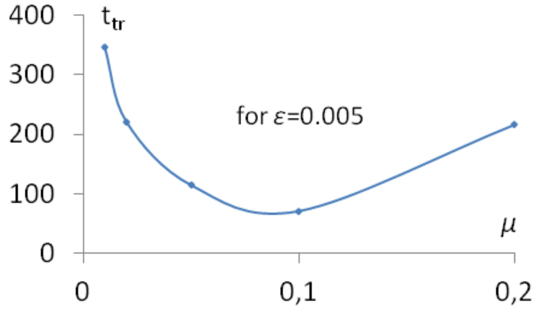

Fig. 3. Dependence of the non-chaotic transient time t_{tr} on the value of μ

As a result of solving the system (8), we obtain the phase portrait characterising the periodic vibrations. The individual steps of the determination of transient time t_{tr} are presented earlier in Section 2.

Fig. 3 presents the chart of the time duration t_{tr} of non-chaotic transient dependence on the value of the dumping coefficient μ for the Van der Pol Eq. (8), based on the proposed numerical criterion.

An example of calculating the transients time t_{tr} based on the proposed method for the point $\mu = 0.05$ in Fig. 3 is shown in Figs. 4 and 5.

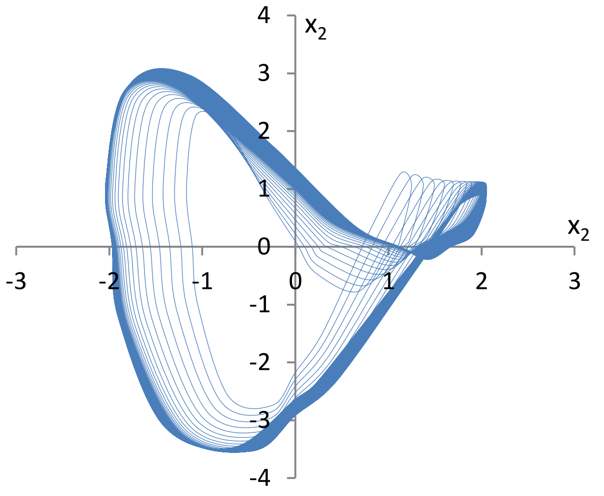

Fig. 4. Phase portrait of Van der Pol system, $\mu = 0.05$, $b_1 = 1.0$, $b_2 = 250$ $x_1(0) = 1$, $x_2(0) = 0$

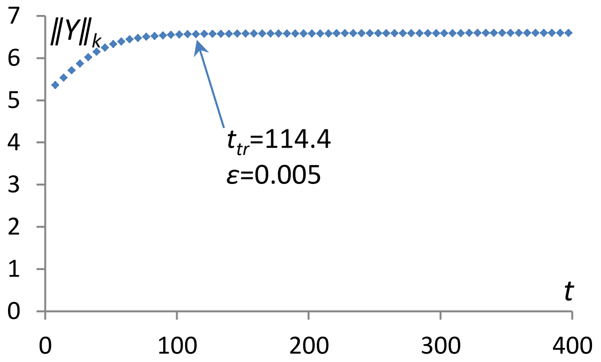

Fig. 5. Chart for $\|Y\|_k = f(t)$, $\mu = 0.05$, $b_1 = 1.0$, $b_2 = 250$ $x_1(0) = 1$, $x_2(0) = 0$

For higher values of the damping factor $\mu >$ 0.2 Eq. (8) in the considered time interval in the system, there are vibrations that characterise the exemplary attractor shown in Fig. 6. In this case, the $\|Y\|_k$ norm does not converge. The chart of the $\|Y\|_k$ norm for the phase portrait from Fig. 6 is shown in Fig. 7.

In further work, the generalisation of the duration of non-chaotic transients into higher-order ODEs equations will be continued. Also, the study of the influence of ε and the other system parameters of the duration on non-chaotic transients will be continued.

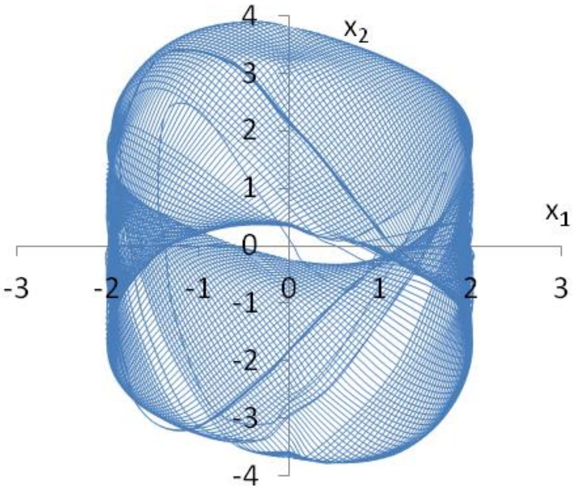

Fig. 6. Phase portrait of Van der Pol system, $\mu = 0.3, b_1 = 1.0, b_2 = 250, x_1(0) = 1, x_2(0) = 0$

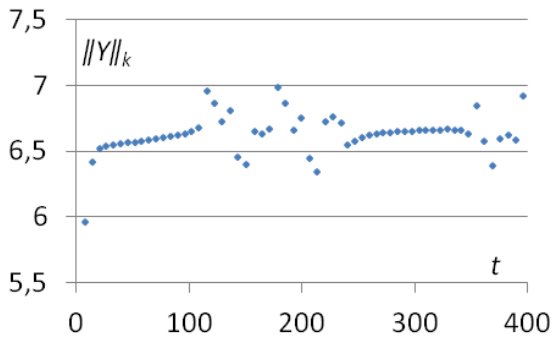

Fig. 7. Chart for $\|Y\|_k = f(t)$, $\mu = 0.3, b_1 = 1.0, b_2 = 250, x_1(0) = 1, x_2(0) = 0$

4. FINAL REMARKS AND CONCLUSIONS

The paper proposes an original numerical criterion for the duration analysis of non-chaotic transients based on the Euclidean norm of a properly defined vector for second-order ODEs systems. The analysed systems are assumed to be stable, and their transient trajectories converge to a small neighbourhood of the limit cycle. In order to assess time t_{tr}, a series of Euclidean norms $\|Y\|_k$ of vector Y are used. The vector's components include the length values of OP_i sections in successive trajectory cycles, where $OP_i = ({x_{1,i}}^2 + {x_{2,i}}^2)^{1/2}$. In a nonlinear stable system with the limit cycle, the $\|Y\|_k$ series is convergent to the mean value of $(\|Y\|_m)_k$ calculated from the end of the time interval, characteristic of the phase portrait reflecting the periodic oscillation. The proposed criterion is illustrated by examples of the analyses for the duration of transient processes in physical systems described by Van der Pol nonlinear equations. The proposed criterion is relatively simple and easy to apply to many practical engineering issues.

The method can be also generalised to higher-order ODEs. For example, when analysing the non-chaotic transients modelled by Lorenz equations, the tests should be carried out in space R^3, with $OP_i = ({x_{1,i}}^2 + {x_{2,i}}^2 + {x_{3,i}}^2)^{1/2}$. In this case, the series of norms $\|Y\|_k$ converges to the mean norm $(\|Y\|_m)_k$ computed in three-dimensional space.

REFERENCES

1. Peitgen H., Jurgens H., Saupe D. Pascal's Triangle: Cellular Automata and Attractors. Chaos and Fractals. Springer New York NY. 2004; 377-422. https://doi.org/10.1007/0-387-21823-8_9
2. Kravtsov S., Sugiyama N., Tsonis A. Transient behavior in the Lorenz model. Nonlinear Processes in Geophysics Discussions. 2014; 1.2: 1905-1917. https://doi.org/10.5194/npgd-1-1905-2014
3. Gear C. Numerical initial value problems in ordinary differential equations. Prentice-Hall series in automatic computation. 1971.
4. Press W. et al. Numerical recipes in C++. The art of scientific computing' 2007; 2: 1002.
5. Wu D. Wang Z. A Mathematica program for the approximate analytical solution to a nonlinear undamped Duffing equation by a new approximate approach. Computer physics communications' 2006; 174.6: 447-463. https://doi.org/10.1016/j.cpc.2005.09.006
6. Wang Z. P-stable linear symmetric multistep methods for periodic initial-value problems. Computer Physics Communications. 2005; 171.3: 162-174. https://doi.org/10.1016/j.cpc.2005.05.004
7. Jordan D., Smith P. Nonlinear ordinary differential equations: an introduction for scientists and engineers. OUP Oxford. 2007; 8.
8. Alghassab M. et al. Nonlinear control of chaotic forced Duffing and van der pol oscillators. International Journal of Modern Nonlinear Theory and Application. 2017; 6.: 26-31. https://doi.org/10.4236/ijmnta.2017.61003
9. Bellman R., Bentsman J., Meerkov S. Vibrational control of nonlinear systems: Vibrational controllability and transient behavior. IEEE Transactions on Automatic Control. 1986; 31.8: 717-724. https://doi.org/10.1109/TAC.1986.1104383
10. Szczebiot R. Jordan A. Criterion for transient behaviour in a nonlinear Duffing oscillator. Przegląd Elektrotechniczny. 2019; 95. https://doi.org/10.15199/48.2019.04.36
11. Tel T. The joy of transient chaos. Chaos: An Interdisciplinary Journal of Nonlinear Science. 2015; 25.9: 097619. https://doi.org/10.1063/1.4917287
12. Kovacic, I., Brennan, M. The Duffing equation: nonlinear oscillators and their behaviour. John Wiley & Sons. 2011. https://doi.org/10.1002/9780470977859
13. Zumdieck A. et al. Long chaotic transients in complex networks. Physical Review Letters. 2004; 93.24: 244103. https://doi.org/10.1103/PhysRevLett.93.244103
14. Tel T., Lai Y. Chaotic transients in spatially extended systems. Physics Reports. 2008; 460.6: 245-275. https://doi.org/10.1016/j.physrep.2008.01.001
15. Cooper M., Heidlauf P., Sands T. Controlling chaos-Forced van der pol equation. Mathematics. 2017; 5.4: 70. https://doi.org/10.3390/math5040070
16. Sabarathinam S., Volos Ch., Thamilmara K. Implementation and study of the nonlinear dynamics of a memristor-based Duffing oscillator. Nonlinear Dynamics' 2017; 87.1: 37-49. https://doi.org/10.1007/s11071-016-3022-8
17. Vahedi H., Gharehpetian G., Karrari M. Application of duffing oscillators for passive islanding detection of inverter-based distributed generation units. IEEE Transactions on Power Delivery' 2012; 27.4: 1973-1983. https://doi.org/10.1109/TPWRD.2012.2212251
18. Tsatsos M. The Van der Pol equation. arXiv preprint arXiv. 2008; 0803.1658. https://arxiv.org/ftp/arxiv/papers/0803/0803.1658.pdf
19. Bobtsov A. et al. Adaptive observer design for a chaotic Duffing system. International Journal of Robust and Nonlinear Control. IFAC-Affiliated Journal. 2009; 19.7: 829-841. https://doi.org/10.1002/rnc.1354
20. Tang Y. Distributed optimization for a class of high-order nonlinear multiagent systems with unknown dynamics. International Journal of Robust and Nonlinear Control. 2018; 28.17: 5545-5556. https://doi.org/10.1002/rnc.4330

21. Zduniak B., Bodnar M., Forys U. A modified van der Pol equation with delay in a description of the heart action. International Journal of Applied Mathematics and Computer Science' 2014; 24.4. https://doi.org/10.2478/amcs-2014-0063
22. Kimiaeifar A. et al. Analytical solution for Van der Pol–Duffing oscillators. Chaos, Solitons & Fractals. 2009; 42.5: 2660-2666. https://doi.org/10.1016/j.chaos.2009.03.145

The author wishes to thank Professor Andrzej Jordan for his insightful remarks and commentaries on the presented paper.

The authors declares that he has no known competing financial interests or personal relationships that could have appeared to influence the work reported in this paper.

RyszardSzczebiot: https://orcid.org/0000-0002-9084-915X

Roman Kaczyński: https://orcid.org/0000-0001-5736-5367

Leszek Gołdyn: https://orcid.org/0000-0002-0689-8590

sciendo

DOI 10. 2478/ama-2022-0047

APPLICATION OF THE DEFORMATION FRACTURE CRITERION TO CRACKING OF DISC SPECIMENS WITH A CENTRAL NARROW SLOT

Andrzej KAZBERUK*

*Faculty of Mechanical Engineering, Bialystok University of Technology, ul. Wiejska 45C, 15-351 Bialystok, Poland

a.kazberuk@b.edu.pl

received 9 October 2022, revised 20 October 2022, accepted 20 October 2022

Abstract: Using the method of singular integral equations, the elastic-plastic problem for cracked Brazilian disk was solved. Based on the Dugdale model and deformation fracture criterion, the relationships between critical load, notch tip opening displacement and length of the plastic strips were established. Also, the comparison between the present solution for the finite domain and the known solution obtained for the semi-infinite notch in the elastic plane was performed.

Key words: cracked Brazilian disc, Dugdale model, plastic strips, fracture deformation criterion, singular integral equations

1. INTRODUCTION

The application of the deformation fracture criterion in determining the basic fracture mechanics parameters requires the knowledge of the relationship between the load level and the opening displacement at the crack tip. This means that for an arbitrary test element, not only the stress field should be determined, but also the strain field considering the changes taking place in the fracture process zone. The general solutions for a crack or notch in the infinite plane are known ([1], see also the literature [2]) but for a particular specimen, these solutions can be only regarded as asymptotic. This work aims to determine the relationship between the load level and the opening displacement at the notch tip for a cylindrical specimen with a central narrow slot.

The Brazilian test is a simple indirect testing method, which is used to obtain the tensile strength of brittle materials such as concrete, rock, and rock-like materials. An up-to-date review of works concerning various aspects of the Brazilian test can be find in the literature [3,4].

A disc with an internal central crack as a convenient experimental specimen was considered analytically by [5–9]. These results concerning stress field distribution and values of the stress intensity factors were confirmed by Atkinsons et al. [10] and Awaji and Sato [11]. Recent works devoted to the investigation of the fracture process in quasi-brittle materials using a compressed disc with a central slot are [12–21].

The basic material parameter in fracture mechanics is the critical stress intensity factor determined experimentally on specimens with initial cracks. In the case of metals, the procedure for determining this parameter is standardised and widely used. The fracture process in this case begins with the fatigue-initiated crack. For quasi-brittle materials such as concrete, ceramics or rocks, it is difficult to obtain an initial crack with strictly defined parameters. Usually, the initial crack is produced at the specimen forming stage. In this way, slots of quite significant (2–4 mm) width and rounded tips are obtained. Also, previously cited sources devoted to analytical investigation of stress concentration in disc specimens refer to strict mathematical crack, i.e. the crack of zero width.

The method of determining the critical stress intensity factor of a quasi-brittle material on a compressed disc specimen with a centrally located narrow slot is presented. Knowing the value of the critical load and standard material constants, the critical stress intensity factor is calculated using the deformation fracture criterion [22] based on the Dugdale model [23,24]. The results were compared to previously published approximate relationships for semi-infinite U-notch in an elastic-plastic plate subjected to tension [25].

2. PROBLEM FORMULATION

There are two equal ($l_2 = l_3 = \ell$) linear cuts (contours L_2 and L_3) emanating from the slot vertices and placed on the axis Ox. These cuts will model the fracture process zone as plastic strips 26]. We assume that that Tresca-Saint Venant plasticity condition is fulfilled in these bands. The overall unknown relative extent of all defects weakening disc specimen we define as $\gamma = (\ell_0 + \ell)/\mathrm{R}$.

The set of dimensionless geometric parameters (ε_0, γ_0 γ) fully describes the domain under consideration. Assuming radius R as the basic unit length, we obtain relationships

$$\ell_0 = \gamma_0 R, \quad \ell = (\gamma - \gamma_0) R, \quad \rho = \varepsilon_0 \gamma_0 R. \tag{1}$$

Suppose that the hole edge (the smooth contour L_1) is free of applied loads. The disc is loaded by two concentrated forces P, which compress the specimen along the Ox axis (Fig.1). Such type of loading causes the concentration of tensile stresses invertices ($\pm\ell_0$) of the hole.

The problem will be solved using the singular integral equation method [27] (see also Savruk and Kazberuk [2]). Complex stress potentials are written in the form [27]

DOI 10.2478/ama-2022-0047

$$\Phi_*(z) = \Phi_0(z) + \Phi(z), \quad \Psi_*(z) = \Psi_0(z) + \Psi(z), \tag{2}$$

where functions [28]:

$$\Phi_0(z) = \sigma_p \frac{z^2+R^2}{2(z^2-R^2)}, \qquad \Psi_0(z) = \sigma_p \frac{2R^4}{(z^2-R^2)^2}. \tag{3}$$

Nominal stress $\sigma_p = P/(\pi R)$ is equal to normal stress σ_y alongside Ox axis, $z = x + iy$.

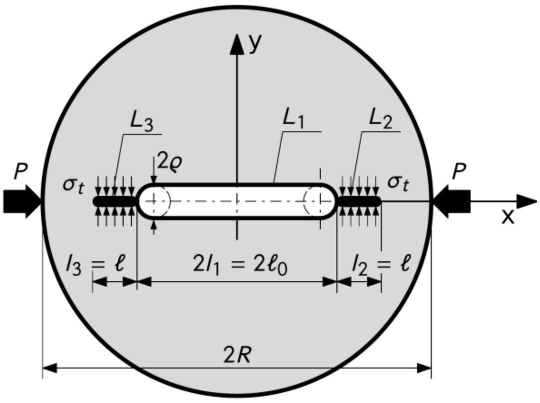

Fig. 1. Disc specimen weakened by central narrow slot and plastic strips subjected to compression by concentrated forces

Functions $\Phi_0(z)$, $\Psi_0(z)$ describe the stress state in the solid disc (i.e. without a hole) loaded by concentrated forces, whereas potentials $\Phi(z)$, $\Psi(z)$ characterise the disturbed stress state induced by the opening (L_1) and cuts (L_2, L_3). These potentials are written in the following form [27]:

$$\begin{aligned}\Phi(z) &= \frac{1}{2\pi}\int_L \left\{\left[\frac{1}{t-z} + \frac{\bar{t}}{z\bar{t}-R^2}\right] g'(t)\,\mathrm{d}t + \right.\\ &\left. + \frac{z(t\bar{t}-R^2)(z\bar{t}-2R^2)}{R^2(z\bar{t}-R^2)^2}\,\overline{g'(t)}\,\mathrm{d}\bar{t}\right\},\end{aligned} \tag{4}$$

$$\begin{aligned}\Psi(z) &= \frac{1}{2\pi}\int_L \left\{\left[\frac{\bar{t}^{\,3}}{(z\bar{t}-R^2)^2} - \frac{\bar{t}}{(t-z)^2}\right] g'(t)\,\mathrm{d}t + \right.\\ &\left. + \left[\frac{1}{t-z} + \frac{\bar{t}}{z\bar{t}-R^2} + \frac{\bar{t}\,(z\bar{t}-3R^2)(t\bar{t}-R^2)}{(z\bar{t}-R^2)^3}\right]\overline{g'(t)}\,\mathrm{d}\bar{t}\right\}.\end{aligned}$$

Here $g'(t)$ $(t \in L_k,\ k = 1,2,3)$ is an unknown function of the derivative of displacement discontinuity vector across the cut contour.

The boundary condition at the contour L has the following form:

$$N(t) + \mathrm{i}T(t) = p(t) \quad t \in L, \quad L = \cup_{k=1}^{3} \; L_k, \tag{5}$$

where N and T are normal and tangential components of the stress vector. The right side of the Eq. (5) is equal [27]:

$$p(t) = \sigma_k - \left\{\Phi_0(t) + \overline{\Phi_0(t)} + \frac{\mathrm{d}\bar{t}}{\mathrm{d}t}\left[t\overline{\Phi_0'(t)} + \overline{\Psi_0(t)}\right]\right\}, \quad t \in L, \tag{6}$$

where

$$\sigma_k = \begin{cases}0, & k = 1,\\ \sigma_t, & k = 2,3\end{cases}. \tag{7}$$

In further calculations, it was assumed that σ_t is equal to the material strength of the specimen determined in the Brazilian test (compressed disc without slot).

In further calculations, it was assumed that σ_t is equal to the material strength of the specimen determined in the Brazilian test (compressed disc without slot).

Fulfilling boundary condition Eq. (5) using potentials Eq. (4) we obtain the system of singular integral equations with unknown functions $g'_m(t)$ $(m = 1,2,3)$

$$\frac{1}{\pi}\sum_{k=1}^{3}\int_{L_k}\left[K_{km}(t,t')g'_m(t)\mathrm{d}t + L_{km}(t,t')\overline{g'_m(t)}\,\mathrm{d}\bar{t}\right] = p_m(t'), \tag{8}$$

$$t' \in L_m, \quad m = 1,2,3,$$

where kernels are as follows:

$$K(t,t') = f_1(t,t') + \overline{f_2(t,t')} + \frac{\mathrm{d}\overline{t'}}{\mathrm{d}t}\left[t'\overline{g_2(t,t')} + \overline{h_2(t,t')}\right],$$

$$L(t,t') = f_2(t,t') + \overline{f_1(t,t')} + \frac{\mathrm{d}\overline{t'}}{\mathrm{d}t}\left[t'\overline{g_1(t,t')} + \overline{h_1(t,t')}\right],$$

and

$$f_1(t,t') = \frac{1}{2}\left[\frac{1}{t-t'} + \frac{\bar{t}}{t'\bar{t} - R^2}\right],$$

$$f_2(t,t') = \frac{t'(t\bar{t} - R^2)(t'\bar{t} - 2R^2)}{2R^2(t'\bar{t} - R^2)^2},$$

$$g_1(t,t') = \frac{1}{2}\left[\frac{1}{(t-t')^2} - \frac{\bar{t}^{\,2}}{(t'\bar{t}-R^2)^2}\right],$$

$$g_2(t,t') = \frac{R^2(t\bar{t}-R^2)}{(t'\bar{t}-R^2)^3},$$

$$h_1(t,t') = \frac{1}{2}\left[-\frac{\bar{t}}{(t-t')^2} + \frac{\bar{t}^{\,3}}{(t'\bar{t}-R^2)^2}\right],$$

$$h_2(t,t') = \frac{1}{2}\left\{\frac{1}{t-t'} + \frac{\bar{t}\left[4R^4 - 3R^2\bar{t}\,(t'+t) + t'\bar{t}^{\,2}(t'+t)\right]}{(t'\bar{t}-R^2)^3}\right\}.$$

3. NUMERICAL SOLUTION OF INTEGRAL SINGULAR EQUATIONS

We assume a clockwise direction of tracing the contour L_1 so the elastic region stays on the left during tracing. Taking into consideration the symmetry of the contour concerning both coordinate axes, we can write its parametric equation in the form [2]:

$$t = R\omega_1(\xi) = R\begin{cases}\omega_q(\xi), & 0 \le \xi < \pi/2,\\ -\overline{\omega_q(\pi-\xi)}, & \pi/2 \le \xi < \pi,\\ -\omega_q(\xi-\pi), & \pi \le \xi < 3\pi/2,\\ \overline{\omega_q(2\pi-\xi)}, & 3\pi/2 \le \xi < 2\pi.\end{cases} \tag{9}$$

Here, the function $\omega_q(\xi)$ describes the segment of contour L_1 laying in the fourth quarter of the coordinate system:

$$\omega_q(\xi) = \begin{cases}1 - \varepsilon_0 + \varepsilon_0(\cos c\xi - \mathrm{i}\sin c\xi), & 0 \le \xi < \pi/(2c),\\ \varepsilon_0 c(\pi/2 - \xi) - \mathrm{i}\varepsilon_0, & \pi/(2c) \le \xi \le \pi/2,\end{cases} \tag{10}$$

where parameter $c = 1 + 2(1/\varepsilon_0 - 1)/\pi$. Total curve L_1 length equals to $2\pi\varepsilon_0\gamma_0\,Rc$.

The parametric equation describing cut L_2 was written in the form

$$t = R\omega_2(\xi) = R\left[\gamma_0 + \tfrac{1}{2}(\gamma - \gamma_0)(1+\xi)\right], \ -1 \le \xi \le 1 \tag{11}$$

Contour L_3 is symmetrical to L_2 concerning the Oy axis so

$$t = R\omega_3(\xi) = -R\,\omega_2(\xi), \quad -1 \le \xi \le 1. \tag{12}$$

Introducing substitutions

$$\begin{aligned}
&t = R\,\omega_1(\xi),\ \ t' = R\,\omega_1(\eta),\\
&t, t' \in L_1,\ \ \ 0 \le \xi,\ \eta \le 2\pi,\\
&t = R\,\omega_k(\xi),\ \ t' = R\,\omega_k(\eta),\\
&t, t' \in L_k,\ \ k = 2{,}3,\ \ -1 \le \xi, \eta \le 1,
\end{aligned} \tag{13}$$

we reduce the system of integral equations Eq. (8) to the canonical form

$$\begin{aligned}
&\frac{1}{\pi}\int_0^{2\pi}\left[M_{1m}(\xi,\eta)g_1'(\xi)+N_{1m}(\xi,\eta)\overline{g_1'(\xi)}\right]\mathrm{d}\xi + \\
&+\ \frac{1}{\pi}\sum_{k=2}^{3}\int_{-1}^{1}\left[M_{km}(\xi,\eta)g_k'(\xi)+N_{km}(\xi,\eta)\overline{g_k'(\xi)}\right]\mathrm{d}\xi = p_m(\eta),\\
&\qquad m = 1,2,3,
\end{aligned} \tag{14}$$

where

$$\begin{aligned}
M_{km}(\xi,\eta) &= RK_{km}^{*}(R\omega_k(\xi), R\omega_m(\eta)),\\
N_{km}(\xi,\eta) &= RL_{km}^{*}(R\omega_k(\xi), R\omega_m(\eta)),\\
g_k'(\xi) &= g'(R\omega_k(\xi))\omega_k'(\xi),\\
p_m(\eta) &= p(R\omega_m(\eta)).
\end{aligned}$$

The solution of the system of integral equations (14) consists of three complex functions $g'_k(\xi)$ assigned to the contours L_k. Function $g_1(\xi)$ $(0 \le \xi \le 2\pi)$ is 2π-periodic continuous function. However, in order to obtain a sufficiently accurate numerical solution, we have to densify quadrature nodes and collocation points in the vicinity of narrow slot tips. We use here a variant of sigmoid transformation [29,30] adapted to periodic case [29]:

$$\xi = G\,(\tau) = \tau - \tfrac{1}{2}\sin 2\tau, \qquad 0 \le \tau \le 2\pi. \tag{15}$$

Consequently, the function we are looking for is as follows

$$u_1(\tau) = g'_1(G\,(\tau)), \quad 0 \le \tau \le 2\pi. \tag{16}$$

A solution of the system of integral equations Eq. (14) for contours L_2 and L_3 is sought in the class of functions, which have an integrable singularity at the ends of the integration interval

$$g'_k(\xi) = \frac{u_k(\xi)}{\sqrt{1-\xi^2}}, \qquad -1 \le \xi \le 1, \tag{17}$$

where $u_k(\xi)$ $(k = 2{,}3)$ are continuous functions.

Finally, a modified system of the singular integral equations Eq. (14) takes the form

$$\begin{aligned}
&\frac{1}{\pi}\int_0^{2\pi}\left[M_{1m}(\xi,\eta)u_1(\tau)+N_{1m}(\xi,\eta)\overline{u_1(\tau)}\right]G(\tau)\mathrm{d}\tau + \\
&+\ \frac{1}{\pi}\sum_{k=2}^{3}\int_{-1}^{1}\left[M_{km}(\xi,\eta)u_k(\xi)+N_{km}(\xi,\eta)\overline{u_k(\xi)}\right]\mathrm{d}\xi = p_m(\eta),\\
&\qquad m = 1,2,3,
\end{aligned} \tag{18}$$

In points $t = \pm\ell_0$ where contours L_2 and L_3 intersect contour L_1 the values of $g'_k(-1)$ $(k = 2{,}3)$ must be finite, thus we should provide two additional equations

$$u_k(-1) = 0, \qquad k = 2{,}3. \tag{19}$$

For numerical integration of the singular integral equation (18) two different methods must be used. For the closed-loop contour L_1, we apply the midpoint rule [31] and Gauss-Chebyshev quadrature [27] for L_2 and L_3 contours. Finally we get a system of complex linear algebraic equations which is the discrete analogue of the respective system of integral equations (18)

$$\begin{aligned}
&\frac{2}{n_1}\sum_{i=1}^{n_1}\left[M_{1m}(\xi_i,\eta_j)u_1(\tau_i)+N_{1m}(\xi_i,\eta_j)\overline{u_1(\tau_i)}\right]G(\tau_i) + \\
&+\sum_{k=2}^{3}\left\{\frac{1}{n_k}\sum_{i=1}^{n_k}\left[M_{km}(\xi_i,\eta_j)u_k(\xi_i)+N_{km}(\xi_i,\eta_j)\overline{u_k(\xi_i)}\right]\right\} = p_m(\eta_j),\\
&m = 1, \quad j = 1,\ldots,n_k,\\
&m = 2,3, \quad j = 1,\ldots,(n_k - 1),
\end{aligned} \tag{20}$$

where quadrature nodes and collocation points are determined by formulas:

$$\begin{aligned}
\xi_i &= G\,(\tau_i),\ \ \tau_i = \tfrac{\pi(2i-1)}{n_1}, && i = 1,\ldots,n_1,\\
\eta_j &= G\,(\theta_j),\ \ \theta_j = \tfrac{2\pi(j-1)}{n_1}, && j = 1,\ldots,n_1,\\
\xi_i &= \cos\tfrac{\pi(2i-1)}{2n_k}, && i = 1,\ldots,n_k,\ \ k = 2{,}3,\\
\eta_j &= \cos\tfrac{\pi j}{n_k}, && j = 1,\ldots,(n_k-1),\ \ k = 2{,}3.
\end{aligned} \tag{21}$$

The linear system Eq. (20) consists of $n_1 + (n_2 - 1) + (n_3 - 1)$ complex equations. Using Lagrange interpolation on Chebyshev nodes [27] to conditions Eq. (19), we obtain two missing equations

$$\tfrac{1}{n_k}\textstyle\sum_{i=1}^{n_k} (-1)^{i+n_k}\tan\tfrac{\pi(2i-1)}{4n_k}\, u_k(\xi_i) = 0, \qquad k = 2{,}3. \tag{22}$$

The right side of the Eq. (20) can be easily calculated using the relationship Eq. (6). Introducing the relationship $\lambda = \sigma_p/\sigma_t$ $(\sigma_p = P/(\pi\,R))$ as a relative load level parameter, we can write down $p_m(\eta_j)$ in compact form:

$$p_m(\eta_j) = \begin{cases} p_1(\eta_j), & m = 1,\\ \left(1 - \frac{1}{\lambda}\right)\, p_1(\eta_j), & m = 2{,}3, \end{cases} \tag{23}$$

where

$$p_1(\eta_j) = \sigma_p \frac{\left|\omega_k(\eta_j)\right|^2 - 1}{\overline{\omega_k(\eta_j)}^{\,2} - 1}\left[\frac{2}{\overline{\omega_k(\eta_j)}^{\,2}-1}\frac{\overline{\omega_k'(\eta_j)}}{\omega_k'(\eta_j)} - \frac{\left|\omega_k(\eta_j)\right|^2+1}{\omega_k(\eta_j)^2-1}\right], \tag{24}$$

$k = 1,2,3.$

The solution to the problem is symmetrical concerning the axis Ox i Oy. The conditions resulting from symmetry concerning the sought function $u_k(\xi)$ and necessary kernel modifications are described in detail in Savruk et al. [32] (see also the literature [2]). Thus, the rank of the linear system Eq. (20) and (23) can be easily reduced by a factor of four.

The obtained values of sought function $u(\xi_k)$ fully determine the stress-strain state in the whole elastic region through an integral representation of complex stress potentials Eq. (4).

The slot edge (contour L_1) is free of applied loads, then the contour stress at the edge can be calculated using a simple formula [2].

$$\sigma_s = -4\sigma_p\,\Im\frac{u_1(\xi)}{\omega_1'(\xi)} = -4\sigma_p\,\Im\frac{u_1(\tau)}{\omega_1'(G(\tau))}. \tag{25}$$

Stress intensity factors in crack tips K_{I} and K_{II} can be directly expressed through the sought function $g'_k(t)$ Eq. (17). Let us introduce corresponding dimensionless stress intensity factors F_{I} and F_{II} using the following relationship

$$K_{\mathrm{I}}^{+} - \mathrm{i}K_{\mathrm{II}}^{+} = \left(F_{\mathrm{I}}^{+} - \mathrm{i}F_{\mathrm{II}}^{+}\right)\sigma_p\sqrt{\pi R}. \tag{26}$$

Here upper indexes $(+)$ indicate crack tip at $\xi = +1$. Taking into account relation Eq. (17), we get coefficients F_{I} and F_{II} [27]

$$F_{\mathrm{I}}^{+} - \mathrm{i}F_{\mathrm{II}}^{+} = -\sqrt{|\omega_{k'}(+1)|}\,\frac{u_k(+1)}{\omega_{k'}(+1)}, \quad k = 2{,}3, \tag{27}$$

where

$$u_k(+1) = -\frac{1}{n}\sum_{i=1}^{n_k}(-1)^i\,u_k(\xi_i)\cot\frac{\pi(2i-1)}{4n}, \quad k = 2{,}3. \tag{28}$$

Cracks L_2 and L_3 simulate fracture process zones (plastic strips) at the tips of narrow slot L_1, thus stresses at the crack L_k end must be finite

$$g'_k\left(t = \pm(\ell_0+\ell)\right) = g'_k\left(R\omega_k(+1)\right) = 0, \quad \rightarrow$$
$$u_k(+1) = 0, \quad k = 2{,}3. \tag{29}$$

This condition allows us to calculate the unknown length $\ell = (\gamma - \gamma_0)R$ using a simple iteration process.

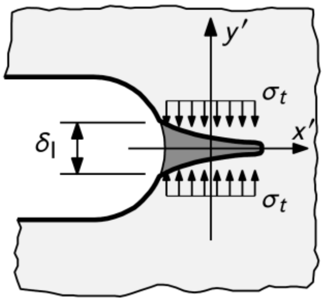

Fig. 2. U-notch tip opening displacement

The opening displacement in the notch tip (Fig. 2) can be calculated based on the known [27] relationship between function $g_k(t)$ $(k = 2{,}3)$ and displacement discontinuity $(v_k^+ - v_k^-)$ across the contour L_k

$$2G\,\frac{\mathrm{d}}{\mathrm{d}x'}(v_k^+ - v_k^-) = (1+\kappa)g'_k(x'),$$
$$x' \in L_k, \quad k = 2{,}3, \tag{30}$$

where x' is a local abscissa at contour L_k, G – shear modulus, κ – Muskhelishvili's constant.

In plane stress state $(1+\kappa)/(4G) = 2/E$, so we come to the formula for crack opening displacement in its left tip $x' = l_k^-$ $(x = \pm\ell_0)$, i.e. in slot tips, in the form [32]

$$\begin{aligned}\delta_{\mathrm{I}} = \delta_{\mathrm{I}}(l_k^-) &= \frac{4}{E}\Re g_k(l_k^-) = -\frac{4}{E}\Re\int_{l_k^-}^{l_k^+} g'_k(t)\mathrm{d}t = \\ &= -\frac{4R\sigma_p}{E}\Re\int_{-1}^{+1}\frac{u_k(\xi)}{\sqrt{1-\xi^2}}\mathrm{d}\xi = \\ &= -\frac{\sigma_p R}{E}\frac{4\pi}{n_k}\sum_{i=1}^{n_k}\Re u_k(\xi_i), \quad k = 2{,}3.\end{aligned} \tag{31}$$

4. NUMRICAL RESULTS

The calculations were performed for the constant rounding radius of slot tips $\rho_0 = 1/75\,R$. Relative slot span γ_0 was chosen from the set $\gamma_0 = \{0.1{,}0.2{,}0.3{,}0.4{,}0.5{,}0.6\}$, so the relative rounding radius of the slot vertices can be easily calculated as $\varepsilon_0 = 1/(75\gamma_0)$. For every slot geometry and for arbitrary load level $\lambda = \sigma_p/\sigma_t$ $(\lambda_{\min} < \lambda < 1)$ the plastic strips range $\gamma = (\ell_0 + \ell)/R$ and notch tip opening displacement δ_{I} were calculated. These values are presented in Figs 3 and 4 respectively.

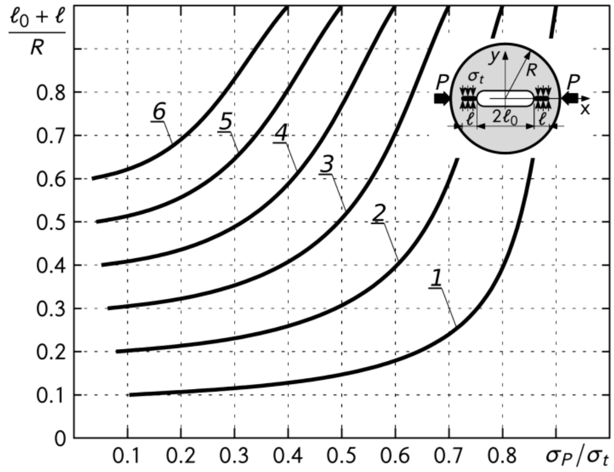

Fig. 3. Relative plastic strips range versus relative load level for the following relative slot span: 1 – 0.1, 2 – 0.2, 3 – 0.3, 4 – 0.4, 5 – 0.5, 6 – 0.6

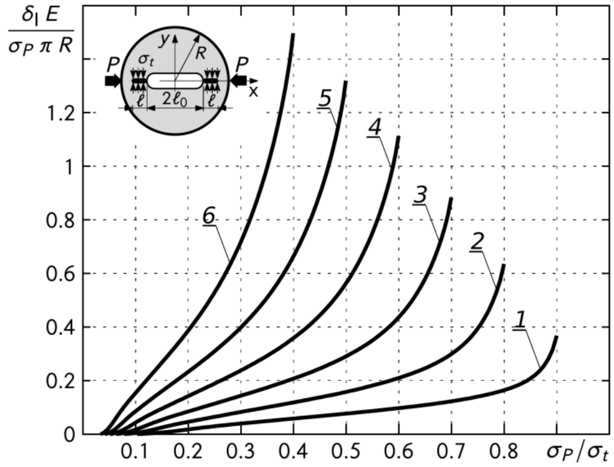

Fig. 4. Dimensionless notch tip opening displacement versus relative load level for the following relative slot spa:n1 – 0.1, 2 – 0.2, 3 – 0.3, 4 – 0.4, 5 – 0.5, 6 – 0.6

As it can be easily seen, the values of relative load level λ start with a certain value $\lambda_{\min}$. Plastic strips arise when the maximum normal stress $\sigma_{\max}$ at the vertex of the narrow slot reaches the limit value σ_t. If we denote the stress concentration factor in the rounded notch tip as k, then $k\sigma_p = \sigma_{\max} \le \sigma_t$ and the minimum value of the load level parameter will be equal to $\lambda_{\min} = 1/k$. Stress concentration factor can be easily calculated (see Savruk and Kazberuk [2]) by solving the system of equations (20) taking into account contour L_1 only and then using Eq. (26). A list of the stress concentration factors for all γ_0 values used here is shown in Tab. 1.

When the plastic deformations are small, the critical stress intensity factor K_c can be calculated with the formula [1,33]

$$K_c = \sqrt{\delta_{\mathrm{I}}\,E\sigma_t} = \sqrt{\tilde{\delta}_{\mathrm{I}}\,\lambda}\;\sigma_t\sqrt{\pi R}. \tag{32}$$

Tab. 1. Stress concentrations factors at the rounded vertex of narrow slot and dimensionless stress intensity factors at the tips of a corresponding central crack in disc specimen

$\gamma_0 = \frac{\ell_0}{R}$	$\varepsilon_0 = \frac{\rho}{\ell_0}$	$k = \frac{\sigma_{\max}}{\sigma_p}$	$F_{\mathrm{I}} = \frac{K_{\mathrm{I}}}{\sigma_p \sqrt{\pi R}}$
0.1	0.1333	9.685	0.3210
0.2	0.0667	12.75	0.4741
0.3	0.0444	15.89	0.6220
0.4	0.0333	19.54	0.7866
0.5	0.0267	24.04	0.9838
0.6	0.0222	29.90	1.2364

Let's compare the obtained results with the approximate estimation calculated for a semi-infinite U-notch [25]. The relative load level parameter is equal

$$\gamma^{\infty} = \frac{1}{\sqrt{2\pi\rho}} \frac{K_{\mathrm{I}}}{\sigma_t} = \frac{F_{\mathrm{I}}}{\sqrt{2\varepsilon_0\gamma_0}} \frac{1}{\sigma_t} \frac{P}{\pi R} = \frac{F_{\mathrm{I}}}{\sqrt{2\varepsilon_0\gamma_0}} \lambda, \tag{33}$$

Dimensionless notch opening displacement is equal [25]

$$\sqrt{\tilde{\delta}_{\mathrm{I}}^{\infty}} = 1 - \frac{1}{R_{\mathrm{I}}^2 (\gamma^{\infty})^2}, \tag{34}$$

where the stress rounding factor [34] is equal $R_{\mathrm{I}} = 2.993$ [35].

The value of the critical stress intensity factor, calculated based on the criteria condition Eq. (32), is equal

$$K_c^{\infty} = \sqrt{\tilde{\delta}_{\mathrm{I}}^{\infty}}\, K_{\mathrm{I}} = F_{\mathrm{I}}\, \lambda \sigma_t \sqrt{\tilde{\delta}_{\mathrm{I}}^{\infty}\, \pi R}, \tag{35}$$

where dimensionless stress intensity factors F_{I} are shown in Tab 1.

In Fig. 5. the comparison of the values of the critical stress intensity factors calculated for the notched disk Eq. (33) and for semi-finite U-notch in the tensile plane Eq. (36) is shown. It can be seen that coarse approximation is only valid for the smallest slot ($\gamma_0 = 0.1$) under load level $0.4 < \lambda < 0.8$. For relative slot span $\gamma_0 = 0.2$ differences between exact and approximated values are much greater – nearly 30% at $\lambda \sim 0.5$.

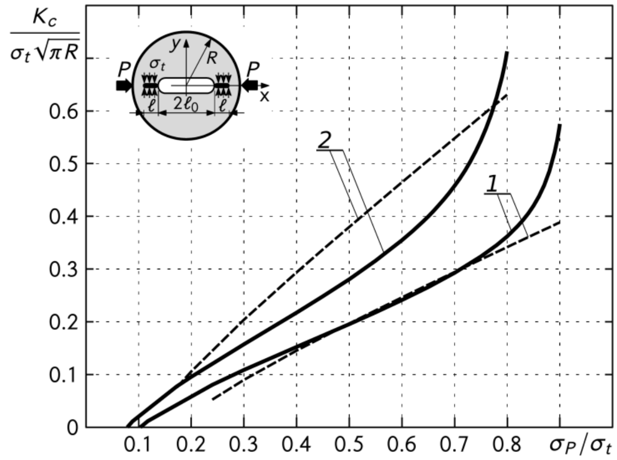

Fig. 5. Comparison of the values of the critical stress intensity factors calculated for notched disc (solid lines) and at the vertex of the semi-infinite U-notch (dashed lines) as a function of the relative load level for the following parameters: $1 - \gamma_0 = 0.1, 2 - \gamma_0 = 0.2$

5. CONCLUSIONS

The elastic-plastic problem for the Brazilian disc with a central narrow slot in the plane stress state condition was solved. The solution was obtained by the method of singular integral equations using complex stress potentials for a system of cracks and openings in the two-dimensional circular elastic domain. All necessary analytical background was documented in detail. Based on the Dugdale model of fracture process zone and deformation fracture criterion, the relationships between critical load, notch tip opening displacement and length of the plastic strips were established. Numerical calculations for arbitrary but representative sets of geometrical parameters were performed. The correctness of the solution was checked by comparing the results with the approximate relationships obtained for the problem of semi-infinite U-notch in an elastic plane subjected to unidirectional tension. For a small relative slot span, both results are in good agreement.

The presented approach, despite the obvious simplifications resulting from the adopted assumptions (plane stress state, fracture process zone as a plastic strip), can be used to estimate the fracture mechanics parameters of quasi-brittle materials determined in the Brazilian test.

REFERENCES

1. Rice JR. Limitations to the small scale yielding approximation for crack tip plasticity. J Mech Phys Solids. 1974;22(1):17-26.
2. Savruk MP, Kazberuk A. Stress Concentration at Notches. Springer International Publishing Switzerland; 2017.
3. Li D, Wong LNY. The Brazilian disc test for rock mechanics applications: review and new insights. Rock mechanics and rock engineering. 2013;46(2):269-87.
4. Garcıa VJ, Marquez CO, Zuniga-Suarez AR, Zuniga-Torres BC, VillaltaGranda LJ. Brazilian Test of Concrete Specimens Subjected to Different Loading Geometries: Review and New Insights. International Journal of Concrete Structures and Materials. 2017;11(2):343-63.
5. Libatskii L, Kovchik S. Fracture of discs containing cracks. Mater Sci. 1967;3(4):334-9.
6. Yarema SY, Krestin GS. Determination of the modulus of cohesion of brittle materials by compressive tests on disc specimens containing cracks. Mater Sci. 1967;2(1):7-10.
7. Yarema SY, Krestin GS. Limiting equilibrium of a disk with a diametral crack. Int Appl Mech. 1968;4(7):55-8.
8. Yarema SY. Stress state of disks with cracks, recommended as specimens for investigating the resistance of materials to crack development. Mater Sci. 1977;12(4):361-74.
9. Yarema SY, Ivanitskaya G, Maistrenko A, Zboromirskii A. Crack development in a sintered carbide in combined deformation of types I and II. Strength of Materials. 1984;16(8):1121-8.
10. Atkinson C, Smelser R, Sanchez J. Combined mode fracture via the cracked Brazilian disk test. Int J Fract. 1982;18(4):279-91.
11. Awaji H, Sato S. Combined mode fracture toughness measurement by the disk test. J Eng Mater Technol. 1978;100:175-82.
12. Zhou S. Fracture Propagation in Brazilian Discs with Multiple Pre-existing Notches by Using a Phase Field Method. Periodica Polytechnica Civil Engineering. 2018;62(3):700-8.
13. Xiankai B, Meng T, Jinchang Z. Study of mixed mode fracture toughness and fracture trajectories in gypsum interlayers in corrosive environment. Royal Society Open Science. 2018;5(1).
14. Tang SB. Stress intensity factors for a Brazilian disc with a central crack subjected to compression. International Journal of Rock Mechanics and Mining Sciences. 2017;93:38 45.

15. Seitl S, Miarka P. Evaluation of mixed mode I/II fracture toughness of C 50/60 from Brazilian disc test. Frattura ed Integrità Strutturale. 2017;11(42):119-27.
16. Ayatollahi MR, Aliha MRM. On the use of Brazilian disc specimen for calculating mixed mode I–II fracture toughness of rock materials. Engineering Fracture Mechanics. 2008;75(16):4631 4641.
17. Ayatollahi MR, Aliha MRM. Wide range data for crack tip parameters in two disc-type specimens under mixed mode loading. Computational Materials Science. 2007;38(4):660 670.
18. Atahan HN, Tasdemir MA, Tasemir C, Ozyurt N, Akyuz S. Mode I and mixed mode fracture studies in brittle materials using the Brazilian disc specimen. Mater Struct. 2005;38:305-12.
19. Dong S. Theoretical analysis of the effects of relative crack length and loading angle on the experimental results for cracked Brazilian disk testing. Engineering Fracture Mechanics. 2008;75(8):2575 2581.
20. Wang QZ, Gou XP, Fan H. The minimum dimensionless stress intensity factor and its upper bound for CCNBD fracture toughness specimen analyzed with straight through crack assumption. Engineering Fracture Mechanics. 2012;82:1 8.
21. Ayatollahi MR, Aliha MRM. Mixed mode fracture in soda lime glass analyzed by using the generalized MTS criterion. International Journal of Solids and Structures. 2009;46(2):311 321.
22. Savruk MP, Kazberuk A. Problems of fracture mechanics of solid bodies with V-shaped notches. Mater Sci. 2009;45(2):162-80.
23. Leonov MY, Panasyuk VV. Development of a nanocrack in a solid. Prikl Mekh. 1959;5(4):391-401.
24. Dugdale D. Yielding of steel sheets containing slits. J Mech Phys Solids. 1960;8:100-4.
25. Kosior-Kazberuk M, Kazberuk A, Bernatowicz A. Estimation of Cement Composites Fracture Parameters Using Deformation Criterion. Materials. 2019;12(24):4206.
26. Panasyuk VV, Savruk MP. Model for plasticity bands in elastoplastic failure mechanics. Mater Sci. 1992;28(1):41-57.
27. Savruk MP. Two-dimensional problems of elasticity for bodies with cracks (in Russian). Naukova Dumka, Kiev; 1981.
28. Muskhelishvili NI. Some Basic Problems of the Mathematical Theory of Elasticity. 2nd ed. Noordhoff International Publishing, Leyden; 1977.
29. Sidi A. A new variable transformation for numerical integration. H Brass H and G Hammerlin, editors, Numerical integration IV. 1993:359-73.
30. Johnston PR. Application of sigmoidal transformations to weakly singular and near-singular boundary element integrals. Int J Numer Meth Eng. 1999;45:1333-48.
31. Belotserkovsky SM, Lifanov IK. Method of discrete vortices. CRC Press LLC, Boca Raton; 1993.
32. Savruk MP, Osiv PN, Prokopchuk IV. Numerical analysis in plane problems of the crack theory (in Russian). Naukova Dumka, Kiev; 1989.
33. Rice JR. The location of plastic deformation. Theor Appl Mech. 1976;1:20720.
34. Benthem JP. Stresses in the region of rounded corners. Int J Solids Struct. 1987;23(2):239-52.
35. Savruk MP, Kazberuk A. Relationship between the stress intensity and stress concentration factors for sharp and rounded notches. Mater Sci. 2006;42(6):725-38.

The work has been accomplished under the research project No. WZ/WM-IIM/3/2020.

Andrzej Kazberuk: https://orcid.org/0000-0003-4179-0312

DOI 10.2478/ama-2022-0048

DETERMINATION OF THERMAL DIFFUSIVITY VALUES BASED ON THE INVERSE PROBLEM OF HEAT CONDUCTION – NUMERICAL ANALYSIS

Adam ADAMOWICZ*

*Faculty of Mechanical Engineering, Bialystok University of Technology, 45C Wiejska Street, 15-351 Białystok, Poland

a.adamowicz@pb.edu.pl

received 3 August 2022, revised 3 September 2022, accepted 3 September 2022

Abstract: This paper presents a discussion on the accuracy of the method of determining the thermal diffusivity of solids using the solution of the inverse heat conduction equation. A new measurement data processing procedure was proposed to improve the effectiveness of the method. Using the numerical model, an analysis of the sensitivity of the method of thermal diffusivity determination to changes in operational and environmental parameters of the test was carried out. The obtained results showed that the method was insensitive to the parameters of the thermal excitation impulse, the thickness of the tested sample, and the significant influence of convection cooling on its accuracy. The work was completed with the formulation of general conclusions concerning the conditions for determining the thermal diffusivity of materials with the use of the described method.

Key words: thermal diffusivity, inverse heat conduction problem, impulse heating, finite element analysis

1. INTRODUCTION

Thermal diffusivity or thermal diffusion coefficient is a parameter describing the heat flow, and in fact, the movement of the isothermal surface in the material, occurring, inter alia, in the differential equation of the Fourier heat conduction:

$$\frac{\partial T}{\partial t} = k\nabla^2 T, \tag{1}$$

where: k - thermal diffusivity, T - temperature, t – time, ∇^2 – Laplacian. The thermal diffusion coefficient combines other thermal material properties, i.e. heat conduction coefficient λ, specific heat c_p and density ρ :

$$k = \frac{\lambda}{c_p \rho} \tag{2}$$

In simulation tests carried out with the use of analytical or numerical models, the key issue is the correct determination of the properties of materials. Even the most perfect calculation model will not allow for obtaining reliable results without correct input data, including material properties. The importance of this issue is evidenced by the multitude of methods for experimentally determining the properties of materials, their improvement and the search for new ones. In the case of thermal diffusivity, its value for a given material can be determined using the Angström method [1], which links the value of the thermal diffusion coefficient with electrical conductivity, several impulse methods. The first paper [2] presents a method of heating one surface of an isolated plane-parallel sample with a pulse of light. Based on the time $t_{1/2}$, reaching half of the maximum value of the temperature on the second surface of the sample, the value of the thermal diffusion coefficient was determined using a simple empirical dependence. In the work [3] an analytical solution to the problem of heat conduction for a cylindrical sample after being forced by a heat impulse was proposed. These results were used in the work [4] to increase the accuracy of the method of determining thermal diffusivity during heating with laser radiation. This method was modified and developed in the works [5, 6, 7] and to this day this subject is the focus of researchers [8, 9].

This paper presents an analysis of the accuracy of one of the methods of determining thermal diffusivity [10]. This method is based on the solution to the problem of inverse heat conduction by impulse heating of a flat sample, which is contrary to the previously described method, where it does not require special equipment, complicated sample preparation or test conditions. The simplicity of the method is counterbalanced by some simplifications that may cause inaccuracies. This study aims to investigate the potential causes of inaccuracies in the thermal diffusivity determination procedure and their impact on the obtained results.

2. THEORY OF THE METHOD OF DETERMINING THERMAL DIFFUSIVITY

Consider an infinite plate (Fig. 1) made of homogeneous, isotropic material of constant thickness g subjected to impulse heating on the wall $x = 0$. It is assumed that the total energy of the pulse with the surface flux density q is absorbed by the plate and there is no heat exchange with the environment.

The heat conduction equation for this one-dimensional problem can be written as follows:

$$\frac{\partial T}{\partial t} = k\frac{\partial^2 T}{\partial x^2} + \frac{1}{\rho c_p} q, \tag{3}$$

The initial boundary conditions for a given case are the initial temperature T_0 , equal to the ambient temperature T_a , the thermal pulse $q = q(t)$ with a rectangular time course and duration t_f :

$$T = T_0: \quad t = 0,$$
$$K\left.\frac{\partial T}{\partial x}\right|_{x=0} = \begin{cases} q(t): & 0 \le t \le t_f, \\ 0: & t > t_f, \end{cases} \qquad (4)$$
$$\left.\frac{\partial T}{\partial x}\right|_{x=0} = \left.\frac{\partial T}{\partial x}\right|_{x=g} = 0: \quad t > 0.$$

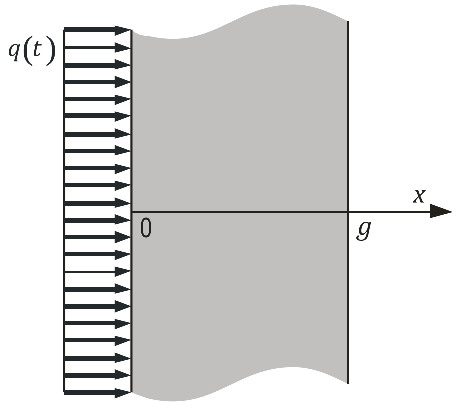

Fig. 1. Diagram of an infinite plate of thickness *g*

The solution to the boundary-initial problem of the heat conduction equation (3), (4) for the surface *x* = *g* with the assumptions made regarding the shape of the heating function *q*(*t*) and the short excitation time t_f and taking into account only one segment of the asymptotic series, it takes the form [10]:

$$T(t, x = g) = T_\infty - 2(T_\infty - T_0)\exp\left(-\frac{\pi^2 k}{g^2}t\right), \qquad (5)$$

where: T_∞ - maximum surface temperature *x* = *g*:

$$T_\infty = T(t \to \infty). \qquad (6)$$

When we logarithm the Eq. (5) we get the linear function of time:

$$\ln[T_\infty - T(t)] = -At + \ln 2(T_\infty - T_0), \qquad (7)$$

with the directional coefficient: $A = \frac{\pi^2 k}{g^2}$. (8)

Eq. (5) shows a linear function of the temperature reached on the surface *x* = *g* of the plate subjected to impulse heating on the surface *x* = 0. It is worth noting that, with the assumptions made, it does not depend on the conditions of thermal excitation *q*(*t*) and knowing the value of the directional coefficient *A* of the Eq. (7) it is easy to determine the value of the required thermal diffusion coefficient:

$$k = \frac{g^2 A}{\pi^2}. \qquad (9)$$

Experimental determination of the value of the thermal diffusion coefficient of the sample material based on solving the problem of inverse heat conduction consists of the following procedures:

- measuring the surface temperature of the plate *x* = *g* during impulse heating of the surface *x* = 0 until reaching the steady state; the results of the measurements are the temperature values for discrete-time values, i.e. *T*(*t*) (Fig. 2);
- determination of the temperature T_∞ and calculation of the value of ln[T_∞ - *T*(*t*)] (Fig. 3); under real conditions, i.e. under conditions of convection, take:

$$T_\infty = \max\{T(t): \quad t > 0\}. \qquad (10)$$

- determination of the directional coefficient *A* of the Eq. (7) by a linear approximation of the dependence ln[T_∞ - *T*(*t*)];
- determination of the value of the thermal diffusion coefficient *k* based on the dependence (9).

The above-mentioned results of temperature measurements during impulse heating (Fig. 2) and an illustration of the linear approximation process (Fig. 3) were made for a sample made of composite brake material. A flash lamp with a maximum flash energy of 6,000 J and a flash duration of 0.2 s was used as a heat source. A Cedip Titanium 560 M thermal imaging camera was used to measure the surface temperature of the plate. Visible in Fig. 2 the temperature peak corresponds to the moment when the flash was triggered (*t* = 0). The geometrical features of the sample, material properties and test conditions are presented in Tab. 1.

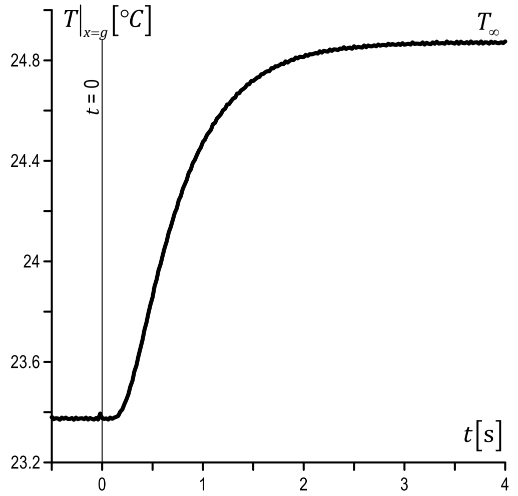

Fig. 2. Temperature increase on the back of the sample during impulse heating

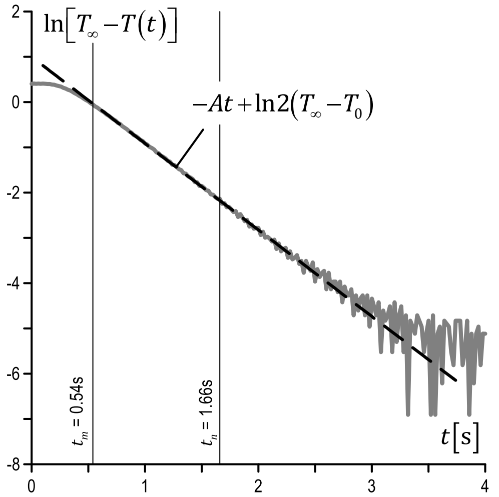

Fig. 3. Illustration of the linear approximation procedure to determine the coefficient *A* and the thermal diffusivity value *k*

Tab. 1. Geometric features and material properties of a material sample

Characteristic	Value
Plate thickness g	1.5 mm
Plate material density ρ	1,930 kg/m^3
Specific heat capacity of the plate c_p	870 J/(kg*K)
Start/ambient temperature T_0	23,375°C.
Maximum temperature T_∞	24,875°C.
Duration of the heat pulse t_f	0.2 s

The accuracy of determining the value of the thermal diffusion coefficient based on the above-described procedure is influenced by several factors related to the assumed model of the heat conduction problem (e.g. assumption of no heat transfer), simplifications of the solution to the inverse problem (one segment of the solution series has been taken into account), the conditions for carrying out measurements (other than the rectangular shape of the heating function) and the method of processing measurement data. Therefore, several questions arise regarding the model and procedure of the experimental determination of the *k* coefficient based on a solution to the inverse problem of heat conduction:

1. In Fig. 3 it can be seen that the nature of the dependence ln[T_∞ - $T(t)$] in its initial and final interval is far from linear. Using the entire available range of measurement data for linear approximation will distort the results obtained. Relying on a subjective evaluation of what range of data to include in a linear approximation can be unreliable. Therefore, the question arises, what range of measurement data $\Delta t = t_n - t_m$ should be used in the procedure to ensure the best quality of linear approximation and accuracy of *k* coefficient determination?
2. The issue of the shape of the impulse heating function $q(t)$ is considered extremely important in the literature. However, the dependencies presented above show that the parameters of the thermal excitation pulse, apart from the requirement of short duration, do not affect the determined value of the thermal diffusion coefficient. It should be investigated whether the method of exciting a heat wave in the material affects the results of the thermal diffusivity determination method.
3. The next element of the model that requires analysis in terms of the influence on the accuracy of the method is the sample thickness *g*.
4. The assumption of the lack of heat exchange between the sample of the tested material and the environment after the completion of the impulse heating seems to be the greatest source of method inaccuracy. Therefore, it would be necessary to investigate how serious the errors are and how to minimize them.

In the next chapter, an algorithm will be presented that ensures optimal conditions for linear approximation for the accuracy of thermal diffusivity determination. The analysis of the remaining issues, specified in points 2–4, will be carried out using the numerical model of the problem, using the finite element method.

3. LINEAR APPROXIMATION OF MEASUREMENT DATA AND CALCULATION RESULTS

The first issue to be considered is to ensure reproducible conditions for the processing of measurement data or the results of numerical calculations. Fig. 3 shows that to find the value of the directional coefficient of the line Eq. (7) for the linear approximation, only the interval of dependence ln[T_∞ - $T(t)$] with linear characteristics should be used. Part of the data corresponding to the beginning and end of the impulse heating process of the tested material sample should be eliminated from the approximation task.

This task will be performed with the procedure looking for such a time interval <t_m, t_n>, for which the quality parameter of the linear approximation of the dependence ln[T_∞ - $T(t)$] reaches its maximum value. The Pearson linear correlation coefficient will be used as a parameter for assessing the quality of the linear approximation:

$$r = \frac{\sum_{i=1}^{n}(x_i-\bar{x})(y_i-\bar{y})}{\sqrt{\sum_{i=1}^{n}(x_i-\bar{x})^2 \sum_{i=1}^{n}(y_i-\bar{y})^2}}, \tag{11}$$

where x_i, y_i are elements of correlated sets. For the case in question, these sets are the measured data:

$$x_i = \ln\left[T_\infty - T(t_i)\right] \tag{12}$$

and the values of the approximation function for the same values of time t_{and} :

$$y_i = -A \cdot t_i + \ln 2\left(T_\infty - T_0\right) \tag{13}$$

$\bar{x}$and$\bar{y}$ are the mean values of the correlated sets:

$$\bar{x} = \frac{1}{n-m}\sum_{i=m}^{n}\ln\left[T_\infty - T(t_i)\right], \bar{y} = \frac{1}{n-m}\sum_{i=m}^{n}\left(A \cdot t_i + B\right). \tag{14}$$

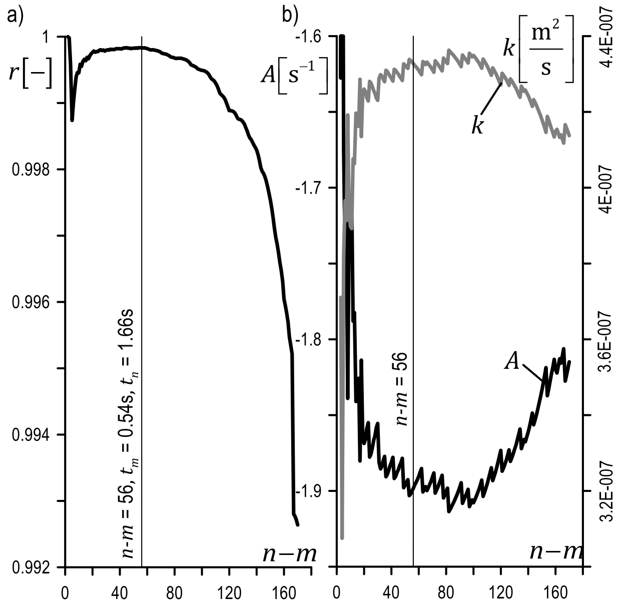

Fig. 4. The maximum value of the linear correlation coefficient *r* (a) and the value of the directional coefficient *A* and the value of the thermal diffusion coefficient *k* (b) depending on the number of measurement data points used in the approximation

An example of searching for optimal approximation conditions is presented in Fig. 4. The highest quality of linear approximation (r = 1) is achieved by definition for each pair of data points (n - m = 2, Fig. 4a). Taking into account more points, the value of the correlation coefficient *r* decreases sharply and then increases again reaching its maximum at n - m = 56 (r_{max} = 0.998) for the time interval from t_m = 0.54s to t_n = 1.66s (Fig. 3).

Picture Fig. 4b shows the value of the coefficient *A* of the linear approximating function and the value of the thermal diffusion coefficient *k* determined based on the approximation. Taking into account the data range optimal for the quality of the approximation, the obtained value was $A = 1.8984\ s^{-1}$ and $k = 4.32793 \cdot 10^{-7}\ m^2\ s^{-1}$. Taking into account the material properties c_p and ρ (Tab. 1) and taking into account the dependency (2), the value of the thermal conductivity coefficient for the tested material is $K = 0.7267$ W/(m · K).

The procedure presented above was used to develop the experimental data (Fig. 3) and in the further part of the work to analyse the results of numerical calculations for the simulation of impulse heating.

4. NUMERICAL MODEL OF THE IMPULSE HEATING ISSUE

The numerical computational model, based on the finite element method, simulates the conditions of impulse heating of a plane parallel plate of material to create a synthetic environment for the sensitivity analysis of the procedure for determining the value of the thermal diffusion coefficient, described in Chapter 0. Using the obtained results of numerical calculations, i.e. time-varying temperature distributions, a linear approximation of the relationship $\ln(T_\infty - T)$ to determine the value of the coefficient *A* will be carried out, and finally thermal diffusion *k* is determined. By recreating the procedure of thermal diffusivity determination based on the results of the numerical model, it is possible to estimate the influence of assumptions simplifying the solution of the inverse problem.

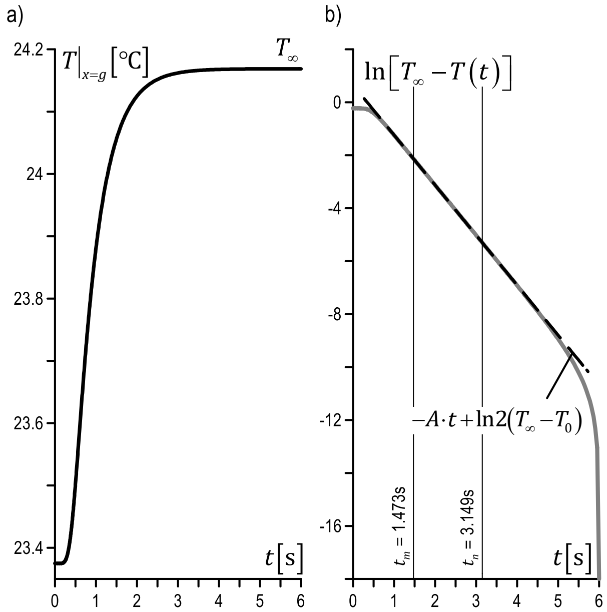

Fig. 5. Simulation of the temperature rise on the back of the sample during impulse heating (a); illustration of the linear approximation procedure to determine the coefficient *A* and the value of thermal diffusivity *k* (b)

To solve the one-dimensional problem of heat conduction, described by the Eq. (3) and with the application of boundary conditions (4), the finite element method was used. Using the material properties of Tab. 1, a rectangular shape of the heating function *q*(*t*) was assumed with the maximum value of the surface density of the heat flux $q = 10\ kW/m^2$ and the previously determined value of the heat conduction coefficient $K = 0.7267$ W/(m · K). The computational model consists of 300 one-dimensional second-order elements (square shape function) with linear length distribution and compaction on the side of the impulse-heated surface. The ratio of the size of the largest to the smallest element is 5, which gives the values $l_{min} = 0.00166$ mm and $l_{max} = 0.00833$ mm. The calculations used a time-dependent solution with a time step determined based on the backward differentiation method The Backward Differentiation Formula (BDF) with an initial step of 1e–9 s. The preliminary calculations showed that the temperature on the surface $x = g$ reaches the state of settling after 6 s and this time was taken as the end of the analysis.

The results of the calculations and the graphical interpretation of the procedure for determining the value of the thermal diffusion coefficient based on these results are shown in Fig. 5 . The lower temperature rise (Fig. 5a) than was observed in experimental studies (Fig. 2) is noteworthy. The difference (0.79°C against 1.50°C) results from an underestimation of the assumed value of the surface density of the heat flux *q* in the calculations. The issue of the influence of thermal excitation impulse parameters on the accuracy of the method will be analysed later in the paper.

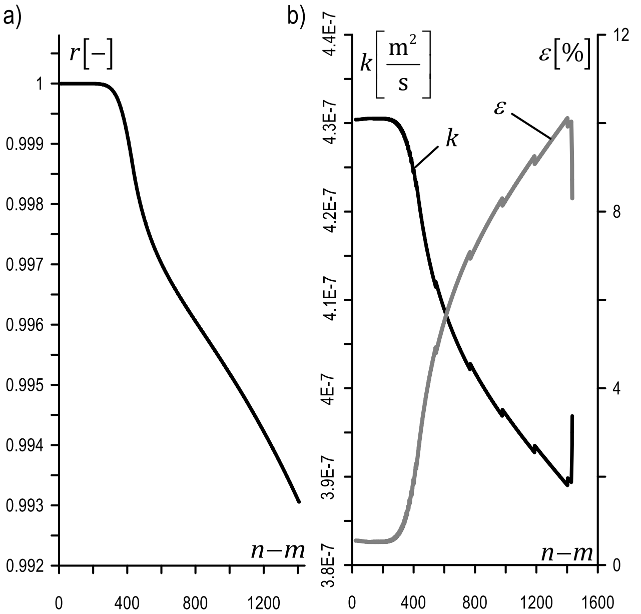

Fig. 6. The maximum value of the linear correlation coefficient *r* (a) and the value of the thermal diffusion coefficient *k* and the relative error of the method of its determination *ε* depending on the number of points included in the linear approximation *n* – *m*

When comparing the results of numerical calculations and experimental tests, it should be emphasized that there is no measurement noise and a much larger amount of data, which facilitates the linear approximation of the data. The value of the regression coefficient *r* remains very high even for a large number of points (Fig. 6a). Assuming the use of $n - m = 100$ points of calculation results, which corresponds to the time interval 1.676 s, the quality of linear approximation of the dependence $\ln[T_\infty - T(t)]$, expressed by the linear regression parameter, is reached at the level $r = 0.999999993$ (Fig. 6b). The values of the determined thermal diffusion coefficient *k* and the values of the accuracy parameter of the *ε* method depending on the conditions of linear approximation are shown in Fig. 6b. The method error is expressed as the relative difference between the obtained result and the reference value k_{ref} of the thermal diffusion coefficient, adopted in the calculations:

$$\varepsilon = \frac{|k-k_{ref}|}{k_{ref}} 100\% \tag{15}$$

For the indicated number of points and the range of data, it gives an accuracy of ε = 0.524%. The result should be assessed as more than satisfactory, especially since the obtained error ε accumulates the inaccuracy of the k coefficient determination method and the inaccuracy of solving the problem using the finite element method.

5. SENSITIVITY STUDY OF THE METHOD FOR DETERMINING THERMAL DIFFUSIVITY

The first parameter, the influence of which on the accuracy of determining the value of the thermal diffusion coefficient was investigated, was the time course of the heat flux $q(t)$, hereinafter referred to as the heating function. Several variants of the heating process were compared while maintaining the same amount of energy supplied to the system during heating, i.e.:

$$\int_0^{t_f} q(t)\mathrm{d}t = const. \tag{16}$$

The above analysed rectangular heating function (1, Fig. 7) with the duration t_f = 0.2 s and the pulse size q = 10 kW/m^2, corresponds to the surface energy of 2 kJ/m^2. Impulse parameters with the course of a parabola (2, Fig. 7) and three variants of triangular waveforms (3–5, Fig. 7) were chosen so that the energy of the heat excitation was identical. The obtained results, in the form of a temperature value change on the plate surface $x = g$, are shown in Fig. 8a. In all cases, the final temperature was T_∞ = 24.17°C, with slight differences in reaching it. Note that for a square (1), parabolic (2) and symmetrical triangle (3) waveform, the differences are negligible.

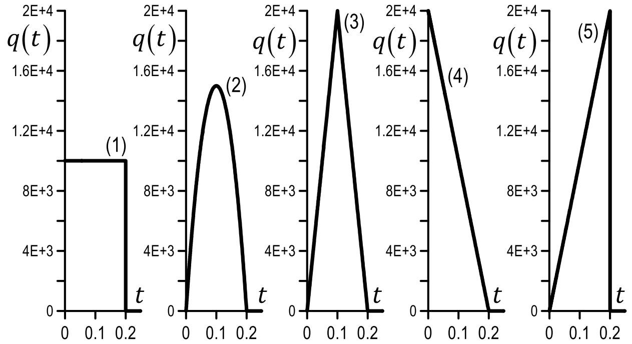

Fig. 7. Time courses of the impulse heating function $q(t)$

By linear approximation of the dependence ln(T_∞ - T) (Fig. 8b) the directional coefficients A and the values of the thermal diffusion coefficient k were determined. The results, including the values of linear regression for r, are provided in Tab. 2. It is worth emphasizing that in the case of variants of the heating function (2–4), the relative error of the method decreased to the value of ε = 0.045%. This should be explained by the improvement of the conditions of the numerical solution of the problem of the finite element method. For the square waveform (1) and the variant (5) of the triangle waveform, there is a sudden jump in the value of the heat flux $q(t)$ from the maximum value to zero, which is a great difficulty for the BDF solver.

Based on the results of the calculations, it can be assumed that the shape of the heating function does not affect the accuracy of the procedure for determining the value of the thermal diffusion coefficient.

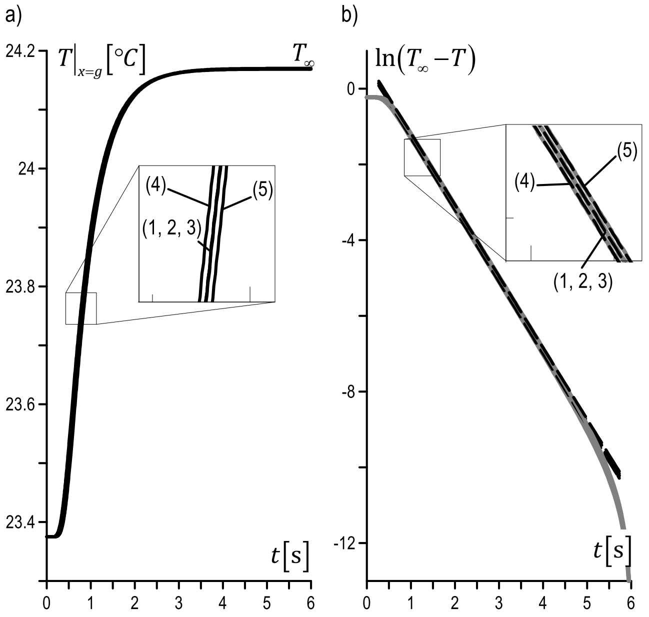
a) b)

Fig. 8. Temperature increase on the back of the sample during impulse heating (a); illustration of the linear approximation procedure to determine the coefficient A and the thermal diffusivity value k (b) for different time courses of the heating function $q(t)$ (1–5)

Tab. 2. Summary of the results of calculations of the thermal diffusion coefficient k for various courses of the heating function $q(t)$

Case	A (s^{-1})	r (-)	k (m^2/s)	ε (%)
(1)	1.88807	0.999999999	4.304e-07	0.546
(2)	1.8993	0.999999989	4.33e-07	0.046
(3)	1.89931	0.999999989	4.33e-07	0.046
(4)	1.89929	0.99999999	4.33e-07	0.045
(5)	1.88806	0.999999999	4.304e-07	0.546

The next analysed parameter of the thermal excitation is its size assuming a constant duration t_f = 0.2s and a rectangular course of the heating function $q(t)$. The surface density of the heat flux varies in the range of q = 10÷10^6 W/m^2. In this calculation variant, the amount of energy supplied to the tested material sample is different, which means that the temperature increase on the sample surface $x = g$ after the completion of heating changes in the range of 0.00079÷79.19°C (Fig. 9a). It is also worth noting that the time of settling the temperature after the end of the thermal pulse is the same regardless of the size of the pulse.

An obvious, but very important conclusion is that the magnitude of the thermal excitation impulse should be selected to obtain the optimal conditions for recording temperature changes on the opposite surface for the applied measurement system. An attempt to determine the value of thermal diffusivity with too small a temperature difference after thermal excitation may be burdened with a significant measurement error.

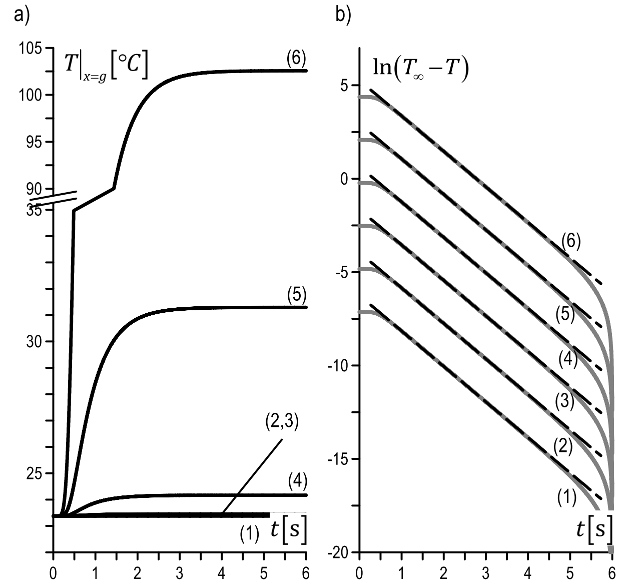

Fig. 9. Temperature increase on the back of the sample during impulse heating (a); illustration of the linear approximation procedure to determine the coefficient *A* and the thermal diffusivity value *k* (b) for different values of the heat flux surface density *q* = 10 (1), 100 (2), 1000 (3), 10000 (4), 2.1544 (5), $1 \cdot 10^6$ (6) W/m^2

Despite the very different end values of T_∞ achieved, in the process of linear approximation of the dependence ln(T_∞ - *T*) the parallel lines (Fig. 9b) were obtained, which showed no effect of the heat impulse size on the accuracy of the procedure for determining the value of the thermal diffusion coefficient. In Tab. 3 the obtained results are presented and, as can be seen in the conditions of the numerical experiment, the method was shown to be insensitive to the heat pulse size.

Tab. 3. Summary of the results of calculations of the thermal diffusion coefficient *k* for different values of the surface density of the heat flux *q*

Case	*q* (W/m^2)	*A* (s^{-1})	*r* (-)	*k* (m^2/s)	*ε* (%)
(1)	10	1.89937	0.999999996	4.33005e-07	0.049
(2)	100	1.89937	0.999999996	4.33005e-07	0.049
(3)	1,000	1.89937	0.999999996	4.33005e-07	0.049
(4)	10,000	1.89937	0.999999996	4.33005e-07	0.049
(5)	100,000	1.89937	0.999999996	4.33005e-07	0.049
(6)	1,000,000	1.89937	0.999999996	4.33005e-07	0.049

Another parameter that may affect the accuracy of determining the value of the thermal diffusion coefficient is the duration of the thermal input pulse t_f . Fig. 10a shows the results of the simulation of impulse heating of the sample with the excitation duration t_f variable in the range from 0.1 s to 10 s and the same values of the surface density of the heat flux *q*. As in the previous calculations, the amount of heat supplied to the test sample is different. However, in this case, the time to reach the steady-state conditions, i.e. reaching the temperature T_∞ is different. The parameters for the calculations and the results are presented in Tab. 4. The plot of the dependence of ln(T_∞ - *T*) in time (Fig. 10b) indicates that the length of the interval with a linear characteristic decreases with the increase of the pulse length t_f. This can be seen especially clearly in Fig. 11, showing the regression values *r* versus the number of points used in the linear approximation (*n* - *m*). For subsequent calculation variants, the range of data for which a high value of the approximation quality parameter is achieved is reduced. For the thermal impulse excitation test with an impulse of length t_f = 10 s, the relative error of the thermal diffusivity determination method was 3.66%.

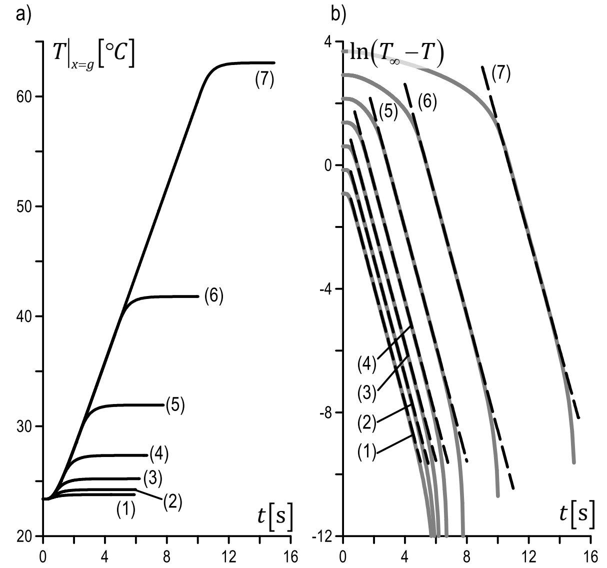

Fig. 10. Impulse heating (a) and determination of thermal diffusivity (b) for different values of the heat pulse duration t_f = 0.1 s (1), 0.21544 s (2), 0.46416 s (3), 1.0 s (4), 2.1544 s (5), 4.6416 s (6), 10 s (7)

Tab. 4. Summary of the results of calculations of the thermal diffusion coefficient *k* for different durations of the heat pulse *t f*

Case	tf (s)	A (s–1)	r (-)	k (m 2/s)	ε (%)
(1)	0.1	1.88852	0.999999999	4.30532e-07	0.522
(2)	0.21544	1.888	0.999999999	4.30412e-07	0.55
(3)	0.46416	1.88686	0.999999998	4.30153e-07	0.61
(4)	1.0	1.88442	0.999999997	4.29597e-07	0.738
(5)	2.1544	1.8792	0.999999996	4.28406e-07	1.01
(6)	4.6416	1.86795	0.999999491	4.25842e-07	1.61
(7)	10.0	1.82894	0.99960493	4.16948e-07	3.66

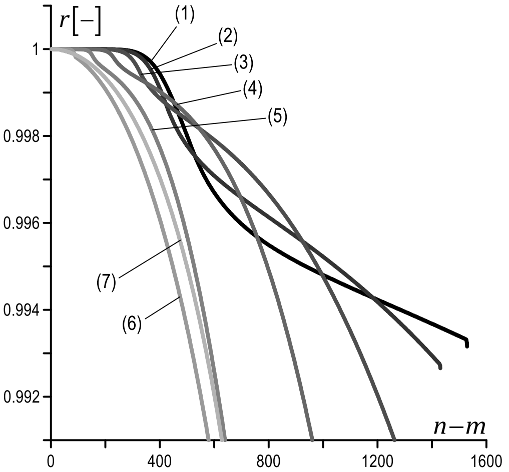

Fig. 11. Maximum regression values *r* obtained for a different number of *n* – *m* points of the linear approximation at the pulse duration t_f = 0.1 s (1), 0.21544 s (2), 0.46416 s (3), 1.0 s (4), 2.1544 s (5), 4.6416 s (6), 10 s (7)

Nevertheless, it should be recognized that the requirement to use a very short duration of the thermal excitation impulse is not a critical condition. Despite a slight reduction in accuracy, it can be assumed that the thermal excitation period is lengthened, e.g., to increase the total thermal energy supplied during the test.

In dependence (8), used to determine the value of the thermal diffusion coefficient k , there is a sample thickness parameter *g*. Its value can be influenced at the stage of preparing samples for conducting experimental trials. Fig. 12a shows the results of the simulation of impulse heating of samples with thicknesses varying from 0.5 mm to 5 mm while maintaining other conditions consistent with those described in Chapter 4. In the process of linear approximation of the dependence ln(T_∞ - T), lines with different directional coefficients *A* (Fig. 12b) were obtained, but after substitution into a dependency (8) the obtained values of the thermal diffusion coefficient (Tab. 5) do not correlate with the sample thickness.

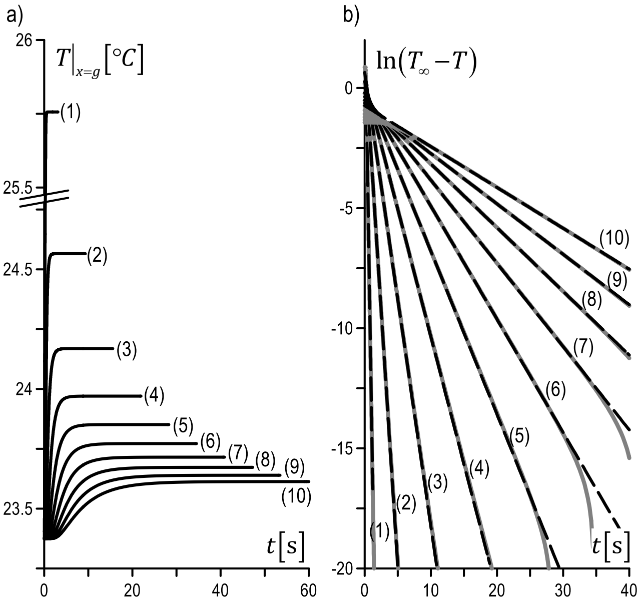

Fig. 12. Impulse heating (a) and determination of thermal diffusivity (b) for different sample thicknesses *g* = 0.5 (1) ÷ 5.0 (10) mm

Tab. 5. Summary of the results of calculations of the thermal diffusion coefficient *k* for various thicknesses of the sample *g*

Case	g (mm)	A (s–1)	r (-)	k (m2/s)	ε (%)
(1)	0.5	16.9289	1.000	4.28815e-07	0.92
(2)	1.0	4.2473	1.000	4.30341e-07	0.57
(3)	1.5	1.88866	1.000	4.30564e-07	0.51
(4)	2.0	1.06254	1.000	4.3063e-07	0.5
(5)	2.5	0.680069	1.000	4.30659e-07	0.49
(6)	3.0	0.472287	1.000	4.30674e-07	0.49
(7)	3.5	0.346998	1.000	4.30688e-07	0.49
(8)	4.0	0.265688	1.000	4.30718e-07	0.48
(9)	4.5	0.209969	1.000	4.30804e-07	0.46
(10)	5.0	0.170174	1.000	4.31055e-07	0.4

As in the previous calculation variant, the time of reaching the conditions set after the thermal impulse excitation is variable and in this case, depends on the thickness of the sample. Proper selection of this parameter can improve the conditions for carrying out measurements during experimental tests. For a given frequency of measurements of the sample surface temperature and for materials with a high speed of heat wave propagation, it may turn out that the number of measurements that are in the linear dependence zone ln(T_∞ - T) will be too small to accurately determine the *A* coefficient and to determine the value of the thermal diffusion coefficient. If it is not possible to carry out measurements at higher registration frequencies, then the test should be performed on a sample of greater thickness.

The above-mentioned conclusions regarding the thickness of the sample and the previous ones concerning the heat impulse duration and its size were formulated based on the results of simulation calculations of impulse heating in a convection-free environment. It can be expected that in real conditions, the process of heat exchange between the heated sample and the environment may affect the accuracy of the determination of the thermal diffusivity value.

The attempt to estimate this impact will be made based on the results of calculations using the finite element method of the impulse heating model of the plate at different values of the convective heat transfer coefficient *h*, included in the analysis in the form of boundary conditions:

$$\begin{aligned} \left.\frac{\partial T}{\partial x}\right|_{x=0} &= h[T(t,x=0)-T_0], \quad t>t_0, \\ \left.\frac{\partial T}{\partial x}\right|_{x=g} &= h[T(t,x=g)-T_0], \quad t>t_0, \end{aligned} \tag{17}$$

assuming that the initial temperature of the plate before heating is equal to the ambient temperature: $T_0 = T_a$. The other boundary conditions comply with the conditions (4).

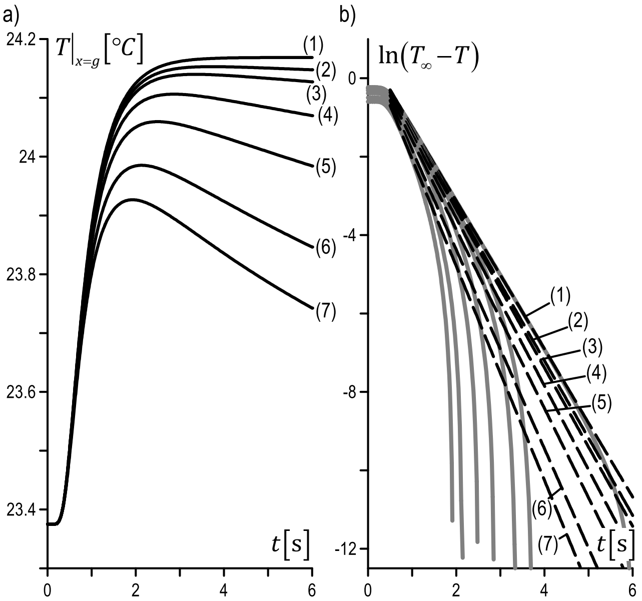

Fig. 13. Temperature increase on the back of the sample during impulse heating (a); illustration of the linear approximation procedure to determine the coefficient *A* and the value of thermal diffusivity *k* (b) for different values of the convective heat transfer coefficient *h* = 0÷150 W/(m^{2}K) (1–7)

The calculation results, in the form of a plot of temperature values on the surface *x* = *g*, are shown in Fig. 13a. For all cases where the value of the convective heat transfer coefficient other than zero was used, no temperature determination was observed in the time interval covered by the analysis. In these cases, the temperature $T_\infty = T_{\max}$ was assumed. Dependence $\ln(T_\infty - T)$ and the results of linear approximation are shown in Fig. 13b and their cursory analysis shows that the presence of convection reduces the length of the linear segment of the dependence. This makes it difficult to carry out a linear approximation and the obtained results are subject to an error (Tab. 6), the greater, the more intense is the heat exchange process by the convection mechanism. Quality analysis of approximation (Fig. 14) confirms this thesis, the number of points lying on the numerical part of the dependence $\ln(T_\infty - T)$ decreases sharply with the onset of convection.

Tab. 6. Summary of the results of calculations of the thermal diffusion coefficient *k* for different values of the convective heat transfer coefficient *h*

Case	h (W/[m2K])	A (s–1)	r (-)	k (m2/s)	ε (%)
(1)	0	1.88807	0.999999999	4.30428e-07	0.55
(2)	5	1.97308	0.999982033	4.49809e-07	3.9
(3)	10	2.02164	0.999962527	4.60878e-07	6.5
(4)	25	2.13749	0.999904664	4.8729e-07	13
(5)	50	2.28404	0.999811522	5.20699e-07	20
(6)	100	2.53275	0.999634372	5.77397e-07	33
(7)	150	2.73303	0.999466132	6.23055e-07	44

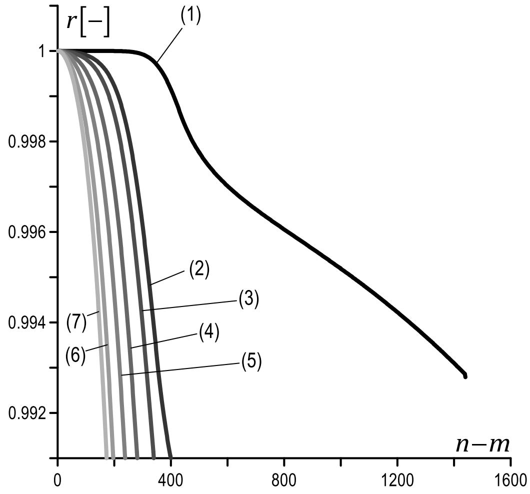

Fig. 14. The maximum regression values *r* obtained for a different number of points *n* - *m* of the linear approximation at different values of the convective heat transfer coefficient $h = 0 \div 150$ W/(m^{2}K) (1–7)

Based on additional calculations, not included in the paper, the following conclusions were formulated regarding the influence of the convection phenomenon on the thermal diffusivity determination procedure:

- The effect of convective cooling on the surface of the impulse-heated sample and the observed surface on the determined value of the thermal diffusion coefficient is the same.
- The error caused by the presence of convection is independent of the magnitude of the thermal excitation impulse *q*. It is not an obvious conclusion and its justification may be the fact that only a short part of the $T(t)$ heating curve is used for the thermal diffusivity value determination procedure.
- The error of the method of determining the value of the thermal diffusion coefficient caused by convection cooling is the greater, the longer the time of determining the maximum temperature on the opposite surface of the sample $T_\infty = T_{\max}$. For a given material, this time is inversely proportional to the thickness of the sample. The requirement to use small sample thicknesses to minimize the effects of convection forces the use of measurement systems with a high frequency of measurement recording, as mentioned above.

An in-depth analysis of the effect of convection cooling on the method of determining the value of the thermal diffusion coefficient goes beyond the scope of this work and requires further calculations. In the literature, for natural convection in air, the value of the heat transfer coefficient *h* is estimated at the level of 5–10 W/(m^2 · K) and, as the calculations have shown, it causes a method error in the range of 3.9%÷6.5%. It should be emphasized, however, that the indicated level of convective heat transfer intensity is achieved under steady-state conditions, with the development of convective air movement. For dynamic conditions, convective heat transfer nucleation, the actual value of the heat transfer coefficient will change over time $h = h(t)$ and for short observation times, it will be lower than the indicated values [11]. It is worth pointing out that in the work of [10], the accuracy of determining the value of the thermal diffusion coefficient of 316 L steel was 0.5%.

6. SUMMARY

Based on the simulations of the impulse heating of a plane-parallel plate of material and the reproduction of the procedure for determining the value of the thermal diffusion coefficient based on the solution of the inverse heat conduction problem, the following conclusions can be drawn:

1. The method is not sensitive to the way impulse heating is carried out. The shape of the heating function, the amount of energy supplied, the size of the pulse, and its height and duration (within reasonable limits) do not affect the accuracy of the method for determining the thermal diffusion coefficient under the conditions of the numerical experiment.
2. The results of the numerical calculations did not show any correlation between the accuracy of the determination of the thermal diffusion coefficient and the characteristics of the sample, i.e. its thickness. One can confidently extend this conclusion to the thermo-physical properties of the material. The method is used both for testing good and weak heat conductors.
3. The temperature change observed during the tests is directly related to the amount of thermal energy supplied to the sample. By selecting the density of the surface heat excitation energy *q*, the impulse duration t_f, it is possible to induce an increase in temperature on the observed surface, adjusted to the sensitivity of the measuring system used.
4. With the given thermo-physical properties of the tested material, the thickness of the sample is directly related to the time of the temperature settling after the end of the impulse of the thermal excitation. This has an impact on the required speed of making and recording temperature measurements.
5. The results of the simulation of impulse heating in conditions of convective heat exchange showed a critical influence on the accuracy of the method of thermal diffusivity determina-

DOI 10.2478/ama-2022-0048

tion. This impact can be minimized without applying special test conditions, by appropriate selection of the test parameters, i.e. heat excitation energy and test duration.

6. The above conclusions indicate that the measuring system used in the tests should be characterized by high sensitivity and frequency of taking and recording temperature measurements. Its absolute accuracy is not critical here.

Despite the described limitations of the method, its advantages, i.e. simplicity, short implementation time, and no special requirements for sample preparation, make it a good tool for determining the value of the thermal diffusion coefficient of materials.

REFERENCES

1. Angström AJ. A new method of determining the thermal conductivity of bodies. Phil. Mag. 25.166 (1863):130-142.
2. Parker WJ, Jenkins RJ, Butler CP, Abbot GL. Flash Method of Determining Thermal Diffusivity, Heat Capacity, and Thermal Conductivity. J. Appl. Phys. 1961;32:1679-1684.
3. Cape JA, Lehman GW. Temperature and Finite Pulse-Time Effects in the Flash Method for Measuring Thermal Diffusivity. J. Appl. Phys. 1963;34(7);1909-1914.
4. Taylor RE, Cape JA. Finite Pulse-Time Effects in the Flash Diffusivity Technique. Appl. Phys. Lett. 1964;5(10):212-214.
5. Larson KB, Koyama K. Correction for FinitePulseTime Effects in Very Thin Samples using the Flash Method of Measuring Thermal Diffusivity. J. Appl. Phys. 1967;38(465):465-474.
6. Akoshima M., Baba T. Thermal Diffusivity Measurements of Candidate Reference Materials by the Laser Flash Method, Int. J. Thermophys. 2005, 26, 1: 151-163.
7. Gembarovic J. Taylor RE A Method for Thermal Diffusivity Determination of Thermal Insulators. Inter. J. Thermophys. 2007;28: 2164-2175.
8. Hay B., Filtz J.R., Hameury J., Rongione R. Uncertainty of Thermal Diffusivity Measurements by Laser Flash Method, Inter. J. Thermophys. 2005; 26, 6: 1883-1898.
9. Hay B, Beaumont O, Failleau G, Fleurence N, Grelard M, Razouk R, Davée G, Hameury J. Uncertainty Assessment for Very High Temperature Thermal Diffusivity Measurements on Molybdenum, Tungsten and Isotropic Graphite. Int. J. Thermophys. 2022: 43, https://doi.org/10.1007/s10765-021-02926-6.
10. Kochanowski K. Oliferuk W. Płochocki Z., Adamowicz A. Determination of thermal diffusivity of austenitic steel using pulsed infrared thermography, Arch. Metall. Mater. 2014: 59: 893-897.
11. Shekriladze I. Boiling Heat Transfer: Convection Controlled by Nucleation. Heat Transfer - Models, Methods and Applications 2018, DOI: 10.5772/intechopen.74418.

Adam Adamowicz: https://orcid.org/0000-0002-4475-968X

DOI 10.2478/ama-2022-0049

EXPERIMENTS AND ANALYSIS OF THE LIMIT STRESSES OF A MAGNETORHEOLOGICAL FLUID

Wojciech HORAK*, **Barbara STĘPIEŃ***, **Bogdan SAPIŃSKI****

*Department of Machine Design and Technology, Faculty of Mechanical Engineering and Robotics,
AGH University of Science and Technology, Al. Mickiewicza 30, 30-059 Kraków, Poland
**Department of Process Control, Faculty of Mechanical Engineering and Robotics,
AGH University of Science and Technology, Al. Mickiewicza 30, 30-059 Kraków, Poland

horak@agh.edu.pl, bstepie@agh.edu.pl, deep@agh.edu.pl

received 29 August 2022, revised 28 October 2022, accepted 4 November 2022

Abstract: This paper presents the results of a rheological test of a commercial magnetorheological (MR) fluid (MRF-132DG). The research includes the problem of measuring and interpreting limit stresses under conditions close to the magnetic saturation of the fluid. Four different limit stresses were determined, two related to the yield point and two related to the flow point. Methods for determining limit stresses, especially due to excitation conditions, were also analysed. The aim of this study is to determine the effect of selected parameters on the values of limit stresses of the selected MR fluid. An additional objective is to highlight the problems of defining and interpreting individual limit stresses in MR fluids, particularly in the context of selecting the values of these stresses for the purpose of modeling systems with MR fluids.

Key words: magnetorheological fluid, yield stress, flow stress, dynamic properties, rheology

1. INTRODUCTION

Among smart materials, there is a group of fluids that are sensitive to changes in the magnetic field. For application purposes, controlling the material's properties with changes in the magnetic field is a convenient and effective method. Nowadays, magnetorheological (MR) fluids are widely applied in systems with controllable characteristics. They are suspensions of magnetic particles in a non-magnetic base fluid. Additives against particle agglomeration and sedimentation are also used as additional components. When the MR fluid is exposed to a magnetic field, the structure of the suspension changes, causing changes in its rheological properties. This reaction is immediate and fully reversible [1-6]. Depending on the configuration of the MR fluid flow and the orientation of the magnetic field acting on it, there are four work mode types that can be distinguished: the flow, shear, squeeze and pinch modes.

In the flow mode (also known as the valve mode), fluid flow is due to the pressure difference. The surfaces of the working geometry are stationary, and the magnetic field is usually oriented perpendicular to the flow direction. The flow mode is found in dampers, shock absorbers and servo valves [7–9].

The second mode of operation is the shear mode, in which the flow of the fluid is achieved by the movement of one or more surfaces interacting with the MR fluid, when the magnetic field is perpendicular to the flow (surface movement) direction. This mode is characteristic for brakes and clutches [10, 11].

In the squeeze-flow mode, the MR fluid is located between the surfaces approaching each other, with the magnetic field induction vector usually parallel to the direction of surface motion and perpendicular to the MR fluid flow direction. This flow mode is observed in some vibration damping devices and low power consumption valves [12–16].

In recent years, a new pinch mode, mainly used in valves, has been proposed [9, 10]. It shares features with the flow mode, but the main difference is the presence of a non-uniform (region of highly concentrated) magnetic field.

For devices working with MR fluids, the key aspect is a change in the apparent viscosity, observed as the ability to transition from a fluid state to a solid consistency. Control in the range of viscosity change is used primarily in vibration dampers [17] and controlled (measuring) brakes, while the control of fluid yield or flow stresses is particularly important for holding brakes [18], clutches [19] and valves [20, 21].

In the present work, attention is paid to the problem of limiting stresses. The main factors that affect the ability to achieve a suitable value of this parameter are the magnetic field strength acting on the fluid and the composition of the MR fluid, especially the quantity, size and magnetic parameters of the ferromagnetic particles used to prepare the suspension [5, 22–26].

As noted earlier, the value of limit stresses in MR fluids is crucial for the operation of certain devices. However, it should be emphasised that for MR fluids, as in other substances with complex rheological properties, the process of transition to the state of plastic deformation is a multifaceted issue. For MR fluids, it is possible to observe the occurrence of the 'two-step yielding' phenomenon, i.e. a two-step transition from a solid to a fluid-like state, due to increasing stress or strain. In this case, two limit stresses can be distinguished. The first, viz. the yield point, refers to the onset of breakage of the fluids' internal structure, while the second, i.e. the flow point, refers to the rupture of the substance's internal integrity.

The aim of this study is to evaluate the conditions for the occurrence of limiting stresses that determine the start of flow of a selected MR fluid. The tested fluid is commercially available and has been applied in vibration dampers and brakes. The scope of the study was limited to high values of magnetic induction, so the results relate to conditions close to the saturation of the tested fluid.

2. METHODS OF DETERMINATION OF THE LIMIT STRESSES

The limit stresses of plastic materials can be defined as the critical amount of applied stress below which it will not flow, but it is a conventional concept and depends on the conditions and method of its determination. It can be distinguished as two forms of that stress: the yield stress is the load that limits the elastic behaviour of the material and the flow stress, and it is usually understood as the point of occurrence of a go-no-go behaviour. The second limit load is commonly used for MR fluids. It is usually given as a material constant.

One of the main criteria of the flow or yield behaviour occurring is the time and (due to the method of measurement) the method followed to control the test, i.e. the controlled shear rate (CSR) or the controlled shear stress (CSS) [27, 28].

Among the main methods used to determine the yield stress is reading the stress curve where the curve intersects the shear stress axis (τ_Y in Fig. 1a). This method is simple, but not very accurate, and can only be used to estimate the value of the flow limit. Attention should be paid here to the method of applying excitation. It is recommended to perform the measurement with a CSS, so that the stress that initiates the flow can be obtained with greater accuracy.

Due to the complexity of the material's transition through the range of the onset of flow, a useful method is to use mathematical models that approximate the points that determine the flow curve. The yield stress is extrapolated as the shear stress corresponding to a shear rate equal to zero. For MR fluids, the most commonly used models are as follows: Bingham (τ_{YB} in Fig. 1a), Herschel–Bulkley, Casson, Sisko, Robertson–Stiff and bi-plastic [29, 30].

The yield stress can be determined as the value of the shear stress at the lowest shear rate (τ_Y in Fig. 1b) or as the shear stress corresponding to a low shear rate, conventionally 0.01 s^{-1} (τ_F in Fig. 1b). Using this method, it is advantageous to represent the flow curves on a double logarithmic scale.

In the method shown in Fig. 1c, a straight line is fitted to low shear rates, and the last point belonging to this straight line is the yield stress (τ_{Y1}). In practice, there is an acceptable deviation of the point value of the fitted straight line, e.g. ±5%. This method can be further developed by fitting a second straight line to points corresponding to high shear rates. The flow limit is then defined as the intersection point of the two straight lines (τ_{Y2}).

However, the above methods do not take into account the occurrence of viscoelasticity, which is a major simplification in the case of MR fluids. In the low-strain range, there can be high elastic stresses in MR fluids [31].

Viscoelasticity can be observed in dynamic mechanical analysis (DMA) tests. Using this method, it is possible to determine the storage modulus G' expressing the elastic properties of the fluid and the loss modulus G'' related to viscosity behaviour (Fig. 1d). Yield stress is defined as the value of shear stress at the end of the linear viscoelastic range (LVE) (τ_Y). In another approach, it is the shear stress for which the G' curve leaves the plateau region. In this concept, it becomes important to assume an appropriate criterion for the occurrence of the end of the LVE range. Typically, the case where there is a 5% or 10% change in G' is taken as the end of the LVE [32].

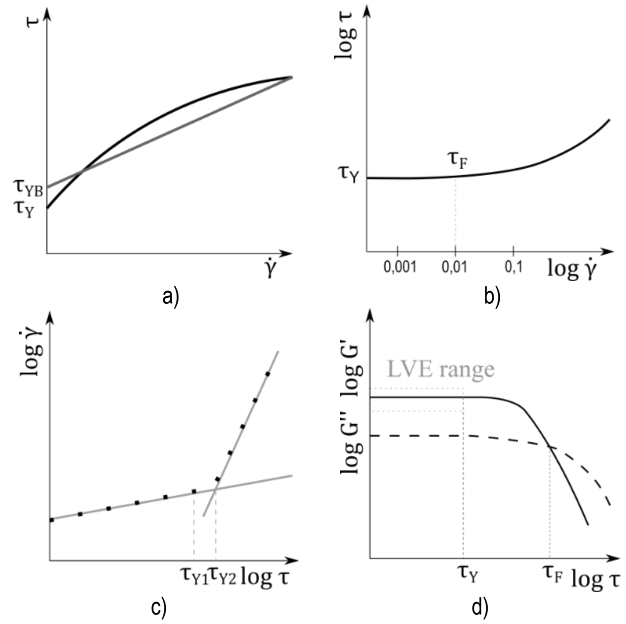

a)
b)
c)
d)

Fig. 1. Methods of determining limit stresses: (a) as the intersection of the flow curve with the stress axis (τ_Y), the Bingham model yield stress (τ_{YB}); (b) as the initial values of the shear stress (τ_Y) on a double logarithmic scale and as the value obtained for a low shear rate of 0.01 s^{-1} (τ_F); (c) using the linear function approximation method (τ_{Y1}, τ_{Y2}); and (d) as the end of the LVE range (τ_Y) and intersection of G' and G'' (τ_F)

Furthermore, the DMA method also allows the flow stress (τ_F) to be determined. This is the stress corresponding to the intersection of the G' and G'' curves. It should be emphasised here that this approach is conventional and uses the typical course of variation in the properties of fluids.

The stress–strain range between the yield point and the flow point is called the yield or the yield/flow transition zone. In this range, $G'>G''$ is still observed, indicating that the fluid exhibits gel-like behaviour. However, there is a dramatic loss of its elastic properties. From the physical side, this behaviour can be explained by changes in the microstructure of MR fluids. All possible elastic deformations have already occurred, and irreversible deformations associated with the degradation of the fluid's internal structure have begun. All these facts contribute to the complexity of the phenomena observed during the transition of MR fluids from the resting state to elastic and plastic deformation.

3. TESTED SAMPLE

The tests were conducted on LORD's MRF-132DG (Cary, North Carolina, USA) commercial fluid. The manufacturer specifies that the fluid is dedicated to shear and valve-mode operation [33].

Tab. 1. Basic properties of MRF-132DG [33]

Property	Value
Density	2.95–3.15 g/cm^3
Dynamic viscosity at 40°C	0.112±0.02 Pa·s
Solid content	80.98 wt.%
Flash point	>150°C
Operating temperature	–40°C to 130°C

The essential properties of the tested fluid, as declared by the manufacturer, are listed in Tab. 1. One of the key features of the tested fluid is the low value of dynamic viscosity under zero magnetic field and the high value of yield stress in the presence of a magnetic field.

Numerous papers that have addressed this fluid's properties cover the range of low and medium magnetic field induction values – usually up to about 400 mT [34-36]. With respect to higher values of the magnetic field, in a previous work [30], studies with values up to 600 mT were carried out. In all these works, the properties of the fluids were related to the well-known Bingham, Herschel–Bulkley and power rheological models, which obtained a fluid stress of 12–16.5 kPa (at B = 300 mT). However, a full evaluation of the ability of this fluid to obtain high shear stresses requires the performance of tests in the higher range of magnetic field. As shown in Fig. 2, the tested MR fluid allows yield stresses of >48 kPa to be obtained, which occurs at a magnetic induction of about 1 T.

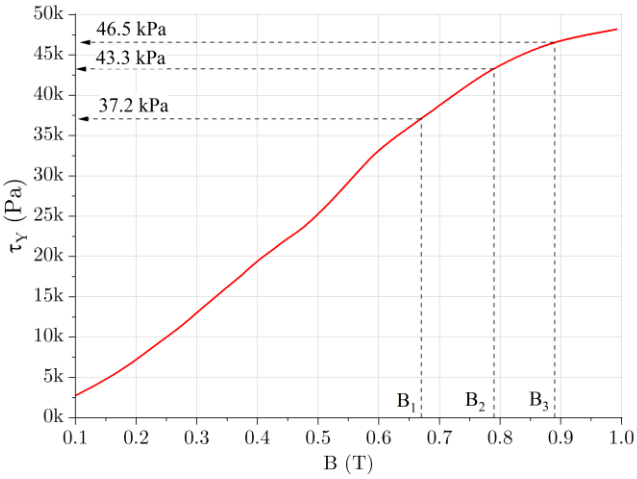

Fig. 2. Yield stress (τ_Y) vs. magnetic induction (B) of MRF-132DG. Based on LORD Corporation's datasheet [33]

The results of the analyses discussed in the present work refer to three values of magnetic field induction. They are marked in Fig. 2 with dashed lines, and the corresponding values of the yield stresses are given. As can be seen, the analysed values of magnetic induction cover the upper range of expected shear stresses.

4. EXPERIMENTS

The experiments were carried out on an MCR-301 rotational rheometer with an MRD180/1T cell, dedicated to conducting tests in the presence of a magnetic field. A plate–plate geometry with the diameter of d = 20 mm was used, and the height of the measuring gap was h = 0.6 mm, for which the sample volume was V = 200 μl. All tests were carried out under thermal stabilisation conditions of t =25°C.

The source of the magnetic field in the measuring cell was an electromagnet, powered from an external DC power supply. For the purpose of this work, the power supply and its control system were modified, which allowed the setting of higher-than-nominal current values ranging from 0 to 5 A to 0 to 6 A. After the modification, the values of magnetic field induction in the working gap of the rheometer were measured. Fig. 3 shows the $B=f(I)$ curves for the modified system. The tests were carried out for three values of electromagnetic current $I_{1,2,3}$ = 4/5/6 A, which correspond to the magnetic field induction $B_{1,2,3}$ = 670/790/890 mT.

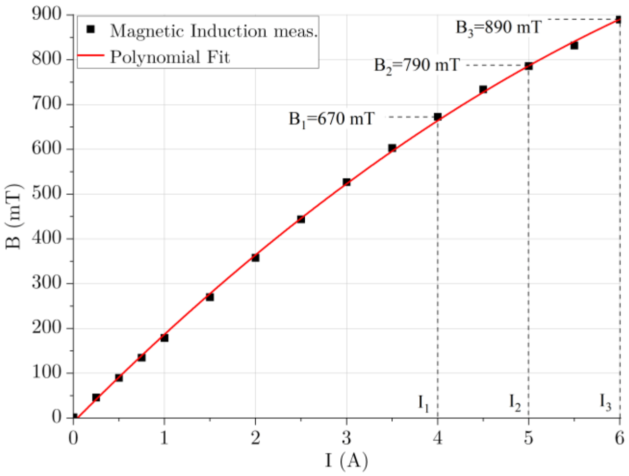

Fig. 3. Magnetic induction (B) vs. current (I) for the modified rheometer measuring cell supply system

The pivotal tests were preceded by preliminary studies, which included Magneto Sweep experiments. This test consists of applying a linearly increasing magnetic field induction during the measurement. It also allows an overall evaluation of the response of the test sample to the application of the magnetic field. Two test types were performed:

- Magneto Sweep at rotational excitation (I = 0–6 A, (B = 0–890 mT), $\dot{\gamma}$ = 0.1/1/10/100 s^{-1});
- Magneto Sweep at oscillatory excitation (I = 0–6 A (B = 0–890 mT), f = 1/10/25 Hz, γ = 0.1%/1%/100%).

The aim of the preliminary tests was to determine the response of the tested fluids to different types of excitation over a wide range of applied magnetic field. The research investigated the effect of the strain value and rate.

The primary research phase included three types of research:

- Rotational CSSt (controlled shear strain) tests
- Rotational CSS tests
- Dynamic DMA (controlled shear strain) tests

The scope of the tests included three values of magnetic induction ($B_{1/2/3}$=670/790/890 mT), three values of the stress increase rate ($v_{1/2/3}$=2.5/5/10 s) in the range 3–30 kPa and three oscillation test frequencies ($f_{1/2/3}$= 1/10/25 Hz). The results of each test were used as input data to determine the corresponding values of each limit stress.

5. RESULTS AND DISCUSSION

5.1. Magneto Sweep - rotational

The results of shear stress measurements under increasing magnetic field induction at different shear rates are shown in Fig. 4. In the lower range of magnetic induction (<400 mT), the effect of shear rate is relatively small, while higher stress occurs at higher shear rates. This is typical behaviour due to the correlation between the apparent viscosity of the fluids and shear stress. As magnetic induction increases, this trend reverses. The change point of this trend occurs for the magnetic induction B =300 mT. The lower the shear rates, the higher are the stress values obtained. In the extreme case, the shear stress for $\dot{\gamma} = 0.1\ \mathrm{s}^{-1}$ is 40% higher than when measured for $\dot{\gamma} = 100\ \mathrm{s}^{-1}$ (25 vs. 35 kPa). The explanation for this behaviour is that lower shear rates promote the preservation of greater internal integrity of structures inside MR fluids, which results in higher deformation resistance.

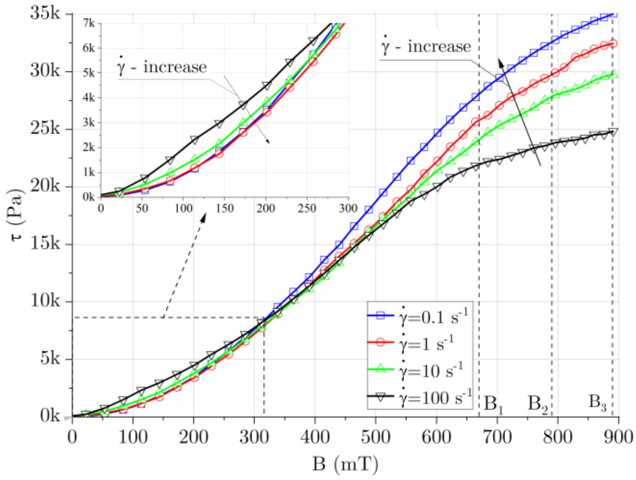

Fig. 4. Shear stress (τ) vs. magnetic induction (B) at rotational excitation

5.2. Magneto Sweep – oscillatory method

Fig. 5 shows the results of measuring shear stress under oscillatory excitation. The tests were performed for three values of strain amplitude. For γ=0.1%, relatively low stress values were obtained, with no change from about B =300 mT onwards. With such a small degree of sample deformation, it was not possible to obtain higher stresses. Excitation levels of 1% and 100% resulted in correspondingly higher stress values. With 1% strain, a decrease in the stress increment in the magnetic induction range greater than B_1 is observed, while for γ = 100%, the stress increases approximately in proportion to the increase in the applied magnetic field induction. Thus, it can be assumed that in the case of 0.1% and 1% strain, a sort of saturation state has been obtained, for which a further increase in magnetic induction does not lead to an increase in stress.

In Fig. 5, the stress ranges corresponding to the three values of magnetic induction, for which analyses were carried out in the following part of the work, are indicated using curly brackets. The obtained results show that the differences in the measured shear stress, which depend on the oscillation frequency, are not significant and are within ±1 kPa.

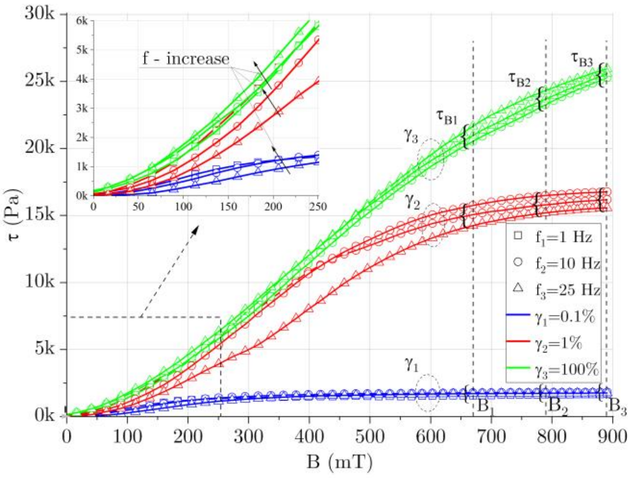

Fig. 5. Shear stress (τ) vs. magnetic induction (B) at oscillatory excitation

5.3. Strain–shear stress relation

Fig. 6 shows the results of the shear stress measurements under controlled strain (γ = 0.01%–100%) and three values of magnetic field. The measurement simulates the method of excitation that occurs in MR fluid systems operating with displacement control.

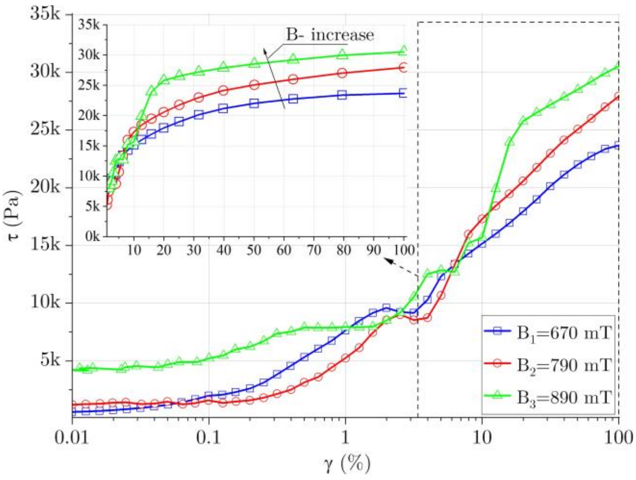

Fig. 6. Shear stress (τ) vs. strain (γ) obtained from controlled strain measurements

In the very low strain range (γ<0.1%), the stress values depend very slightly on the strain, which is visible as a plateau region in the first part of the curves. The second characteristic value that can be indicated is γ>10%, for which the behaviour of the fluids is consistent with typical rheological models. From the perspective of this paper, an important aspect is the analysis of the transition range (strain from 0.1% to about 1%), with this range including the excitation at which the fluid starts to flow, i.e. yield stress and flow stress.

Fig. 7 shows the result of the stress measurement, but in this case, the test was carried out with CSS. This is the recommended method for determining limit stresses in fluids. The test was based on logarithmically increasing the stress in the range of 3-–30 kPa and observing the sample deformation. The measurements were repeated for three stress increase rates v = 2.5/5/10 s (which correspond to the gradients of stress change, respectively, $\Delta\tau$=10.8/5.4/2.7 kPa·s^{-1}). The results shown in Fig. 7 were used to determine the flow stress (τ_Y).

In the inset in Fig. 7, the arrows indicate the direction of increase in the stress gradient. For the two lower values of magnetic induction, the increase in the rate of stress change results in an increase in the obtained stresses, while with B_3, the trend is reversed. While the behaviour observed for B_3 is consistent with the previous results (see Fig. 4), the measurement results for B_1 and B_2 can be explained as the effect of the measurement duration. With a lower magnetic field, the shorter test time resulted in lower stress values. This may result from the fact that, at lower values of the magnetic field, the MR fluid structure was not as strong as it was in the higher one. This thread requires further research. From the point of view of this work, it is important to determine the flow stress, which in the case of this measurement can be determined as the break point of the curve.

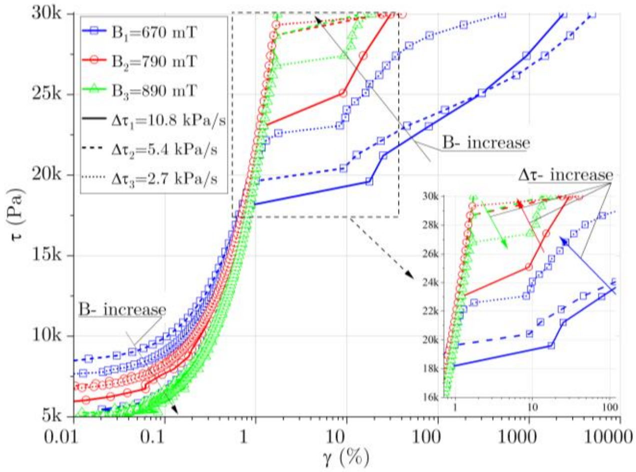

Fig. 7. Shear stress (τ) vs. strain (γ) obtained from controlled shear stress measurements (Solid, dashed and dotted lines represent $\Delta\tau$ = 10.8/5.4/2.7 kPa s^{-1}, respectively)

It should be noted that, in the case of the highest analysed magnetic field induction, at the lowest rate of stress increase, no fluid flow was obtained. This indicates that the flow stress for this measurement is >30kPa.

5.4. Limit stresses

5.4.1. Rotational test-stress ramp

Based on the data from CSS-type measurements, the values of the yield stress (τ_{CSS}) were determined for different gradients of stress increase. The results are shown in Fig. 8. The gradient of stress increase can significantly affect the value of the limit stress. This is particularly visible at lower values of magnetic field induction, which may result from the aforementioned duration of the measurement.

The inset in Fig. 8 shows the average values of flow stress calculated from the measurement results for different gradients of stress increase. The extreme values (minimum/maximum [min/max]) are marked using the error bar. For B_1 = 670 mT and B_2 = 790 mT, the change in τ_{CSS} from the average value is approximately 12%, while for B_3 = 890 mT, it is <4%. Since, for the measurement of B_3 and $\Delta\tau_1$, the limiting stress was not reached, the yield stress value of 30 kPa was used for the analysis.

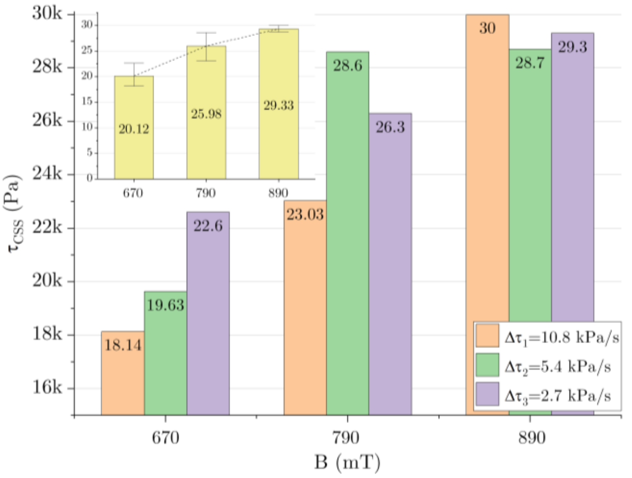

Fig. 8. Yield stress (τ_{CSS}) vs. magnetic induction (B) obtained from controlled shear stress measurements

5.4.2. Oscillatory test

Fig. 9 summarises the results of the dynamic (oscillation) measurements. The tests were carried out for three values of magnetic induction with a logarithmic strain ramp γ = 0.01%–1,000% and three oscillation frequencies ($f_{1,2,3}$ = 1/10/25 Hz). Thus, for a strain equal to 100%, the shear rate will be 6.3, 63 and 157 s^{-1}, respectively.

Due to the quite high values of magnetic induction (starting from B =690 mT) and a wide range of deformation, reaching very small deformation (up to 0.01%), high values of the elastic modulus (G') were obtained in all measurements and a distinct LVE range was observed. The end of this, for all analysed cases, falls under a deformation of about 1%.

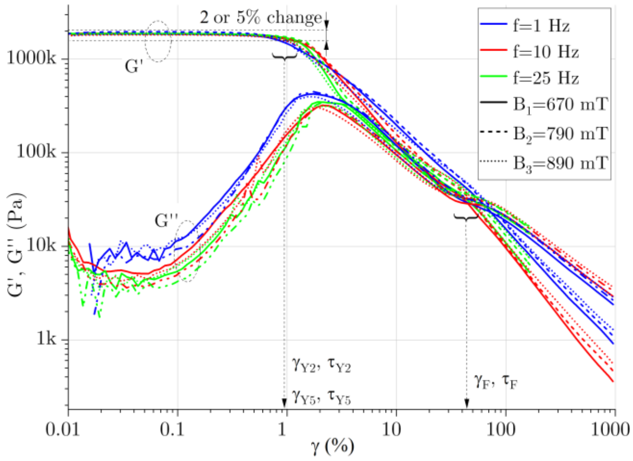

Fig. 9. Storage (G') and loss (G'') modulus vs. strain (γ)

The data shown in Fig. 9 were used to determine yield and flow stresses. In the case of yield stress, two values were established corresponding to two criteria for its determination. It was arbitrarily assumed that the stress that occurs when the elastic modulus changes by 2% or 5% would be considered as the value of these yield stresses. The notation for these parameters was adopted as $\tau_{Y2\%}$ and $\tau_{Y5\%}$.

On the basis of the discussed results of dynamic tests, the flow point was also determined as the stress corresponding to the balance point *G'*=*G'* and denoted as τ_F. Fig. 9 symbolically denotes the discussed ranges and parameters (stresses and corresponding strains) using dashed lines.

Fig. 10 summarises the limit stresses determined from the dynamic tests. As expected, the yield stresses $\tau_{Y2\%}$ and $\tau_{Y5\%}$ have a similar course. It should be emphasised that increasing the tolerance in the method of determining the yield stress from 2% to 5% results in an increase in the value of this stress by an average of 42% (min: 33%; max: 51%). This result indicates that the choice of the yield stress criterion has a significant effect on its value.

Analysing the effect of the excitation frequency on yield stresses ($\tau_{Y2\%}$, $\tau_{Y5\%}$), it can be observed that yield stress increases as the deformation rate of the specimen increases. This is especially evident when increasing the frequency from 1 Hz to 10 Hz. On the contrary, the opposite trend is seen in the case of flow stress (τ_F). Note that the nature of the flow stress variation is similar both qualitatively and quantitatively to τ_{CSS} (Fig. 8).

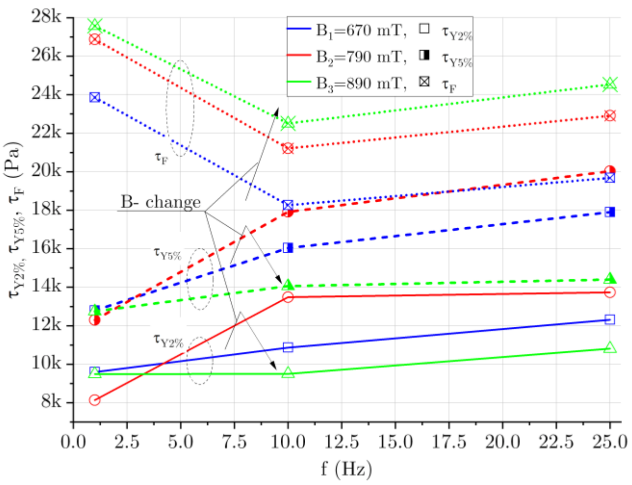

Fig. 10. Yield stresses ($\tau_{Y2\%}$, $\tau_{Y5\%}$) and flow stress (τ_F) vs. frequency (*f*) obtained from oscillatory tests

Furthermore, Fig. 11 shows the strain values corresponding to the values of the respective limit stresses. For the yield stress (τ_Y), an increase in excitation frequency results in an increase in the strain at which the flow occurred, while for the flow stress (τ_F), a significant reduction in the strain corresponding to the flow is observed for tests performed at higher frequency.

Thus, an increase in the rate of the sample deformation, in the case of yield stress, causes an increase in the degree of deformation at which it occurs, as well as the corresponding stress. In the case of flow stress, the trend is the opposite.

The test method used makes it possible to observe the behaviour of the samples in the range between yield stresses (τ_Y) and flow stresses (τ_F). To represent the behaviour of the test sample before flow occurs, Fig. 12 shows plots of the variation of the damping ratio (*tan(δ) = G''/G'*) as a function of the applied strain.

The characteristic value for the discussed analysis is *tan(δ)* =1, which corresponds to the flow point of the tested sample. As shown in Fig. 11, the deformation corresponding to the yield stress (τ_Y) is in the range of 0.4%–1.25% and corresponds to the initial phase of the graphs shown in Fig. 12. In this range of deformation, there is a high modulus of elasticity (*G''*) with relatively low values of the loss modulus (*G'*). A rapid change in the ratio of *G'* and *G'' is* observed at strains of about 3%–5%. In this range, the maximum value of the loss modulus is exceeded, and a sharp decrease in the elastic modulus begins (compare with Fig. 9).

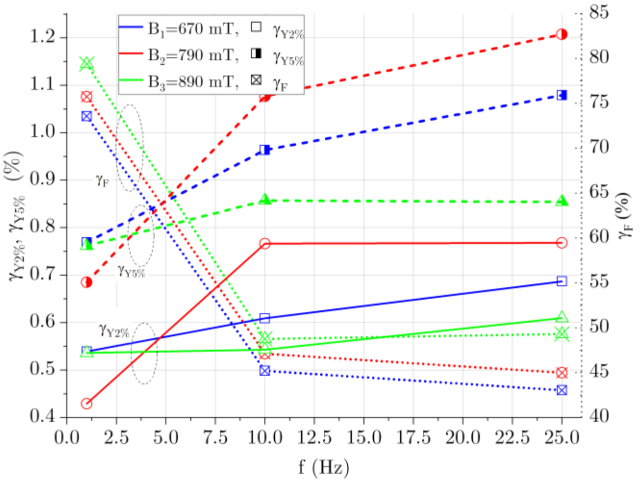

Fig. 11. Yield strain ($\gamma_{2\%}$, $\gamma_{5\%}$) (left axis) and flow strain (γ_F) (right axis and dashed lines) vs. frequency (*f*) obtained from oscillatory tests

This corresponds to the non-linear range of *tan(δ)* variation and ends in the deformation range of 30%–40%, which corresponds to the approach of the values of individual stiffness modules. In the discussed diagram, the ranges of deformation corresponding to individual limit stresses are marked with the use of curly brackets.

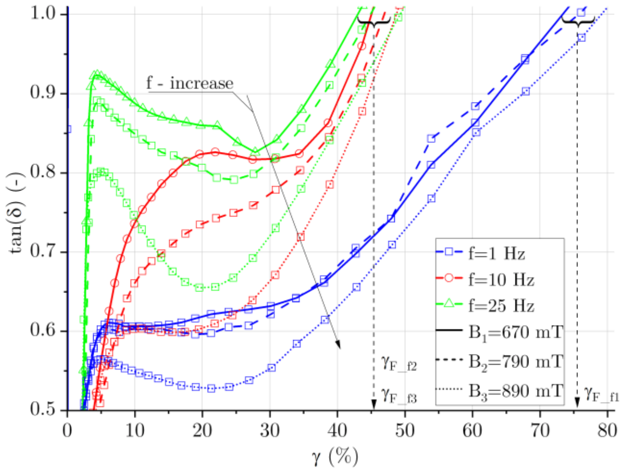

Fig. 12. Damping factor (*tan(δ)*) vs. strain (*γ*) in the post-yield region

From an application perspective, it is important to evaluate the variation of the shear stress in terms of excitation after the yield stress (τ_Y) and before the flow stress (τ_F). For this purpose, in Fig. 13, the relation of shear stress to the damping coefficient tan(δ) is shown.

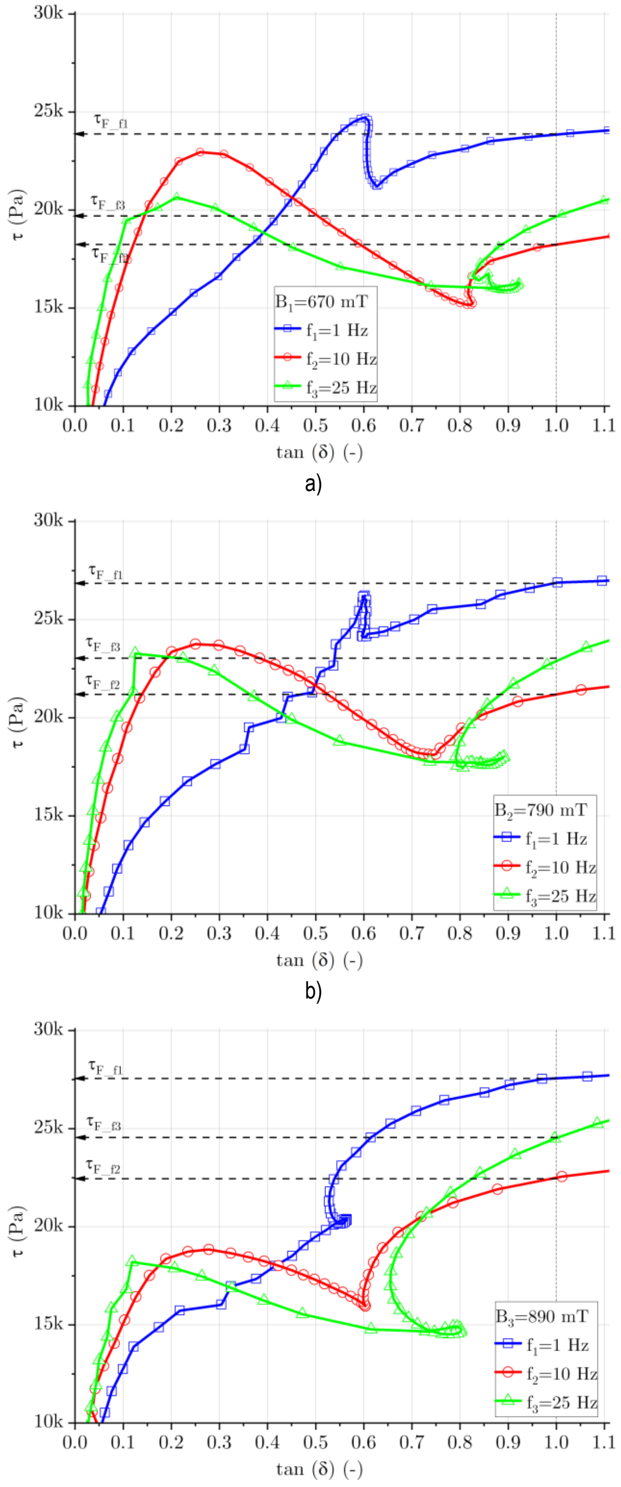

a)

b)

c)

Fig. 13. Shear stress (τ) vs. damping factor (*tan(δ)*) in the post-yield region for variable magnetic induction (a) B_1 = 670 mT; (b) B_2 = 790 mT; and (c) B_3 = 890 mT

In the diagrams, the stress values corresponding to the flow stress (τ_F) are marked with arrows. For the lowest magnetic field induction (B_1), the shear stress value in the range of $tan(\delta)<1$ is higher than the flow stress (τ_F). Therefore, it is possible that the stress in the fluid exceeds the flow stress value before the fluid flows. In the transient region, there are strong non-linear relationships between the dynamic properties of the tested MR fluids and stress. In particular, at higher excitation frequencies and higher values of magnetic induction, there is a tendency to 'loop' the discussed relationship, i.e. before reaching the flow stress (τ_F), there is a sharp decrease in *tan(δ)*, which is visible on the graphs as a collapse or looping in the curves.

5.4.3. Analysis of the limit stresses

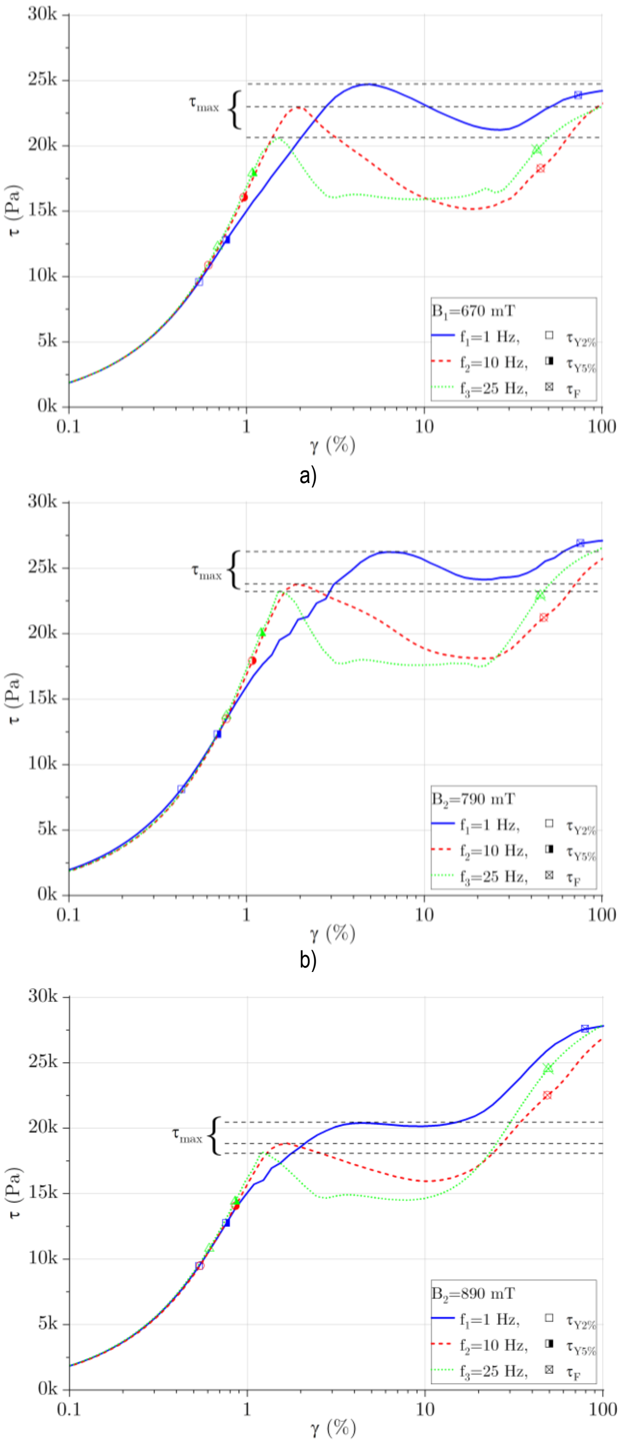

a)

b)

c)

Fig. 14. Shear stress (τ) vs. strain (γ) for variable magnetic induction: (a) B_1 = 670 mT; (b) B_2 = 790 mT; and (c) B_3 = 890 mT (The open marks correspond to $\tau_{Y2\%}$, half-coloured regions correspond to $\tau_{Y5\%}$ and the crossed marks correspond to τ_F)

Fig. 14 summarises the curves of stresses as a function of strain, determined from oscillatory measurements. The points corresponding to the previously determined limit stresses are marked on the curves. As discussed earlier, the non-linearities can be seen as stress fluctuations in the transient region. After reaching the yield stress (τ_Y), there is a further increase in stress in each of the analysed cases, passing into the 'plateau' range and then increasing at the strain preceding the flow stress (τ_F) (compare Fig. 12).

It should be noted that, similar to what was observed in the context of *tan(δ)*, at lower values of the magnetic field, the stresses in the transition range exceed the values of the flow stress (τ_F). Naturally, this is related to the measurement method in which the controlled stress allowed this to occur. This behaviour is important for all systems operating under controlled deformation. In the context of the design of such systems in particular, it is to be expected that, at sufficiently low strains, it is possible for stresses to occur higher than those derived from the flow stress determined by the CSS method, by CSR or from dynamic tests.

To summarise the results of the determined limit stresses, Fig. 15 shows all of the results as a bar graph. As can be seen, the highest limit stress values were obtained from the CSS test method (τ_{CSS}), but are close to the flow stress (τ_F) determined from oscillatory measurements. This is an expected result, as dynamic tests allow detection of the beginning of changes in the MR fluid structure at an earlier stage of internal integrity loss. In the context of the yield stress (τ_F), the strong effect of the excitation frequency on the value of the boundary stress is distinguishable.

To highlight the complexity of interpreting limit stresses for MR fluids, Fig. 16 shows the average value of all limit stresses (both yield and flow states) obtained for three values of magnetic field induction. The bars correspond to the average value, and the points correspond to the values of individual measurements, while the box represents the range of stress variation.

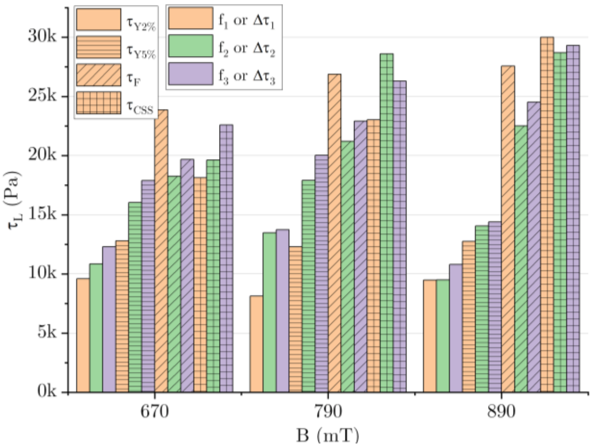

Fig. 15. Limit stresses (τ_L) vs. magnetic induction (*B*)

As can be observed, the criterion for determining the limit stress and the conditions of measurement have a significantly stronger influence on the obtained value than the value of magnetic field induction. Therefore, for the design and analysis of systems with MR fluids, for which the value of limit stresses is crucial, it is important to evaluate the criterion for determining a specific limit stress.

It is noteworthy that the stresses declared by the manufacturer (see Fig. 2) were not obtained in any of the performed measurements. This may be related to the difference between the test methods and the parameters presented in the present work and those used by the manufacturer. However, it should be noted that, in the case of the highest value of the magnetic field induction value (*B* = 790 mT), the difference reaches 55% (from 46.5 kPa declared by the manufacturer; 30 kPa was obtained instead). However, good correspondence was obtained with the results of some previous works [34–37] related to the study of MRF-132DG fluids, in the range of low magnetic field induction, where the expected shear stresses are at the level of several kilopascals.

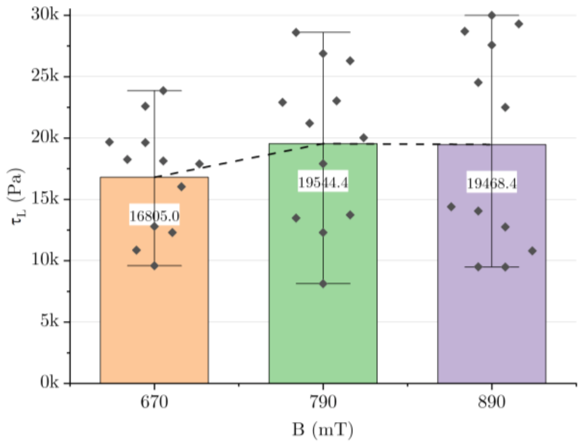

Fig. 16 Limit stresses (τ_L) vs. magnetic induction (*B*) (bar: mean limit stress, dots: each measurement, error bar: min–max range)

6. CONCLUSION

The paper presents an analysis of the variation of limit stresses of the MRF–132DG fluid, under a magnetic field value close to the saturation state.

The complexity of the problem concerning the methodology for determining limit stresses is shown. The values of the yield (τ_Y) and the flow (τ_F) stresses are significantly dependent on the deformation rate. However, for yield stress, an increase in the deformation rate results in an increase in its value, whereas for flow stress, the trend is the opposite.

Furthermore, it has been shown that the rate of stress change can significantly affect the value of the limit stresses.

The selection of the value of the tolerance change *G*' as an indicator of yield stress occurrence is of significant importance for the obtained stress values. A change from 2% to 5% results in an increase in yield stress of an average of 42%.

It has also been shown that adopting an appropriate value of the limiting stresses suitable for a given application can be crucial in predicting how it will perform. Under specific operating conditions (such as very small strains), taking into account the relation $\tau=f(B)$ as a simple function, without considering the conditions for measuring this parameter, may be an oversimplification.

REFERENCES

1. Khajehsaeid H, Alaghehband N, Bavil PK. On the yield stress of magnetorheological fluids. Chemical Engineering Science. 2022;256:117699.
2. Kumar M, Kumar A, Bharti RK, Yadav HNS, Das M. A review on rheological properties of magnetorheological fluid for engineering components polishing. Materials Today: Proceedings. 2022;56(3):A6-A12.

3. de Vicente J, Klingenberg DJ, Hidalgo-Alvarez R. Magnetorheological fluids: a review. Soft Matter. 2011;7:3701-3710.
4. Yang J, Yan H, Wang X, Hu Z. Enhanced yield stress of magnetorheological fluids with dimer acid. Materials Letters. 2016;167:27-29.
5. Asiaban R, Khajehsaeid H, Ghobani E, Jabbari M. New magnetorheological fluid with high stability: Experimental study and constitutive modelling. Polymer Testing. 2020;8:106512.
6. Kubík M, Válek J, Žáček J, Jeniš F, Borin D, et al. Transient response of magnetorheological fluid on a rapid change of magnetic field in shear mode. Scientific Reports. 2022;12:10612.
7. Giorgetti A, Baldanzini N, Biasiotto M, Citti P. Design and testing of a MRF rotational damper for vehicle applications. Smart Materials and Structures. 2010;19(6):065006.
8. Li DD, Keogh DF, Huang K, Chan QN, Yuen ACY, Menictas C et al. Modeling the response of magnetorheological fluid dampes under seismic conditions.
9. Kubík M, Macháček O, Strecker Z, Roupec J, Mazůrek I. Design and testing of magnetorheological valve with fast force response time and great dynamic force range. Smart Materials and Structures. 2017;26(4):047002.
10. Thakur MK, Sarkar C. Experimental and numerical study of magnetorheological clutch with sealing at larger radius disc. Defence Science Journal. 2020;70(6):575-582.
11. Patel S, Upadhyay R, Patel D. Design optimization of magnetorheological brake using structural parameter: evaluation and validation. IOP Conference Series: Materials Science and Engineering. 2020;992:012004.
12. Horak W. Modeling of magnetorheological fluid in quasi-static squeeze flow mode. Smart Materials and Structures. 2018; 27: 065022.
13. Sapiński B, Gołdasz J. Development and performance evaluation of an MR squeeze-mode damper. Smart Materials and Structures. 2015;24(11):115007.
14. Sapiński B, Rosół M, Jastrzębski Ł, Gołdasz J. Outlook on the dynamic behavior of an magnetorheological squeeze-mode damper prototype. Journal of Intelligent Material Systems and Structures. 2017;28(20):3025-3038.
15. Goncalves FD, Carlson JD. An alternate operation mode for MR fluids – Magnetic Gradient Pinch. Journal of Physics: Conference Series. 2009;149:012050.
16. Gołdasz J, Sapiński B. Magnetostatic analysis of a pinch mode magnetorheological valve. Acta Mechanica et Automatica. 2017;11(3):229-232.
17. Sapiński B, Horak W. Rheological properties of MR fluids recommended for use in shock absorbers. Acta Mechanica et Automatica. 2013;7(2):107-110.
18. Quoc NV, Tuan LD, Hiep LD, Quoc HN, Choi SB. Material characterization of MR fluid on performance of MRF based brake. Frontiers in Materials. 2019; 6: 125.
19. Lokhande SB, Patil SR. Experimental characterization and evaluation of magnetorheological clutch for an electric two-wheeler application. Measurement. 2021;175:109150.
20. Strecker Z, Jeniš F, Kubík M, Macháček O, Choi SB. Novel approaches to the design of an ultra-fast magnetorheological valve for semi-active control. Materials. 2021;14(10):2500.
21. Gołdasz J, Sapiński B, Kubík M, Macháček O, Bańkosz W et al. Review: a survey on configurations and performance of flow-mode MR valves. Applied Sciences. 2022;12(12):6260.
22. Laun H.M, Gabril C, Kieburg Ch. Twin gap magneorheometer using ferromagnetic steel plates – Performance and validation. Journal of Rheology. 2010;54:327-354.
23. Wang K, Dong X, Li J, Shi K. Yield dimensionless magnetic effect and shear thinning for magnetorheological grease. Results in Physics. 2020;18:103328.
24. Han S, Choi J, Han HN, Kim S, Seo Y. Effect of particle shape anisotropy on the performance and stability of magnetorheological fluids. ACS Applied Electronic Materials. 2021;3:2526-2533.
25. Jeon J, Koo S. Viscosity and dispersion state of magnetic suspensions. Journal of Magnetism and Magnetic Materials. 2012;324: 424-429.
26. Nagdeve L, Sidpara A, Jain VK, Ramkumar J. On the effect of relative size of magnetic particles and abrasive particles in MR fluid-based finishing process. Machining Science and Technology. 2018;22(3):493-506.
27. Acharya S, Tak RSS, Singh SB, Kumar H. Characterization of magnetorheological brake utilizing synthesized and commercial fluids. Materials Today: Procedings. 2021;46(19):9419-9424.
28. Mezger TG. The Rheology Handbook. 4th edition. Hanover: Vincentz Network GmbH & Co; 2014.
29. Elsaady W, Oyadiji SO, Nasser A. A review on multi-physics numerical modelling in different applications of magnetorheological fluids. Journal of Intelligent Systems and Structures. 2020;31(16):1855-1897.
30. Chaudhuri A, Wereley NM, Radhakrishnan R, Choi SB. Rheological parameter estimation for a ferrous nanoparticle-based magnetorheological fluid using genetic algorithms. Journal of Intelligent Material Systems and Structures. 2006;17(3):261-269.
31. Laun HM, Gabriel C, Kieburg C. Magnetorheological fluid (MRF) in oscillatory shear and parametrization with regard to MR device properties. Journal of Physics: Conference Series. 2009;149:012067.
32. Wereley NM, Chaudhuri A, Yoo J-H, John S, Kotha S, Suggs A et al. Bidisperse magnetorheological fluids using Fe particles at nanometer and micron scale. Journal of Intelligent Material Systems and Structures. 2006;17(5):393-401.
33. LORD Corporation. MRF-132DG Magneto-Rheological Fluid. DS7015 datasheet [Internet]. 2011 Nov [cited 2022 Jul 15]. Available from: https://lordfulfillment.com/pdf/44/DS7015_MRF-132DGMRFluid.pdf
34. Barnes HA. The yield stress – a review or ‘παντα ρει’—everything flows? Journal of Non-Newtonian Fluid Mechanics. 1999;81 (1-2):133-178.
35. Ichwan B, Mazlan SA, Imaduddin F, Ubaidillah, Zamzuri H. Performance simulation on a magnetorheological valve module using three different commercial magnetorheological fluid. Advanced Materials Research. 2015;1123:35-41.
36. Szakal RA, Susan-Resiga D, Muntean S, Ladislau V. Magnetorheological fluids flow modelling used in a magnetorheological brake configuration. 2019 International Conference on ENERGY and ENVIRONMENT (CIEM). 2019:403-407.
37. Szakal RA, Mecea D, Bosioc AI, Borbáth I, Muntean S. Design and testing a magneto-rheological brake with cylindrical configuration. Proceeding of the Romanian Academy – Series A: Mathematics, Physics, Technical Sciences, Information Science. 2021;22(2/2021):189-197.

The authors wish to acknowledge the kind support of the Czech Science Foundation (Grantová Agentura České Republiky—GACR) and the National Science Centre (Narodowe Centrum Nauki—NCN, Poland)—grant IDs: GACR 21-45236L (CZ) and 2020/39/I/ST8/02916 (PL).

Wojciech Horak: https://orcid.org/0000-0002-2258-4233

Barbara Stępień: https://orcid.org/0000-0001-7802-4342

Bogdan Sapiński: https://orcid.org/0000-0001-6952-8303

DOI 10.2478/ama-2022-0050

acta mechanica et automatica, vol.16 no.4 (2022)

SECOND LAW ANALYSIS OF MHD FORCED CONVECTIVE NANOLIQUID FLOW THROUGH A TWO-DIMENSIONAL CHANNEL

Rached MIRI*, Mohamed A. ABBASSI*, Mokhtar FERHI, Ridha DJEBALI****

*Research Lab, Technology Energy and Innovative Materials, Faculty of Sciences, University of Gafsa, Gafsa 2112, Tunisia
**UR: Modelling Optimization and Augmented Engineering, ISLAIB, University of Jendouba, Av. de l'UMA, Jendouba 8189, Tunisia

rachedmiri111@gmail.com, abbassima@gmail.com, moktar.ferhi@gmail.com, jbelii_r@hotmail.fr

received 17 September 2022, revised 3 November 2022, accepted 6 November 2022

Abstract: The present study deals with fluid flow, heat transfer and entropy generation in a two-dimensional channel filled with Cu–water nanoliquid and containing a hot block. The nanoliquid flow is driven along the channel by a constant velocity and a cold temperature at the inlet, and the partially heated horizontal walls. The aim of this work is to study the influence of the most important parameters such as nanoparticle volume fraction ($0\%\leq\phi\leq4\%$), nanoparticle diameter ($5\ \text{nm}\leq dp\leq55\ \text{nm}$), Reynolds number ($50\leq Re\leq200$), Hartmann number ($0\leq Ha\leq90$), magnetic field inclination angle ($0\leq\gamma\leq\pi$) and Brownian motion on the hydrodynamic and thermal characteristics and entropy generation. We used the lattice Boltzmann method (LBM: SRT-BGK model) to solve the continuity, momentum and energy equations. The obtained results show that the maximum value of the average Nusselt number is found for case (3) when the hot block is placed between the two hot walls. The minimum value is calculated for case (2) when the hot block is placed between the two insulated walls. The increase in Reynolds and Hartmann numbers enhances the heat transfer and the total entropy generation. In addition, the nanoparticle diameter increase reduces the heat transfer and the irreversibility, the impact of the magnetic field inclination angle on the heat transfer and the total entropy generation is investigated, and the Brownian motion enhances the heat transfer and the total entropy generation.

Key words: MHD, LBM, channel flow, nanoliquid, entropy generation, Brownian motion

1. INTRODUCTION

In the last few decades, simulation of flow, convective heat transfer and irreversibility in channels has attracted considerable attention due to various industrial applications, such as air conditioning systems in buildings, cooling of electronic components, compact heat exchangers and biomedical equipment. Several research studies are developed in this context using different emerging CFD methods, such as finite volume method, finite element method and lattice Boltzmann method (LBM).

Recently, the LBM based on the LB equation has been viewed as a novel alternative to discretisation methods. This technique is a powerful approach for scrutinising fluid flow and heat transfer difficulties because it is a second-order accuracy in both time and space; it is easy to code and may be used to handle the extended range of flow regimes ranging from microscopic to continuum scales. Besides, the application of the LBM technique has received continuous interest in the last decades for the simulation of classic and emerging CFD [1-2].

Since the importance of the heat transfer phenomenon and its applications in various fields, it is necessary to present a few examples of research work, interlaced by the various parameters and various boundary condition influencing the rate of heat transfer. Mishra et al. [3] studied the forced convection heat transfer from an isothermal heated cone in Bingham plastic fluids using the finite element method. They found that the heat transfer rate exhibits a positive dependence on Reynolds and Prandtl numbers. Kim [4] used the finite element method to study the forced convection heat transfer and fluid flow between parallel plates under uniform heat flux. They concluded that the formulation for the Nusselt number has been derived based on the analytically described velocity and flow rate. Peyghambarzadeh et al. [5] studied the forced convection and sub cooled flow boiling heat transfer to pure water and n-heptane in an annular heat exchanger using experimental correlations. They concluded that although n-heptane leaves the heat exchanger warmer at similar operating conditions, it has a less heat transfer coefficient than water, and the heat transfer coefficient is a direct function of heat flux, sub cooling temperature and fluid flow rate. Arastehet al. [6] performed a 2-D numerical study of hydrothermal performance of a porous sinusoidal double-layered heat sink using silver–water nanofluid in a laminar regime. They showed that the dimensionless optimum porous thicknesses are equal to 0.8, 0.8 and 0.2 for the cases when Darcy numbers are equal to10-4, 10-3 and 10-2, respectively. The maximum performance evaluation criteria number equal to 2.12 is obtained for the case with Darcy number equal to 10-2, Reynolds number equal to 40, and volume fraction of nanoparticles equal to 0.04.Farooq et al. [7] studied the 3D bioconvection flow of carreau nanofluid in the presence of thermal radiation. The results show that a higher temperature profile is observed with higher values of thermal Biot number, exponential basic sink parameter and thermal relaxation, while a decrease in temperature is observed with an increase in mixed convection. Also, they found that the concentration profile shows a growing tendency with the mass concentration parameter and the concentration relaxation parameter, and the microorganism field depends directly on the Peclet number and bioconvection Lewis number. Xiong et al. [8] explained the important aspects of viscous dissipation on the magneto-cross-nanofluid flow crossed by a needle placed in a porous environment. As we know, the heat transfer of the most conventional fluids is not suitable for many actual processes due to the low thermal conductivity. Adding nanoparticles to the base fluid is a new idea for improving heat transfer in these types of fluid, named ‘nanofluids’. Santra et al. [9] used the control volume approach to investigate the heat transfer enhancement due to nanofluid flow through two isothermally heated parallel plates. The obtained results show that the increase in the solid volume fraction improves the heat transfer rate. Heidary and Kermani [10] investigated the flow and heat transfer in sinusoidal wall channel crossed with the Cu–water nanofluid. They concluded that the heat transfer increases with the increasing nanoparticle volume fraction and Reynolds numbers. Minakov et al. [11] experimentally studied the forced convection of nanofluids with CuO nanoparticles in a copper tube of a length of 1 m, an outer diameter of 6 mm and an inner diameter of 4 mm. The average heat transfer coefficient increased with the mass flow rate. The concentration of nanoparticles had a significant influence on the dependency of the average heat transfer coefficient on the flow rate. Ma et al. [12] investigated the convective heat transfer of the Al2O3–water in a bent channel using the LBM. The results of this study show that the local and average Nusselt numbers increased with the increasing nanoparticle volume fraction, regardless of the Re and vertical passage ratio. Moreover, the effect of the nanofluid concentration on the increment of heat transfer was more remarkable at higher values of the Reynolds number. Simulations show that by increasing the Reynolds number or decreasing the vertical passage ratio, the local and average Nusselt numbers increase. Ramin et al. [13] analysed thermal and hydrodynamic characteristics of Al2O3/Cu–water hybrid nanofluid in a 3D sinusoidal double-layered microchannel heat sink. They found that the sinusoidal shape of the microchannel walls and addition of solid nanoparticle volume fraction (Al2O3/Cu) in the base fluid have a positive effect on increasing heat transfer, and the value of Nusselt number increases about 23%, 22%, 19% and 13% for Re = 50, 300, 700 and 1,200, with a nanoparticle volume fraction of 2%. Also, the results show that adding nanoparticles to the traditional fluid elevates temperature and dynamic viscosity of the base fluid. Mohebbi et al. [14] studied the forced convection heat transfer from surface mounted blocks attached to the bottom wall of a horizontal channel with the Cu–water nanofluid using the second-order LBM. The results show that heat transfer in channels can be enhanced by using the block on the walls and adding nanoparticles. There is a maximum value of 39.04% increase in the average heat transfer coefficient for the all examined cases compared to the base fluid. Lotfi et al. [15] studied the forced convective heat transfer of Al2O3–water in horizontal tubes using the two-phase Eulerian model. The results show that the rate of thermal enhancement decreases with the increase of nanoparticle volume concentration. Mahian et al. [16] studied the advantages of using nanofluids. The results show that the addition of nanoparticles and the use of smaller size nanoparticles lead to higher heat transfer improvement rates. Almohammadi et al. [17] experimentally investigated the thermal conductivity of Al2O3–water in the laminar flow regime in a circular tube. The results emphasise that the average heat transfer coefficient is improved by 27% and 20% for a volume concentration of Al2O3 equal to 1% and 0.5%, respectively, compared to the base fluid. Heris et al. [18] experimentally investigated the laminar flow convective heat transfer through a circular tube crossed with CuO–water and Al2O3–water. The obtained results show that the higher heat transfer enhancement is observed for Al2O3–water.Ruhani et al. [19]experimentally studied the new model for rheological behaviour of silica–ethylene glycol/water (30-70 vol.%) hybrid Newtonian nanofluid. The results indicate that as the volume fraction increases, the relative viscosity increases due to the greater dispersion of the nanoparticles in water. They found that when the relationship between shear stress and shear rate is linear, then the desired fluid is Newtonian. Abbasi et al. [20] investigated the blood flow in the presence of hybrid nanoparticles through a tapered complex wavy curved channel. The results show that the velocity of the blood is abated by the nanoparticle concentration and assisted in the non-uniform channel. Also, they found that the nanoparticle volume fraction and the dimensionless curvature of the channel reduce the temperature profile.

Recently, the control of nanofluid flow and forced convection heat transfer in channels is realised by the application of magnetic field. In this context, Mehrez and El Cafsi [21] studied the MHD forced convection of Al2O3–Cu/water hybrid nanofluid flow over a backward-facing step using the finite volume method. The obtained results show that the reattachment length is reduced when increasing nanoparticle volume fraction and by decreasing Reynolds number. The average Nusselt number increases by increasing volume fraction of nanoparticles and varies with the Hartmann number. Hussain and Ahmed [22] studied the MHD forced convection of Fe3O4-water in horizontal channel over a backward facing step including a rotating cylinder. The results show that the application of the electromagnetic force leads to diminution of the velocity of ferrofluid and improve the drag coefficient. Khan et al. [23] numerically investigated the impacts of Hartman number and variable thermal conductivity flow on velocity and temperature profile of Powell–Eyring fluid. The results show that the velocity profile enhances for larger magnetic parameter. Also, they found that the temperature profile decreases for increasing the Prandtl number (Pr), and enhances for increasing the value of thermal conductivity. Chu et al. [24] studied the impact of activation energy on bio-convection magnetohydrodynamic flow of third-grade fluid over a stretched subsurface. They found that the velocity field is declined when rising magnetic parameter. The thermal field and associated layer thickness is more subject to larger Brownian motion and thermophoresis parameters.

In another sense, researchers are very interested in the geometric form of the canal walls. In this context Pengand Peterson [25] experimentally studied the single-phase forced convective heat transfer and fluid flow in a microchannel with a small rectangular hot block. The obtained results show that the geometric configurations of the microchannel plate and individual microchannels have a critical effect on the single-phase convective heat transfer. The laminar and the turbulent convective heat transfer are quite different. Toghraie et al. [26] performed a 3D numerical study of convective heat transfer through a microconcentric annulus governing non-uniform heat flux boundary conditions employing water–Al2O3nanofluid. They showed that the model (when the exposing surface area is divided axially) leads to higher Nusselt numbers compared to the model when the exposing surface area is divided radially. Also, they found that the average Nusselt number is increased up to 142% and 83% when the exposing surface area is divided radially to eight parts with a Reynolds number equal to 10 and when the model when the exposing surface area is divided axially to eight parts with a Reynolds number equal to 1,000, respectively. Moraveji and Toghraie [27] studied the impacts of a number of inlets, tube length and diameter of the cold outlet on temperature and on flow rates passing in the vortex tube. Their results showed that the increase in the diameter and the length of the vortex tube have positive impacts on the passing flow rate from a cold outlet. Also, they conclude that the temperatures at both outlets decreased as the number of inlets increased, while an increase is observed as the radius of the cold outlet is increased. Togun [28] numerically investigated simulation by using the finite volume method, the CuO–nanofluid and heat transfers in a backward-facing step with and without obstacles. The obtained results show that the maximum augmentation in heat transfer was about 22% for the backward-facing step with an obstacle of 4.5 mm and using CuO nanoparticles at a Reynolds number of 225 compared to the backward-facing step without an obstacle. It is also observed that the increase in the size of the recirculation region with an increase in the height obstacle on the channel wall has a remarkable effect on thermal performance. The results also found that the pressure drop increases by an increasing Reynolds number, obstacle height and volume fractions of CuO nanoparticles. Alamyane and Mohamad [29] investigated the forced convection heat transfer in a two-dimensional channel with extended surfaces, the computed results show that the spacing between extended surfaces and their height directly affects the heat transfer process, and the Nusselt number is decreased as the spacing is increased. In addition, as the Reynolds number increases the heat transfer rate also increases. Anas and Mussa [30] studied the forced convection in a channel with a wing shaped block using the finite volume method. The obtained results revealed that the heat transfer depends on the form of the block. Two directions of the flow are studied, and the maximum value of heat transfer is detected at the case when the flow comes from the left side. Yang et al. [31] investigated forced convection in a horizontal parallel plate channel with a transverse fin located at the lower wall using the control volume method. The obtained results show that the temperature profiles exhibit a great dependence on the value of ratio of fin length to fin height. Maia et al. [32] studied the forced convective heat transfer in laminar flow of non-Newtonian fluids in ducts with an elliptical section using the generalised integral transform technique (GITT). The obtained results exhibit a strong dependence of the heat transfer parameters with the aspect ratio. Khodabandeh et al. [33] analysed the heat transfer of water nanofluid/grapheme nanoplatelet–sodium in a microchannel in the presence of sinusoidal cavities with rectangular ribs. Their results showed that this configuration of the microchannel can have a substantial increase in the Nusselt number and heat transfer. The average Nusselt number increases about 20% when the nanoparticle mass fraction is equal to 0.1% compared with the base fluid. Fanambinantsoa et al. [34] investigated the forced convection in a rectangular channel with a sinusoidal protuberance. They concluded that a change in the magnitude of the protrusion significantly affects the heat transfer. Besides, the heat transfer is more intense in the area where the vortex zones are created. Buyruk and Karabulut [35] analysed numerically (FLUENT) the heat transfer in a rectangular channel filled with air for different types of fins. The results show that the pressure drop increases when using a channel with zigzag on the lower plate compared to the flat channel. Dixit and Patil [36] experimentally investigated the heat transfer between two plates with three forms of fins such as simple fins, fins with inclined groove (V) and fins with multiple (V). The results show that the fin with inclined groove had the highest value of enhancement among all fin types. Most of the research studies cited before considered the importance of the geometric shape of the obstacle in heat transfer, and the obtained results show that the complexity of the shape of the obstacle implies a variation in the heat transfer rate.

Entropy generation is among the most important parameters in heat transfer problems [37–41], and it was found that the total entropy generation number depends on many parameters such as the volume fraction of nanoparticles, Reynolds number and Hartmann number.

In the present work, 2D numerical simulations of the MHD forced convective flow in a channel with a heat source and the partially heated walls are studied. The novelty of this work compared to the existing literature is the study involving nanoliquid forced convection with different boundary conditions (insulated–hot–insulated–hot–insulated) and the position of the hot block, which is placed inside the channel. This position is optimised based on the calculation of entropy generation. To the authors' best knowledge, this study is not undertaken in the open literature in the presence of uniform magnetic field. For this specific problem, Brownian motion is taken into account and compared with the cases without Brownian motion. Also, this study gathers many other studies dealing with the Reynolds effect, Hartman number effect, nanoparticle concentration effect, nanoparticle diameter effect and magnetic field inclination angle effect.

2. PROBLEM STATEMENT

The physical problem of the current study consists of a two-dimensional channel of length L and height H (L/H=6) crossed by Cu–water nanoliquid and containing a heat source Fig. 1.

The nanoliquid flow is driven along the channel by a constant velocity Uin and a cold temperature Tin at the inlet. Parts of the channel walls, located near the entrance, the middle and the outlet of the channel are insulated (L1=L2/2 and L2=L3=b). At the remaining parts, a uniform temperature of nanoliquid flow is equal to 1 (Tw=1). A uniform magnetic field is applied. Its orientation forms an angle γ with the horizontal plate. The nanoliquid is simulated using the single-phase model, Newtonian, laminar and incompressible. The thermo-physical properties of water and Cu nanoparticles are displayed in Tab.1.

Tab. 1. Physical properties of water and Cu nanoparticles [7] at 20°C

Physical property	Water	Cu
$\boldsymbol{Cp(J.kg^{-1}.K^{-1})}$	4181.8	383.1
$\boldsymbol{\rho(kg.m^{-3})}$	$1{,}000.52$	$8{,}954$
$\boldsymbol{k(W.m^{-1}.K^{-1})}$	0.597	386
$\boldsymbol{\beta(K^{-1})}$	21×10^{-5}	51×10^{-6}
$\boldsymbol{\sigma(\Omega.m)^{-1}}$	0.05	2.7×10^{-8}
$\boldsymbol{\mu\times10^{4}(kg/m.s)}$	8.55	-

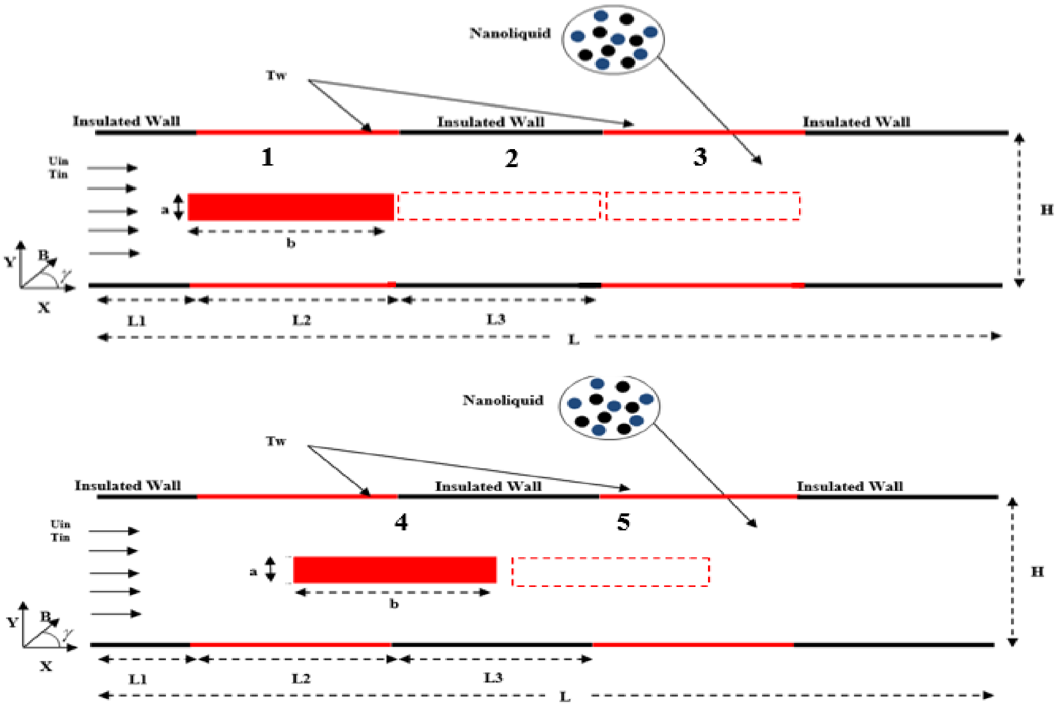

Fig. 1. Physical configuration

3. MATHEMATICAL FORMULATION AND BOUNDARY CONDITIONS

3.1. Mathematical formulation

The governing Eqs (1–4) are made dimensionless using the following variables:

$$\mathrm{X}=\frac{x}{H},\mathrm{Y}=\frac{y}{H},\mathrm{U}=\frac{u}{u_{in}},\mathrm{V}=\frac{v}{u_{in}},\mathrm{Pr}=\frac{\nu_{nl}}{\alpha_{nl}},$$

$$\theta=\frac{T-T_{in}}{T_w-T_{in}},\mathrm{Re}=\frac{u_{in}D_h}{\nu_{nl}},\mathrm{P}=\frac{p}{u_{in}^2},\mathrm{Ha}=\mathrm{H}B_0\sqrt{\frac{\sigma_{nl}}{\mu_{nl}}}$$

Accordingly, the governing equations are given as follows:

$$\frac{\partial \mathrm{U}}{\partial \mathrm{X}}+\frac{\partial V}{\partial Y}=0 \tag{1}$$

$$U\frac{\partial \mathrm{U}}{\partial \mathrm{X}}+V\frac{\partial V}{\partial Y}=-\frac{\partial P}{\partial X}+\frac{1}{Re}\left(\frac{\partial^2 \mathrm{U}}{\partial X^2}+\frac{\partial^2 \mathrm{U}}{\partial Y^2}\right)+ \frac{Ha^2}{Re}\left(V\sin(\gamma)\cos(\gamma)-U sin^2(\gamma)\right) \tag{2}$$

$$U\frac{\partial \mathrm{V}}{\partial \mathrm{X}}+V\frac{\partial \mathrm{V}}{\partial Y}=-\frac{\partial P}{\partial Y}+\frac{1}{Re}\left(\frac{\partial^2 \mathrm{V}}{\partial X^2}+\frac{\partial^2 \mathrm{V}}{\partial Y^2}\right)+ \frac{Ha^2}{Re}\left(U\sin(\gamma)\cos(\gamma)-V cos^2(\gamma)\right) \tag{3}$$

$$U\frac{\partial \theta}{\partial \mathrm{X}}+V\frac{\partial \theta}{\partial Y}=\frac{1}{Pr.Re}\left(\frac{\partial^2 \theta}{\partial X^2}+\frac{\partial^2 \theta}{\partial Y^2}\right) \tag{4}$$

4. BOUNDARY CONDITIONS

At the inlet of channel,

$$\mathrm{U}=1;\mathrm{V}=0;\theta=0 \tag{5}$$

At the outlet of channel,

$$\frac{\partial \mathrm{U}}{\partial \mathrm{x}}=\frac{\partial \mathrm{V}}{\partial \mathrm{x}}=0 \tag{6}$$

$$\frac{\partial \theta}{\partial \mathrm{x}}=0 \tag{7}$$

At the hot block,

$$\mathrm{U}=0;\mathrm{V}=0;\theta=1 \tag{8}$$

5. NUMERICAL PROCEDURE

5.1. Solution method

The LBM has been successfully used in various classic and emerging scientific and engineering fields [29, 41, 48]. LBM has several advantages over other conventional CFD methods, especially in dealing with complex boundaries, incorporating microscopic interactions and parallelisation of the algorithm. A different interpretation of the lattice Boltzmann equation (LBE) is that of a discrete-velocity Boltzmann equation. The numerical methods for the solution of partial differential equations give rise to a discrete map, which can be interpreted as the propagation and collision of fictitious particles. To simulate flow and heat transfer in a two-dimensional channel, the LBM is used with the D2Q9 model Fig. 2 (a) for the dynamic field and with the D2Q4 for the thermal field Fig. 2 (b), and the selected grid size is uniform ($\Delta x=\Delta y=1$).

The LBE with an external term force is solved using the BGK approximation. Consequently, the obtained LBE with a single relation time is written as follows:

$$f_k(x+c_k\Delta t,t+\Delta t)= f_k(x,t)+\frac{\Delta t}{\tau}\left[f_k^{eq}(x,t)-f_k(x,t)\right]+\Delta t F_k \tag{9}$$

where $\Delta t, \tau, c_k, F_k and f_k^{eq}$ denote, respectively, the lattice time step, relaxation time, discrete lattice velocity in direction (i), external force in the direction of lattice velocity and the equilibrium distribution function.

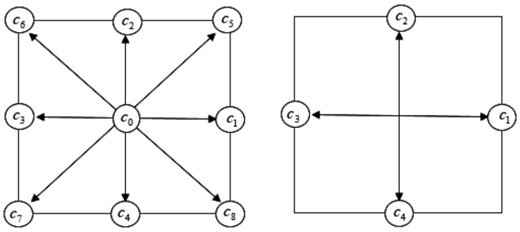

(a) (b)

Fig. 2. D2Q9- D2Q4 models: for the velocity field (a) and for temperature field (b)

5.2. LBE for dynamic and thermal fields

For the dynamic field,

$$f_k(x + c_k\Delta t, t + \Delta t) = f_k(x,t) + \frac{\Delta t}{\tau_v}\left[f_k^{eq}(x,t) - f_k(x,t)\right] + \Delta t c_k F_k \tag{10}$$

For the temperature field,

$$g_k(x + c_k\Delta t, t + \Delta t) = g_k(x,t) + \frac{\Delta t}{\tau_g}\left[g_k^{eq}(x,t) - g_k(x,t)\right] \tag{11}$$

where $\tau_v$and$\tau_g$are the relaxation times for the flow and temperature fields, and$f_k^{eq}$and g_k^{eq} are the equilibrium distribution functions given for the D2Q9-D2Q4 models, respectively,which are given as follows:

$$f_k^{eq} = \rho\omega_k\left[1 + 3\frac{c_k.u_i}{c^2} + \frac{9(c_k.u_i)^2}{2c^4} - \frac{3u_i^2}{2c^2}\right] \tag{12}$$

$$g_k^{eq} = 0.25\theta[1 + 2c_k.u_i] \tag{13}$$

For the D2Q9, the weighting factors and the discrete particle velocity vectors are defined as follows:

$$\begin{pmatrix}\omega_k\\ c_{k,x}\\ c_{k,y}\end{pmatrix} = \begin{pmatrix}\frac{4}{9},\frac{1}{9},\frac{1}{9},\frac{1}{9},\frac{1}{9},\frac{1}{36},\frac{1}{36},\frac{1}{36},\frac{1}{36}\\ 0,1,0,-1,0,1,-1,-1,1\\ 0,0,1,0,-1,1,1,-1,-1\end{pmatrix}$$

The macroscopic quantities are calculated by the following equations:

$$\rho(x,y) = \sum_{k=0-8} f_k \tag{14}$$

$$\rho u(x,t) = \sum_{k=0-8} f_k c_k + \Delta t F \tag{15}$$

$$\theta = \sum_{k=0-4} g_k \tag{16}$$

5.3. LB boundary condition treatment

One of the important and crucial issues in LBM simulation of flow and temperature is accurate modelling of the boundary conditions.

5.3.1. Hydrodynamic boundary conditions

At the inlet, the unknown distribution functions are calculated using the boundary condition proposed by Zou and He[42] as follows:

$$\rho_{in} = \frac{f_0 + f_1 + f_2 + f_4 + 2(f_3 + f_6 + f_7)}{1 - u_{in}} \tag{17}$$

$$f_1 = f_3 + \frac{2}{3}\rho u_{in} \tag{18}$$

$$f_5 = f_7 + \frac{1}{2}(f_4 - f_2) + \frac{1}{6}\rho u_{inlet} \tag{19}$$

$$f_8 = f_6 + \frac{1}{2}(f_4 - f_2) + \frac{1}{6}\rho u_{inlet} \tag{20}$$

At the outlet, a second-order extrapolation scheme is used by Mohamad [43]:

$$f_3(n,j) = 2 \times f_3(n-1,j) - f_3(n-2,j) \tag{21}$$

$$f_6(n,j) = 2 \times f_6(n-1,j) - f_6(n-2,j) \tag{22}$$

$$f_7(n,j) = 2 \times f_7(n-1,j) - f_7(n-2,j) \tag{23}$$

The bounce-back boundary condition is applied on all solid boundaries. For instance, for the top boundary, the following conditions are imposed:

$$f_4(i,m) = f_2(i,m) \tag{24}$$

$$f_7(i,m) = f_5(i,m) \tag{25}$$

$$f_8(i,m) = f_6(i,m) \tag{26}$$

5.3.2. Thermal boundary conditions

At the inlet,

$$g_1 = \theta\big(\omega(1) + \omega(3)\big) - g_3 \tag{27}$$

$$g_5 = \theta\big(\omega(5) + \omega(7)\big) - g_7 \tag{28}$$

$$g_8 = \theta\big(\omega(8) + \omega(6)\big) - g_6 \tag{29}$$

At the outlet,

$$g_3(n,j) = 2 \times g_3(n-1,j) - g_3(n-2,j) \tag{30}$$

$$g_6(n,j) = 2 \times g_6(n-1,j) - g_6(n-2,j) \tag{31}$$

$$g_7(n,j) = 2 \times g_7(n-1,j) - g_7(n-2,j) \tag{32}$$

At the insulated part of the walls, the bounce-back boundary condition (adiabatic) is used on the north and the south boundaries. For instance, for the top boundary, the following conditions are imposed:

$$g_4(i,m) = g_4(i,m-1) \tag{33}$$

$$g_7(i,m) = g_7(i,m-1) \tag{34}$$

$$g_8(i,m) = g_8(i,m-1) \tag{35}$$

At the heated part of the walls, the temperature is known, θ=1, for instance, for the top wall, and the following conditions are imposed:

$$g_4 = \theta\big(\omega(4) + \omega(2)\big) - g_2(i,m) \tag{36}$$

$$g_7 = \theta\big(\omega(7) + \omega(5)\big) - g_5(i,m) \tag{37}$$

$$g_8 = \theta\big(\omega(8) + \omega(6)\big) - g_6(i,m) \tag{38}$$

5.4. Nanoliquid property calculation

The terms$(\rho Cp)_{nl}, \rho_{nl}, \alpha_{nl}$, the heat capacitance, nanoliquid density and the thermal diffusivity are approximated as follows [39]:

$$(\rho Cp)_{nl} = (1-\phi)(\rho Cp)_l + \phi(\rho Cp)_p \tag{39}$$

$$\rho_{nl} = (1-\phi)\rho_l + \phi\rho_p \tag{40}$$

$$\alpha_{nl} = k_{nl}/(\rho Cp)_{nl} \tag{41}$$

Thermal conductivity is given by Koo and Kleinstreuer [45]:

$$k_{nl} = k_{static} + k_{Browinan} \tag{42}$$

where the static thermal conductivity is based on the Maxwell classical equation:

$$k_{static} = k_l \frac{k_p + 2k_l - 2\phi(k_l - k_p)}{k_p + 2k_l + \phi(k_l - k_p)} \tag{43}$$

The thermal conductivity is due to the enhanced thermal conductivity by micro-scale convective heat transfer of a particle's Brownian motion:

$$k_{Brownian} = 5 \times 10^4 \beta\phi\rho_l Cp_l \sqrt{\frac{k_b T}{\rho_p \mathrm{d_p}}} f(T,\phi) \tag{44}$$

where β and f are two functions that combine the interaction between nanoparticles:

$$\beta = 0.0137(100\phi)^{-0.8229} for \phi < 1\% \tag{45}$$

$$\beta = 0.0011(100\phi)^{-0.7272} for \phi > 1\% \tag{46}$$

$$f(T,\phi) = (-6.04\phi + 0.4705)T + (1.7223\phi - 134.63) for 1\% \le f \le 4\% \tag{47}$$

This equation is valid for temperatures in the range of$300K \le T \le 325K.$

The effective viscosity of the nanoliquid is given by Koo and Kleinstreuer as [44, 45]:

$$\mu_{eff} = \mu_{static} + \mu_{Brawnian} \tag{48}$$

where μ_{static} is the static viscosity of the nanoliquid and $\mu_{Brownian}$ is the effective viscosity due to Brownian motion:

$$\mu_{static} = \frac{\mu_l}{(1-\phi)^{2.5}} \tag{49}$$

$$\mu_{Brownian} = 5 \times 10^4 \beta\phi\rho_l \sqrt{\frac{k_b T}{\rho_p \mathrm{d}_p}} f(T,\phi) \tag{50}$$

The electrical conductivity of the nanoliquid is giving by Maxwell's model:

$$\sigma_{nl} = \sigma_l \left[1 + \frac{3(\sigma_s/\sigma_l - 1)\phi}{(\sigma_s/\sigma_s + 2) - (\sigma_s/\sigma_l - 1)\phi}\right] \tag{51}$$

5.5. Physical quantities of interest

5.5.1. Nusselt number

The convective heat transfer is described using the local and average Nusselt number along the hot wall, and the local Nusselt number is expressed as follows:

$$Nu = -\frac{k_{nl}}{k_l}\left(\frac{\partial\theta}{\partial Y}\right)\Big|_{Y=0} \tag{52}$$

The average Nusselt number is expressed as follows:

$$Nu_{avg} = \frac{1}{L}\int_0^L Nu\, dX \tag{53}$$

where L is the channel length.

5.5.2. Entropy generation:

The local dimensionless entropy generation is the result of the sum of the irreversible heat transfer, fluid friction and magnetic field [46]:

$$S_{gen} = S_{gen,h} + S_{gen,v} + S_{gen,M} \tag{54}$$

The first term relative to the heat transfer irreversibility is as follows:

$$S_{gen,h} = \frac{k_{nl}}{k_l}\left[\left(\frac{\partial\theta}{\partial X}\right)^2 + \left(\frac{\partial\theta}{\partial Y}\right)^2\right] \tag{55}$$

The second term corresponding to the fluid friction irreversibility is as follows:

$$S_{gen,v} = \chi\frac{\mu_{nl}}{\mu_l}\left\{2\left[\left(\frac{\partial U}{\partial X}\right)^2 + \left(\frac{\partial V}{\partial Y}\right)^2\right] + \left[\left(\frac{\partial U}{\partial Y}\right) + \left(\frac{\partial V}{\partial X}\right)\right]^2\right\} \tag{56}$$

The last term associated with the magnetic field irreversibility is as follows:

$$S_{gen,M} = \chi \times Ha^2 \times \left[(1-\phi) + \phi\frac{\rho_s}{\rho_l}\right] \times [U\sin(\gamma) - V\cos(\gamma)]^2 \tag{57}$$

where χrepresents the irreversibility factor and is given by [45]:

$$\chi = \frac{\mu_l T_{in} U_{in}^2}{k_l (T_w - T_{in})^2} \tag{58}$$

The Bejan number (Be), which is important while discussing the entropy generation, is defined as the ratio of entropy generations due to heat transfer and total entropy generation:

$$Be_{Local} = \frac{S_{gen,h}}{S_{gen}} \tag{59}$$

The total entropy generation, S_{gen}, and the Bejan number, Be, are calculated by the integration over the whole domain Ω as follows:

$$S_{gen} = \iint_\Omega S_{gen} dXdY and Be = \iint_\Omega Be_{local} dXdY \tag{60}$$

DOI 10.2478/ama-2022-0050

6. GRID INDEPENDENCE TEST AND CODE VALIDATION

The grid sensitivity is tested to let our code giving accurate independent solution. Tab. 2 shows the effect of grid size on the Nuavg through the two-dimensional channel. The grid node 60x360 is the appropriate and is selected for the next computations.

The case of two-dimensional heated channel crossed with cold air (Pr=0.71) was taken as a benchmark test in order to ensure that the obtained results are reliable. The channel was heated from its top and bottom walls.

Tab. 2. Dependence of Nu_{avg} on mesh resolution for Re = 150 and ϕ= 0.02

Mesh	30 x 180	60 x 360	90 x 540	120 x 720
Nu_{avg}	12.32	11.65	11.73	11.97

First, the velocity profiles at different sections of the channel are compared with those obtained by [37-47-48](Fig. 3) (a). Second, the velocity profile are compared to the analytical solution for the fully developed flow between two parallel plates Fig. 3 (b). Results show a good agreement for the two cases. We conclude that the results of Fortran code calculations are acceptable.

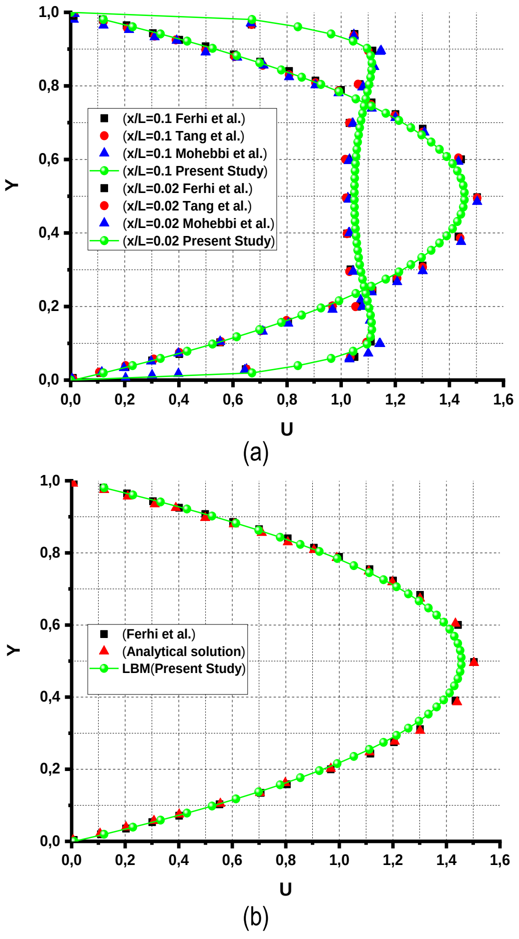

(a)

(b)

Fig. 3. Comparison of the velocity profiles at different channel sections with literature findings (a) and analytical solution (b)

7. RESULTS AND DISCUSIONS

In the following sections, a numerical investigation has been carried out to appraise the effects of emerging parameters on the MHD hydrodynamic and thermal characteristics and entropy generation inside a channel crossed by Cu–water nanoliquid with a constant velocity and driven by a cold temperature at the inlet containing a heat source. Particular efforts have been focused on the effects of key parameters such as Reynolds number (Re =50–200), nanoparticle volume fraction ($\phi = 1\% - 4\%$), nanoparticle diameter (dp=5–45nm), Hartmann number (Ha =0–90) and the magnetic field inclination angle ($\gamma = 0 - \pi$), on the convective nanoliquid flow, heat transfer and the second law analysis inside the studied configuration. The Brownian motion is taken into consideration via the theoretical models of Koo and Kleinstreur (43) for nanoliquid thermal conductivity and dynamic viscosity. In this study, the case in which the heat source is placed in the middle of the channel (case 2) is adopted, due to the maximum value of the average Nusselt number detected in this position of the block.

7.1. Heat source position effects

Fig. 4 presents the variation of the heat transfer as a function of the heat source position. It is seen that the heat transfer, which is described by the average Nusselt number, is minimum when the heat source is placed near the insulated wall. In this position, the heat exchange is produced only between the heat source and the nanoliquid. The heat exchange is remarkable when the heated block is placed near the active walls. The heat transfer is transferred by convection between the heat source and the walls of the channel by means of the nanoliquid. Besides, the nanoliquid is rapidly heated by the heat source and the walls.

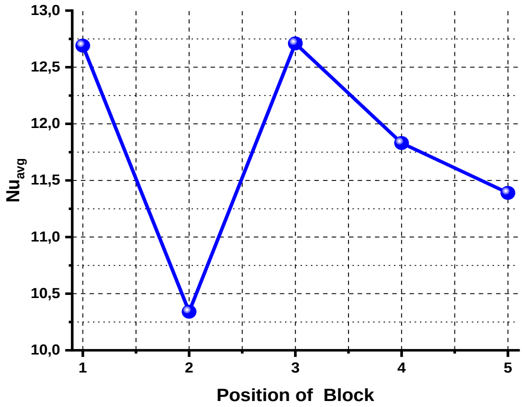

Fig. 4. Variation of average Nusselt number for different positions of the heated obstacle

7.2. Nanoparticle volume fraction effects

Fig. 5 shows the effect of the copper nanoparticle volume fraction on the heat transfer (a), Sgen (b) and Be (c) for different Re numbers at Ha=50, dp=25nm and$\gamma = 0$. It is seen clearly that the increase in ϕ leads to enhance the heat transfer in the bottom wall. Besides, the addition of nanoparticles to the base fluid causes the augmentation of the thermal conductivity in the channel consequently the heat transfer increases Fig. 5 (a).

The impact of the nanoparticle volume fraction on the entropy generation for different Re numbers is depicted in Fig. 5 (b). The enhancement of heat transfer increases the total entropy generation in the channel. Besides, as ϕ increases, the heat transfer and the viscosity of the mixture in the medium increase, this led to improve the heat transfer and the fluid friction irreversibility. The evolution of the Be number versus the nanoparticle volume fraction is illustrated in Fig. 5 (c). The Be number increases as ϕ increases. This result indicated that the convective mode is dominant. It can be concluded that the profiles of Nuavg, Sgen and Be increase, and these performances are due to enhancing the thermal conductivity of nanoliquid.

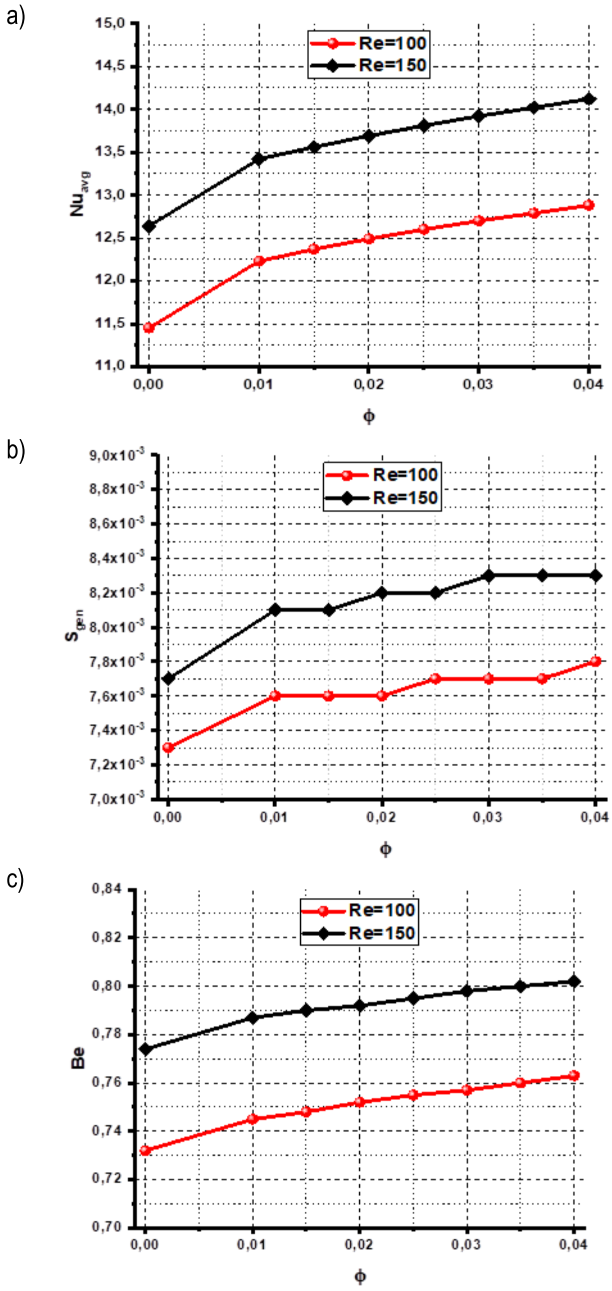

Fig. 5. Variations of the Nu_{avg}; a) S_{gen}; b) and Be; c) as a function of nanoparticles volume fraction for different Re numbers for Ha = 50, dp = 25 nm and γ = 0

7.3. Nanoparticle size effects

Fig. 6 describes the influence of nanoparticle diameter on Nuavg (a), Sgen (b) and Be (c) for different nanoparticle volume fraction at Re =150, Ha=50 and $\gamma = 0$. It is clear that the augmentation of the nanoparticle diameter leads to a decrease in the heat transfer, the entropy generation and the Bejan number in the entire of the channel. We noticed that the curve can be divided into two zones: in the first zone (5nm<dp<35nm), the calculated parameters (Nuavg, Sgen and Be) are decreasing and degrade rapidly, but in the second zone (dp>35nm), the curve tends towards stabilisation. In case of nanoliquid, decreasing dp leads to a higher heat transfer rate as a result of a higher heat transfer surface area (contact area between particles and liquid), aggregation of nanoparticles and more intensified Brownian motion, causing higher thermal conductivity of the nanoliquid. At a fixed volume fraction and decreasing dp, the particle number increases, which augments the total surface and therefore contributes to the rise of nanoliquid thermal conductivity.

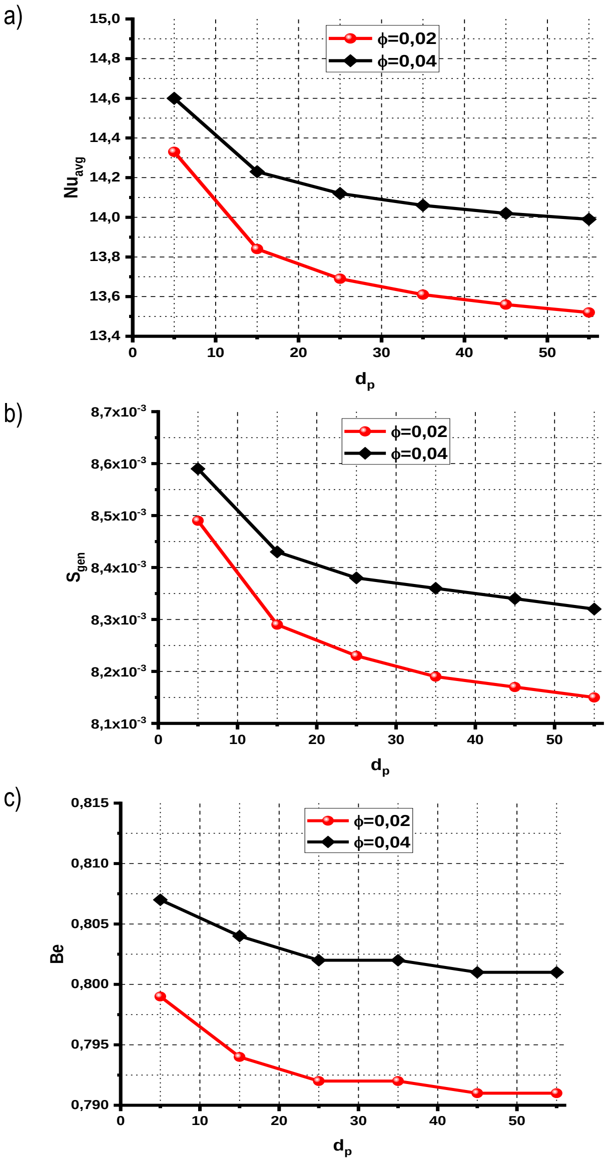

Fig. 6. Variations of the Nu_{avg}; a) S_{gen}; b) and Be; c) as a function of nanoparticle diameter for Re = 150, Ha = 50 and γ = 0

7.4. Reynolds number effects

Fig. 7 illustrates the effects of Re numbers on the streamlines (left) and isotherms (right) for$\phi = 2\%$, dp=25 nm and Ha=50. As Re increases, a recirculation zone appears behind the heat source Fig. 7 (left). The size and shape of this zone depend on the shape of the obstacle and the Reynolds number.

Fig. 7 (left) presents the streamlines, and the increase in the Reynolds number has a direct influence on the streamlines, and the lines are more compact when the Reynolds numbers increase, and this is due to the enhancement of the inertial force. This can be clearly seen in the velocity profile illustrated in Fig. 8.

Fig. 7 (right) presents the distribution of the isotherms in the nanoliquid. The figure indicates that the evolutionary temperature contours break down when the Re number of nanoliquid is increased, and this due to reduction of the boundary layer. The convection mechanism becomes stronger and isotherms are distorted, so temperature gradient near the hot surface augments.

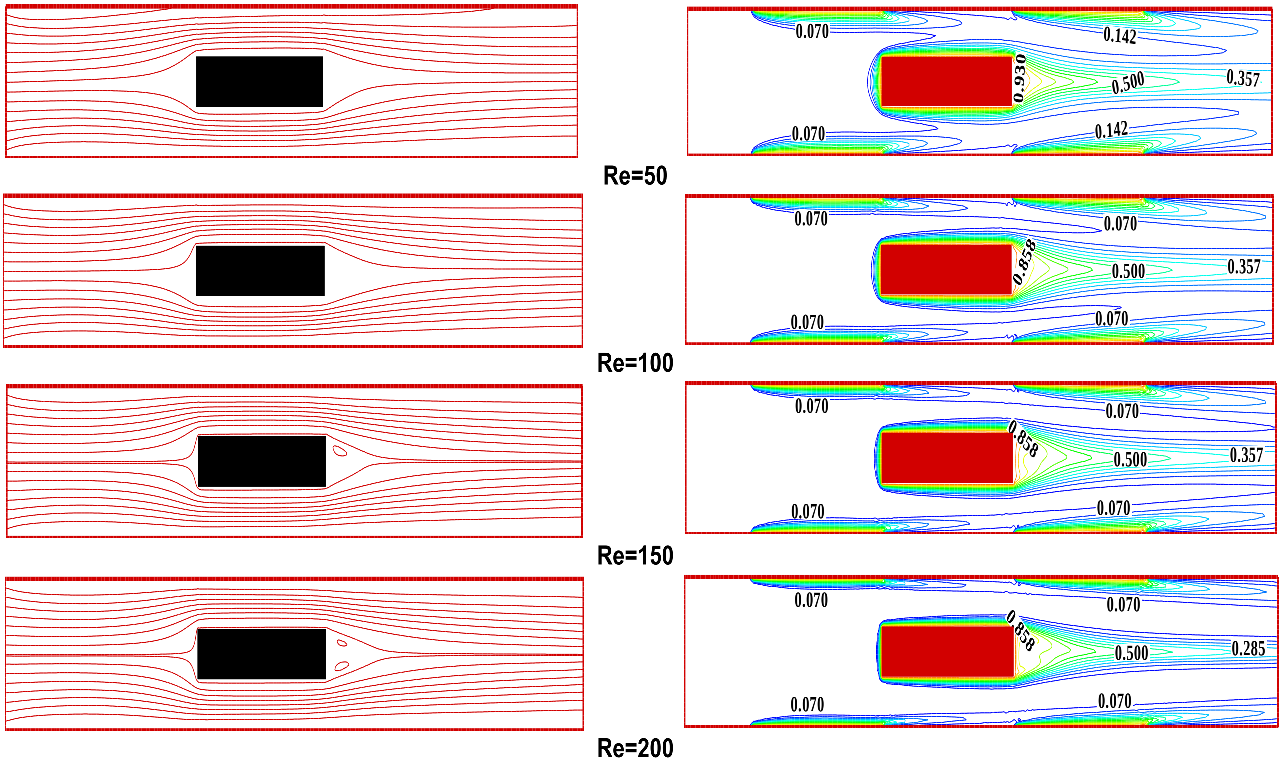

Fig. 7. Streamlines (left) and isotherms (right) for different Reynolds numbers at $\phi = 0.02$, Ha = 50 and γ = 0

Fig. 8 shows the variation of Nuavg (a), Sgen (b) and Be (c) as a function of Reynolds numbers. The augmentation of Re numbers causes to increase the average Nusselt number, and consequently, the curve of total entropy generation and the Bejan number of the nanoliquid increase.

In Fig. 8 (a), the Nuavg enhances by 20% when Re numbers increase from 50 to 190. The heat transfer of nanoliquid increases linearly as a function of Re. As a result, the heat transfer due to the convective mode is dominated.

Fig. 8 (b) depicts the evolution of the total entropy generation as a function of Reynolds numbers. It is shown from the figure that at a low Reynolds number, the total entropy generation decreases, and the minimum value of the total entropy generation is detected for Re=80 equal to $S_{gen} = 7.55 \times 10^{-3}$. This decrease of the curve is caused by the passage of the flow between two cold walls, and also because of the decrease of the first term of equation (54). For $Re > 80$, the heat transfer due to the convective mode dominates. There is an increase in the velocity of the nanoliquid and, by consequence; the second term of Eq. (54) dominates the other term of the equation, which indicates a linear increase in the curve of the total entropy generation as a function of the Reynolds number.

The impact of Reynolds numbers on the Bejan number is illustrated in Fig. 8 (c). It is found that the curve of the Bejan number as a function of the Reynolds number tends towards stability. This result is due to augmentation of the term relative to heat transfer irreversibility.

Comparing nanoliquid with $\phi = 0.04$ to the nanoliquid with$\phi = 0.02$, it shows that when adding low-volume fractions of nanoparticles and/or increasing Reynolds number causes higher frictional entropy generation. The addition of low-volume fractions of nanoparticles intensifies the hydrodynamic inter-particle interactions, causing a higher viscosity of the nanoliquid. This result is due to higher thermal conductivity of nanoparticles. Based on Eq. (55), the thermal entropy generation is related to temperature gradients. By increasing the nanoparticle volume fraction, the nanoliquid viscosity increases, which makes conventionalliquid molecules slower and creates a smoother temperature profile by stabilising the flow field.

Fig. 9 describes the variation of the velocity profiles along the vertical centreline (a) and the horizontal velocity (b) for different Reynolds numbers (Re=50,100,150), Ha=50 and γ=0. The figure reveals that the rise in Re reduces the velocity in the regions between the walls and the heat source. Fig. 9 (a). The curve is divided into three sections: one is linear, and the other are two parabolic and symmetric sections. The increase in the Reynolds number gives results in a decrease in the amplitude of the vertical velocity profile (direction Y), and on the other hand, the amplitude of the horizontal velocity profile (direction X) increases.

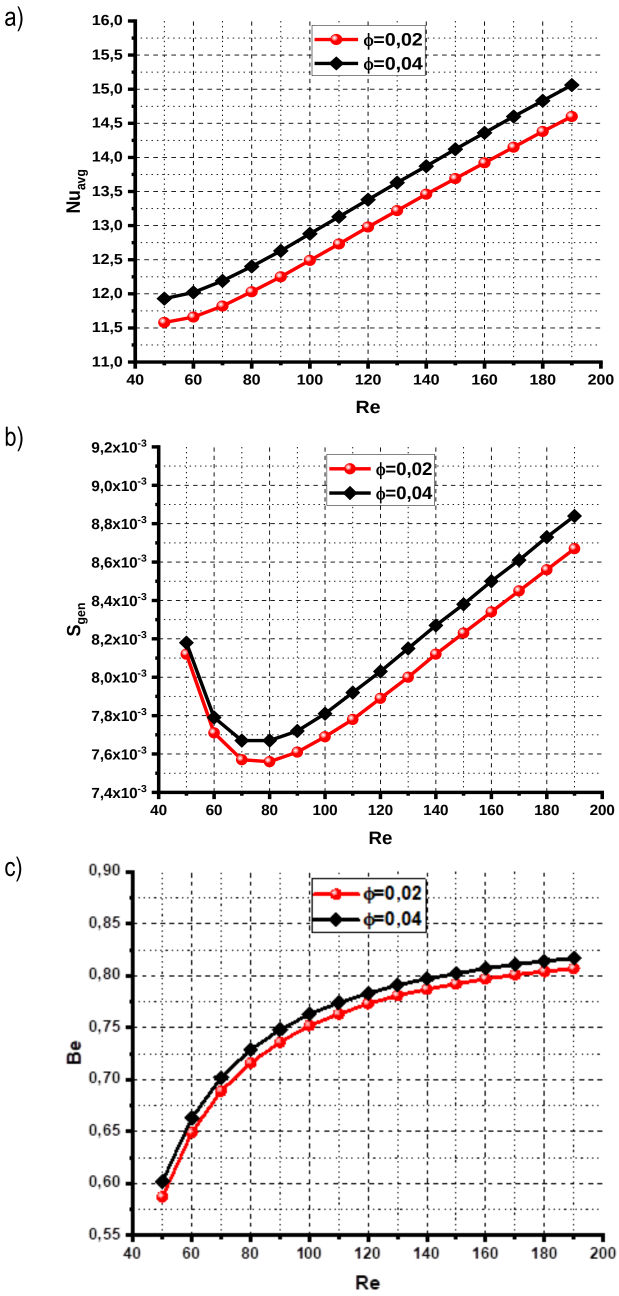

Fig. 8. Variations of the Nu$_{avg}$; a) S$_{gen}$; b) and Be; c) as a function of Re numbers for Ha = 50 and γ = 0

The profile of the dimensionless horizontal velocity of the nanoliquid along the channel centreline for different Reynolds numbers (Re=50,100,150), Ha=50 and $\gamma = 0$ is depicted in Fig. 9 (b). Four zones are in this curve: in the first zone $(0 \leq X \leq 0.33)$as Re numbers increase, the velocity component and the amplitude of the velocity component for the nanoliquid increase, and the minimum value of velocity increases about 38.7% when the number of Reynolds increases from 50 to 150. For this zone, the velocity profile is slightly increased; this is due to the passage of the nanoliquid between two cold walls when the slip velocity increment of the nanoliquid velocity on boundaries. To conclude, the impact of inertial forces dominates in this zone.

In the second zone$(0.33 < X < 0.55)$, the velocity profile is equal to zero because of the presence of the obstacle in the middle of the channel.

The third zone $(0.55 \leq X \leq 0.61)$ when the recirculation zone is obtained, as Re number decreases, the amplitude of the velocity profile for nanoliquid increases. In this zone, the sign of the velocity component changes from positive to negative, and the minimum value of velocity increases by 59.3% when the number of Reynolds increases from 50 to 150. The inertial forces decrease, and the impact of viscous forces is presented.

The last zone$(0.61 < X \leq 1)$ and for the height Reynolds number, the minimum value of velocity increases about 99.98% when the number of Reynolds increases from 50 to 150. This is due to the heat recirculation zone formed behind the block, and it is responsible for changing the sign of the velocity. In this zone, the heat transfer due to the conductive mode dominates.

We noticed that the velocity profile depends on the number of Reynolds, in both zones after and before the position of the obstacle. As the first zone, the velocity profile is slightly increased, which is due to the domination of conductive mode. On the other side and after the position of the recirculation zone, the velocity profile of the nanoliquid increases rapidly in the same distance, this is due to the passage of flow between the hot walls and the contact with the outside surface of the hot obstacle. So the boundary condition plays a very important role in increasing or decreasing the flow rate of nanoliquids; therefore, the viscous force directly depends on the limiting condition imposed on the walls of the channel.

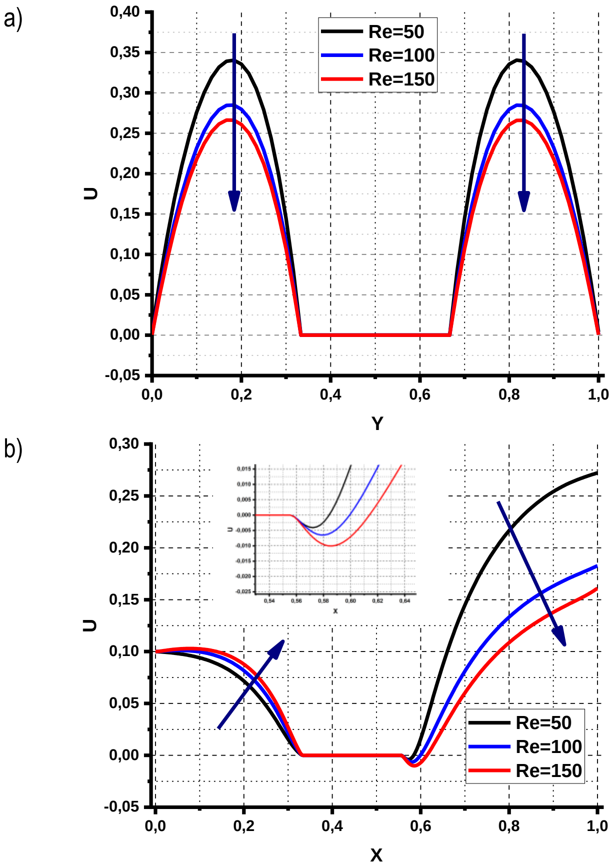

Fig. 9. U(0.5, Y); a) U(X, 0.5); b) and θ(X, 0.5) for different Reynolds numbers at Ha = 50 and γ = 0

7.5. Effect of Hartmann number

Fig. 10 presents the evolution of Nuavg (a), Sgen (b) and Be (c) as a function of Hartmann number for two Re numbers (100 and 150). It is seen that heat transfer is enhanced by increasing Ha for all values of Re number. Fig. 10 (a). For example, for a Reynolds number equal to 100, the inertia force deepens by the heightening of the magnetic field. This fact increases the convective heat transfer mode.

The impact of magnetic field intensity on the Sgen and Be number is depicted in Fig. 10 (b) and (c). It is clear that the total entropy generation increases as the Ha number increases. In this curve, we have detected an intersection, and this intersection can be interpreted by the presence of the recirculation zone, and it has been detected when Re is greater than 100, and this zone has an opposite effect to the Reynolds number.

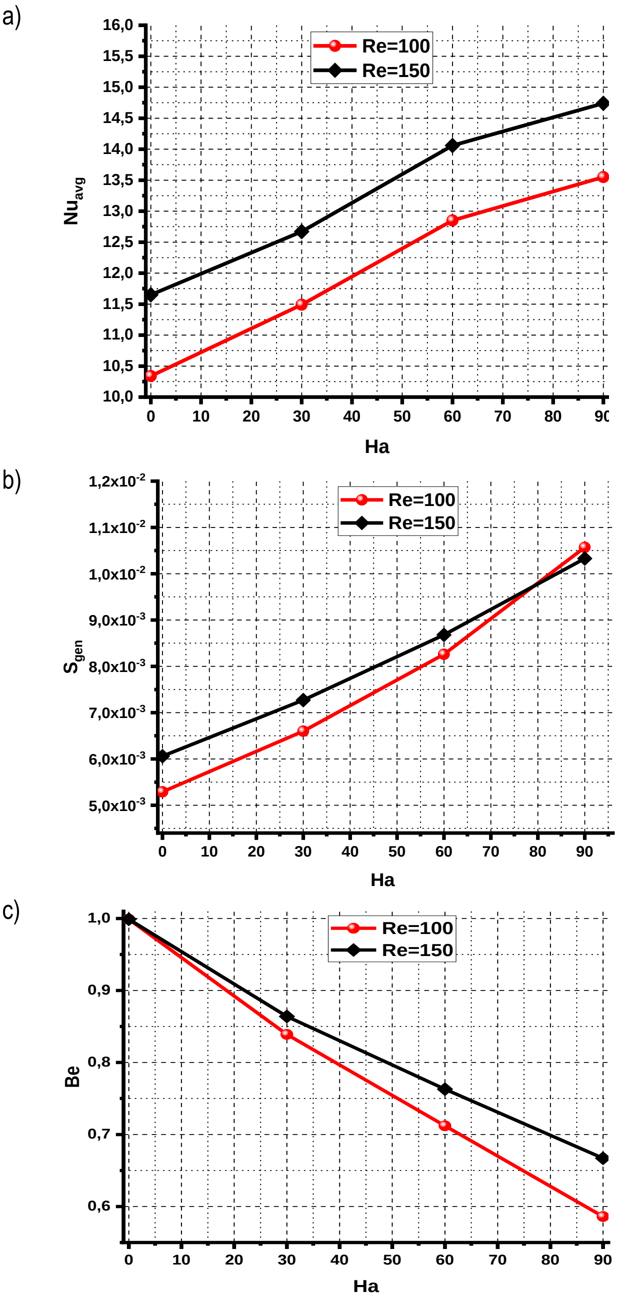

Fig. 10. Variations of the average Nusselt number; a) S_{gen} ;b) and Be; c) as a function of Ha numbers for $\phi = 2\%$ and γ = 0

Fig. 10 (c) depicts the variation of the Be number in the function of Hartmann number, and it shows that the mode of heat transfer changes from conduction to convection. Besides, the Be is reduced by 41.4% for Re=100, while the Be is reduced by about 33.3% for Re= 150. This happens when the Ha increases from 0 to 90. This is due to augmentation of the term relative to the heat transfer irreversibility Eq. (55).

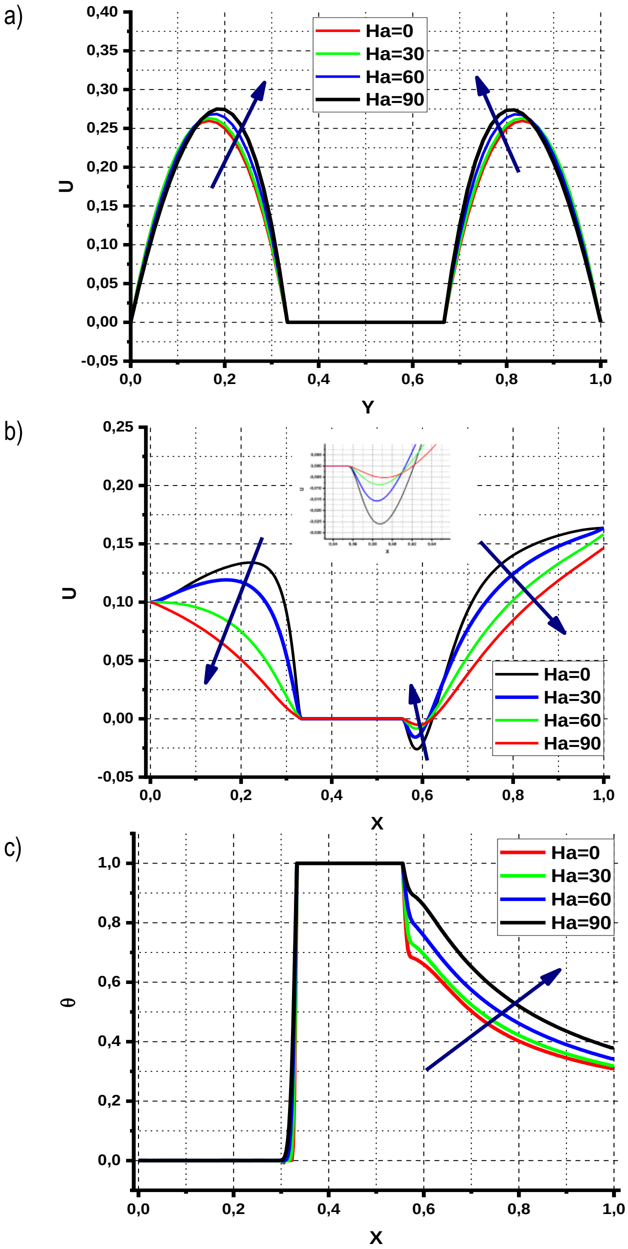

Fig. 11. U(0.5, Y); a) U(X, 0.5); b) and θ(X, 0.5); c) for different Ha numbers at Re = 150, $\phi = 0.02$, dp = 25 nm and γ = 0

Fig. 11 describes the variation of the velocity profiles along the vertical centreline (a), the horizontal velocity (b) and the temperature profile in the X direction for Ha=0,30,60,90 and Re=150. It shows that the flow is fully developed with two parabolic profiles. It is noted that the Ha number causes an improvement of the velocity in the zone between the heat source and the channel walls. Fig. 11 (a). When increasing the Hartmann number, a positive effect of electromagnetic force is shown, so the amplitude of vertical velocity increases.

Fig. 11 (b) illustrates the dimensionless horizontal velocity profiles in the X direction for different values of Hartmann number (Ha=0, 30, 60 and 90), and it shows that the velocity profile is maximum when Ha=0. Four zones in this curve are shown, and the first zone is situated between $(0 \leq X \leq 0.33)$. The amplitude of the velocity profile of nanoliquid decreases when the Ha number increases, and the maximum value of the velocity profile decreases almost 74.43% when the Hartmann number increases from 0 to 90. This is due to the improvement of the term source term described in Eqs (2) and (3). In this zone, the electromagnetic force is dominant.

In the second zone$(0.33 < X < 0.55)$, the velocity profile is equal to zero due to the presence of the obstacle in the middle of the channel. In the third zone $(0.55 \leq X \leq 0.61)$, a recirculation zone is obtained, and behind the heat source, we can detect that the amplitude of the velocity profile increases. The maximum value of the velocity profile increases about 20% when the Hartmann number increases from 0 to 90. In this zone, the viscous force is dominant. For the last zone $(0.61 < X \leq 1)$, the amplitude of velocity profile decreases with an increasing Ha; at the same time, the horizontal velocity profile increases. The maximum value of the velocity profile decreases almost 89.57% when the Hartmann number increases from 0 to 90. This can be explained by the domination of the conduction heat transfer mode and the effect of Lorentz force. Fig. 11 (c) describes the variation of the temperature profiles along the horizontal direction for different Hartmann numbers. This figure shows that for all values of the Hartmann number, the temperature profile of the nanoliquid in the channel increases in the zone behind the heat source. The augmentation of Hartmann number (from 0 to 90) gives a positive effect on the amplitude of the temperature profile. As a result, the enhancement of Hartmann number gives a diminution of the convective heat transfer mode and augmentation of the conductive heat transfer mode.

7.6. Effect of magnetic field inclination angle

Fig. 12 shows the effect of magnetic field inclination angle on the Nuavg (left) and Sgen (right) for Ha=50, Re=150 and $\phi = 0.02$. In Fig. 12 (a), the average Nusselt number varies with different values ofγ. Besides, the heat transfer is maximum for$(\gamma = 0, \pi/3, 2\pi/3, \pi)$. The result indicates a diminution in the Nuavg about 5.65% when the magnetic field inclination angle changes from inclination $(\gamma = 0)$ to$(\gamma = \pi/2)$.This can be explained by the existence of magnetic force in the term of volume forces.

Fig. 12 (b) presents the influence of the magnetic field inclination angle on the total entropy generation for Re=100 and 150. The total entropy generation varies with the magnetic field inclination angle(γ). The main responsibility of this evaluation is the increase in the term due to the magnetic field irreversibility. Also, when increasing the angle of inclination $(\gamma = \pi/2)$,the vertical velocity of the flow is increased, and the maximum value of total entropy generation is detected. On the other hand, when the angle of inclination is equal to zero$(\gamma = 0)$, the horizontal velocity is increased, and we can detect the minimum value of the total entropy generation.

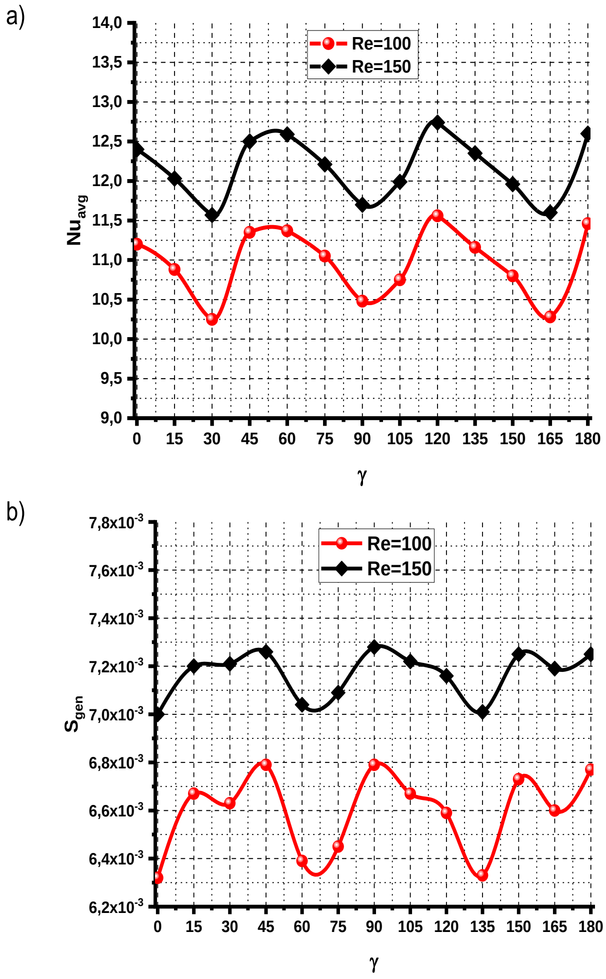

Fig. 12. Variations of the Nu_{avg}(left) and S_{gen} (right) versus the magnetic inclination angle for Ha = 50, Re = 150 and $\phi = 0.02$

7.7. Effect of Brownian motion

Fig. 13 illustrates the impact of the Brownian motion on the Nuavg (a), Sgen (b) and Be (c) for Re=150, Ha=50 and$\gamma = 0$. The results show that the average Nusselt number is an increasing function of nanoparticle volume fraction. Fig. 13 (a). As ϕincreases, the heat transfer becomes very important for the case with Brownian motion. Besides, this improvement can be explained by the high thermal conductivity of the mixture in the nanoliquid. The heat transfer is enhanced by 10% for the two cases for $1\% \leq \phi \leq 4\%$. The collision between the particles causes an increase in Brownian diffusivity. Therefore, the Brownian motion increases in nanoliquid, which gives an increase in the Nuavg.

Fig. 13 (b) and (c) illustrate the impact of the Brownian motion on the total entropy generation and Bejan number, respectively. The results show that the

The curves in Fig. 13 (b) and (c) shows that the variations of total entropy generation and the curve of the Bejan number are similar to the curve of the average Nusselt number. A great part of the Sgen is due to the increasing heat transfer by the Re increase.

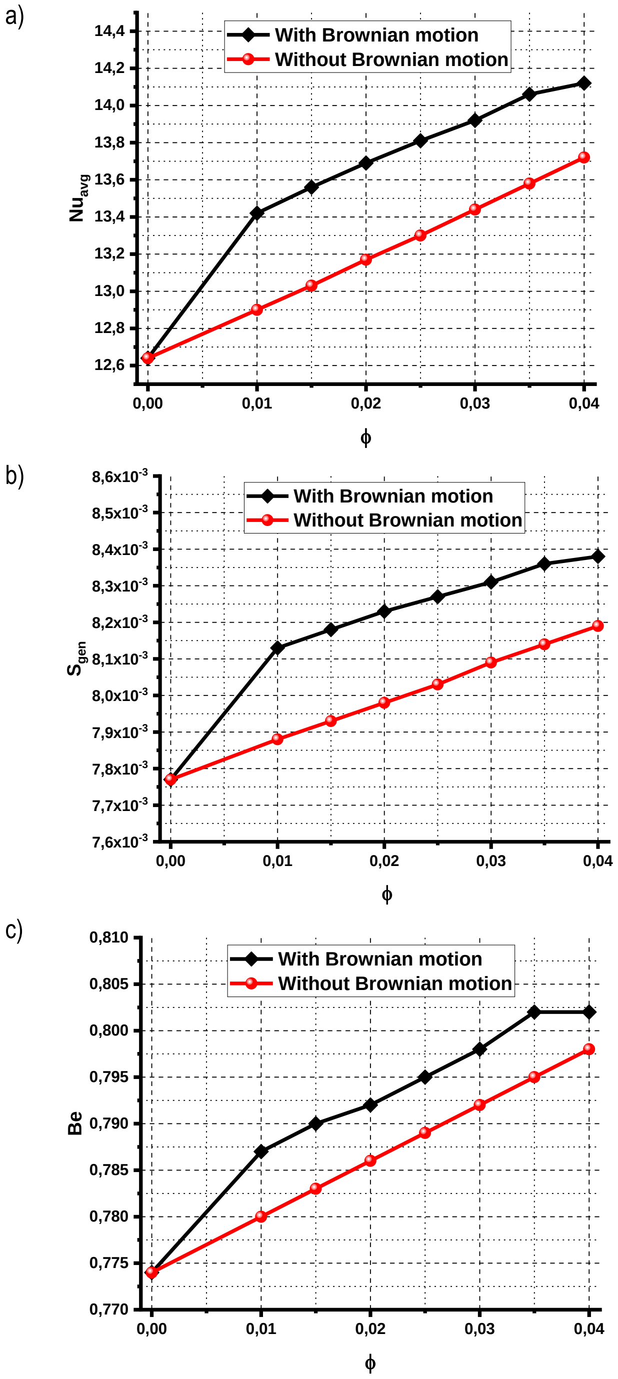

Fig. 13. Impact of Brownian motion on the average Nusselt number (a), S_{gen} (b) and Be (c) for Re = 150, Ha = 50 and $\gamma = 0$

8. CONCLUSIONS

This numerical study performs MHD forced convection in a channel containing a hot block, flowed with a cold nanoliquid at the inlet and crossed with Cu–water nanoliquid. The LBM is used for resolving the governing equations. The flow characteristics is studied under the effect of several parameters ($0\% \le \phi \le 4\%$, 5 nm≤dp≤55 nm, 50≤Re≤200, 0≤Ha≤90, $0 \le \gamma \le \pi$) and Brownian motion. We have given particular attention to the impact of several parameters on velocity and temperature profiles after and behind the hot block. The most important findings are concluded as follows:

- The maximum value of the average Nusselt number is found for case (3) when the hot block is placed between the two hot walls. The minimum value of the average Nusselt number is found for case (2) when the hot block is situated between the two insulated walls. Also, the total entropy generation is minimal for case (2) and maximal for case (1).
- Asϕ, Re and Ha increase, the heat transfer, total entropy generation and Bejan number are enhanced.
- As the size of nanoparticles increases, the heat transfer, total entropy generation and Bejan number reduced.
- The recirculation zone is detected behind the hot block for high values of Re numbers (Re=150), and it has an opposite effect to the Reynolds number on the heat transfer.
- The Hartmann number has a positive effect, and the impact of electromagnetic force is detected for$(Ha > 0)$, so the amplitude of vertical velocity increases.
- The magnetic field inclination angle has a very important role to the orientation of the nanoliquid. Consequently, diminution in the Nuavg about 5.65% when the magnetic field inclination angle changes from $(\gamma = 0)$ to $(\gamma = \pi/2)$.
- The maximum of the total entropy generation is detected with the angle of inclination $(\gamma = \pi/2)$, and the minimum value is detected for the angle of inclination $(\gamma = 0)$.
- The Be reduces with 41.4% for Re=100, and it reduces about 33.3% for Re= 150 when the Ha increases from 0 to 90.
- The results show that the presence of Brownian motion gives an increasing effect on Nuavg, and the total entropy generation is enhanced by 2.4% for the case with Brownian motion compared to the case without Brownian motion.

REFERENCES

1. Karimipour A, Nezhad AH, D'Orazio A, Esfe MH, Safaei MR, Shirani E. Simulation of copper–water nanofluid in a microchannel in slip flow regime using the lattice Boltzmann method. European Journal of Mechanics-B/Fluids. 2015; 49(A):89-99.
2. Sheikholeslami M, Ashorynejad H, Rana P. Lattice Boltzmann simulation of nanofluid heat transfer enhancement and entropy generation. Journal of Molecular Liquids. 2016; 214:86-95.
3. Mishra P, Tiwari A, Chhabra R. Effect of orientation on forced convection heat transfer from a heated cone in Bingham plastic fluids. International Communications in Heat and Mass Transfer. 2018; 93:34-40.
4. Kim SK. Forced convection heat transfer for the fully-developed laminar flow of the cross fluid between parallel plates. Journal of Non-Newtonian Fluid Mechanics. 2020; 276:104226-1042231.
5. Peyghambarzadeh S, Sarafraz MM, Vaeli N, Ameri E, Vatani A, Jamialahmadi M. Forced convective and subcooled flow boiling heat transfer to pure water and n-heptane in an annular heat exchanger. Annals of Nuclear Energy. 2013; 53:401-410.
6. Arasteh H, Mashayekhi R, Goodarzi M, Motaharpour SH, Dahari M, Toghraie D. Heat and fluid flow analysis of metal foam embedded in a double-layered sinusoidal heat sink under local thermal non-equilibrium condition using nanofluid. Journal of Thermal Analysis and Calorimetry. 2019; 138(2):1461-1476.
7. Farooq U, Waqas H, Khan MI, Khan SU, Chu Y-M, Kadry S. Thermally radioactive bioconvection flow of Carreau nanofluid with modified Cattaneo-Christov expressions and exponential space-based heat source. Alexandria Engineering Journal. 2021; 60(3):3073-3086.
8. Xiong P-Y, Hamid A, Chu Y-M, Khan MI, Gowda R, Kumar RN, et al. Dynamics of multiple solutions of Darcy–Forchheimer saturated flow of Cross nanofluid by a vertical thin needle point. The European Physical Journal Plus. 2021; 136(3):1-22.

9. Santra AK, Sen S, Chakraborty N. Study of heat transfer due to laminar flow of copper–water nanofluid through two isothermally heated parallel plates. International journal of thermal sciences. 2009; 48(2):391-400.
10. Heidary H, Kermani M. Effect of nano-particles on forced convection in sinusoidal-wall channel. International Communications in Heat and Mass Transfer. 2010; 37(10):1520-1527.
11. Minakov A, Lobasov A, Guzei D, Pryazhnikov M, Rudyak VY. The experimental and theoretical study of laminar forced convection of nanofluids in the round channel. Applied Thermal Engineering. 2015; 88:140-148.
12. Ma Y, Mohebbi R, Rashidi M, Yang Z. Study of nanofluid forced convection heat transfer in a bent channel by means of lattice Boltzmann method. Physics of Fluids. 2018; 30(3):032001.
13. Ramin M, Erfan K, Omid A. A, Davood T, Mehdi B, Milad G. CFD analysis of thermal and hydrodynamic characteristics of hybrid nanofluid in a new designed sinusoidal double-layered microchannel heat sink. Journal of Thermal Analysis and Calorimetry 2018; 134(3):2305–2315.
14. Mohebbi R, Lakzayi H, Sidik NAC, Japar WMAA. Lattice Boltzmann method based study of the heat transfer augmentation associated with Cu/water nanofluid in a channel with surface mounted blocks. International Journal of Heat and Mass Transfer. 2018; 117:425-435.
15. Lotfi R, Saboohi Y, Rashidi A. Numerical study of forced convective heat transfer of nanofluids: comparison of different approaches. International Communications in Heat and Mass Transfer. 2010; 37(1):74-78.
16. Mahian O, Kolsi L, Amani M, Estellé P, Ahmadi G, Kleinstreuer C, et al. Recent advances in modeling and simulation of nanofluid flows-Part I: Fundamentals and theory. Physics reports. 2019; 790:1-48.
17. Almohammadi H, Vatan SN, Esmaeilzadeh E, Motezaker A, Nokhosteen A. Experimental investigation of convective heat transfer and pressure drop of Al_2O_3/water nanofluid in laminar flow regime inside a circular tube. International Journal of Mechanical and Mechatronics Engineering. 2012; 6(8):1750-1755.
18. Heris SZ, Etemad SG, Esfahany MN. Experimental investigation of oxide nanofluids laminar flow convective heat transfer. International communications in heat and mass transfer. 2006; 33(4):529-535.
19. Ruhani B, Toghraie D, Hekmatifar M, Hadian M. Statistical investigation for developing a new model for rheological behavior of ZnO–Ag (50%–50%)/ Water hybrid Newtonian nanofluid using experimental data. Physica A: Statistical Mechanics and its Applications. 2019; 525:741-751.
20. Abbasi A, Farooq W, Tag-ElDin ESM, Khan SU, Khan MI, Guedri K, et al. Heat transport exploration for hybrid nanoparticle (Cu, Fe3O4) based blood flow via tapered complex wavy curved channel with slip features. Micromachines. 2022; 13(9):1415-1430.
21. Mehrez Z, El Cafsi A.Forced convection magneto-hydrodynamic Al_2O_3–Cu/water hybrid nanofluid flow over a backward-facing step. Journal of Thermal Analysis and Calorimetry. 2019; 135(2): 1417-1427.
22. Hussain S, Ahmed SE. Unsteady MHD forced convection over a backward facing step including a rotating cylinder utilizing Fe3O4-water ferrofluid. Journal of Magnetism and Magnetic Materials. 2019; 484:356-366.
23. Khan MI, Kiyani M, Malik M, Yasmeen T, Khan MWA, Abbas T. Numerical investigation of magnetohydrodynamic stagnation point flow with variable properties. Alexandria Engineering Journal. 2016; 55(3):2367-2673.
24. Chu Y-M, Khan MI, Khan NB, Kadry S, Khan SU, Tlili I, et al. Significance of activation energy, bio-convection and magnetohydrodynamic in flow of third grade fluid (non-Newtonian) towards stretched surface: A Buongiorno model analysis. International Communications in Heat and Mass Transfer. 2020; 118:104893.
25. Peng X, Peterson G. Convective heat transfer and flow friction for water flow in microchannel structures. International journal of heat and mass transfer. 1996; 39(12):2599-2608.
26. Toghraie D, Mashayekhi R, Arasteh H, Sheykhi S, Niknejadi M, Chamkha AJ. Two-phase investigation of water-Al_2O_3 nanofluid in a micro concentric annulus under non-uniform heat flux boundary conditions. International Journal of Numerical Methods for Heat and Fluid Flow. 2019; 30(4):1759-1814.
27. Moraveji A, Toghraie D. Computational fluid dynamics simulation of heat transfer and fluid flow characteristics in a vortex tube by considering the various parameters. International Journal of Heat and Mass Transfer. 2017; 113:432-443.
28. Togun H. Laminar CuO–water nano-fluid flow and heat transfer in a backward-facing step with and without obstacle. Applied Nanoscience. 2016; 6(3):371-378.
29. Alamyane AA, Mohamad AA. Simulation of forced convection in a channel with extended surfaces by the lattice Boltzmann method. Computers and Mathematics with Applications. 2010; 59(7):2421-2451.
30. Anas RQ, Mussa MA. Maximization of heat transfer density from a single-row cross-flow heat exchanger with wing-shaped tubes using constructal design. Heat Transfer. 2021; 50(6):5906-5924.
31. Yang M-H, Yeh R-H, Hwang J-J. Forced convective cooling of a fin in a channel. Energy Conversion and Management. 2010; 51(6):1277-1286.
32. Maia CRM, Aparecido JB, Milanez LF. Heat transfer in laminar flow of non-Newtonian fluids in ducts of elliptical section. International Journal of Thermal Sciences. 2006; 45(11):1066-1072.
33. Khodabandeh E, Rozati SA, Joshaghani M, Akbari OA, Akbari S, Toghraie D. Thermal performance improvement in water nanofluid/GNP–SDBS in novel design of double-layer microchannel heat sink with sinusoidal cavities and rectangular ribs. Journal of Thermal Analysis and Calorimetry. 2019; 136(3):1333-1345.
34. Fanambinantsoa HV, Rakotomanga FdA, Randriaza-namparany MA. Étude numérique de la convection forcée dans un canal rectangulaire horizontal muni d'une protubérance sinusoïdale. Afrique Scince. 2016; 12(6):353-364.
35. Buyruk E, Karabulut K. Enhancement of heat transfer for plate fin heat exchangers considering the effects of fin arrangements. Heat Transfer Engineering. 2018; 39 (15): 1392-1404.
36. Dixit A, Patil AK. Heat transfer characteristics of grooved fin under forced convection. Heat Transfer Engineering. 2015; 36(16): 1409-1416.
37. Ferhi M, Djebali R. Heat Transfer Appraising and Second Law Analysis of Cu-Water Nanoliquid Filled Microchannel: Slip Flow Regime. Romanian Journal of Physics. 2022; 67:605-630.
38. Mejri I, Mahmoudi A, Abbassi MA, Omri A. Magnetic field effect on entropy generation in a nanofluid-filled enclosure with sinusoidal heating on both side walls. Powder Technology.2014; 266:340-353.
39. Atashafrooz M, Sheikholeslami M, Sajjadi H, Delouei AA. Interaction effects of an inclined magnetic field and nanofluid on forced convection heat transfer and flow irreversibility in a duct with an abrupt contraction. Journal of Magnetism and Magnetic Materials. 2019; 478:216-226.
40. Ferhi M, Djebali R, Mebarek-Oudina F, Abu-Hamdeh NH, Abboudi S. Magnetohydrodynamic Free Convection Through Entropy Generation Scrutiny of Eco-Friendly Nanoliquid in a Divided L-Shaped Heat Exchanger with Lattice Boltzmann Method Simulation. Journal of Nanofluids.2022; 11(1):99-112.
41. Djebali R, Jaouabi A, Naffouti T, Abboudi S. Accurate LBM appraising of pin-fins heat dissipation performance and entropy generation in enclosures as application to power electronic cooling. International Journal of Numerical Methods for Heat and Fluid Flow. 2019; 30(2):742-768.
42. Zou Q, He X. On pressure and velocity boundary conditions for the lattice Boltzmann BGK model. Physics of fluids. 1997; 9(6):1591-1598.
43. Mohamad A. Lattice Boltzmann Method: Fundamentals and Engineering Applications with Computer Codes: Springer Science and Business Media; 2011:70.

44. Brinkman HC. The viscosity of concentrated suspensions and solutions. The Journal of chemical physics. 1952; 20(4):571-579.
45. Koo J, Kleinstreuer C. Laminar nanofluid flow in microheat-sinks. International journal of heat and mass transfer. 2005; 48(13):2652-2661.
46. Hussain S, Ahmed SE, Akbar T. Entropy generation analysis in MHD mixed convection of hybrid nanofluid in an open cavity with a horizontal channel containing an adiabatic obstacle. International Journal of Heat and Mass Transfer. 2017; 114:1054-1066.
47. Tang G, Tao W, He Y. Simulation of fluid flow and heat transfer in a plane channel using the lattice Boltzmann method. International journal of modern physics B. 2003; 17(1):183-187.
48. Izadi M, Mohebbi R, Karimi D, Sheremet MA. Numerical simulation of natural convection heat transfer inside a⊥ shaped cavity filled by a MWCNT-Fe3O4/water hybrid nanofluids using LBM. Chemical Engineering and Processing-Process Intensification. 2018; 125:56-66.

Acknowledgement: This work was supported by the Tunisian Ministry of Higher Education and Scientific Research under grant 20/PRD-22.

Rached Miri: https://orcid.org/0000-0001-9113-5370

Mohamed A. Abbassi: https://orcid.org/0000-0002-1915-0944

Mokhtar Ferhi: https://orcid.org/0000-0002-6677-3335

Ridha Djebali: https://orcid.org/0000-0002-1017-3410